Spin transfer effects in nanopillars with perpendicular magnetizations

Julien Cucchiara

To cite this version:

Julien Cucchiara. Spin transfer effects in nanopillars with perpendicular magnetizations. Other [cond-mat.other]. Université Henri Poincaré - Nancy 1, 2011. English. NNT : 2011NAN10008 . tel-01746394v1

HAL Id: tel-01746394
https://hal.univ-lorraine.fr/tel-01746394v1

Submitted on 29 Mar 2018 (v1), last revised 17 Aug 2011 (v2)

U.F.R. Faculté des Sciences et Technologies
Ecole doctorale EMMA
D.F.D. Physique, spécialité Nanosciences

Thèse

présentée pour obtenir le grade de

Docteur de l'Université Henri Poincaré
Nancy Université

en Physique

par Julien CUCCHIARA

Spin-transfer effects in nanopillars with perpendicular magnetizations

---

Effets de transfert de spin dans des nanopiliers aux aimantations perpendiculaires

Soutenue publiquement le 18 janvier 2011 devant le jury composé de

Président	M. Daniel Malterre	Professeur de l'Université Henri Poincaré
Rapporteurs	M. Russel Cowburn	Professeur de l'Université de Cambridge
	M. Vincent Cros	Directeur de recherche du CNRS
Examinateurs	M. Eric Fullerton	Professeur de l'Université de Californie San Diego
	M. Andrew Kent	Professeur de l'Université de New York
	M. Dafiné Ravelosona	Directeur de recherche du CNRS
Directeur de thèse	M. Stéphane Mangin	Professeur de l'Université Henri Poincaré

Thèse préparée au sein de l'Institut Jean Lamour, UMR CNRS 7198, Nancy Université, France

Contents

Acknowledgments
Remerciements

Ce travail de thèse a été réalisé au sein de l'Institut Jean Lamour à Nancy. Je tiens donc particulièrement à remercier son directeur, M. Jean-Marie Dubois, ainsi que le directeur du département de Physique de la Matière et des Matériaux et de l'ancien laboratoire de Physique des Matériaux où cette thèse a débuté, M. Michel Vergnat.

Je souhaite également remercier les membres de mon jury de thèse qui ont accepté d'analyser ce travail. Je remercie M. Daniel Malterre d'avoir présidé ce jury et MM. Russel Cowburn et Vincent Cros d'avoir accepté d'être les rapporteurs de ce manuscrit. Je remercie MM. Eric Fullerton, Andrew Kent et Dafiné Ravelosona pour leur participation à ce jury. J'aimerais aussi les remercier d'avoir fait le déplacement, parfois de très loin, jusqu'à Nancy pour assister à ma soutenance.

Ce travail n'aurait pas été possible sans la supervision de Stéphane Mangin, mon directeur de thèse. Je suis très content d'avoir travaillé avec toi durant bientôt plus de quatre ans, depuis mon stage de master en réalité. Je dois dire que la pertinence de tes remarques et de ta direction ainsi que ta gentillesse et ton attention ont énormément contribué à rendre mes années de doctorat très enrichissantes aussi bien sur le plan scientifique que sur le plan humain. Je garderai toujours un très bon souvenir de nos discussions, parfois animées, autour d'un tableau parsemé de flèches se concluant souvent par des questions sans réponse mais aussi quelque fois par la sensation grisante d'avoir progressé dans la compréhension de nos systèmes.

Evidemment, un travail de thèse se nourrit des échanges et des collaborations que l'on peut nouer avec d'autres chercheurs et laboratoires. Je tiens à remercier Yves Henry de l'Institut de Physique et Chimie des Matériaux de Strasbourg pour avoir partagé son savoir-faire avec moi pour le wire-bonding et la mesure électrique de ces échantillons ainsi que pour les discussions fructueuses que nous avons eues autour de la compréhension de leur diagramme de phase. Je tiens à re-

mercier également Liliana Buda-Prejbeanu que j'ai eu le plaisir de rencontrer dès le début de ma thèse durant l'Ecole Européenne de Magnétisme à Cluj-Napoca en Roumanie et qui m'a beaucoup aidé à démarrer mes simulations micromagnétiques. J'ai eu la chance de pouvoir discuter également de mes résultats avec beaucoup de chercheurs rencontrés à divers moments de ma thèse et je tiens à les remercier pour leur écoute, leurs encouragements et leurs suggestions : Eric Fullerton de l'Université de Californie San Diego, Dafiné Ravelosona de l'Institut d'Electronique Fondamentale à Orsay, Andrew Kent de l'Université de New York, Andreas Berger du laboratoire NanoGUN à San Sebastian, Peter Fischer du Lawrence Berkeley National Laboratory, Jean-Philippe Attané de l'INAC à Grenoble et Günter Dumpich de l'Université de Duisburg-Essen.

Tout au long de ma thèse, j'ai également bénéficié de l'aide et du soutien des membres de mon laboratoire. Tout d'abord, je remercie Daniel Lacour et François Montaigne pour toute leur disponibilité et l'aide qu'ils m'ont apportée avec les mesures de transport : que ce soit mes premiers pas avec Monique et Thérèse, le montage de mon propre banc de transport ou la programmation sur LabView. Je tiens également à remercier Michel Hehn pour les discussions toujours très instructives que nous avons eues sur la propagation de parois dans des nanopiliers et les simulations micromagnétiques. Merci à Christine Bellouard pour son aide avec les mesures à basse température. Dommage qu'elles n'aient pu aboutir. Je voudrais aussi remercier toute les équipes techniques et administratives du laboratoire qui nous facilitent le travail au quotidien. Je pense en particulier à Christian Senet pour sa gestion du parc informatique et ses explications pédagogiques, à Laurent Bouvot pour le wire-bonding, à Stéphane Suire pour son aide dans le montage des bancs de transport, à Damien Engeldinger pour toutes ses réparations et installations diverses, à Jean-Georges Mussot pour ces portes-échantillons, à Pierre Schmitt pour ses conseils en électronique, à Hélène Huon, Martine Gaulier et Valérie Madeline pour leur travail avec l'administration et la comptabilité et à Martine pour son entretien des bureaux. Un grand merci à tous les membres l'équipe Nanomagnétisme et Electronique de spin pour le très bon accueil que vous m'avez réservé et grâce à qui mon ambiance de travail a toujours été agréable. En plus de ceux déjà cités plus haut, je remercie Marc Alnot, Stéphane Andrieu, Catherine Dufour, Karine Dumesnil, Hélène Fischer, Thomas Hauet, Gwladys Lengaigne, Olivier Lenoble, Yuan Lu, Hamid M'Jahed, Danielle Pierre, Sylvie Robert et Coriolan Tiusan.

Je ne voudrais pas oublier mes collègues thésards et post-doctorants. Tout d'abord Fanny Greullet et Frédéric Bonell avec qui j'ai partagé de très bon mo-

ments en Roumanie et à Strasbourg. Je pense aussi à Matthias Gottwald, Béatrice Négulescu, Stéphanie Girod, Amandine Duluard, Christel Berthelot, Nicolas Gonzalez, Julien Bernos, Weiwei Lin, Kaname Mitsuzuka et Hanna Riahi.

Je remercie aussi toutes les équipes de l'Université Henri Poincaré qui m'ont accompagné dans mes premières années d'enseignant. Je pense en particulier à Isabelle Boucher ma tutrice pendant mes trois années de monitorat.

Je tiens également à remercier tout les professeurs qui m'ont encouragé au cours de ma scolarité à poursuivre mon travail jusqu'à ce niveau. Pour mes études secondaires, je pense en particulier à Mme Jambois, à Mme Hervé et à M. Wisnicki. Pour mes études supérieures, je pense à mes professeurs de physique et de chimie de classes préparatoires, Mmes Lartigue, Sanz et Brichet ainsi que M. Mallet, grâce auxquelles j'ai appris tant de choses qu'il m'aura fallu plusieurs années pour les digérer et peut-être même encore plusieurs. Je remercie également Marie-Odile Selme à l'Ecole des Mines de Nancy pour tous ces encouragements à poursuivre dans la voie de la recherche.

Un grand merci à tous ceux grâce à qui j'ai profité de ces années nancéiennes. Je pense aux mémés et au tachyon. Un grand merci à tous mes amis de Nancy-Sud grâce pour votre soutient et votre compagnie qui m'ont aidé à bien évoluer durant mes années de doctorat. En particulier, un grand merci à Jo et sa puce.

Enfin, je voudrais remercier ceux qui m'ont permis de poursuivre mes études jusque là, sans encombre : mes parents. Merci pour votre soutien, votre éducation et votre affection. Et un grand merci à ma grande soeur pour tous ses encouragements !

List of notations

Here is a list of the main notations used in this manuscript.

A_{exc}	Exchange constant
α	Damping constant
β	Spin transfer constant
E	Magnetic energy
E_{ani}	Magnetocrystalline anisotropy energy
E_{dem}	Demagnetizing field energy
E_{dip}	Dipolar field energy
E_{exc}	Exchange energy
e	Elementary charge
ε_{F}	Energie at the Fermi level
$\mathcal{G}(\theta)$	Angular dependence function of the spin transfer torque
Γ_{dam}	Damping torque
Γ_{eff}	Effective field torque
Γ_{str}	Spin transfer torque
γ	Gyromagnetic ratio
H	Magnetic field
H_{ani}	Anisotropy field
H_{c}	Coercive field
H_{dem}	Demagnetizing field
H_{dip}	Dipolar field
H_{eff}	Effective magnetic field
$\hbar$	Reduced Planck constant
I	Intensity of the electric current
K	Anisotropy constant
$\mathcal{L}$	Angular momentum
$\mathcal{L}_{\mathrm{o}}$	Orbital angular momentum
$\mathcal{L}_{\mathrm{s}}$	Spin angular momentum

$\mathcal{M}$	Magnetic moment
$\mathcal{M}_{\mathrm{o}}$	Orbital magnetic moment
$\mathcal{M}_{\mathrm{s}}$	Spin magnetic moment
M	Magnetization
M_{s}	Saturation magnetization
m	Mass of an electron
$\boldsymbol{m}$	Unitary vector in the direction of the free layer magnetization
μ	Chemical potential
μ_0	Permeability of free space
μ_{B}	Bohr magneton
P	Spin polarization of the current
$\boldsymbol{p}$	Unitary vector in the direction of the polarizer magnetization
R_{AP}	Resistance of the antiparallel state of a spin valve
R_{P}	Resistance of the parallel state of a spin valve
ρ	Resistivity
T_{C}	Curie temperature
$\%_{\mathrm{GMR}}$	Giant magnetoresistance ratio

Introduction

The 2007 Nobel prize awarded to Albert Fert and Peter Grünberg highlighted the outstanding evolution of spintronics from fundamental researches on spin dependent transport in magnetic multilayers to applications in magnetic data storage technologies. Nowadays, electronic devices are mainly based on the electric properties of the electrons, linked to their electric charge. In addition to these properties, spintronics intends to make the most of the magnetic properties of the electrons, linked to their spin angular momentum, to fabricate efficient new devices. Starting from the discovery of the giant magnetoresistance effect[1,2] in 1988, which was awarded by the Nobel prize mentioned above, spintronics quickly progressed during the nineties. Thanks to a better control of nanofabrication processes, the development of the spin-valve structure and of the magnetic tunnel junctions lead to the first industrial success of spintronics: giant magnetoresistive read heads. They helped to increase significantly the density of information stored on a hard disk drive insomuch that every hard drives have been equipped with this type of read head for almost ten years. A new kind of memory device based on the giant magnetoresistance effect is also now available on the market: the Magnetic Random Access Memory or M-RAM. It combines the advantages of the random access memories such as a quick access to the stored information with a permanent storage.

In 1996, Luc Berger and John Slonczewski predicted a new promising phenomenon: the spin-transfer effect[3,4]. It is a direct consequence of the conservation law of the angular momentum. Indeed, a spin polarized current where the spins of the conduction electrons have a preferential orientation, carries a spin angular momentum. Injected through a magnetic layer, a part of this angular momentum can be transferred to the magnetization which will be set in motion. The first experimental demonstrations of current induced magnetization dynamics quickly followed these predictions and gave birth to lots of new exciting physics allowing to manipulate a magnetization without a magnetic field. It generates mainly three new behaviors: current-induced switching[5], current-induced precessions of magnetization[6–8] or more recently vortex oscillations[9] and current-induced domain wall motion[10,11]. All of them are interesting from an industrial perspective. Current-induced switching may be very helpful to increase the storage density of M-RAMs. For that matter, some prototypes using this effect are currently developed by companies such as Hitachi, Sony or Toshiba. Current-induced precessions of magnetization or vortex oscillations could also generate a new generation of scalable high frequency oscillators to improve telecommunication devices. In the end, many patterns were registered over the last years based on current-induced domain wall motion to fabricate solid state memories with very high storage density. Among them, the most famous project certainly is the race-track memory proposed by Stuart Parkin from IBM[12].

On top of the limitations of spin-transfer technologies is the high current density of the order of 10^7 A.cm^{-2} needed to observe this phenomenon. Experimentally, electron beam lithography is used to reduce the spin-valves to nanopillars or nanowires with lateral dimensions close to 100 nm so that the critical currents required to observe spin-transfer are of the order of few mA. All the first experiments on spin-transfer were performed on in-plane magnetized samples. A lot of results were quickly obtained for switching, precession and domain wall motion but still many problems remain unsolved. During this thesis, we focused on the switching behavior of nanopillar spin-valves with out-of-plane magnetizations where the critical currents can be scaled down more easily[13]. Moreover, thanks to their high symmetry, they form model systems. The first results[14–16] on this configuration were published in 2006. To understand their behavior we studied the effect of the magnetic field and of the spin polarized current on the two processes ruling the reversal: domain nucleation and domain wall propagation.

This manuscript is divided into five parts. The first part consists in a state of the art both experimental and theoretical about magnetism leading to the description of the spin-transfer effect. The second part presents the samples studied during this thesis and the experimental setup used to measure their properties. The third part deals with the global understanding of these samples behavior under the application of a magnetic field and of a spin polarized current thanks to the study of a special figure called a phase diagram. The fourth part focuses on the influence of a magnetic field and of a spin polarized current on domain wall states present inside these samples with perpendicular magnetizations but not observed with in-plane magnetized devices. Finally, the fifth part is composed of appendices to complete or clarify the previous parts.

French introduction

Introduction

La remise du prix Nobel de physique 2007 à Albert Fert et Peter Grünberg pour leur découverte conjointe de la magnétorésistance géante a mis en lumière l'incroyable évolution de l'électronique de spin. En effet, quelques années ont suffi à transférer les efforts de recherche fondamentale sur le transport dépendant du spin dans des hétérostructures magnétiques vers des applications indispensables à l'avancée de l'industrie du stockage de données sur support magnétique, applications dont chaque utilisateur d'ordinateur bénéficie aujourd'hui. Jusqu'à présent, les dispositifs électroniques exploitaient uniquement les propriétés électriques des électrons liées à leur charge. L'électronique de spin y ajoute l'exploitation de leurs propriétés magnétiques afin de développer de nouveaux dispositifs. L'acte fondateur de l'électronique de spin a été la découverte de la magnétorésistance géante[1,2] en 1988. Dès lors, les progrès ont été fulgurants. Grâce à un meilleur contrôle des processus de nanofabrication, le développement de structures dites de vanne de spin et des jonctions tunnels magnétiques a conduit au premier succès industriel de l'électronique de spin : les têtes de lecture magnétorésistives. Cette avancée a permis d'augmenter de manière significative les capacités de stockage des disques durs à tel point que tous les disques durs fabriqués depuis dix ans en sont équipés. Dernièrement, un nouveau type de mémoires magnétiques basé sur l'effet de magnétorésistance géante est devenu disponible dans le commerce, les mémoires magnétiques à accès aléatoire ou M-RAMs selon leur anacronyme anglophone. Elles combinent à la fois la rapidité d'accès aux données des mémoires à accès aléatoire avec un stockage permanent de l'information.

En 1996, Luc Berger et John Slonczewski prédirent théoriquement l'existence d'un nouveau phénomène : le transfert de spin[3,4]. Il s'agit en réalité d'une conséquence directe de la loi de conservation du moment cinétique. En effet, un courant polarisé en spin, c'est à dire dont les spins des électrons qui le composent possèdent une orientation privilégiée, transporte un moment cinétique. Ainsi peut-il en transférer une partie à l'aimantation d'une couche magnétique qu'il traverse. Elle se met alors en mouvement. Les premières démonstrations expérimentales de ce phénomène suivirent rapidement ces prédictions et donnèrent naissance à toute une nouvelle physique où une aimantation est manipulée sans champ magnétique. Trois effets sont principalement observés grâce au transfert de spin : le renversement d'aimantation induit par un courant polarisé en spin[5], la précession de l'aimantation induite par courant polarisé en spin[6–8] ou plus récemment les oscillations de vortex induites par courant polarisé en spin[9] et la propagation de paroi de domaines magnétiques par un courant polarisé en spin[10,11]. Tous les trois sont prometteurs d'un point de vue industriel. En effet, le renversement d'aimantation par courant polarisé en spin est une piste très sérieuse pour améliorer les capacités de stockage des M-RAMs. Certains prototypes ont d'ailleurs été développés par de grandes firmes telles qu'Hitachi, Sony ou Toshiba. La précession de l'aimantation induite par courant polarisé en spin pourrait permettre l'arrivée d'une nouvelle génération d'oscillateurs à hautes fréquences pour l'industrie des télécommunications. Enfin, beaucoup de brevets ont été déposés ces dernières années exploitant le déplacement de paroi sous courant polarisé en spin pour élaborer des mémoires solides à haute capacité de stockage. Parmi tous ces projets, le plus célèbre est certainement celui de « *race-track memory* » proposé par Stuart Parkin de la société IBM[12].

Cependant, ces potentiels d'applications sont à l'heure actuelle fortement limités par la densité de courant nécessaire à l'apparition du transfert de spin, de l'ordre de 10^7 A.cm^{-2}. Expérimentalement, les échantillons sont réduits à la taille de nanopiliers d'environ 100 nm de côté grâce à la lithographie électronique de sorte que les courants critiques à injecter soient de l'ordre de quelques milliampères. Les premières expériences sur le transfert de spin ont exploité des couches magnétiques à aimantation planaire plus facile à élaborer. D'importants résultats ont été obtenus grâce à cette géométrie dans tous les domaines évoqués plus haut mais beaucoup d'interrogations restent néanmoins sans réponse. Durant cette thése, nous nous sommes intéresser à une nouvelle géométrie utilisant des couches magnétiques à aimantation perpendiculaire. C'est en 2006 que les premiers résultats dans cette configuration ont été publiés[14–16]. Ces échantillons possèdent deux avantages majeurs : la possibilité de réduire les courants critiques et surtout une symétrie importante qui en fait des systèmes modèles. Afin de mieux comprendre leur comportement, nous avons étudiés l'effet d'un champ magnétique et d'un courant polarisé en spin sur les deux processus à l'origine du renversement de l’aimantation dans ces systèmes : la nucléation de domaine et la propagation de paroi de domaines.

Ce manuscrit se divise en cinq parties. La première consiste en un état de l’art expérimental et théorique des connaissances actuelles sur le magnétisme permettant d’appréhender le phénomène de transfert de spin. La seconde partie présente les échantillons étudiés pour cette thèse et le dispositif permettant la mesure de leurs propriétés. La troisième partie s’intéresse à la compréhension globale du comportement de ces échantillons en champ magnétique et en courant polarisé en spin grâce à l’interprétation d’une figure appelée diagramme de phase. Elle représente les différents états magnétiques disponibles pour un échantillon sur une carte champ courant et son étude permet de dégager les principales influences à l’origine de leur comportement. La quatrième partie se focalise sur l’influence du champ magnétique et du courant polarisé en spin sur des parois de domaines présentes dans ces échantillons dans des configurations qui ne sont pas observées dans les géométries planaires. Enfin, la cinquième et dernière partie se compose d’annexes venant compléter ou préciser certaines des parties précédentes.

Part I

State of the art
Etat de l'art

French summary

Résumé en français

Cette partie présente un état de l'art des connaissances actuelles en magnétisme liées à la compréhension du phénomène de transfert de spin. Après s'être intéressé dans le premier chapitre à la dynamique d'aimantation et avoir présenté les différentes interactions à l'origine du comportement magnétique d'un matériau, le second chapitre traite du phénomène de magnétorésistance géante. Le troisième chapitre explique le phénomène de transfert de spin. Pour finir, l'impact de l'activation thermique sur la dynamique de l'aimantation est introduit dans le dernier chapitre.

La plupart des atomes présents dans la nature possèdent un moment magnétique lié à la précession de leurs électrons autour de leur noyau et à une contribution intrinsèque de ces électrons, leur spin. Pourtant, la plupart des solides ne sont pas magnétiques. En effet, l'environnement électronique des atomes dans cet état de la matière est modifié si bien qu'ils perdent généralement leurs propriétés magnétiques. Il s'agit de l'effet du champ cristallin. Les atomes doivent posséder, en réalité, des sous-couches électroniques incomplètes suffisamment profondes pour former un solide magnétique. Ce dernier est alors souvent caractérisé par son aimantation.

Différentes interactions sont à l'origine du comportement d'un solide magnétique. Tout d'abord, l'interaction d'échange ordonne les moments magnétiques des atomes du solide. Il s'agit d'une interaction à courte portée liée à la compétition entre la répulsion coulombienne des électrons et le principe d'exclusion de Pauli. Les deux principaux ordres magnétiques générés par cette interaction sont le ferromagnetisme où tous les moments magnétiques sont alignés dans la même direction et l'antiferromagnétisme où deux moments magnétiques consécutifs sont orientés dans des directions opposées (voir figure 1.3 page 19). Un ferromagnétique possède donc une aimantation non-nulle contrairement à un antiferromagnétique. D'autres ordres magnétiques peuvent exister tels que le ferrimagnétisme ou l'hélimagnétisme. Dans tous les cas, ils n'apparaissent que si l'agitation thermique est suffisamment faible pour permettre cet ordonnancement. L'application d'un champ magnétique à un ferromagnétique génère une interaction entre ce champ et l'aimantation de l'aimant. Il s'agit de l'interaction Zeeman. Elle a tendance à positionner cette aimantation dans la direction du champ magnétique appliqué. L'aimantation d'un ferromagnétique génère également un champ magnétique dans l'espace. Lorsqu'on considère l'interaction de ce champ magnétique avec l'aimantation d'un autre ferromagnétique, on parle d'interaction du champ dipolaire. En revanche, lorsqu'on considère l'interaction de ce champ magnétique généré par un ferromagnétique sur lui-même, on parle d'interaction du champ démagnétisant car il s'oppose généralement à l'aimantation qui lui donne naissance. Cette dernière interaction crée des directions privilégiées d'orientation de l'aimantation dans l'espace dépendantes de la géométrie du solide. Elle est donc aussi appelée anisotropie de forme. Enfin, la dernière grande interaction présente dans les solides magnétiques est l'anisotropie magnétocristalline. Liée au couplage spin-orbite, elle oriente l'aimantation dans des directions cristallographiques privilégiées du solide. La compétition entre ces interactions génère différents comportements magnétiques. Par exemple, la compétition entre l'interaction d'échange et l'interaction du champ démagnétisant peut briser l'aimantation uniforme d'un solide ferromagnétique en plusieurs domaines magnétiques d'aimantations opposées (voir figure 1.6 page 23). A la frontière entre chaque domaine, l'aimantation évolue continuement et forme une paroi de domaine magnétique dont la taille dépend de la compétition entre l'interaction d'échange et l'anisotropie magnétocristalline. Le renversement hystérétique de l'aimantation d'un ferromagnétique est, quant à lui, lié à la compétition entre l'interaction Zeeman et l'anisotropie magnétocristalline (voir figure 1.7b page 25).

La prise en compte de toutes ces interactions permet de décrire l'évolution temporelle de la trajectoire d'une aimantation grâce à l'équation Landau-Lifshitz-Gilbert (LLG) :

$$\frac{d\boldsymbol{m}}{dt} = -\gamma_0 \boldsymbol{m} \times \boldsymbol{H}_{\mathbf{eff}} + \alpha \boldsymbol{m} \times \frac{d\boldsymbol{m}}{dt}$$

où $\boldsymbol{m}$ est un vecteur unitaire dans la direction de l'aimantation. Chaque interaction décrite précédemment se traduit par l'action de plusieurs champs magnétiques sur l'aimantation dont la résultante est appelée le champ effectif noté $\boldsymbol{H}_{\mathbf{eff}}$. Le premier terme dans la partie droite de l'équation représente donc le couple exercé sur l'aimantation par toutes ces interactions. Le second terme est un terme phénomènologique ajouté de façon à ce que l'aimantation finisse par s'aligner dans la direction du champ effectif (voir figure 1.8b page 27). Cette équation est incontournable pour l'étude de la dynamique d'aimantation.

Le phénomène de magnétorésistance géante s'observe dans des empilements de couches magnétiques séparées par des couches non-magnétiques. Il se manifeste par une forte variation de la résistance d'une hétérostructure magnétique sous l'effet d'un champ magnétique (voir figure 2.1 page 30). La plus simple structure utilisée pour étudier ce phénomène est une vanne de spin constituée de deux couches magnétiques séparées par une couche non-magnétique mais conductrice découplant magnétiquement les deux autres couches. Si cette dernière couche est isolante, on parle d'une jonction tunnel magnétique. Généralement, les couches magnétiques présentes dans une vanne de spin possèdent un axe d'orientation privilégié de l'aimantation identique. Cependant, une des deux couches est dite plus dure que l'autre car retourner son aimantation nécessite l'application d'un plus grand champ magnétique. Ainsi, la vanne de spin existe dans deux états magnétiques différents : un état parallèle où les deux aimantations pointent dans la même direction et un état antiparallèle où elles pointent dans des directions opposées.

La magnétorésistance géante résulte de l'effet de filtrage de spin qu'exerce une couche magnétique sur les électrons de conduction la traversant. Dans le cas d'un filtrage parfait, une couche magnétique ne laisse passer que les électrons de conduction dont le spin est orienté dans la même direction que son aimantation. Les autres sont réfléchis à l'interface. Par conséquent, dans l'état parallèle, une direction de spin va pouvoir se propager à travers la structure et conduire le courant alors que la direction opposée ne pourra pas être transmise (voir figure 2.3a page 33). En revanche, dans l'état antiparallèle, aucune direction de spin ne peut se propager (voir figure 2.3b page 33). Le courant ne peut donc pas circuler. L'état parallèle est donc un état de faible résistance comparé à l'état antiparallèle. Comme le champ magnétique permet de passer d'un état à l'autre, la résistance de la vanne de spin dépend fortement du champ magnétique appliqué. Dans la réalité, le courant peut toujours circuler mais plus ou moins facilement suivant la configuration magnétique de la vanne de spin.

Lorsque le courant est injecté perpendiculairement aux couches de la structure, la traversée de la première couche magnétique polarise le courant dans une direction privilégiée de l'espace. Pour que l'effet de magnétorésistance géante soit observable, il est donc nécessaire que cette polarisation soit conservée à travers la couche non-magnétique jusqu'à la seconde couche magnétique. Cela est possible car à l'interface entre un matériau ferromagnétique et un matériau conducteur non-magnétique une accumulation de spin se produit. Cette accumulation entraîne la diffusion d'un courant polarisé en spin à travers la couche conductrice sur une distance caractéristique liée à la longueur de diffusion de spin. Cette longueur correspond à la distance moyenne parcourue par un électron avant de renverser son spin. Ce phénomène limite l'épaisseur des couches utilisées à quelques dizaines de nanomètres de manière à conserver une bonne polarisation d'où l'intérêt du développement des techniques de nanofabrications.

Le phénomène de transfert de spin s'observe également dans une structure vanne de spin. Tout comme pour la magnétorésistance géante, la première couche magnétique sert à polariser le courant électrique qui est ensuite injecté vers la seconde couche magnétique à travers la couche conductrice. Le transfert de spin est lié à la conservation du moment cinétique d'un système. En effet, lorsque le courant polarisé en spin traverse la seconde couche magnétique, le spin de ses électrons va s'orienter parallèlement à l'aimantation de cette couche. Par conséquent, leur moment cinétique va varier (voir figure 3.2 page 41). Il est alors possible d'envisager l'absorption de cette variation par l'aimantation de la couche magnétique de manière à conserver le moment cinétique total de la structure. Cette prédiction théorique a été démontrée expérimentalement à de nombreuses reprises depuis le début des années 2000. Il est donc possible d'agir sur le comportement d'une aimantation grâce à l'injection d'un courant polarisé en spin.

Plusieurs études théoriques cherchent à expliquer l'origine physique du transfert de spin ainsi qu'à reproduire les résultats expérimentaux. Néanmoins, aucune à ce jour n'y est entièrement parvenue. Parmi toutes ces théories, ce manuscrit présente en détail un raisonnement développé par Mark Stiles, qui a l'avantage d'être abordable avec quelques notions de mécanique quantique et qui s'interprète facilement d'un point de vue physique. Au final, toutes ces théories calculent le couple de transfert de spin qui traduit l'action du courant polarisé sur l'aimantation. Il peut être ensuite directement ajouté aux couples du champ effectif et d'amortissement présents dans l'équation LLG. De manière générale, ce couple peut s'écrire de la façon suivante :

$$\frac{\mathbf{\Gamma_{str}}}{M_{\mathrm{s}}} = -\beta I \mathcal{G}(\theta) \boldsymbol{m} \times (\boldsymbol{m} \times \boldsymbol{p})$$

où β est une constante, I l'intensité du courant injecté, $\mathcal{G}(\theta)$ une fonction qui traduit la dépendance du couple de transfert de spin vis-à-vis de l'orientation relative des deux aimantations de la vanne de spin, $\boldsymbol{m}$ l'orientation de l'aimantation de la couche sur laquelle le courant polarisé agit et $\boldsymbol{p}$ l'orientation de l'aimantation de la couche polarisant le courant électrique. La différence principale entre toutes les théories existantes est la forme de la dépendance angulaire du couple de transfert de spin (voir figure 3.3 page 46). Grâce à cette expression du couple de transfert de spin, on peut montrer que son action est similaire à celle du couple d'amortissement (voir figure 3.4 page 47). Son signe dépend du sens d'injection du courant électrique. Il peut donc soit s'ajouter à l'amortissement et favoriser un retour à l'équilibre plus rapide, soit s'y opposer. S'il le compense exactement, alors l'aimantation entre dans un mouvement de précession auto-entretenue autour de la direction du champ effectif. S'il est plus important, alors il peut entrainer un renversement de l'aimantation. Il est donc possible d'obtenir un renversement hystérétique de l'aimantation d'une couche magnétique uniquement grâce à l'injection d'un courant électrique (voir figure 3.5 page 48).

Cette thèse s'intéresse exclusivement aux vannes de spin dont l'aimantation des couches magnétiques est perpendiculaire aux plans de ces couches. L'intérêt de ces structures par rapport à celles dont les aimantations sont dans le plan des couches est d'avoir un système avec une forte symétrie. Il s'agit donc de système modèle où l'étude du transfert de spin est facilité. De plus, cette géométrie permet de diminuer les courants critiques nécessaires pour renverser une aimantation. L'efficacité de cette méthode a été prouvée à maintes reprises. Néanmoins, très peu d'études ont été réalisées afin d'étudier en détail les phénomènes de renversement d'aimantation dans ces structures. D'où l'intérêt de ce travail de thèse. On peut également noter que d'autres structures existent. Elles mixent des couches à aimantation perpendiculaire et à aimantation planaire souvent afin d'optimiser les phénomènes de précession de l'aimantation induite par courant polarisé en spin. Dans cette thèse, nous nous sommes focalisé principalement sur les processus de renversement de l'aimantation.

Toutes les mesures présentées dans ce manuscrit ont été obtenues à température ambiante. Or, l'agitation thermique affecte fortement la dynamique de l'aimantation. Celle-ci est prise en compte dans l'équation LLG par l'introduction d'un nouveau champ magnétique s'ajoutant au champ effectif. Il correspond à un bruit blanc de moyenne temporelle nulle dont l'intensité varie avec la température.

Du fait de l'activation thermique, le renversement de l'aimantation devient stochastique. On définit alors une probabilité temporelle de renversement dont l'augmentation attendue est exponentielle :

$$P_{\mathrm{rev}}\left(t\right) = 1 - \exp\left(-\frac{t}{\tau}\right) \text{ avec } \tau = \tau_0 \exp\left(\frac{E_{\mathrm{b}}\left(H\right)}{k_{\mathrm{B}}T}\right)$$

où τ est un temps caractéristique de vie de l'état magnétique considéré. Ce temps dépend du temps caractéristique de fluctuation de l'aimantation noté τ_0, de la hauteur d'énergie de barrière $E_{\mathrm{b}}\left(H\right)$ entre les deux états magnétiques de la vanne de spin et de la température notée T (voir figure 4.1 page 52). Les expériences ont souvent permis de vérifier la fiabilité de ce modèle dit de Néel-Brown.

Dans le développement précédent, l'effet du transfert de spin n'a pas été pris en compte dans l'expression du temps de vie. Le problème est que l'action du courant ne peut pas se traduire directement dans l'expression d'une énergie de barière car le transfert de spin place le système dans un état hors équilibre. Néanmoins, grâce à une approche basée sur le théorème de fluctuation-dissipation, il est possible de prédire son effet théorique. L'expression du temps de vie devient alors :

$$\tau = \tau_0 \exp\left[\frac{E_{\mathrm{b}}\left(H\right)}{k_{\mathrm{B}}T}\left(1 - \frac{I}{I_{\mathrm{sw}}}\right)\right]$$

où I_{sw} est le courant nécessaire au renversement considéré à champ magnétique et température nuls. Ici encore, de nombreuses expériences ont validé l'exactitude de ce modèle qui sera utilisé dans la suite de cette thèse.

Chapter 1

Magnetization dynamics

The phenomena studied in this manuscript mainly focus on magnetization reversal. The aim of this chapter is to briefly remind the origin of magnetism and to present different contributions influencing the behavior of a magnetization. It leads to the essential Landau-Lipschitz-Gilbert equation governing magnetization dynamics.

1.1 Origin of magnetism

1.1.1 Origin of the atomic magnetic moment

In the approach of the Bohr model, the negatively charged electrons have a uniform circular trajectory around the positively charged nucleus. This circulation of negative charges results in a current I generating an orbital magnetic moment $\boldsymbol{\mathcal{M}_\mathrm{o}}$ just as a current injected in a circular wire generates a magnetic field. In this simple model, $\boldsymbol{\mathcal{M}_\mathrm{o}} = IS\boldsymbol{n}$ with S the surface defined by the trajectory of an electron and $\boldsymbol{n}$ a unitary vector oriented in the $\boldsymbol{v} \times \boldsymbol{r}$ direction where $\boldsymbol{v}$ is the velocity and $\boldsymbol{r}$ the position of the electron (see figure 1.1). The current I can be estimated by the product of the charge of an electron by its frequency of rotation around the nucleus so that its orbital magnetic moment is $\boldsymbol{\mathcal{M}_\mathrm{o}} = -\frac{e}{2m}\boldsymbol{\mathcal{L}_\mathrm{o}}$ with $\boldsymbol{\mathcal{L}_\mathrm{o}} = \boldsymbol{r} \times m\boldsymbol{v}$ its orbital angular momentum. The projection of the orbital angular momentum of an electron is quantized along the quantization axis z by its quantic magnetic number m_l so that $l_\mathrm{o,z} = \hbar m_l$ with $m_l \in \mathbb{Z}$. Therefore, the projection of its orbital magnetic moment along this axis is also quantized and

$$\mathcal{M}_\mathrm{o,z} = \mu_\mathrm{B} m_l \tag{1.1}$$

where $\mu_\mathrm{B} = \frac{\hbar e}{2m}$ is the Bohr magneton.

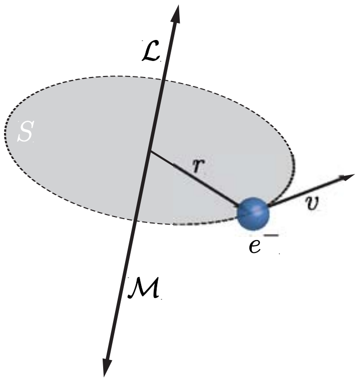

Figure 1.1 – Trajectory of an electron around the nucleus.

Along with this orbital angular momentum, the existence of an intrinsic angular momentum for the electrons called the spin angular momentum was confirmed in 1922 by the Stern-Gerlach experiment. Its projection is also quantized along the quantization axis z by a quantic spin number s that is to say $l_{\mathrm{s,z}} = \hbar s$ with $s = \pm\frac{1}{2}$. This spin angular momentum generates by analogy with the orbital angular momentum a proportional spin magnetic moment

$$\mathcal{M}_{\mathrm{s,z}} = -g_{\mathrm{s}}\mu_{\mathrm{B}}s \tag{1.2}$$

where $g_{\mathrm{s}} \simeq 2$ is the Landé factor of the electron spin.

Therefore, the total angular momentum and the total magnetic moment of an atom are always proportional, $\boldsymbol{\mathcal{M}} = -\gamma\boldsymbol{\mathcal{L}}$ where γ is called the gyromagnetic ratio. This magnetic moment comes from the combined effect of the orbital and spin angular momenta of all the electrons. Besides, there is an interaction between these two contributions called the spin-orbit coupling so that the total magnetic moment of an atom is calculated thanks to the Hund rules. These rules imply that only the atoms with incomplete atomic shells are magnetic.

This description works well for of an isolated atom. As soon as a magnetic atom is inside a solid structure, however, the formation of chemical bonds generally modifies its electronic structure insomuch that its magnetism vanishes. Consequently, only few solids are magnetic, those made up of atoms with internal incomplete shells which are weakly affected by chemical bonds. Among them, the solids made of rare earth elements are well described by the model above since their 4f shell is incomplete and well isolated from the outside. On the contrary, the magnetic properties of 3d metals cannot be described by this model because their incomplete 3d shell is partially involved in the chemical bonds. Nevertheless, they can be roughly described by the Stoner model of itinerant magnetism.

1.1.2 Origin of the itinerant magnetism: Stoner model

In 3d metals, the atomic orbital magnetic moments are quenched by the crystal field of the solid due to the chemical bonds. Therefore, their magnetism arises from an imbalance between the populations of spin $\frac{1}{2}$ and of spin $-\frac{1}{2}$. It creates a magnetization defined by $\boldsymbol{M} = \frac{1}{V}\Sigma_i \boldsymbol{\mathcal{M}}_i$ where the sum is over all the atomic magnetic moments $\boldsymbol{\mathcal{M}}_i$ of the system and V is the volume of the magnetic solid. Stoner model gives a description of the origin of this imbalance[17].

In this model, the 3d electrons are considered as free electrons with parabolic density of states divided into two branches: one for the spin up electrons which magnetic moment is aligned with the magnetization of the solid and one for the spin down electrons which magnetic moment is opposite to the magnetization of the solid (see figure 1.2). A magnetization appears with an excess of spin up or down. Stoner's explanation starts from Pauli exclusion principle: two electrons with the same spin cannot exist in the same quantic state and therefore in the same region of space. As a result, the Coulomb repulsion between two electrons with opposite spins is higher than between two electrons with the same spins since they can come closer to each other. This effect is taken into account in Stoner model by a potential energy of interaction between electrons given by $\eta N_\uparrow N_\downarrow$ where η represents the difference of repulsion between two electrons of identical and of opposite spins and $N_\uparrow$ (resp. $N_\downarrow$) the number of electrons of spin up (resp. down). The system is made up of N electrons.

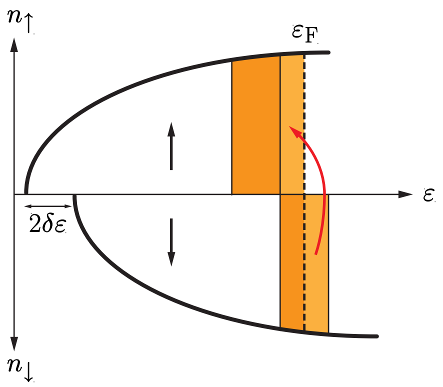

Figure 1.2 – Evolution of populating of the 3d band in Stoner model. (↑) and (↓) are respectively for the spin up and down electrons.

Stoner model calculates the difference of energy between a non-magnetic state where the two branches of density of states are symmetric and a magnetic state where they are slightly split by an energy $2\delta\varepsilon$ (see figure 1.2). Due to the splitting, the quantity $n(\varepsilon_{\mathrm{F}})\delta\varepsilon$ of spins down become spins up with $n(\varepsilon_{\mathrm{F}})$ the density of state at the Fermi level. Therefore, the variation of kinetic energy is given by $\Delta E_{\mathrm{k}} = n(\varepsilon_{\mathrm{F}})(\delta\varepsilon)^2$ and the variation of potential energy by $\Delta E_{\mathrm{p}} = \eta[\frac{N}{2} + n(\varepsilon_{\mathrm{F}})\delta\varepsilon][\frac{N}{2} - n(\varepsilon_{\mathrm{F}})\delta\varepsilon] - \eta(\frac{N}{2})^2 = -\eta[n(\varepsilon_F)\delta\varepsilon]^2$. The total variation of energy of the system is so given by

$$\Delta E = n(\varepsilon_{\mathrm{F}})(\delta\varepsilon)^2[1 - \eta n(\varepsilon_F)] \tag{1.3}$$

The magnetic state is stable only if $\Delta E < 0$ that is to say $\eta n(\varepsilon_F) > 1$. This is called the Stoner stability criterion. The parameter η is hardly assessable but it means that a high density of states at the Fermi level favors a magnetic state. Since iron, cobalt and nickel have very narrow 3d band around their Fermi level they are magnetic contrary to the other 3d metals.

1.2 Magnetic interactions

The previous section shows that solids can be magnetic. Their magnetism is often characterized by their magnetization $\boldsymbol{M} = \frac{1}{V}\Sigma_i \boldsymbol{\mathcal{M}}_i$ where the sum is over all their atomic magnetic moments $\boldsymbol{\mathcal{M}}_i$. The orientation of these magnetic moments is controled by various interactions which determine in the end the intensity, the orientation and the dynamic of the magnetization.

1.2.1 Exchange interaction

Inside a magnetic material, the magnetic atoms interact with one another. Among these interactions, the exchange interaction has a non-magnetic origin. It comes indeed from Pauli exclusion principle and electrostatic considerations similarly to Stoner model. It appears when the wave functions of two electrons overlaps so this is a short range interaction. Only the interaction between two first neighbors is usually taken into account. Because of it, the energy between two interacting electrons is reduced or increased depending on the relative orientation of their magnetic moments. The exchange energy associated to this exchange interaction expressed between the magnetic moments of two atoms i and j is given by

$$E_{\mathrm{exc}} = -\mu_0 A_{\mathrm{exc}} \boldsymbol{\mathcal{M}}_{\mathrm{i}} \boldsymbol{\mathcal{M}}_{\mathrm{j}} \tag{1.4}$$

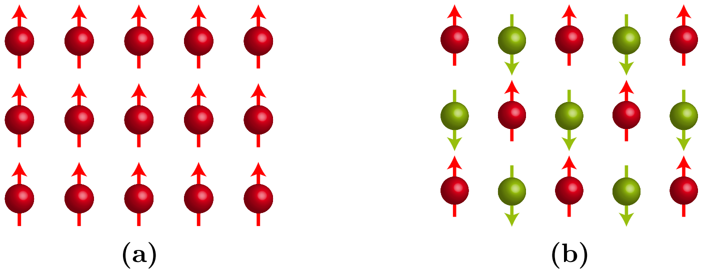

Figure 1.3 – Two examples of magnetic ordering: (a) ferromagnetism and (b) antiferromagnetism.

where A_{exc} characterizes the intensity and the nature of the exchange interaction.

This energy leads to a magnetic ordering of the magnetic material. For instance, if $A_{\text{exc}} > 0$ two neighbour atomic magnetic moments will be parallel. It results in a ferromagnetic order like in iron, cobalt or nickel where the magnetic material has a non-zero magnetization (see figure 1.3a). On the contrary, if $A_{\text{exc}} < 0$ two neighbour atomic magnetic moments will be antiparallel. It results in an antiferromagnetic order where the magnetic material has no magnetization (see figure 1.3b). Between these two extremal cases, many other magnetic orders exist such as ferrimagnetism or helimagnetism.

The temperature affects the magnetic ordering. It consequently appears below a critical temperature called the Curie temperature for the ferromagnets and the Néel temperature for the antiferromagnets. Above these temperatures, the magnetic moments are randomly agitated by the temperature insomuch that even a ferromagnet loses its magnetization and becomes paramagnetic.

1.2.2 Zeeman interaction

The Zeeman interaction describes the action of an external magnetic field $\boldsymbol{H}$ applied on a magnetic moment $\boldsymbol{\mathcal{M}}$. This magnetic moment gets an energy given by $-\mu_0 \boldsymbol{\mathcal{M}} \cdot \boldsymbol{H}$. For a ferromagnet, its behavior is reduced to the behavior of its magnetization $\boldsymbol{M}$. Therefore, the energy transfered to the magnetization of a ferromagnet by the Zeeman interaction is

$$E_{\text{zee}} = -\mu_0 V \boldsymbol{M} \cdot \boldsymbol{H} \tag{1.5}$$

with V the volume of the ferromagnet. This energy is minimized when the magnetization is oriented in the same direction as the applied magnetic field.

1.2.3 Dipolar interaction

A magnetic moment generates a magnetic field known as the dipolar field so the magnetic atoms of a magnetic solid also interact with one another by the mean of this magnetic field. The dipolar interaction can be divided into two contributions. The dipolar field interaction considers the action of the dipolar field created by a magnet on another magnet whereas the demagnetizing field interaction considers the action of the dipolar field created by a magnet on itself.

Dipolar field interaction

A ferromagnet with a magnetization $\boldsymbol{M}$ produces a magnetic field which expression is given at a distance $\boldsymbol{r}$ far from it by $\boldsymbol{H}_{\mathbf{dip}} = \frac{1}{4\pi}[\frac{(\boldsymbol{M}\cdot\boldsymbol{r})\boldsymbol{r}}{r^5} - \frac{\boldsymbol{M}}{r^3}]$. Its evolution in $\frac{1}{r^3}$ shows that the dipolar field interaction contrary to the exchange interaction is long range. Let's consider the action of a magnetic field $\boldsymbol{H}^{\mathbf{12}}_{\mathbf{dip}}$ produced by a first magnet on a second magnet of magnetization $\boldsymbol{M_2}$ and small enough to consider that $\boldsymbol{H}^{\mathbf{12}}_{\mathbf{dip}}$ is uniform on it. The energy due to this interaction is

$$E_{\text{dip}} = -\mu_0 V \boldsymbol{M_2} \cdot \boldsymbol{H}^{\mathbf{12}}_{\mathbf{dip}} \tag{1.6}$$

with V the volume of the second magnet. If the direction of $\boldsymbol{r}$ is aligned with the direction of the magnetization of the first magnet, this energy is minimized when the two magnetizations are parallel (see the red arrows on figure 1.4). On the contrary, if the direction of $\boldsymbol{r}$ is perpendicular to the direction of the magnetization of the first magnet, the magnetizations prefer to be antiparallel (see the green arrows on figure 1.4).

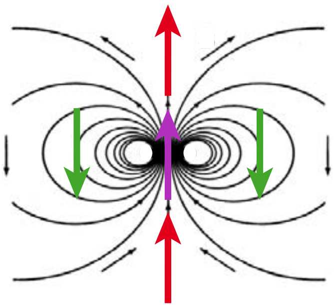

Figure 1.4 – Dipolar field emitted by a magnetization positioned at the center and its influence on the orientation of magnetizations at its periphery.

Demagnetizing field interaction

Looking at the action of the dipolar field created by a magnetization on itself, its projection is often opposite to the direction of the magnetization, hence the name of demagnetizing field. In the most general case, it is linked to the magnetization by a second order tensor $\hat{\boldsymbol{N}}$ so that $\boldsymbol{H}_{\mathbf{dem}} = -\hat{\boldsymbol{N}}\boldsymbol{M}$. The energy related to this interaction is

$$E_{\text{dem}} = -\frac{\mu_0 V}{2}\boldsymbol{M}\cdot\boldsymbol{H}_{\mathbf{dem}} \tag{1.7}$$

with V is volume of the magnet. $\hat{\boldsymbol{N}}$ only depends on the geometry of the magnet. It can be calculated analytically in the unique case of a spheroid magnet. In the limit of a thin film, that is to say an infinite oblate spheroid, $\hat{\boldsymbol{N}}$ is reduced to its eigenvalues: 1 in the direction perpendicular to the plane of the thin film and 0 in the two in-plane directions. As a result, this energy is minimized for a thin film when the magnetization lies in the plane of the magnetic layer. The magnetization lies more generally in the most elongated direction of the magnet where the demagnetizing field is the lowest. Therefore, the geometry of a magnet induces preferential orientations for its magnetization. This phenomenon is called the shape anisotropy.

1.2.4 Magnetocrystalline anisotropy

By the mean of the spin-orbit coupling and of the crystal field, the microscopic arrangement of the magnetic atoms inside a solid has an influence on the orientation of its magnetization. Indeed, the specific arrangement of its atoms frizzes the electronic orbitals in specific orientations. The orbital magnetic moment of the magnetic atoms consequently has a preferential orientation in space determined by the crystallography of the solid. Since the orbital and the spin magnetic moments are coupled via the spin-orbit interaction, the spin magnetic moment also has a preferential orientation. In the end, the magnetization of a ferromagnet is preferentially aligned in specific crystallographic directions. This is the magnetocrystalline anisotropy.

It exists various types of magnetocrystalline anisotropies each one described by a different energy landscape (see figure 1.5). For instance, a ferromagnet can have an uniaxial anisotropy. It means that its magnetization prefers to lie only in one crystallographic direction called the easy anisotropy axis. This behavior is described by a magnetocrystalline anisotropy energy (see figure 1.5a) given by

$$E_{\text{ani}} = KV\sin^2\theta \tag{1.8}$$

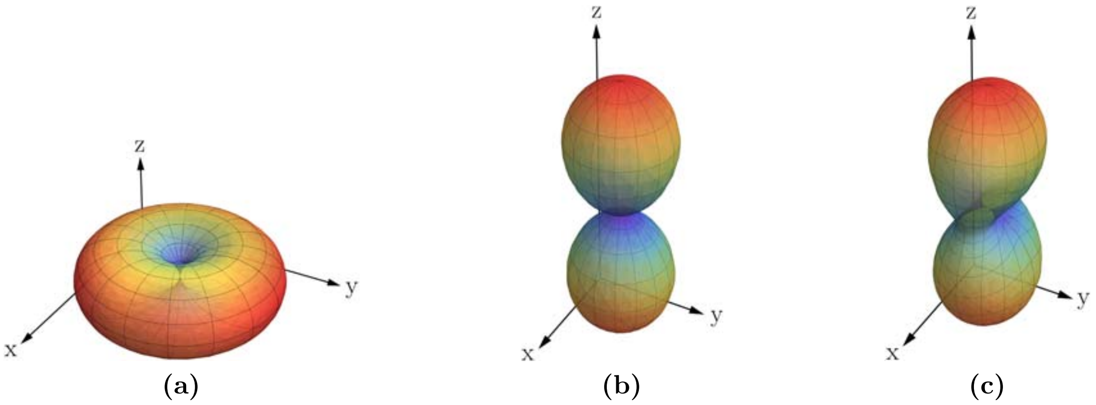

Figure 1.5 – Evolution of the magnetocrystalline anisotropy energy as a function of the magnetization orientation in the case (a) of an easy axis in the z direction, (b) of an easy xy plane and (c) of an easy xy plane plus a shape anisotropy due to an elongated shape in the y direction.

with K the anisotropy constant, V the volume of the layer and θ the angle between the easy anisotropy axis and the magnetization. Another case is the easy plane anisotropy or hard axis anisotropy. It is the opposite configuration of the previous one because now the magnetization prefers to lie in a plane perpendicular to the hard axis direction. This behavior is described by a magnetocrystalline anisotropy energy (see figure 1.5b) given by

$$E_{\mathrm{ani}} = KV\cos^2\theta \tag{1.9}$$

with K the anisotropy constant, V the volume of the layer and θ the angle between the hard anisotropy axis and the magnetization. More generally, this interaction can be described by an effective anisotropy field given by $\boldsymbol{H}_{\mathbf{ani}} = -\frac{1}{\mu_0 V}\frac{\partial E_{\mathrm{ani}}}{\partial \boldsymbol{M}}$ where V is the volume of the ferromagnet. The magnetocrystalline anisotropy energy is then given by $E_{\mathrm{ani}} = -\mu_0 V \boldsymbol{M}\cdot\boldsymbol{H}_{\mathbf{ani}}$.

Along with this magnetocrystalline anisotropy, the shape anisotropy also adds its contribution. For instance, let's look at the case of a magnetic thin film with an easy plane anisotropy. If this thin film has an elongated shape in one direction of the plane all the in-plane directions will not be equivalent because of the shape anisotropy (see figure 1.5c). Therefore, in the absence of any external magnetic field, the magnetization of a ferromagnet lies preferentially in the minimum of energy defined both by the shape and the magnetocrystalline anisotropies.

1.3 Competition between magnetic interaction

1.3.1 Formation of domains

In a ferromagnet, the effects of the demagnetizing field and of the exchange interaction are antagonist. Indeed, the exchange interaction favors a parallel alignment of the magnetic moments and leads to the highest magnetization state. On the contrary, the demagnetizing field interaction couples the magnetic moments in opposite directions to decrease the magnetization. The competition between these two interactions is ruled by their range: short for the exchange and long for the demagnetizing field. Consequently, a characteristic length determines the predominant interaction, below the exchange and above the demagnetizing field. This length is called the exchange length and is given by

$$l_{\mathrm{exc}} = \sqrt{\frac{A_{\mathrm{exc}}}{\mu_0 M_{\mathrm{s}}^2}} \tag{1.10}$$

If the size of a ferromagnet exceeds this length, its uniform magnetization will break into domains. Within a domain the magnetization is more or less uniform but the magnetizations of two consecutive domains point in different directions (see figure 1.6). As a result, the total magnetization of the ferromagnet is reduced by the demagnetizing field.

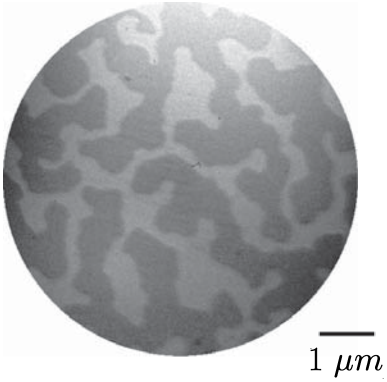

Figure 1.6 – Magnetic domains of an amorphous Gd-Fe system imaged by X-ray magnetic circular dichroism at the Fe L_3 edge. The light and the dark grey colors represent two opposite orientations of the magnetization compare to the direction of the X-ray beam. Figure extracted from Fischer *et al.*[18].

At the interface between two domains, the magnetic moments evolve continuously from one direction to the other. This region of non-uniform magnetization is called a domain wall. The exchange favors a smooth evolution of the direction of the magnetic moments that is to say large domain walls. On the contrary, the anisotropy prefers an abrupt evolution of the magnetization between two directions of low energy that is to say short domain walls. Therefore, there is also a competition between the exchange and the anisotropy interactions which determine the size of the domain walls. For instance, the thickness of a Bloch wall (one particular type of domain wall) is proportional to $\sqrt{A_{\text{exc}}/K}$. Besides, the formation of domain walls costs energy. So, they appear only if the gain in demagnetizing energy is high enough to compensate the energy required to create them. For instance, the surface energy of a Bloch wall is proportional to $\sqrt{A_{\text{exc}}K}$.

In the previous description of the different magnetic interactions, we implicitly supposed that the ferromagnet was uniformly magnetized in a monodomain state at any time. In this case, all its atomic magnetic moments are parallel and the description of its magnetism is reduced to the study of its magnetization. Actually, a ferromagnet rarely is uniformly magnetized even if it is in a monodomain state. However, the consequences of these non-uniformities are often negligible and its magnetization is considered as uniform inside a domain. For a monodomain state considered as uniformly magnetized this approximation is called the macrospin approximation.

1.3.2 Hysteresis cycle

Let's consider a ferromagnet in the macrospin approach with an easy anisotropy axis along the z axis. Initially, the magnetization lies in one of the two minimum of energy present along the z axis (see figure 1.5a page 22). Looking at the energy of the system there is no difference between a magnetization parallel or antiparallel to the z axis. As a result, if a magnetic field is applied along the z axis in the opposite direction of the magnetization, it will reverse the magnetization because the Zeeman energy is minimized when the magnetization and the applied magnetic field are parallel. However, to reverse, the system has to cross an energy barrier corresponding to the passage trough the hard magnetization plane. Therefore, the applied magnetic field has to reach a critical value to be able reverse the magnetization.

Considering the magnetocrystalline anisotropy and the Zeeman interactions, the volume energy of the system in this configuration is given by $E = K\sin^2\theta - \mu_0 M_{\text{s}} H\cos\theta$ where θ is the angle between the magnetization and the z axis (see

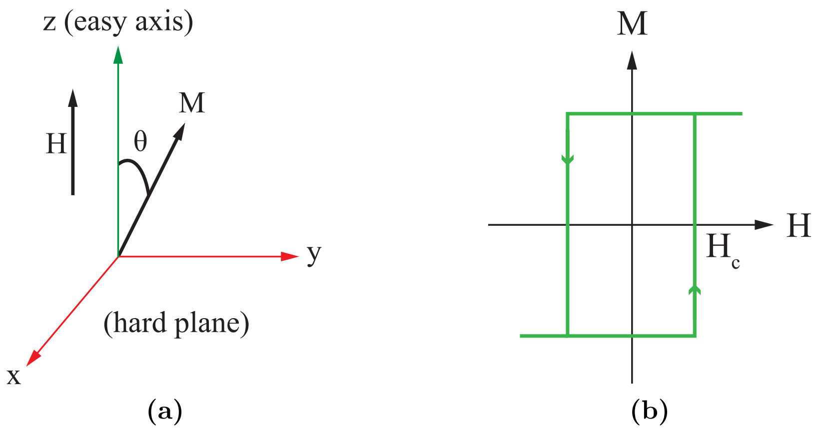

Figure 1.7 – (a) Illustration of Stoner-Wohlfarth model. (b) Magnetization evolution as a function of the applied magnetic field of a macrospin with an uniaxial anisotropy when the field is applied in the same direction as the easy anisotropy axis.

figure 1.7a). According to the Stoner-Wohlfarth model[19], the magnetization reverses as soon as the energy barrier between two stable positions vanishes. The positions of the energy extrema are given by $\frac{dE}{d\theta} = 0 \Leftrightarrow \sin\theta(2K\cos\theta + \mu_0 M_\mathrm{s} H) = 0$. The first solution, $\sin\theta = 0$, gives the available positions of the magnetization along the z axis, $\theta = 0$ or π. They are either a maximum or a minimum of energy. The second solution, $2K\cos\theta + \mu_0 M_\mathrm{s} H = 0 \Leftrightarrow \cos\theta = -\frac{\mu_0 M_\mathrm{s}}{2K} H$, gives the position of the energy barrier between the two previous positions when it exists. It disappears as soon as $\frac{d^2E}{d\theta^2} = 0$ at this position, that is to say $H = \pm H_\mathrm{c} = \pm\frac{2K}{\mu_0 M_\mathrm{s}}$. These two fields correspond to the two available transitions, from $\theta = 0$ to $\theta = \pi$ and inversely. Starting from $\theta = 0$ (resp. $\theta = \pi$) the magnetization reverses for an applied magnetic field of $-H_\mathrm{c}$ (resp. H_c). Therefore, the magnetization reversal is hysteretic (see figure 1.7b). This behavior is at the basis of magnetic recording.

In the case of a macroscopic ferromagnet divided in various domains, a magnetic field applied along the easy anisotropy axis favors the growing of the domains parallel to it. So, its magnetization becomes more and more uniform. Its reversal is still hysteretic but the transition is smoother due to the displacement of domain walls.

1.4 Equation of magnetization dynamics

Above, we discuss transitions between two stable and static states. This description does not explained how the magnetization switches from one direction to another. An equation of magnetization dynamics is required to determine this trajectory.

1.4.1 Dynamic of a magnetization with a magnetic field

Let's consider a ferromagnet in the macrospin approach composed of magnetic moments $\boldsymbol{\mathcal{M}}_i$ aligned to form a magnetization $\boldsymbol{M}$. In a uniform magnetic field $\boldsymbol{H}$ each magnetic moment feels a torque $\boldsymbol{\Gamma} = \mu_0 \boldsymbol{\mathcal{M}} \times \boldsymbol{H}$. The conservation law of the angular momentum of the system gives $\frac{d\boldsymbol{\mathcal{L}}}{dt} = \Sigma_i(\mu_0 \boldsymbol{\mathcal{M}}_i \times \boldsymbol{H})$. Since the ferromagnet is described by a macrospin, the magnetic moments are directly related to the magnetization by $\Sigma_i \boldsymbol{\mathcal{M}}_i = V\boldsymbol{M}$ with V the volume of the ferromagnet. Besides, the angular momentum of the system and the magnetic moments are proportional and $\boldsymbol{\mathcal{L}} = -\frac{1}{\gamma}\Sigma_i \boldsymbol{\mathcal{M}}_i = -\frac{V}{\gamma}\boldsymbol{M}$. The dynamic of a magnetization with a magnetic field is so ruled by

$$\frac{d\boldsymbol{m}}{dt} = -\gamma_0 \boldsymbol{m} \times \boldsymbol{H} \tag{1.11}$$

with $\gamma_0 = \gamma\mu_0$ and $\boldsymbol{m} = \frac{\boldsymbol{M}}{M_\mathrm{s}}$ a unitary vector in the direction of the magnetization. Therefore, if the magnetization is misaligned with the magnetic field, it will precess around at the frequency $\gamma_0 H$ (see figure 1.8a).

However, in a ferromagnet the magnetization feels various interactions affecting its dynamic even if no magnetic field is applied: the dipolar and the magnetocrystalline anisotropy interactions (the only effect of the exchange interaction here is to allow the macrospin approximation). To introduce these effects in the equation of motion of the magnetization one has to remind that they all can be described as the action of a magnetic field. As a result, everything behaves just as if the magnetization evolves in an effective magnetic field given by $\boldsymbol{H}_\mathbf{eff} = \boldsymbol{H} + \boldsymbol{H}_\mathbf{dip} + \boldsymbol{H}_\mathbf{dem} + \boldsymbol{H}_\mathbf{ani}$. The magnetization dynamics is then governed by

$$\frac{d\boldsymbol{m}}{dt} = -\gamma_0 \boldsymbol{m} \times \boldsymbol{H}_\mathbf{eff} \tag{1.12}$$

The consequences of this equation are similar to the previous one. If the magnetization is misaligned with the effective magnetic field, it will precess around it at the frequency $\gamma_0 H_\mathrm{eff}$ (see figure 1.8a). The effective field is related to the total magnetic energy E of the ferromagnet by

$$\boldsymbol{H}_{\mathbf{eff}} = -\frac{1}{\mu_0 V}\frac{\partial E}{\partial \boldsymbol{M}} \tag{1.13}$$

Since the the dipolar and the magnetocrystalline anisotropy interactions are conservative, there is always an effective field which can be derived from them.

1.4.2 The Landau-Lifshitz-Gilbert equation

The previous equation of magnetization dynamics considers only conservative interactions so the magnetization has to precess indefinitely around the direction of the effective field. Actually, the magnetization always dissipates energy, for instance by emitting phonons or magnons, and ends by reaching its stable and static equilibrium position parallel to the effective field. To take into account this phenomenon in the magnetization dynamics, a dissipation term has to be included in the equation. This is the Landau-Lifshitz-Gilbert or LLG equation of motion of the magnetization[20,21]

$$\frac{d\boldsymbol{m}}{dt} = -\gamma_0 \boldsymbol{m} \times \boldsymbol{H}_{\mathbf{eff}} + \alpha \boldsymbol{m} \times \frac{d\boldsymbol{m}}{dt} \tag{1.14}$$

where α is a damping constant characterizing the intensity of the dissipation. As a result, if the magnetization is misaligned with the effective field direction it will exhibit damped oscillations around until it aligns parallel to it (see figure 1.8b). The period of these oscillations is of the order of few picoseconds and the characteristic time of the damping is of the order of few nanoseconds.

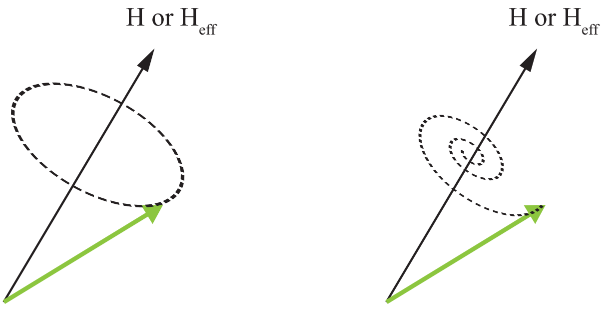

(a) **(b)**

Figure 1.8 – Trajectory of a magnetization with a magnetic field (a) without and (b) with dissipation.

Chapter 2

Giant magnetoresistance phenomenon

The giant magnetoresistance effect was discovered jointly in 1988 by Albert Fert[1] in magnetic multilayers and Peter Grünberg[2] in spin-valves. It manifests itself by a change in the resistance of a magnetic structure induced by a magnetic field. As mentioned in the introduction, its discover gave birth to the spintronics. Besides, it is still nowadays the main effect used to study the spin-transfer phenomenon.

This chapter starts by a very simple description of the giant magnetoresistance effect based on the two currents model to introduce important concepts of electronic transport in ferromagnets. Then, it addresses the problematic of the injection of a spin polarized current from a ferromagnet to a non-magnetic metal highlighting some aspects of the Valet-Fert model. We will mainly focus on the giant magnetoresistance effect in current perpendicular to the plane geometry (that is to say when the current is injected perpendicularly to the layers) but the two currents model also works for the current in plane geometry.

2.1 Origin of the giant magnetoresistance

2.1.1 First experiments on giant magnetoresistance

The first experiments on giant magnetoresistance effect were performed in Fe/Cr thin films with a layer thickness of the order of few nanometers. Actually, the control of nanofabrication processes is a critical issue for every experiments in spintronics and the reason will be pointed out later in this chapter (see subsection 2.2.1 page 35). In these multilayers, two successive iron layers are antiparallely coupled through a spacer of chromium. Applying a high enough magnetic

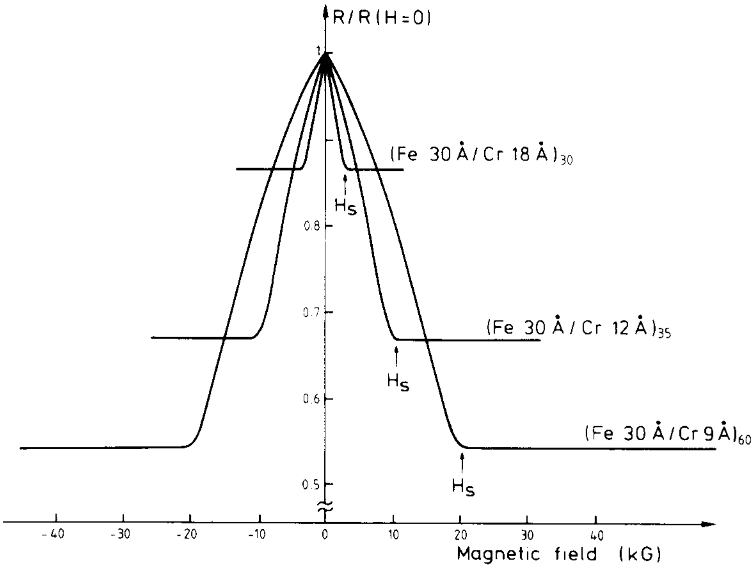

Figure 2.1 – Giant magnetoresistance of three Fe/Cr superlattices at 4.2 K with the current and the magnetic field applied in the plane of the layers. Figure extracted from Baibich *et al.*[1].

field, the magnetizations of all the iron layers align parallel to one another. During this evolution, the resistance of the system decreases of about 50% for a multilayer[1,22] (see figure 2.1) and of about 1.5% for a bilayer[2]. This variation of resistance is dramatically higher than the one obtained with conventional anisotropic magnetoresistance, a phenomenon where the resistance of the magnetic material depends on the angle between the current flow and the magnetic field. As a result, it allows the detection of smaller magnetic fields which leads for the hard drive industries to the reduction of the size of the memory bits.

2.1.2 Two currents model

The origin of giant magnetoresistance is directly related to the electron transport properties inside a ferromagnet such as iron, cobalt or nickel. Indeed, in these metals the current is divided into two channels[23], one for the spin up electrons and one for the spin down electrons (see chapter 1 subsection 1.1.2 page 17 for the definition of spin up and down). In first approximation and at low temperature ($T \ll T_c$) these two channels are independent which means that an electron cannot reverse its spin.

Both 3s and 3d electrons are present at the Fermi level of a ferromagnetic transition metal. Since the effective mass is larger for the d electrons than for the s electrons the current is carried by a majority of 3s electrons. For their

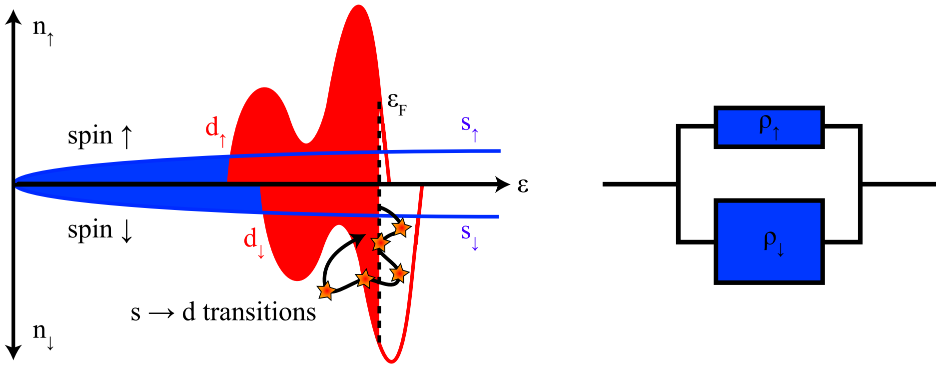

Figure 2.2 – Schematic view of the band diagram of a ferromagnet and its electric equivalent in the two currents model.

part, the 3d electrons are responsible for the magnetism. According to the itinerant magnetism theory of Stoner, the 3d bands for the up and down electrons are splitted so that their density of states at the Fermi level are not equal (see figure 2.2). More states are generally available for the down electrons than for the up electrons. Since the electrons conserve their spin, the transitions from the 3s to the 3d band, proportional to the density of state available in the 3d band, are consequently more important for the down electrons than for the up electrons. However, when a s electron moves to the d band it stops to participate to the current flow. As a result, each s to d transition increases the resistivity of the ferromagnet. So, looking at the two conduction channels, the up one will generally exhibit a lower resistivity than the down one ($\rho_\uparrow < \rho_\downarrow$).

Along with the intrinsic 3d band splitting, the presence of impurities inside or at the surface of the ferromagnet also creates a spin dependent diffusion. Depending of all these considerations, one of the channel will become more resistive than the other so the current densities coming from the up and down electrons are different[24]. The current flowing through a ferromagnet is therefore spin polarized: it is composed of more electrons from one spin direction than the other. This spin polarization is given by

$$P = \frac{j_\uparrow - j_\downarrow}{j_\uparrow + j_\downarrow} \tag{2.1}$$

with $P = 0$ if the current is not spin polarized and $|P| = 1$ if it is fully polarized.

The use of a ferromagnet to polarize the current that is to say to choose a preferential spin orientation for the spins of the conduction electrons is the key to obtain the giant magnetoresistance effect. Moreover, the obtention of a spin polarized current is the first step required to observe spin-transfer.

2.1.3 Application to the spin-valve structure

Description of a spin-valve

A spin-valve structure consists of two magnetic layers separated by a non-magnetic layer. If this spacer is metallic the system exhibits giant magnetoresistance. If it is insulating it exhibits tunnel magnetoresistance, a phenomenon discovered in 1975 and explained by the Jullière model[25]. Usually, the two magnetic layers have an easy anisotropy axis so that their magnetizations can only lie in one direction and different coercivities so that one reverses its magnetization more easily. This layer is called the soft or free layer and the other one the hard layer or the polarizer.

From these considerations, the spin-valve exhibits four different magnetic states: $\uparrow\uparrow$, $\uparrow\downarrow$, $\downarrow\uparrow$ and $\downarrow\downarrow$. Two of them correspond to a parallel alignment of the magnetizations ($\uparrow\uparrow$ and $\downarrow\downarrow$) and the two others to an antiparallel alignment ($\uparrow\downarrow$ and $\downarrow\uparrow$). These two different alignments act differently on the current flowing through the spin-valve which causes the giant magnetoresistance effect.

Spin filtering effect in a spin-valve

Let's consider a spin-valve structure composed of two ferromagnetic layers separated by a non-magnetic metallic layer. According to the two currents model the current is divided inside this structure into two independent and parallel channels. In the following, the channel $+$ (resp. $-$) will correspond to the channel of a spin up (resp. down) electron relatively to the magnetization of the first magnetic layer it comes across. For each channel, the magnetic layers correspond to resistive elements mounted in series which resistance depends on the relative orientation of the spin magnetic moment of the conduction electrons and of the magnetization. Supposing $\rho_\uparrow < \rho_\downarrow$ this resistance is low (noted r) if they have the same orientation and high (noted R) if they have opposite orientations. In the limit where the current is fully polarized by the ferromagnets $r = 0$ and $R = \infty$.

In the case of a parallel alignment of the magnetizations (see figure 2.3a), the resistivity of the channel $+$ is very low compare to the resistivity of the channel $-$. Indeed, in the channel $+$ both magnetic layers limit the s to d transitions whereas in the channel $-$ they increase these transitions. Let's calculate the total resistance of this configuration

$$\frac{1}{R_\mathrm{P}} = \frac{1}{r+r} + \frac{1}{R+R} \Leftrightarrow R_\mathrm{P} = \frac{2rR}{r+R} \approx 2r \text{ if } r \ll R \tag{2.2}$$

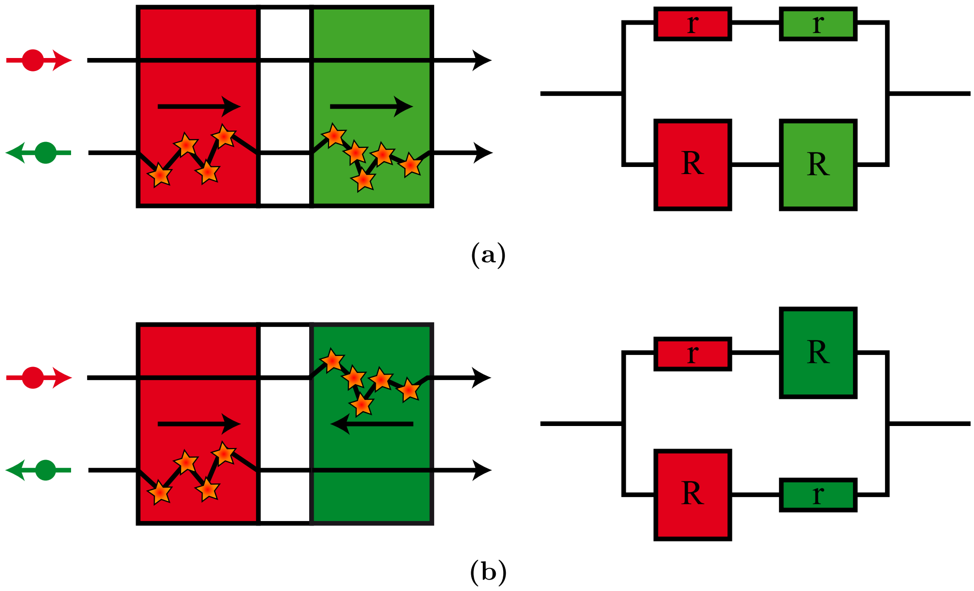

Figure 2.3 – Spin-valve and its equivalent electric circuit in the (a) parallel and (b) antiparallel states.

In the limit where the current is fully polarized the down electrons are totally filtered and only the up electrons can flow through the spin-valve.

On the contrary, in the case of an antiparallel alignment of the magnetizations (see figure 2.3b), the resistivity of the two channels is equal. Indeed an electron up for one magnetic layer becomes down for the other magnetic layer. As a result, the total resistance of this configuration is given by

$$\frac{1}{R_{\mathrm{AP}}} = \frac{1}{r+R} + \frac{1}{R+r} \Leftrightarrow R_{\mathrm{AP}} = \frac{r+R}{2} \approx \frac{R}{2} \text{ if } r \ll R \tag{2.3}$$

In the limit where the current is fully polarized, no current comes out of the spin-valve and its resistance is infinite.

Thanks to the application of a magnetic field the magnetic state of a spin-valve can reverse from a parallel to an antiparallel alignment. Since their resistances are different, the giant magnetoresistance effect as it has been defined at the beginning of this chapter arises. The giant magnetoresistance ratio is then defined by

$$\%_{\mathrm{GMR}} = \frac{R_{\mathrm{AP}} - R_{\mathrm{P}}}{R_{\mathrm{P}}} = \frac{(r-R)^2}{4rR} \approx \frac{R}{4r} \text{ if } r \ll R \tag{2.4}$$

This ratio increases with the difference of resistivity between the two spin channels $(\rho_{\downarrow} - \rho_{\uparrow})$. In the limit where the current is fully polarized this ratio becomes infinite. The spin-valve structure acts actually like a polarizer-analyzer system for a polarized light. If their orientation is parallel the flow of current is maximum and it decreases as soon as their orientation becomes more and more antiparallel.

A binary memory unit

A spin-valve structure as the one described above has two distinct resistance states: one for a parallel alignment and one for an antiparallel alignment of the magnetizations. The application of a magnetic field allows to switch from one alignment to another. As a result, a spin-valve can be use to build a binary permanent memory bit. Indeed, for the writing process the magnetic state is controlled by the application of a magnetic field and for the reading process a small current is injected through the structure to measure its resistivity related to its magnetic state. The magnetic random access memories are built following this principle using a spin-valve structure where the hard layer is usually pinned in one direction by exchange coupling with an antiferromagnet[26].

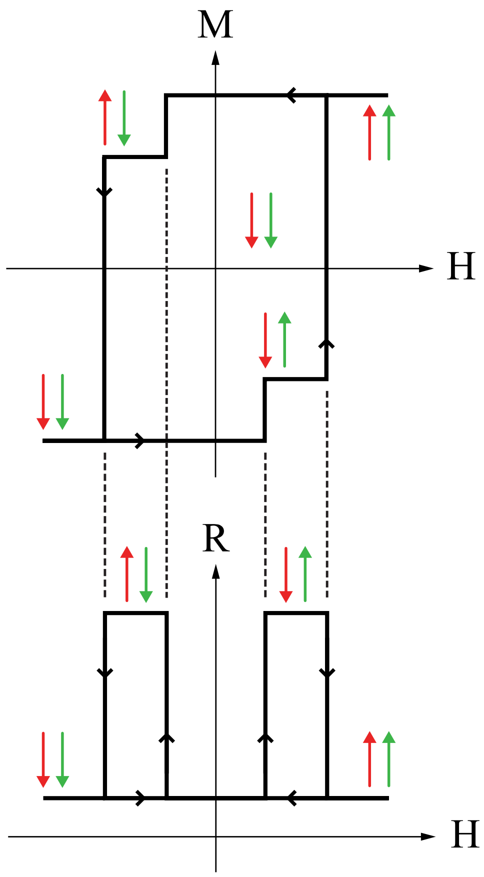

Figure 2.4 – Schematic evolution of the total magnetization of a spin-valve as a function of the applied magnetic field with the corresponding resistance evolution due to the giant magnetoresistance.

This property is also very important from an experimental point of view since it allows to study the evolution of the magnetic state of the spin-valve. Indeed injecting a small current and measuring the voltage permits to obtain its hysteresis cycle following the evolution of its resistivity with the applied magnetic field (see figure 2.4). It is actually the base of all the electric measurements performed during this thesis (see chapter 6 page 69 for a detailed presentation of the measurement setup).

2.2 Injection of a spin polarized current

The simple two currents model presented above is enough to get a general overview about the giant magnetoresistance effect. However, it does not explained how the polarization of the current can be transfered from one ferromagnet to another through the metallic spacer. This is a critical issue to observe not only giant magnetoresistance in perpendicular to the plane geometry but also spin-transfer.

2.2.1 Spin accumulation effect

Let's consider an interface between two semi-infinite metals, one ferromagnetic and the other one non-magnetic, with a current flowing from the ferromagnet to the non-magnetic metal (see figure 2.5). This interface breaks the equilibrium between the spin up and spin down channels[27]. Indeed, on the left side of the ferromagnet the current is spin polarized that is to say that there is more spin up flowing trough it than spin down whereas on the right side of the non-magnetic metal there are as many spin up than spin down electrons contributing to the current. Therefore, there are too many spin up trying to enter into the non-magnetic metal and they accumulate inside the ferromagnet close to the interface. At the same time, there is a deficit of spin down which are pumped into the non-magnetic metal.

This accumulation of spins at the interface generates strong variations of the chemical potential of the up and down electrons at the interface. Due to the apparition of this gradient in the chemical potential two spin polarized currents diffuse through the system. The first one goes from the interface to the ferromagnet reducing the polarization of the current coming to the interface. The second one goes from the interface to the non-magnetic metal. As a result, a spin polarized current can be injected from the ferromagnet to the non-magnetic layer thanks to the spin accumulation.

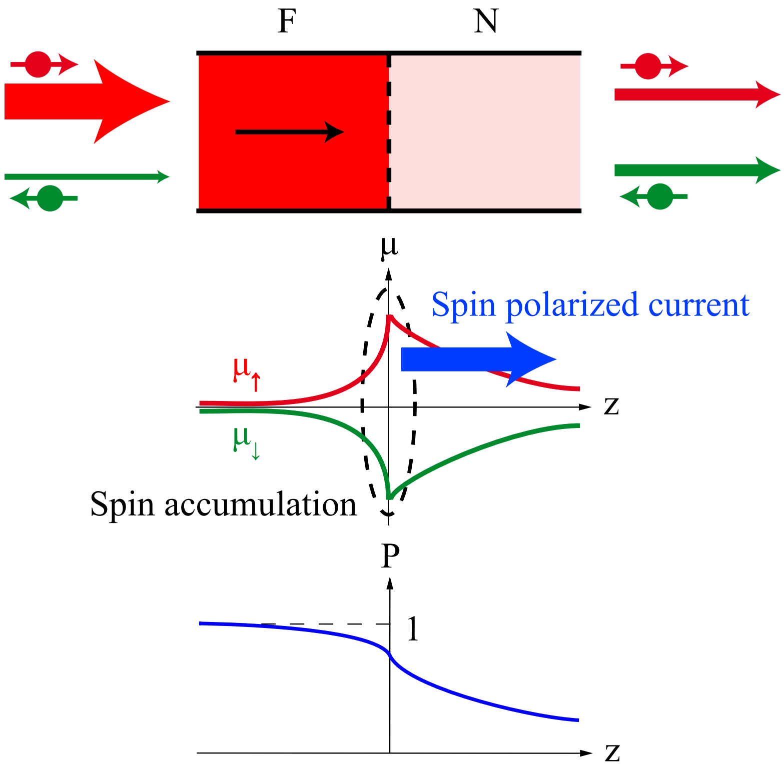

Figure 2.5 – Scheme of a ferromagnetic / non-magnetic metals junction with its profile of chemical potential and of current spin polarization.

Since the spins cannot accumulate indefinitely at the interface the spin accumulation occurs over a distance related to the spin diffusion length. This characteristic length corresponds to the mean distance covered by an electron without changing its spin. The system ends up reaching a state where the spin relaxation equilibrates the spin accumulation. The polarization of the current consequently decreases inside the non-magnetic layer over a distance close to the spin diffusion length. Therefore, to observe the giant magnetoresistance effect in a spin-valve structure the thickness of the spacer has to be thinner than this spin diffusion length. In copper for example, this length is of the order of few hundreds of nanometer. This is the reason why spintronics definitely needs nanofabrication processes to develop.

2.2.2 Transport equations: Valet-Fert model

Thierry Valet and Albert Fert developed in 1993 a model based on the resolution of Boltzmann equation to calculate the transport properties of magnetic multilayers depending on the orientation of their magnetizations[28,29]. In this model, the density of states of all the layers are parabolic and the spin accumulation

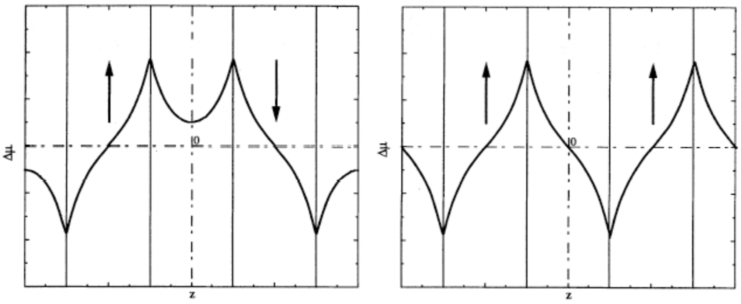

Figure 2.6 – Variation of the difference of chemical potential along a non-magnetic / ferromagnetic / non-magnetic / ferromagnetic / non-magnetic metals structure for the antiparallel and the parallel state of the spin-valve. Pictures extracted from Valet and Fert[29].

is taken into account by introducing a chemical potential for the up and down electrons varying along the layers.

Let's note $n_\sigma = n_0 + \delta n_\sigma$ the density of electrons in the channel σ with $\sigma \in \{+,-\}$ and n_0 the density of electrons at the equilibrium. The spin accumulation is defined by $\Delta s = \frac{\hbar}{2}(\delta n_+ - \delta n_-)$. The difference of chemical potential $\Delta\mu = \mu_+ - \mu_-$ is related to the spin accumulation by $\Delta\mu = \frac{2}{\hbar N(\varepsilon_\mathrm{F})}\Delta s$. Finally, the spin current density is given by $j_\mathrm{s} = -\frac{\hbar}{2e}(j_+ - j_-)$. In the limit where the mean free path of the electrons is small compare to the spin diffusion length, the Valet-Fert model shows that the transport equations for a current injected in the z direction can be summarized by

$$j_{+(-)} = \frac{1}{e\rho_{+(-)}} \frac{\partial \mu_{+(-)}}{\partial z} \tag{2.5}$$

$$j = j_+ + j_- \tag{2.6}$$

$$\frac{\partial (j_+ - j_-)}{\partial z} = \frac{eN(\varepsilon_\mathrm{F})\Delta\mu}{\tau_\mathrm{sd}} \tag{2.7}$$

with τ_sd the spin relaxation time of the electrons linked to the spin diffusion length. The equation 2.5 is the generalized Ohm law. The equations 2.6 and 2.7 represent respectively the conservation of the charge current and the conservation of the spin current. From these equations not only the spin accumulation profiles (see figure 2.6) and the spin currents can be deduced trough the system but also the resistance of the spin-valve in its different magnetic states and the giant magnetoresistance ratio. In the extremal case where all the spin diffusion lengths are very large compare to the thicknesses of the layers, this model is equivalent to the two currents model.

Besides, from equations 2.5 and 2.6 one can determine the density of spin current in the entire system

$$j_{\mathrm{s}} = -\frac{\hbar}{2e}\left(\xi j + \frac{1}{2e\rho_{\mathrm{F}}^{*}}\frac{\partial \Delta\mu}{\partial z}\right) \tag{2.8}$$

with $\xi = \frac{\rho_{\downarrow}-\rho_{\uparrow}}{\rho_{\uparrow}+\rho_{\downarrow}}$ the spin asymmetry ratio and ρ_{F}^{*} the mean resistivity of the electrons at the Fermi level defined by $\rho_{\uparrow(\downarrow)} = 2\rho_{\mathrm{F}}^{*}(1\mp\xi)$. This equation shows that the spin current flowing through the spin-valve is separated into two contributions. The first one corresponds to the conventional polarization of a current flowing through a ferromagnet. Since $\xi \neq 0$ only in the ferromagnets this term does not exist in the non-magnetic spacer. On the contrary, the second one is responsible for the injection of the spin polarized current inside the spacer and arises from a gradient of spin accumulation at the interfaces as mentioned previously.

This possibility to inject a spin polarized current through a non-magnetic metallic spacer is essential to observe giant magnetoresistance since the current has to conserve its polarization between the two ferromagnets. Besides, it is also required to observe spin-transfer phenomenon.

Chapter 3

Spin-transfer phenomenon

The first works related to spin-transfer occurred in the late 1970's when Luc Berger predicted that spin-transfer torque should be able to move a magnetic domain wall[30,31]. A few years later, the first experimental current-induced domain wall motion were performed[32,33] but the large currents up to 45 A needed to observe this effect in macroscopic samples limited the interest at that time. In 1996, thanks to huge progress in nanofabrication techniques, the critical current required to observe spin-transfer decreased to few mA. Theoretical works still from Luc Berger[3] and also from John Slonczewski[4] drew the attention to the new possibilities generated by this effect combined with the nanofabrication techniques. Since then, lots of work has been performed to study the spin-transfer effect.

The previous chapter explains how to spin polarize a current and transport it to a magnetic layer. Inside a spin-valve structure, the hard layer now called the polarizer is used to polarize the current which flows through the spacer to the soft layer now called the free layer. These are the two first steps required to observe spin-transfer. This chapter focuses on the next and last step of this effect occurring at the interface between the spacer and the free layer, the transfer of spin angular momentum from a spin polarized current to a magnetization.

3.1 Qualitative description of spin-transfer

Like giant magnetoresistance, spin-transfer arises from the filtering effect exerted by a magnetization on the spin of the conduction electrons. Indeed, inside a magnetic material there is an effective magnetic field along which its magnetization is aligned (see chapter 1 subsection 1.4.1 page 26). Therefore, any magnetic moments entering into a ferromagnet, for instance the spin of a conduction electron,

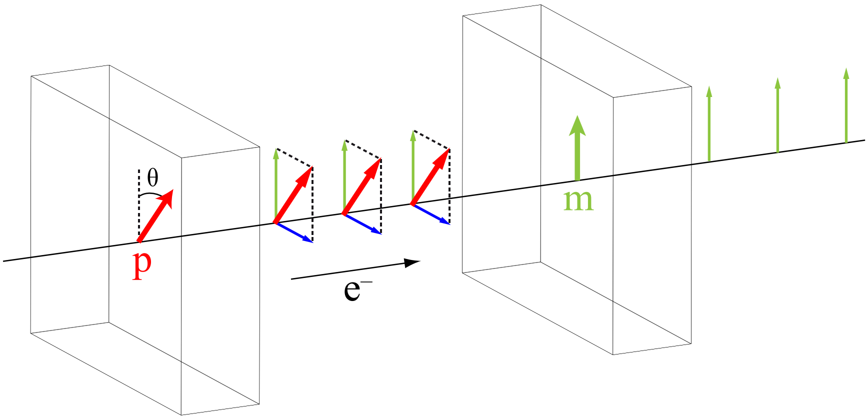

Figure 3.1 – Illustration of the spin-transfer phenomenon. **p** and **m** represent respectively the polarizer and the free layer magnetizations.

precesses around this field until it aligns with it and at the same time with the magnetization. During this process, the electron loses its transverse to the magnetization component of its spin angular momentum (in blue on figure 3.1) which can be absorbed by the magnetization so that the total spin angular momentum of the system is conserved. This variation of spin angular momentum leads to a new torque, the spin-transfer torque acting on the magnetization. This new torque will add to the other torques acting on the magnetization as introduced in subsection 1.4.2 page 27. If the current is spin polarized, the contributions of all the conduction electrons add to one another and can finally help the magnetization to overcome the action of the damping torque.

There are various models in the literature explaining quantitatively this mechanism of exchange of spin angular moment[3,4,34–46] but until now, no one has been able to described all the experimental observations. To introduce the concept of spin-transfer torque, I chose among all of them a simple model proposed by Marc Stiles which has the benefit to present clearly many of the key aspects of this phenomenon[38–40]. The main idea is to calculate the net variation of spin current density before and after the interaction with a ferromagnet to deduce the loss of spin angular momentum of the spin polarized current flowing through it.

3.2 Quantitative model of spin-transfer

3.2.1 Framework of the model

Space is defined by a direct orthogonal basis $(\mathbf{e_x}, \mathbf{e_y}, \mathbf{e_z})$ corresponding to the three directions of space $(\mathrm{x}, \mathrm{y}, \mathrm{z})$ with z the quantification axis. We will consider a single electron flowing in the z direction with a wave vector k whose spin is polarized in the xz plane at an angle θ with the z direction (see figure 3.2). In the basis $(|\uparrow\rangle, |\downarrow\rangle)$ formed from the spin up and the spin down states this electron is represented by a planar wave function of the form

$$\varphi = \frac{\exp(\mathrm{i}kz)}{\sqrt{\Omega}} \left(a\,|\uparrow\rangle + b\,|\downarrow\rangle\right) \tag{3.1}$$

where Ω is a normalization volume. It is incident onto a ferromagnet whose magnetization points in the z direction. This ferromagnet is described using a Stoner approach. Inside it, the electrons experience an exchange splitting Δ which shifts the states of the down electrons to higher energy than the spin up electrons. Consequently, the electrons scatter at the interface with the ferromagnet from a rectangular potential energy step that depends on the spin state. For simplicity, we will consider that the height of the potential energy step is zero for the spin up state and Δ for the spin down state (see figure 3.2). Assuming a free electron dispersion and the energy of the electrons being $E > \Delta$, the electrons have a wave vector $k = \sqrt{2mE}/\hbar$ outside the ferromagnet and wave vectors $k_\uparrow = k$ and $k_\downarrow = \sqrt{2m(E-\Delta)}/\hbar$ inside the ferromagnet respectively for the spin up and down states.

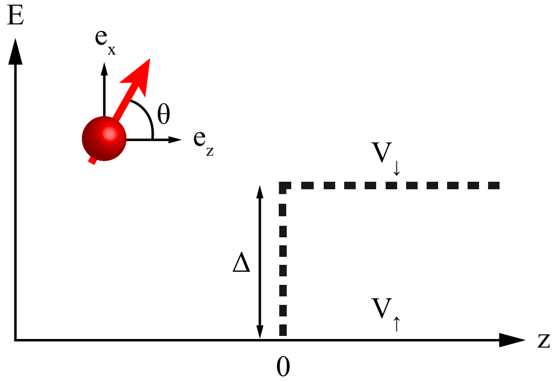

Figure 3.2 – Scheme of the potential energy step in the Stiles model

3.2.2 Quantum definition of spin current density

This model focuses on the calculation of spin current densities. A spin current density represents a number of spins flowing through a surface per surface and time units. It is related to the orientation of the spins in space and to the direction of their flow so this is a second order tensor quantity. It is given classically for a single electron by the outer product of the average electron velocity with the spin density $\boldsymbol{j}_{\mathbf{s}} = \boldsymbol{v} \otimes \boldsymbol{s}$.

In quantum mechanics, the spin is associated to the operator $\frac{\hbar}{2}\boldsymbol{\sigma}$ where $\boldsymbol{\sigma}$ is one of the Pauli matrices. In the framework of the model described here, they are three 2×2 matrices stated in the basis $(|\uparrow\rangle, |\downarrow\rangle)$, one for each space direction.

$$\boldsymbol{\sigma}_{\mathbf{x}} = \begin{pmatrix} 0 & 1 \\ 1 & 0 \end{pmatrix} \qquad \boldsymbol{\sigma}_{\mathbf{y}} = \begin{pmatrix} 0 & -i \\ i & 0 \end{pmatrix} \qquad \boldsymbol{\sigma}_{\mathbf{z}} = \begin{pmatrix} 1 & 0 \\ 0 & -1 \end{pmatrix}$$

Besides, the operator associated to the velocity is $\frac{\hbar}{im}\boldsymbol{\nabla}$ and the average velocity of a single electron waveform $\boldsymbol{\varphi}$ is therefore $\frac{\hbar}{\mathrm{i}m} \langle\boldsymbol{\varphi}|\boldsymbol{\nabla}|\boldsymbol{\varphi}\rangle$ related to the probability current density $\frac{\hbar}{m}\Im(\boldsymbol{\varphi}^{*}\boldsymbol{\nabla}\boldsymbol{\varphi})$. By analogy with its classical formulation, the quantum expression of the spin current density is so given by

$$\boldsymbol{j}_{\mathbf{s}} = \frac{\hbar^2}{2m}\Im\left(\boldsymbol{\varphi}^{*}\boldsymbol{\sigma} \otimes \boldsymbol{\nabla}\boldsymbol{\varphi}\right) \tag{3.2}$$

3.2.3 Calculation of the spin-transfer torque

Here is just presented a summary of all the steps required to get the expression of the spin-transfer torque. The detailed calculations can be found in appendix A.

Calculation of the wave functions

To calculate the variation of spin current density, first we need to calculate the wave function of an electron flowing in the energy landscape described in figure 3.2. This is a scattering problem so we have to calculate the expressions of the incident, reflected and transmitted part of the wave function, the general forms of which are given by equation 3.1.

The incident part of the electron wave function propagates in the non-magnetic material and its projections on the spin up and down states are determined by the orientation of the spin respectively to the quantization axis. After solving a system of two equations, one can finally found the expression of the incident wave function.

$$\boldsymbol{\varphi}_{\mathbf{in}} = \frac{\exp\left(\mathrm{i}kz\right)}{\sqrt{\Omega}}\left(\cos\frac{\theta}{2}\left|\uparrow\right\rangle + \sin\frac{\theta}{2}\left|\downarrow\right\rangle\right) \tag{3.3}$$

As soon as the incident part of the wave function reaches the interface with the ferromagnet, one part of it is reflected and the other one is transmitted through the magnet. The reflected wave function propagates in the non-magnetic material and the transmitted wave function propagates inside the ferromagnets where the spin up and down states do not have the same wave vectors. The coordinates of the wave function in the basis $(|\uparrow\rangle, |\downarrow\rangle)$ are determined by its continuity and the continuity of its derivative at the interface with the ferromagnet. Finally, solving these equations leads to the expressions of the reflected and the transmitted parts of the wave function.

$$\boldsymbol{\varphi}_{\mathbf{re}} = \frac{\exp(-\mathrm{i}kz)}{\sqrt{\Omega}} \frac{k-k_\downarrow}{k+k_\downarrow} \sin\frac{\theta}{2} |\downarrow\rangle \tag{3.4}$$

$$\boldsymbol{\varphi}_{\mathbf{tr}} = \frac{\exp(\mathrm{i}k_\uparrow z)}{\sqrt{\Omega}} \cos\frac{\theta}{2} |\uparrow\rangle + \frac{\exp(\mathrm{i}k_\downarrow z)}{\sqrt{\Omega}} \frac{2k}{k+k_\downarrow} \sin\frac{\theta}{2} |\downarrow\rangle \tag{3.5}$$

Now, all the necessary ingredients to calculate the spin current density through the entire system are gathered thanks to equations 3.3, 3.4 and 3.5.

Calculation of the spin current densities

Each wave function contributes to the total spin current density. We will calculate the spin current density coming from each one taking into account that the second order tensor of the spin current density is reduced to a vector since the wave functions propagate in the z direction only.

Applying the equation 3.2 to the incident, reflected and transmitted wave functions calculated above, the spin current densities can be determined.

$$\boldsymbol{j}_{\mathbf{s}}^{\mathbf{in}} = \frac{\hbar^2 k}{2m\Omega} (\sin\theta \mathbf{e_x} + \cos\theta \mathbf{e_z}) \tag{3.6}$$

$$\boldsymbol{j}_{\mathbf{s}}^{\mathbf{re}} = \frac{\hbar^2 k}{2m\Omega} \left(\frac{k-k_\downarrow}{k+k_\downarrow} \sin\frac{\theta}{2}\right)^2 \mathbf{e_z} \tag{3.7}$$

$$\begin{aligned}\boldsymbol{j}_{\mathbf{s}}^{\mathbf{tr}} = \frac{\hbar^2 k}{2m\Omega} \Bigg[& \sin\theta \cos\left[(k_\uparrow - k_\downarrow) z\right] \mathbf{e_x} - \sin\theta \sin\left[(k_\uparrow - k_\downarrow) z\right] \mathbf{e_y} \\ & + \left(\cos^2\frac{\theta}{2} - \frac{4kk_\downarrow}{(k+k_\downarrow)^2} \sin^2\frac{\theta}{2}\right) \mathbf{e_z} \Bigg]\end{aligned} \tag{3.8}$$

Calculation of the spin-transfer torque

The expressions of the spin current densities show that the spin current density flowing on the left side of the magnet $\boldsymbol{j}_{\mathbf{s}}^{\mathbf{in}} + \boldsymbol{j}_{\mathbf{s}}^{\mathbf{re}}$ is not equal to the spin current density flowing through the magnet $\boldsymbol{j}_{\mathbf{s}}^{\mathbf{tr}}$. Therefore, the spin angular momentum of the spin polarized current is not conserved.

This net variation of spin angular momentum of the spin polarized current can be transferred however to the magnetization of the ferromagnet so that the total angular momentum of the system is conserved. Assuming that the totality of this variation is transferred to the magnetization, the net variation of spin angular momentum per unit of time absorbed by the magnetization, that is to say the torque exerts on the magnetization, is given by $\mathbf{\Gamma_{str}} = S(\boldsymbol{j}_\mathbf{s}^\mathbf{in} + \boldsymbol{j}_\mathbf{s}^\mathbf{re} - \boldsymbol{j}_\mathbf{s}^\mathbf{tr})$ with S the surface of the interface. Injecting in this formula the equations 3.6, 3.7 and 3.8, the expression of the spin-transfer torque becomes

$$\mathbf{\Gamma_{str}} = S\frac{\hbar^2 k}{2m\Omega}\sin\theta\left[\left(1-\cos\left[\left(k_\uparrow - k_\downarrow\right)z\right]\right)\mathbf{e_x} + \sin\left[\left(k_\uparrow - k_\downarrow\right)z\right]\mathbf{e_y}\right] \tag{3.9}$$

3.2.4 Analysis of the spin-transfer torque

The model presented here shows that a spin polarized current going from a non-magnetic metal to a ferromagnet loses spin angular momentum. This variation of spin angular momentum generates a new torque acting on the magnetization, the spin-transfer torque, given by the formula 3.9. From it, various conclusions about the spin-transfer phenomenon can be drawn.

First of all, the previous calculations demonstrate that the absorption of spin angular momentum from the spin polarized current by a ferromagnet can generate a torque on its magnetization. This torque is perpendicular to the magnetization and equal to zero if the magnetization and the spin polarization are perfectly aligned ($\theta = 0$ or $\theta = \pi$). The angular evolution of the spin-transfer torque is discussed into more details in the next subsection. The spin-transfer torque also goes to zero if $k_\uparrow = k_\downarrow$ which means that it comes from the spin filtering effect of the ferromagnet.

Moreover, this model describes how the transfer of spin angular momentum could take place. The spin torque is composed of a constant term absorbed at the interface, due to the potential energy step and called the Slonczewski term $\mathbf{\Gamma_{str}^{sl}} = S\frac{\hbar^2 k}{2m\Omega}\sin\theta\mathbf{e_x}$. It is equal to the component perpendicular to the magnetization of the incident spin current density. The remaining terms of the spin torque form the so-called field like term $\mathbf{\Gamma_{str}^{fl}} = S\frac{\hbar^2 k}{2m\Omega}\left(\cos\left[\left(k_\uparrow - k_\downarrow\right)z\right]\mathbf{e_x} + \sin\left[\left(k_\uparrow - k_\downarrow\right)z\right]\mathbf{e_y}\right)$ created by the oscillations of the transmitted spins around the effective magnetic field as they propagate through the ferromagnet. The wavelength of these precessions $\frac{2\pi}{k_\uparrow - k_\downarrow}$ is generally very short for typical transition metals, of the order of few atomic layers. In a more rigorous calculation, one should take into account the fact that at the interface between two metals the electrons come from many different space directions so that the their precessions are not in phase. Integrating the effect of all these electrons at the interface, their precessions are quickly dephased and the mean value of the field like term becomes close to zero. In the end, the spin-transfer torque mainly comes from the absorption of the perpendicular to the magnetization component of the incident spin current density, at least in a spin-valve with a metallic spacer.

$$\boldsymbol{\Gamma}_{\mathbf{str}} \simeq S \left(\boldsymbol{j}_{\mathbf{s}}^{\mathbf{in}} \cdot \mathbf{e_x} \right) \mathbf{e_x} = S \frac{\hbar^2 k}{2m\Omega} \sin\theta \mathbf{e_x} \tag{3.10}$$

Indeed, in magnetic tunnel junctions where the spacer is an insulator the transport of the spin current from the polarizer to the free layer is due to a tunneling effect. The wave vectors of the tunneling electrons are strictly selected by the band structure of the junction. The same phenomenon occurs if the ferromagnet is a magnetic semiconductor. The dephasing process mentioned before is therefore less efficient. This is the reason why the field like term is generally taken into account when dealing with insulating spacers or magnetic semiconductors and not with metallic spacer.

One last important point to mention is that this model gives the false impression that the existence of a spin current requires a charge current in the same space region. Spin currents can actually flow within part of a device where there is no charge current. As a consequence, the spin-transfer effect can occur in a ferromagnet that do not carry charge current. This is a phenomenon pointed out by John Slonczewski calculating the interlayer exchange coupling in magnetic tunnel junctions[47]. It also appears in this model considering the case where both spin up and down components of the wave function are completely reflected. These pure spin currents are more and more studied in non-local geometries with multiterminal devices where a charge current is injected between two selected terminals and a spin current can diffuse throughout the rest of the device[48].

3.2.5 Comparisons with others spin-transfer models

The first theoretical studies on spin-transfer torque were performed within a ballistic approach[3,4,34–36]. In these models, the magnetic multilayer is connected to infinite reservoir of spins and the spin polarization arises from the spin dependent reflections at the interfaces with the magnetic layers. Nevertheless, like giant magnetoresistance in current-perpendicular-to-the-plane geometry (see chapter 1 section 2.2 page 35), the aspects of a diffusive transport through the entire spin-valve have a huge impact on the properties of the spin-transfer torque as it has been highlighted by some experimental works[49–52]. Therefore, the most recent theoretical studies on spin-transfer mixes these two approaches[37–46]: a diffusive transport inside the layers and a ballistic absorption of spin angular momentum at the interfaces. The main difference between these theories lies in their pre-

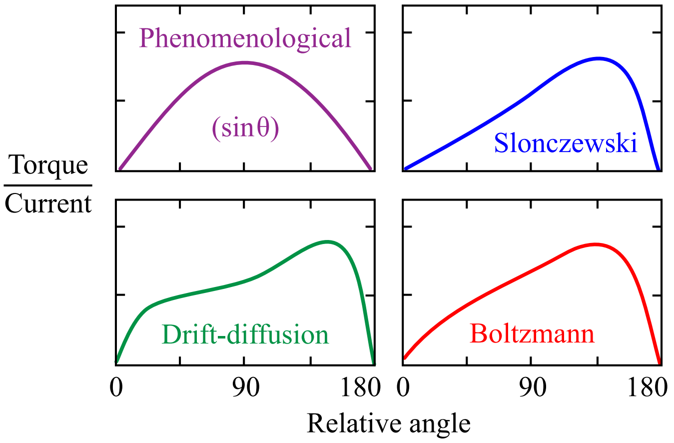

Figure 3.3 – Angular variation of the spin torque in various approaches.

diction of the spin-transfer torque evolution as a function of the relative angle between the polarizer and the free layer magnetizations (see figure 3.3).

In the simple model presented above the spin-transfer torque evolution is symmetric between the parallel and the antiparallel states (see the phenomenological curve of figure 3.3). In more complex models (the approaches of John Slonczewski[4,42], of the drift-diffusion theory[35,41,46] or of Boltzmann transport theory[44,45]) it is assymetric (see the Slonczewski, the drift-diffusion and the Boltzmann curves of figure 3.3). Indeed, the torque becomes larger around the antiparallel configuration than around the parallel one. It can even sometimes change sign if the interfaces are rightly chosen[51]. This result supports the argument that the angular variation of the spin-transfer torque and of the giant magnetoresistance in current-perpendicular-to-the-plane geometry are correlated[53,54]. At the end, one can express the spin-transfer torque by this formula[42,44]

$$\frac{\boldsymbol{\Gamma}_{\mathbf{str}}}{M_s} = -\beta I \mathcal{G}(\theta)\, \boldsymbol{m} \times (\boldsymbol{m} \times \boldsymbol{p}) \tag{3.11}$$

$$\text{with } \beta = \frac{\hbar\gamma_0}{2\mu_0 M_s V e} \tag{3.12}$$

$$\text{and } \mathcal{G}(\theta) = \frac{q_+}{A + B\cos\theta} + \frac{q_-}{A - B\cos\theta} \tag{3.13}$$

where $\boldsymbol{m}$ (resp. $\boldsymbol{p}$) is the unitary vector in the direction of the free layer (resp. polarizer) magnetization, V the volume of the free layer. The parameters q_+, q_-, A and B depend on the structure and on the materials of the spin-valve. The ratio $\frac{q_-}{q_+}$ is related to the asymmetry of the structure and the ratio $\frac{B}{A}$ to the asymmetry in the angular variation of the spin torque. From now on, we will use the equation 3.11 to express the spin-transfer torque.

3.3 Influence on the magnetization dynamics

Injecting a current through a spin-valve, the spin-transfer torque modifies the magnetization dynamics. One has to had this new torque in the LLG equation (see subsection 1.4.2 page 27). It becomes then the Landau-Lipschitz-Gilbert-Slonczewski or LLGS equation

$$\frac{d\boldsymbol{m}}{dt} = -\gamma_0 \boldsymbol{m} \times \boldsymbol{H}_{\mathbf{eff}} + \alpha \boldsymbol{m} \times \frac{d\boldsymbol{m}}{dt} - \beta I \mathcal{G}\left(\theta\right) \boldsymbol{m} \times \left(\boldsymbol{m} \times \boldsymbol{p}\right) \tag{3.14}$$

where the magnetization dynamics is ruled by three torques: the effective field torque ($\mathbf{\Gamma_{eff}}$), the damping torque ($\mathbf{\Gamma_{dam}}$) and the spin-transfer torque ($\mathbf{\Gamma_{str}}$).

If the damping constant α is small enough the damping torque can be approximate to $-\alpha\gamma_0 \boldsymbol{m} \times \boldsymbol{m} \times \boldsymbol{H}_{\mathbf{eff}}$. If the magnetic effective field inside the free layer is aligned with the polarizer magnetization, the damping and the spin torques are therefore aligned. Let's say that the effective field and the polarizer magnetization point in the z direction. In spherical coordinates, the LLGS equation becomes $\frac{d\boldsymbol{m}}{dt} = \sin\theta \left(\gamma_0 H_{\text{eff}} \mathbf{e}_{\boldsymbol{\phi}} - \left[\alpha\gamma_0 H_{\text{eff}} + \beta I \mathcal{G}\left(\theta\right)\right] \mathbf{e}_{\boldsymbol{\theta}}\right)$. It clearly confirms that the effective field induces a rotation of the magnetization around itself. On the contrary, the damping torque tries to align the magnetization with the effective field. Besides, it shows that spin-transfer can either have the same or the opposite effect of the damping torque (see figure 3.4). The spin torque can consequently generate two new behaviors. First, if it is opposed to the damping torque the magnetization may reverse by the only action of the injected current[5,55–58].

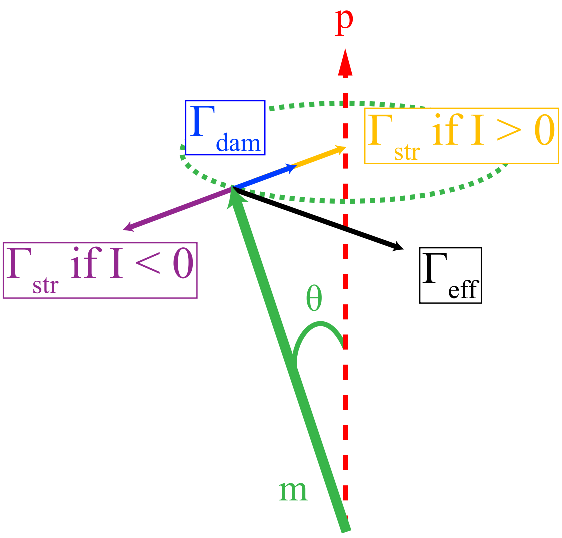

Figure 3.4 – Torques ruling the free layer magnetization dynamics

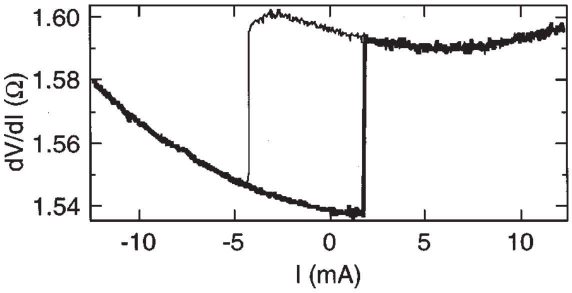

Figure 3.5 – Evolution of the differential resistance of a nanopillar as a function of the injected current. Figure extracted from Albert *et al.*[55].

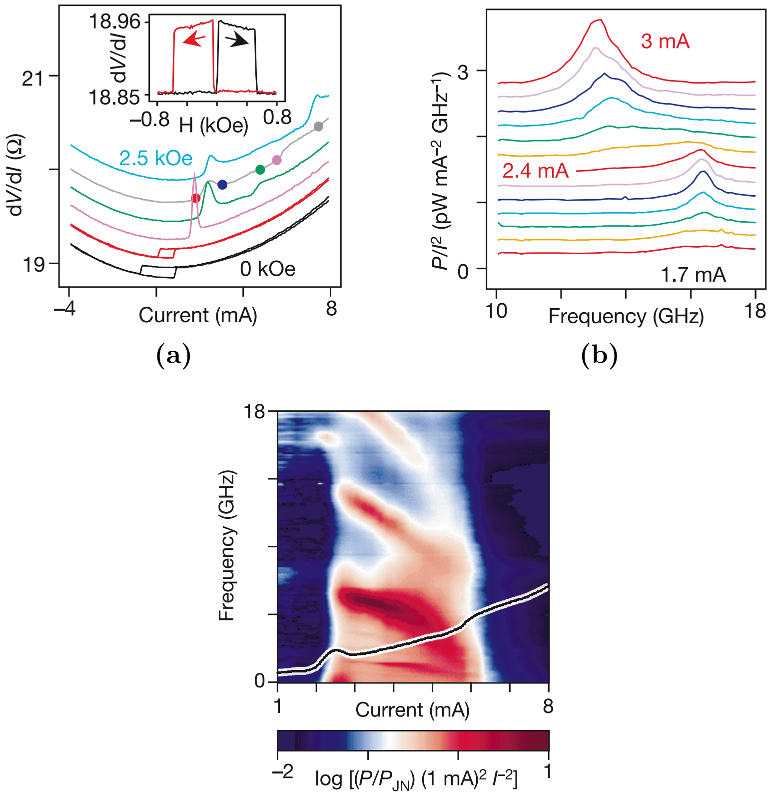

(a) (b)

(c)

Figure 3.6 – Current-induced magnetization precession. (a) Evolution of the differential resistance of a nanopillar as a function of the injected current. At low currents the reversal is hysteretic but at high currents pics appear on the curve. They are the sign of magnetization oscillations. (b) Power spectrum as a function of the frequency for various injected current. At high current pics appear centered on the frequency of the alternative current generated by magnetization precessions. (c) Power map as a function of the frequency and the injected current. The magnetization precessions start above 2 mA. Figures extracted from Kiselev *et al.*[8].

This is the current-induced magnetization switching. Since the sign of the spin-transfer torque depends on the sign of the current, the current-induced reversal of a magnetization is hysteretic (see figure 3.5). Second, if the spin torque exactly compensates the damping torque the magnetization presents continuous oscillations around the effective field[6–8,59–61]. This is the current-induced magnetization precession. In spin-valves with in-plane anisotropy, these oscillations generate an alternative current via the angular dependance of the giant magnetoresistance. This current is detected with a power spectrum analyzer to determine its frequency which is the same as the magnetization oscillation frequency (see figure 3.6). The tremendous interest of the magnetism community around the spin-transfer phenomenon arises from these new opportunities to control the magnetization dynamics without the need of an applied magnetic field.

3.4 Interest of perpendicular magnetizations

This thesis focuses on spin-transfer phenomenon in spin-valves with perpendicular magnetic anisotropy. Their magnetic layers have an easy anisotropy axis pointing in the out-of-plane direction. The first spin-valve measured for spin-transfer experiments had planar magnetic anisotropy because its the easiest anisotropy obtained with thin films (see chapter 1 subsection 1.2.3 page 20). Their magnetizations lied in one of the in-plane directions, often pinned in one specific direction thanks to shape anisotropy. Few years ago, new geometries appeared trying to improve the efficiency of spin-transfer torque. Some mix magnetic layers with perpendicular and planar magnetic anisotropies in order to optimize the current-induced magnetization precession[62,63] or reversal[64].

The aim of a spin-valve with both the polarizer and the free layer having perpendicular magnetic anisotropy is to develop a uniaxial model system (all the contributions in this system are expected to be aligned along the same axis) and to decrease the switching current required to observe current-induced magnetization reversal[14–16,65,66]. It is a critical issue to develop new magnetic memories based on this effect[67]. Indeed, the efficiency for magnetization reversal of a spin-valve with out-of-plane anisotropy is better than with in-plane anisotropy. The difference comes from the effect of the demagnetizing field in the two geometries. In a way, it supports the reversal in the out-of-plane case and slows it down in the in-plane case. The table below points out the differences between these two cases. The main point is that the switching current required to reverse the magnetization in the in-plane case has a constant term due to the demagnetization field impeding

Anisotropy	In-plane	Out-of-plane
$H_{\text{eff}}^{\text{P}\to\text{AP}}$	$H + H_{\text{dip}} + H_{\text{K}\parallel} + 2\pi M_{\text{s}}$	$H + H_{\text{dip}} + H_{\text{K}\perp} - 4\pi M_{\text{s}}$
$U_{\text{K}}\,(H = H_{\text{dip}})$	$\frac{M_{\text{s}} V H_{\text{K}\parallel}}{2}$	$\frac{M_{\text{s}} V (H_{\text{K}\perp} - 4\pi M_{\text{s}})}{2}$
$I_{\text{sw}}\,(H = H_{\text{dip}})$	$\frac{2e}{\hbar}\frac{2\alpha}{\mathcal{G}(\theta)}\left(U_{\text{K}} + \pi\mu_0 M_{\text{s}}^2 V\right)$	$\frac{2e}{\hbar}\frac{2\alpha}{\mathcal{G}(\theta)} U_{\text{K}}$

Figure 3.7 – Comparison between the effective magnetic field (H_{eff}), the energy barrier between the two stable magnetic states (U_{K}) and the switching current (I_{sw}) of spin-valves with in-plane or out-of-plane anisotropy. The polarizer in red has a fixed magnetization whereas the free layer in green can align parallel of antiparallel to it.

to reduce it at will. On the contrary, in the out-of-plane case the switching current is directly proportional to the height of the energy barrier between the parallel and the antiparallel states. The switching current can therefore be theoretically reduced to zero by taking down this energy barrier tuning the physical properties, the size and the shape of the magnetic layers. Nevertheless, the height of the energy barrier also controls the thermal stability of the magnetic states so that it cannot be reduced to nothing especially in the perspective of memory applications. Therefore, one needs to find a compromise between the thermal stability of the stored information and the intensity of the switching current. Thanks to this perpendicular anisotropy, the critical switching current can be reduced by one order of magnitude, down to 100 μA, while keeping enough thermal stability for applications[13].

Chapter 4

Finite temperature and magnetization dynamics

Usually, experiments in magnetism are performed at finite temperature. Moreover, the technologies based on magnetism such as magnetic memories are often used at room temperature. This chapter briefly presents how the magnetization dynamics is modified by finite temperature effects. We will focus first on conventional magnetization dynamics without spin-transfer torque before taking it into account subsequently.

4.1 Finite temperature and LLG equation

4.1.1 Finite temperature LLG equation

Thermal activation gives or takes randomly energy to a magnetic system generating fluctuations of the magnetization. The common approach to introduce this effect in the LLG equation was developed by Brown[68] in the early 1960's and is still improved nowadays[69]. It consists in adding a Langevin random field $\boldsymbol{H}_{\mathbf{L}}$ to the effective magnetic field. This field is related to the temperature of the system T by its components $H_{\mathrm{L,i}} = \sqrt{2\alpha k_{\mathrm{B}}T/\gamma_0 M_{\mathrm{s}} V}\,\delta_{\mathrm{i}}(t)$ with $\mathrm{i} \in \{\mathrm{x}, \mathrm{y}, \mathrm{z}\}$ and V the volume of the magnetic layer. $\delta_{\mathrm{i}}(t)$ is a gaussian random function of mean value $\langle \delta_{\mathrm{i}}(t) \rangle = 0$ and of mean square root $\sqrt{\langle \delta_{\mathrm{i}}^2(t) \rangle} = 1$. The aim of this theoretical Langevin field is to reproduce fluctuations of the magnetization. As a result, the finite temperature LLG equation is

$$\frac{d\boldsymbol{m}}{dt} = -\gamma_0 \boldsymbol{m} \times (\boldsymbol{H}_{\mathbf{eff}} + \boldsymbol{H}_{\mathbf{L}}) + \alpha \boldsymbol{m} \times \frac{d\boldsymbol{m}}{dt} \tag{4.1}$$

This equation is numerically solved to get the magnetization trajectories and its equilibrium states. However, this is a stochastic equation which means that every computation of it gives a different results. For instance, the reversal field of the magnetization is now distributed around its value at zero temperature. This distribution is proportional to the Langevin field and so broadens when the temperature increases. Therefore, this equation requires a statistical analysis.

4.1.2 Thermal activation and lifetime: Néel-Brown model

Since the magnetization reversal is now thermally activated, as soon as the magnetic system becomes bistable there is a non-zero probability to reverse. This probability was introduced by Néel[70] and further developed by Brown[68] thanks to a Fokker-Planck analysis of the finite temperature LLG equation. It increases exponentially with time and is characterized by a time constant. Both Néel and Brown supposed that this time constant follows the Boltzmann statistics and the value of the Langevin field components derives from this assumption. At the end, the magnetization reversal probability is described by these laws

$$P_{\mathrm{rev}}(t) = 1 - \exp\left(-\frac{t}{\tau}\right) \tag{4.2}$$

$$\text{with } \tau = \tau_0 \exp\left(\frac{E_{\mathrm{b}}(H)}{k_{\mathrm{B}}T}\right) \tag{4.3}$$

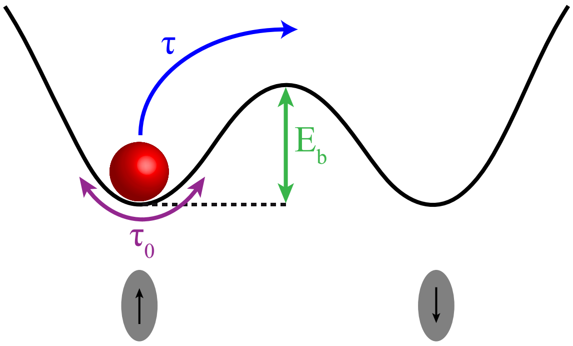

Figure 4.1 – Magnetic system in a double well energy potential landscape corresponding to two stable magnetic configurations separated by an energy barrier E_{b}. τ is the mean lifetime of the system in one well before crossing the barrier by thermal activation. τ_0 is a characteristic time of the magnetization fluctuations inside a well.

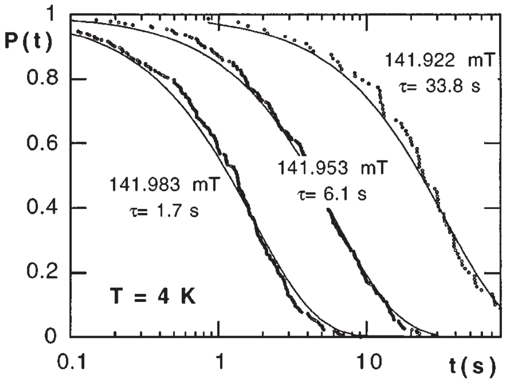

Figure 4.2 – Probability of not reversing the magnetization as a function of time for different applied fields and at 4K. Full lines are fits to the data with the Néel-Brown model. Figure extracted from Wernsdorfer *et al.*[75].

where $E_\mathrm{b}(H)$ is the potential energy barrier height seen from the local minimum around which the magnetization fluctuates at the attempt frequency $\frac{1}{\tau_0}$ (see figure 4.1). The physical meaning of the time constant τ is related to the mean lifetime of the magnetic system in this equilibrium state.

The main difference between Néel and Brown approaches is their theoretical expression for the attempt frequency. Actually, the debate around the value of τ_0 is still unsolved[71] and there are a lot of studies either experimental of theoretical trying to predict its evolutions with different parameters such as the direction of application of the magnetic field[72], the damping constant[73] or the size and the shape of the ferromagnet[74]. Nevertheless, the experimental studies on thermal relaxation of magnetization usually assume successfully a constant attempt frequency. In this case, the statistical law presented before forms the so-called Néel-Brown model. These equations are derived only for $E_\mathrm{b} \gg k_\mathrm{B}T$ which is therefore a limitation to their use.

This model proved to be very hard to verify experimentally because it requires to study only one single magnetic particle at a time, small enough and properly prepared so that defects, end or surface effects do not mask the role of thermal activation on magnetization reversal. As a result, the experimental confirmation[75] of the Néel-Brown model came only in 1997 studying ferromagnetic nanoparticles from 15 to 30 nm at very low temperature from 0.1 to 6 K and measuring for the first time a magnetization reversal probability described by equations 4.2 and 4.3 (see figure 4.2).

4.2 Finite temperature and spin-transfer

4.2.1 Finite temperature LLGS equation

Assuming that the spin-transfer torque does not modify the random Langevin field, one can integrate it into the finite temperature LLG equation. In this case, the finite temperature LLGS equation becomes

$$\frac{d\boldsymbol{m}}{dt} = -\gamma_0 \boldsymbol{m} \times (\boldsymbol{H}_{\mathbf{eff}} + \boldsymbol{H}_{\mathbf{L}}) + \alpha \boldsymbol{m} \times \frac{d\boldsymbol{m}}{dt} - \beta I \mathcal{G}(\theta)\, \boldsymbol{m} \times \boldsymbol{m} \times \boldsymbol{p} \tag{4.4}$$

where $\boldsymbol{H}_{\mathbf{L}}$ is defined as in subsection 4.1.1

4.2.2 Spin-transfer and lifetime

Adding the spin-transfer torque into the finite temperature equation of magnetization dynamics modifies the expression of the mean lifetime τ. However, it does not derive from an energy contrary to the effective field and cannot be introduced directly in the energy barrier E_{b}.

Let's look at the case of a ferromagnet with an uniaxial anisotropy and where the effective field and the polarizer are both collinear to its easy axis. As in chapter 3 section 3.3 page 47, we will consider a small damping so that the damping torque can be approximate to $-\alpha\gamma_0 \boldsymbol{m} \times \boldsymbol{m} \times \boldsymbol{H}_{\mathbf{eff}}$. The finite temperature LLG equation becomes

$$\frac{d\boldsymbol{m}}{dt} = -\gamma_0 \boldsymbol{m} \times (\boldsymbol{H}_{\mathbf{eff}} + \boldsymbol{H}_{\mathbf{L}}) - \alpha\gamma_0 \boldsymbol{m} \times \boldsymbol{m} \times \boldsymbol{H}_{\mathbf{eff}} \tag{4.5}$$

Since the effective field and the polarizer are collinear, $\boldsymbol{p} = {}^{\boldsymbol{H}_{\mathbf{eff}}}/_{H_{\mathrm{eff}}}$. The finite temperature LLGS equation becomes

$$\frac{d\boldsymbol{m}}{dt} = -\gamma_0 \boldsymbol{m} \times (\boldsymbol{H}_{\mathbf{eff}} + \boldsymbol{H}_{\mathbf{L}}) - \tilde{\alpha}\gamma_0 \boldsymbol{m} \times \boldsymbol{m} \times \boldsymbol{H}_{\mathbf{eff}} \tag{4.6}$$

where $\tilde{\alpha} = \alpha \left(1 + \frac{I}{I_{\mathrm{sw}}}\right)$ with $I_{\mathrm{sw}} = \frac{\alpha\gamma_0 H_{\mathrm{eff}}}{\beta\mathcal{G}(\theta)}$ the switching current at zero temperature. Equations 4.6 and 4.5 are mathematically equivalent with the same amplitude of the Langevin field. It suggests that the expression of the Langevin field components in the finite temperature LLG equation $H_{\mathrm{L,i}} = \sqrt{{}^{2\alpha k_{\mathrm{B}} T}/_{\gamma_0 M_{\mathrm{s}} V}}\,\delta_{\mathrm{i}}(t)$ remains valid but with the damping coefficient α replaced by $\tilde{\alpha}$. Yet, to write the finite temperature LLGS equation we assume that the spin-transfer torque does not modify the random Langevin field. To maintain this assumption, the magnetization has to experience a fictitious temperature $\tilde{T}$ such as $\tilde{\alpha}\tilde{T} = \alpha T$.

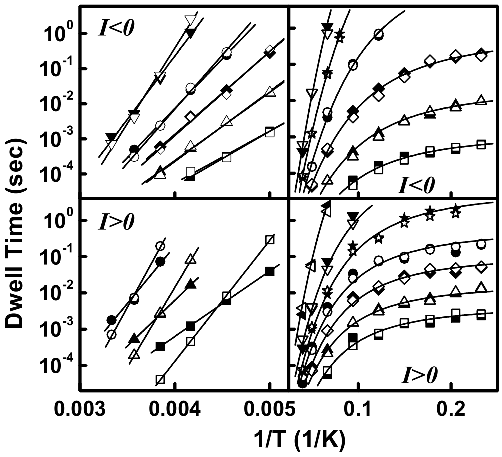

Figure 4.3 – Temperature dependance of the lifetime measured during magnetic telegraph noise in a spin-valve for different injected currents and applied magnetic fields. The open symbols are for AP to P transitions and the solid symbols for P to AP transitions. The lines are fits using a modified Néel-Brown model with a linear behavior of the current. Figure extracted from Krivorotov *et al.*[84].

Since equation 4.6 is now equivalent to a magnetization at temperature $\tilde{T}$ with damping $\tilde{\alpha}$, one may further deduce that the magnetization reversal probability is still given by equations 4.2 and 4.3 with a rescaled temperature $\tilde{T}$.

$$\begin{aligned} \tau &= \tau_0 \exp\left(\frac{E_\mathrm{b}(H)}{k_\mathrm{B}\tilde{T}}\right) = \tau_0 \exp\left[\frac{E_\mathrm{b}(H)}{k_\mathrm{B}T}\left(\frac{\tilde{\alpha}}{\alpha}\right)\right] \\ \Leftrightarrow \tau &= \tau_0 \exp\left[\frac{E_\mathrm{b}(H)}{k_\mathrm{B}T}\left(1-\frac{I}{I_\mathrm{sw}}\right)\right] \end{aligned} \tag{4.7}$$

This linear behavior obtained thanks to a simple model proposed by Jonathan Sun[76] has been derived in a more rigorous way following the original Fokker-Planck approach of Brown by Li and Zhang[77] and Apalkov and Visscher[78,79]. This law is still valid only for $E_\mathrm{b} \gg k_\mathrm{B}T$. This modified Néel-Brown model has been verified experimentally[77,80–86] in many cases involving magnetization reversal (see figure 4.3). However, it is valid only for quasistatic measurements because if short time current pulses are applied to the system the switching probability becomes determined by the spin angular momentum carried by the current pulse so that the switching probability is not a simple exponential anymore[87].

Part II

Samples and experimental setup
Echantillons et dispositif expérimental

French summary
Résumé en français

Cette partie se divise en deux chapitres. Après s'être intéressé à la fabrication des échantillons, le dispositif permettant la mesure de leurs propriétés est présenté.

Les vannes de spin mesurées durant cette thèse sont constituées de couches magnétiques aux anisotropies perpendiculaires. A cause de l'anisotropie de forme, l'aimantation d'une couche mince magnétique a tendance à s'orienter dans le plan de ces couches. Pour lutter contre cet effet et obtenir une couche aimantée perpendiculairement, on peut utiliser le phénomène d'anisotropie de surface ou d'interface. En effet, l'orientation particulière des orbitales atomiques de certains matériaux à leur surface ou à l'interface avec d'autres matériaux peut générer du fait du couplage spin-orbite une anisotropie perpendiculaire. En général, cet effet est rapidement masqué par l'anisotropie de forme si l'épaisseur de la couche dépasse quelques plans atomiques (voir figure 5.2 page 63), c'est pourquoi nous avons utilisé des couches magnétiques composées d'un empilement de bicouches dont l'anisotropie d'interface et les épaisseurs des deux couches la composant permettent d'obtenir une anisotropie perpendiculaire. Il est ainsi possible de former des couches magnétiques de plusieurs nanomètres d'épaisseur avec une anisotropie perpendiculaire.

Pour élaborer une vanne de spin à aimantations perpendiculaires dédiée à l'étude du transfert de spin, nous avons utilisé deux types de multicouches possédant une anisotropie perpendiculaire : [Co/Pt] et [Co/Ni]. Les multicouches de [Co/Pt] possèdent une plus forte anisotropie perpendiculaire que celles de [Co/Ni] (voir figure 5.3 page 64). Elles sont donc utilisées pour la fabrication d'une couche de référence ou couche dure dont l'aimantation reste fixe dans les conditions expérimentales usuelles. De leur côté, les multicouches de [Co/Ni] sont utiles pour fabriquer la couche douce ou libre dont l'aimantation doit pouvoir facilement se renverser. Le problème des multicouches de [Co/Pt] est leur faible pouvoir polarisant lié au platine. Or, la couche de référence doit également servir de polariseur le transfert de spin. On utilise donc un mélange des multicouches [Co/Pt] et [Co/Ni] pour élaborer un bon polariseur avec une forte anisotropie perpendiculaire (voir figure 5.5a page 65).

Une fois la structure déposée par pulvérisation cathodique sur un substrat, ses dimensions latérales sont réduites à quelques dizaines de nanomètres afin de diminuer l'intensité du courant critique d'observation du transfert de spin. La vanne de spin prend alors la forme d'un nanopilier. Cette étape très complexe à cause de la réalisation de contacts électriques est effectuée par le laboratoire de recherche d'Hitachi GST en Californie et combine l'utilisation de la lithographie électronique avec la gravure chimique. Au final, une vanne de spin sous forme d'un nanopilier est construite avec des électrodes permettant se connexion à un système de mesure électrique macroscopique (voir figure 5.7 page 67).

Ce système de mesure électrique permet l'étude du renversement de l'aimantation de la couche libre de ces nanopiliers grâce au suivi de l'évolution de sa résistance électrique sous l'influence de plusieurs paramètres tels que le champ magnétique appliqué ou le courant électrique injecté. Pour ce faire, nous avons utilisé un électroaimant bipolaire permettant d'appliquer un champ magnétique allant jusqu'à 0,7 T. Le courant est injecté avec une source de courant continu. Tout le dispositif expérimental est contrôlé par ordinateur via le protocole GPIB (voir figure 6.1 page 70).

Une méthode de mesure 4 pointes permettant d'éliminer les résistances parasites dues aux câbles de connexion et aux résistances de contact est utilisée. Deux techniques complémentaires permettent de déduire la résistance du nanopilier. La première est une mesure classique de résistance basée sur la loi d'Ohm combinant le courant continu injecté pour le transfert de spin à une mesure de tension continue. Elle ne permet donc pas d'étudier le nanopilier en l'absence de transfert de spin. La seconde méthode utilise un amplificateur à détection synchrone. Cet appareil injecte un faible courant alternatif à une fréquence donnée et mesure la réponse en tension du nanopilier à cette même fréquence permettant ainsi de réduite fortement l'intensité du courant injecté tout en conservant une bonne résolution sur la mesure de tension. Il s'agit d'une mesure de résistance différentielle. Son résultat n'est identique à la mesure de résistance classique que si le renversement de l'aimantation est purement hystérétique. Tout phénomène réversible se traduit généralement par l'apparition de pics dans la mesure de résistance différentielle (voir figure 6.3b page 74). Ces deux techniques sont donc bien complémentaires.

Chapter 5

Nanopillar spin-valves perpendicularly magnetized

As mentioned previously, the first experiments performed on spin-transfer used spin-valves with in-plane magnetizations because the demagnetizing field usually pushes the magnetization of a magnetic thin film in its plane (see chapter 1 subsection 1.2.3 page 20). The aim of this chapter is to explain how the magnetization of a thin film can overcome the action of the demagnetizing field to point out-of-plane and what kind of magnetic materials with perpendicular magnetic anisotropy is required to design a spin-valve dedicated to spin torque applications.

5.1 Thin films with perpendicular anisotropy

Going from a bulk material to a thin film, one dimension has to be reduced so the surface and interface effects becomes larger. The demagnetizing field increases drastically in the direction of the reduced dimension and the magnetization tends to lie in the plane of the layer.

However, magnetic thin films can be perpendicularly magnetized thanks to magnetic surface anisotropy. The bulk magnetic anisotropy arises from the fixed orientation of the atomic orbitals of the bulk. The surface magnetic anisotropy is a similar phenomenon appearing at a surface or an interface. Néel attributed it to the symmetry breaking of the surface or the interface[89]. This surface anisotropy increases as the thickness of the thin film decreases and can become larger than the shape anisotropy created by the demagnetizing field[90]. In some materials, such as in cobalt (111) grown between two gold layers, this surface anisotropy is perpendicular and forces the magnetization to point out-of-plane[88]. Nevertheless,

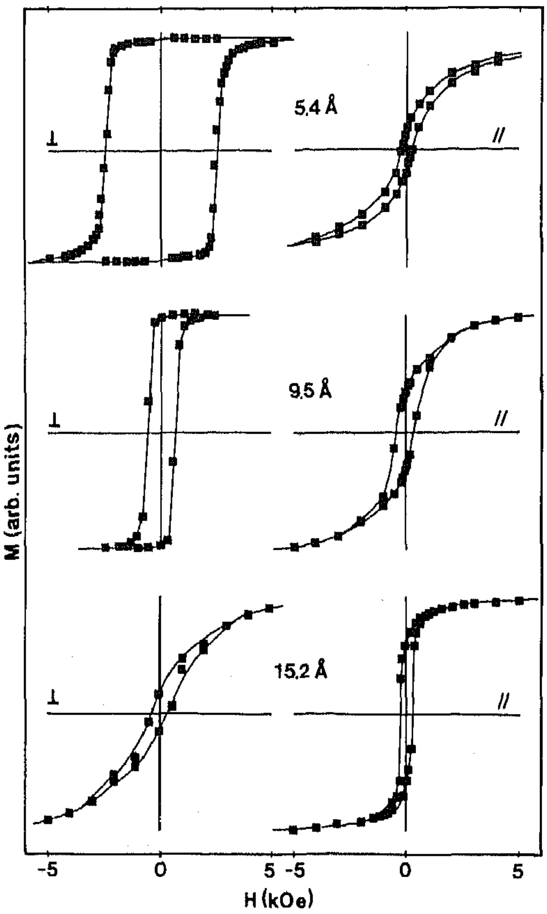

Figure 5.1 – Magnetization as a function of the magnetic field applied perpendicularly (⊥) and parallel (||) to the thin films plane for Au/Co/Au sandwiches of thickness 5.4, 9.5 and 15.4 Å at $T = 10$ K. The surface of the cobalt is oriented as (111) plane. When the thickness of the cobalt layer increases the hysteresis loop with the perpendicular applied magnetic field becomes less and less square because the magnetization falls into the plane. Figures extracted from Chappert *et al.*[88].

this effect quickly disappears after the deposition of only few atomic layers and requires a proper control of the surface roughness (see figure 5.1).

One way to increase the thickness of a magnetic layer while keeping the perpendicular magnetization is to grow a multilayer made of two different materials A and B having a perpendicular anisotropy at their interface. Each layer of A or B has to be thin enough for the perpendicular interface anisotropy of the bilayer AB to balance its planar shape anisotropy. Even if the thickness of a single bilayer is very low to maintain a perpendicular magnetization, the total magnetic layer can contain as many repetitions of it as desired. For instance, the use of

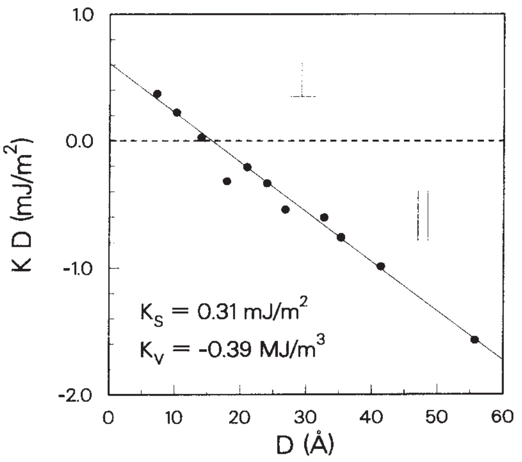

Figure 5.2 – Total anisotropy constant (taking into account the surface and the volume anisotropies) obtained from torque measurement times D the bilayer thickness as a function of D for [Co/Ni] multilayers with a constant thickness ratio. As soon as the thickness of the bilayer increases, the magnetic anisotropy first perpendicular ($K > 0$) becomes planar ($K < 0$). Figure extracted from Daalderop *et al.*[93].

a transition metal like cobalt or iron with platinum, palladium or gold results in large perpendicular magnetic anisotropy such as in [Co/Pd][91] or [Co/Pt][92] multilayers. Besides, some combinations of two transition metals like in [Co/Ni][93] multilayers also lead to perpendicular magnetizations (see figure 5.2). These two approaches are very useful to design a spin-valve with perpendicular magnetizations for spin-transfer applications.

5.2 For the purpose of spin-transfer applications

[Co/Pt] multilayers exhibit strong perpendicular magnetic anisotropy with high coercive fields if the layers of cobalt and of platinum are thin enough (see figure 5.3a). [Co/Ni] multilayers can also exhibit perpendicular magnetic anisotropy but with lower coercive fields (see figure 5.3b). As a result, [Co/Pt] is a good material to make a perpendicularly magnetized hard layer whereas [Co/Ni] can be used to make a perpendicularly magnetized free layer.

However, in a spin-valve structure dedicated to spin-transfer applications the hard layer also have to polarize the current because the higher the polarization of the current is the more efficient is the spin-transfer effect. Platinum or palladium are non-magnetic materials with a very high spin-orbit coupling so they reduce drastically the spin polarization of the current. For instance, the giant magnetore-

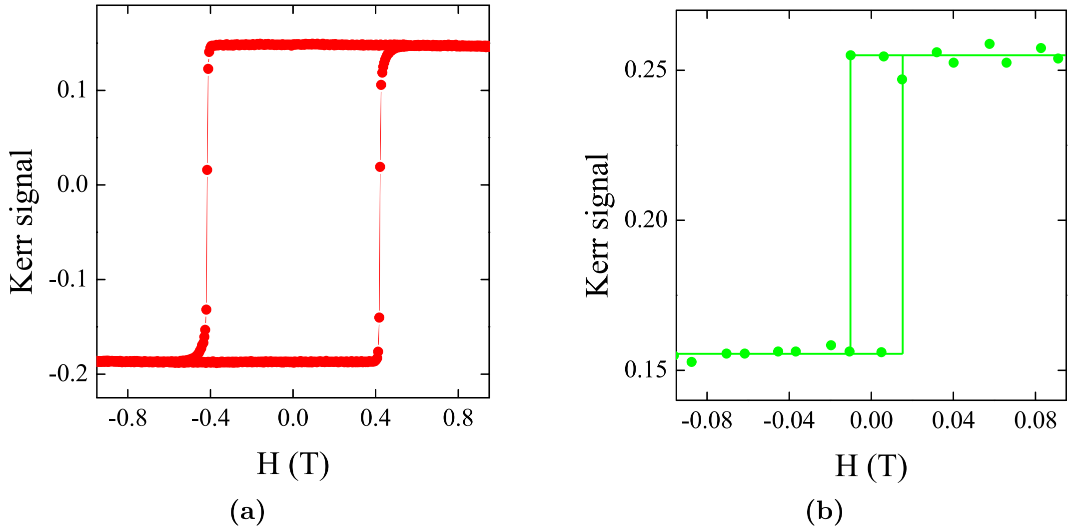

Figure 5.3 – Kerr signal as a function of the perpendicular applied magnetic field (a) for five repetitions of Co (2.5 Å) and Pt (5.2 Å) bilayer and (b) for five repetitions of Co (1 Å) and Ni (6 Å) bilayer. The square loops show that these systems are perpendicularly magnetized but the coercive field is ten times higher for the [Co/Pt] than for [Co/Ni].

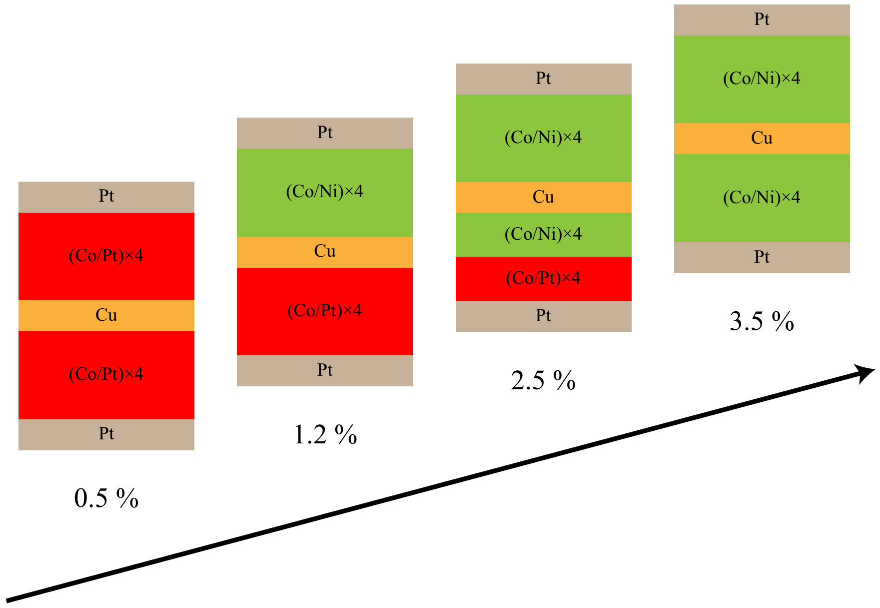

Figure 5.4 – Evolution of the magnetoresistance ratio measured with the current injected in-plane of spin-valves made of [Co/Pt] and [Co/Ni] multilayers removing more and more [Co/Pt] stacks.

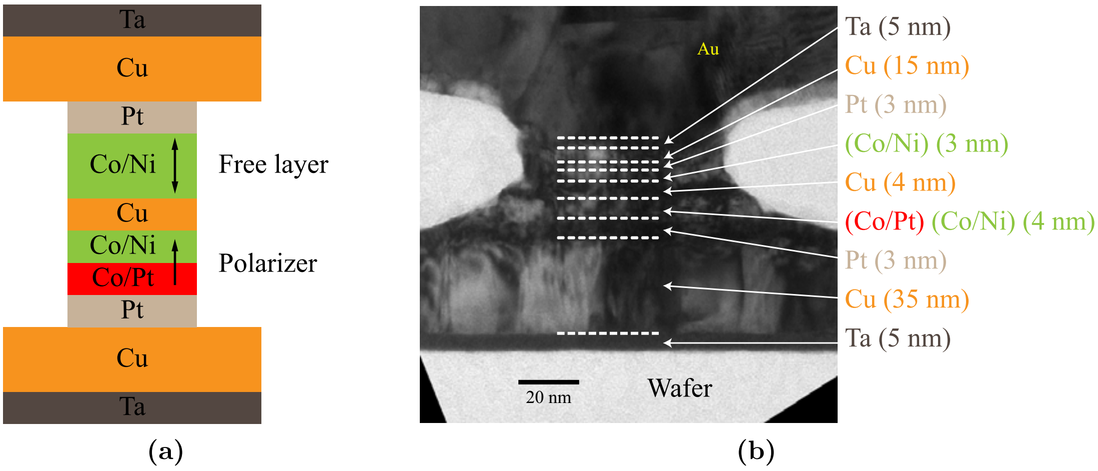

Figure 5.5 – (a) Scheme of the spin-valve structure used in this thesis. Note that the top platinum layer is not present on every samples. (b) Cross section view of a nanopillar obtained by scanning electron microscopy.

sistance ratio of a spin-valve made of [Co/Pt] and [Co/Ni] multilayers increases as soon as the proportion of [Co/Pt] stacks decreases (see figure 5.4) thanks to a better polarization of the current. The coercivity of the hard layer decreases at the same time. Consequently, a compromise between a good polarizing material such as [Co/Ni] and a high coercivity material such as [Co/Pt] is required to design the hard layer of the spin-valve. During this thesis, we used spin-valve with a polarizer made both of [Co/Pt] and of [Co/Ni] multilayers and with a free layer made of [Co/Ni] multilayers (see figure 5.5a). Some of the samples have a free layer covered by a thin platinum layer increasing their perpendicular magnetic anisotropy but reducing the magnetoresistance. The leads for the electrical measurements and the spacer are made of copper. Figure 5.5b presents a cross section view of a nanopillar obtained by scanning electron microscopy.

5.3 From thin films to nanopillars

I did not participate to the growth of the samples measured in these thesis so I will just present briefly here the different stages required to fabricate a nanopillar spin-valve with electric contacts. All the samples presented in this manuscript were made in the Hitachi Global Storage Technologies center of research in San Jose, California, USA.

To begin, the structure composed of all the metallic layers presented on figure 5.5 has to be deposited. It was grown by coevaporation and dc magnetron sputtering. Then, it is patterned in different shapes such as circle, ellipse, hexagon or square using electron beam lithography and ion beam etching. The patterning process can generally be summarized in five steps (see figure 5.6):

1. A mask of the dimension of the required nanopillar is defined on top of the multilayer. To do so, a layer of photoresist is deposited on top of the multilayer. Then, electron beam lithography is used to draw on the resist the shape of the nanopillar. Due to the interaction between the resist and the electron beam, the non-illuminated part of the resist can be removed thanks to a chemical development whereas the illuminated part is not affected and forms the mask.

2. The nanopillar is etched thanks to ion beam etching. The mask protects the multilayer underneath so that the nanopillar shape is obtained. The remaining steps are required to add to the structure a top electric contacts.

3. A layer of insulator is deposited to insulate the bottom and the top electric contacts.

4. The insulator on top of the nanopillar is removed. The small size of the nanopillar makes this planarization step particularly tricky. One method is to use a resist mask for the step one, to depose the insulator and then to remove the insulator on top of the nanopillar thanks to a chemical solution attacking the mask of resist. This is a lift-off process. Another method used for the samples presented in this thesis consists in a chemical-mechanical polishing combining chemical etching and mechanical polishing.

5. The top electrode is deposited.

At the end of all this process, nanopillar spin-valves are obtained of different shapes and sizes of the order of 100 nm (see figure 5.7a). The bottom and the top electrodes are connected to four micrometric square pads (see figure 5.7b), two pads for one electrode, in order to perform four-terminal sensing.

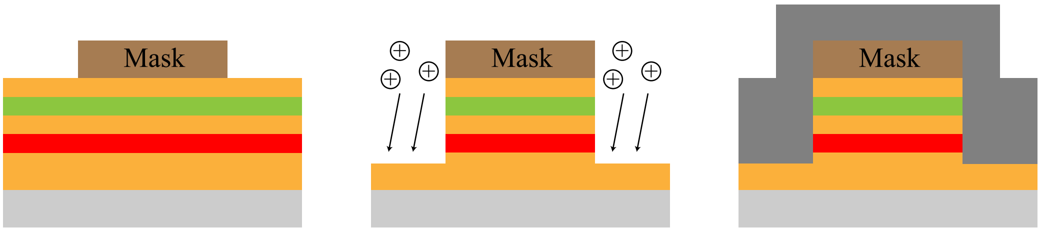

1. Elaboration of a mask for the etching

2. Ion beam etching of the nanopillar

3. Deposition of the insulator

4. Planarization

5. Deposition of the top electrode

Figure 5.6 – The five principal steps to fabricate a nanopillar with electric contacts.

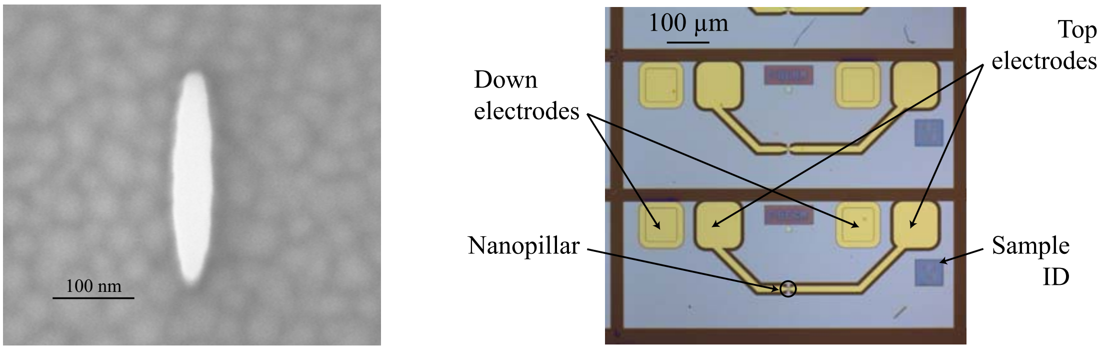

(a)

(b)

Figure 5.7 – (a) Scanning electron microscopy top view of a nanopillar spin-valve of elliptical shape of 50 nm by 300 nm. (b) Optical microscopy image of a sample composed of a nanopillar spin-valve connected to four electrical contacts.

Chapter 6

Electric measurement of spin-valves

This chapter presents the experimental setup built during this thesis to measure the nanopillar spin-valves described in the previous chapter. Every sample is connected to a chip easy to manipulate by hand thanks to wire bonding. The chip is then connected to the measurement setup.

6.1 Organization of the experimental setup

The study of the magnetic properties of our spin-valves requires to perform transport measurement under the action of a magnetic field. To do so, we built at the beginning of this thesis a transport measurement setup (see figure 6.1). This section presents briefly the key aspects of this setup and a detailed description of the equipments can be found in appendix B page 175.

We used an electromagnet cooled down by water with its power supply to apply a magnetic field up to 0.7 T and a dc current source to generate the spin-transfer effect. Since the determination of the spin-valves magnetic configuration is based on the giant magnetoresistance effect (see chapter 2 page 29), an experimental access to the resistance of the nanopillar is necessary. We used two complementary technics to measure it. First, we measured the conventional dc resistance injecting a dc current with a dc current source (the same as the one used to generate the spin-transfer effect) and measuring the dc voltage across the nanopillar with a nanovoltmeter. The main problem of this technic is that it requires at least a current of 0.5 mA to get enough resolution to discriminate the parallel and the antiparallel resistance states. As a result, it is impossible to record the behavior of the spin-valve the spin-transfer torque. The second technic

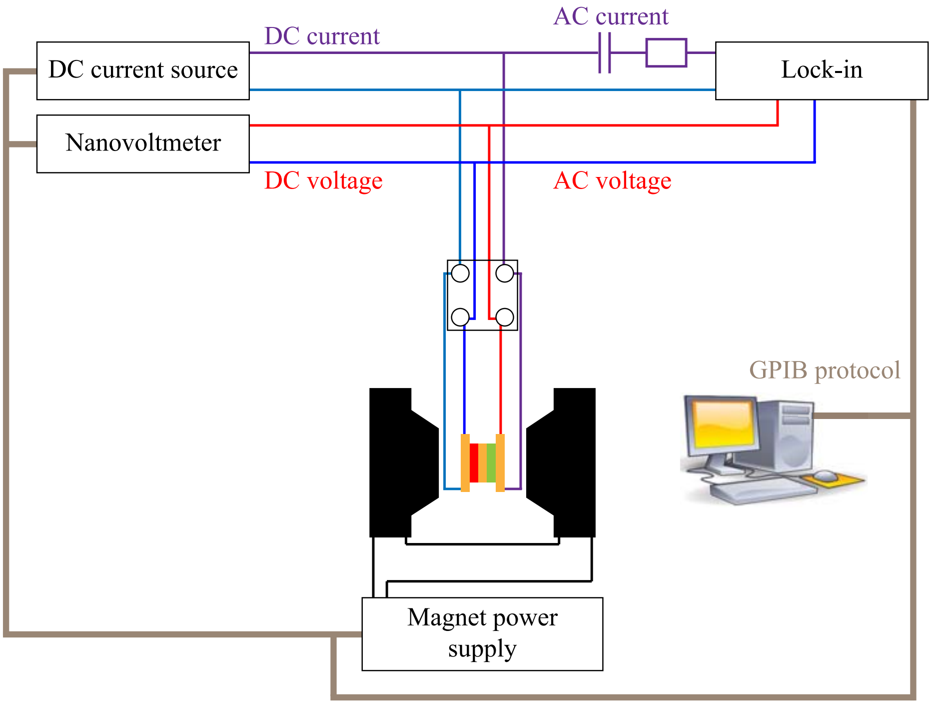

Figure 6.1 – Scheme of the experimental setup

we used is more complicated but works for currents ten times smaller than the previous one so that the spin-transfer effect becomes negligible. It consists in the use of a lock-in or an ac-bridge that injects a small ac current (the resistance at the output of the lock-in in figure 6.1 transforms the ac voltage of the lock-in into an ac current) at a fixed frequency and measures the voltage response of the sample at the same frequency. The resolution with this ac measurement is similar to the resolution of the dc measurement at high current. All these equipments are remotely controlled by a computer via the GPIB protocol.

Special care has to be taken to secure and improve the resolution of this setup. First, mixing ac and dc current can lead to a general decrease of the measurement resolution. The nanovoltmeter is very sensitive to the ac current at low frequency but it is usually built with a low-pass filter so the frequency of the ac current has to be higher than its cutoff frequency. The lock-in has similarly to be protected from the dc current thanks to a capacitor. Then, the nanopillars can be broken because of electrostatic charges. To secure their connection and disconnection to the setup the best is to shortcut its four connections thanks to a switch. Finally, the resistances of the connections and of the wires can be significantly higher than the resistance of the pillar. Therefore, four-terminal sensing is very helpful to measure the resistance of the nanopillar only.

The two next sections describes into more details the interest of the four-terminal sensing and the principle of dual-phase lock-in technics.

6.2 Interest of four-terminal sensing

An ohmmeter is composed of a constant current source and of a voltmeter. It injects a current through the sample and measures its voltage response to get its resistance thanks to the Ohm's law. Two measurement configurations can exists: one where the current source and the voltmeter are connected to the same points, this is the two-terminal sensing configuration, and one where they are connected to different points, this is the four-terminal sensing (see figure 6.2). In this two cases, the injected current modifies the voltage of the entire system that is to say of the sample but also of the wires and of the contacts so the measured voltage depends on the position of the voltmeter. Let's calculate the resistance measured in these two configurations taking into account the resistances of the wires (r_{w}), of the contacts (r_{c}) and of the voltmeter (R_{v}).

In the two-terminal configuration, the voltmeter measures the influence of the current on the resistance itself but also on the shared wires with the current source and on the contacts. They are all connected in series and the resistance of the voltmeter is in parallel. So the measured voltage is given by $U = R_{\mathrm{tot}} I$ with $R_{\mathrm{tot}} = \frac{(R+r_{\mathrm{w}}+r_{\mathrm{c}})R_{\mathrm{v}}}{(R+r_{\mathrm{w}}+r_{\mathrm{c}})+R_{\mathrm{v}}}$. Since the resistance of the voltmeter is very high (1 MΩ for our experimental setup), the voltage can be approximate to $U = (R + r_{\mathrm{w}} + r_{\mathrm{c}})\, I \simeq RI$ only if r_{w}, $r_{\mathrm{c}} \ll R$. For metallic nanopillar this condition

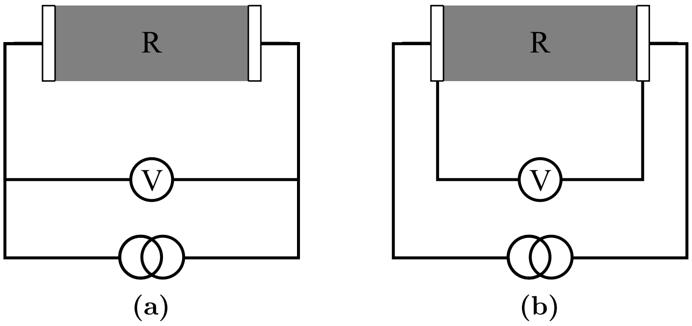

(a) (b)

Figure 6.2 – Resistance measurement configurations (a) in a two-terminal sensing and (b) in a four-terminal sensing.

is not often valid and the measured resistance is generally overestimated with this configuration. For instance, the experimental setup used during this thesis estimates the resistance of a 4 Ω nanopillar to 20 Ω with two-terminal sensing.

In the four-terminal configuration, the voltmeter has no common wires and contacts with the current source. Consequently, the system is composed of the resistance with in parallel the resistance of the wires, of the contacts and of the voltmeter all three connected in series. So the measured voltage is given by $U = R_{\mathrm{tot}} I$ with $R_{\mathrm{tot}} = \frac{(r_{\mathrm{w}}+r_{\mathrm{c}}+R_{\mathrm{v}})R}{(r_{\mathrm{w}}+r_{\mathrm{c}}+R_{\mathrm{v}})+R}$. Since the resistance of the wires and of the contacts are negligible compare to the resistance of the voltmeter, the voltage can be approximate to $U = \frac{RR_{\mathrm{v}}}{R+R_{\mathrm{v}}} I \simeq RI$ because for a metallic nanopillar $R \ll R_{\mathrm{v}}$.

Therefore, four-terminal sensing allows to access to the resistance of the spin-valve structure only.

6.3 The dual-phase lock-in amplifier

6.3.1 Principle of the dual-phase lock-in amplifier

Lock-in amplifiers are very convenient to detect and measure a very small ac signal even if it is obscured by larger noise sources. They use a phase sensitive detection to single out the component of the signal at a specific reference frequency and phase. Noise signals at other frequencies than the reference frequency are rejected and do not affect the measurement. A simple band pass filter is not enough to reduce the noise signals because its bandwidth is still too large even with an high quality factor.

A dual-phase lock-in amplifier generates its own sine wave reference signal $V_{\mathrm{l}} = V_{\mathrm{l}}^0 \sin(\omega_{\mathrm{l}} t + \theta_{\mathrm{l}})$. Then it measures the response signal of the sample, amplifies and multiplies it by its reference signal thanks to a first phase sensitive detector or multiplier. To start, let's assume that the measured signal is also a sine wave $V_{\mathrm{s}} = V_{\mathrm{s}}^0 \sin(\omega_{\mathrm{s}} t + \theta_{\mathrm{s}})$. The signal at the output of the first phase sensitive detector is so given by $V_{\mathrm{psd1}} = V_{\mathrm{s}}^0 V_{\mathrm{l}}^0 \sin(\omega_{\mathrm{s}} t + \theta_{\mathrm{s}}) \sin(\omega_{\mathrm{l}} t + \theta_{\mathrm{l}})$ which is the sum of two cosine waves.

$$V_{\mathrm{psd1}} = \frac{1}{2} V_{\mathrm{s}}^0 V_{\mathrm{l}}^0 \left[\cos\left([\omega_{\mathrm{s}} - \omega_{\mathrm{l}}]\, t + \theta_{\mathrm{s}} - \theta_{\mathrm{l}}\right) - \cos\left([\omega_{\mathrm{s}} + \omega_{\mathrm{l}}]\, t + \theta_{\mathrm{s}} + \theta_{\mathrm{l}}\right)\right]$$

The frequency of these two ac signals are $(\omega_{\mathrm{s}} + \omega_{\mathrm{l}})$ and $(\omega_{\mathrm{s}} - \omega_{\mathrm{l}})$.

If the phase sensitive detector signal is passed through a low pass filter with a low cutoff frequency generally no signal will be left. However, if $\omega_{\mathrm{s}} = \omega_{\mathrm{l}}$ the difference frequency component will be a dc signal. In this case, the filtered phase sensitive detector output signal is

$$V_{\mathrm{psd1}} = \frac{1}{2} V_{\mathrm{s}}^{0} V_{\mathrm{l}}^{0} \cos\left(\theta_{\mathrm{s}} - \theta_{\mathrm{l}}\right)$$

If a noise signal is not at the reference frequency it will be attenuated by the low pass filter. A proper choose of the reference frequency can so greatly improve the measurement. Indeed, only the signal at the reference frequency results in a true dc signal that is not affected by the low pass filter. However, not only do the frequencies have to be identical but the difference of phase $\theta_{\mathrm{s}} - \theta_{\mathrm{l}}$ cannot change with time, otherwise V_{psd1} will not be a dc signal. Lock-in amplifiers use a phase locked loop to track changes of phase and reduce them.

Until now the filtered output of the first phase sensitive detector is proportional to the difference of phase between the signals. This phase dependency can be eliminated by adding a second phase sensitive detector that multiplies the measured raw signal with the reference signal shifted by 90°. In this case, its low pass filtered output is

$$V_{\mathrm{psd2}} = \frac{1}{2} V_{\mathrm{s}}^{0} V_{\mathrm{l}}^{0} \sin\left(\theta_{\mathrm{s}} - \theta_{\mathrm{l}}\right)$$

Now, we have two outputs proportional to $\cos\left(\theta_{\mathrm{s}} - \theta_{\mathrm{l}}\right)$ and to $\sin\left(\theta_{\mathrm{s}} - \theta_{\mathrm{l}}\right)$. By computing them, the phase dependency is removed: $\frac{1}{2} V_{\mathrm{s}}^{0} V_{\mathrm{l}}^{0} = \sqrt{V_{\mathrm{psd1}}^{2} + V_{\mathrm{psd2}}^{2}}$. Knowing precisely the amplitude of the reference signal, the dual phase lock-in amplifier allows to access to the desired signal even if it is very small. Therefore, the resistance of nanopillars can be measured with small enough current excitations that do not generate a significant spin-transfer effect.

6.3.2 Interests of the dual-phase lock-in amplifier

In addition to the possibility of small current excitation measurements mentioned above, dual-phase lock-in technic has another interest concerning the measurement of magnetization reversal. Indeed, it can discriminate between the irreversible hysteretic processes and the reversible ones.

Let's consider a nanopillar spin-valve measured with the experimental setup described in figure 6.1 page 70. The resistance of this spin-valve depends on the dc injected current I because of the spin-transfer effect. The dc current source and the nanovoltmeter give an access to the conventional resistance of the nanopillar, noted R_{dc}. Besides, with the dual-phase lock-in technic a small ac current excitation, noted dI, is added to the dc injected current and the small ac voltage variation of the nanopillar resulted from this excitation, noted dV, is measured. This small ac voltage response depends on the resistance of the spin-

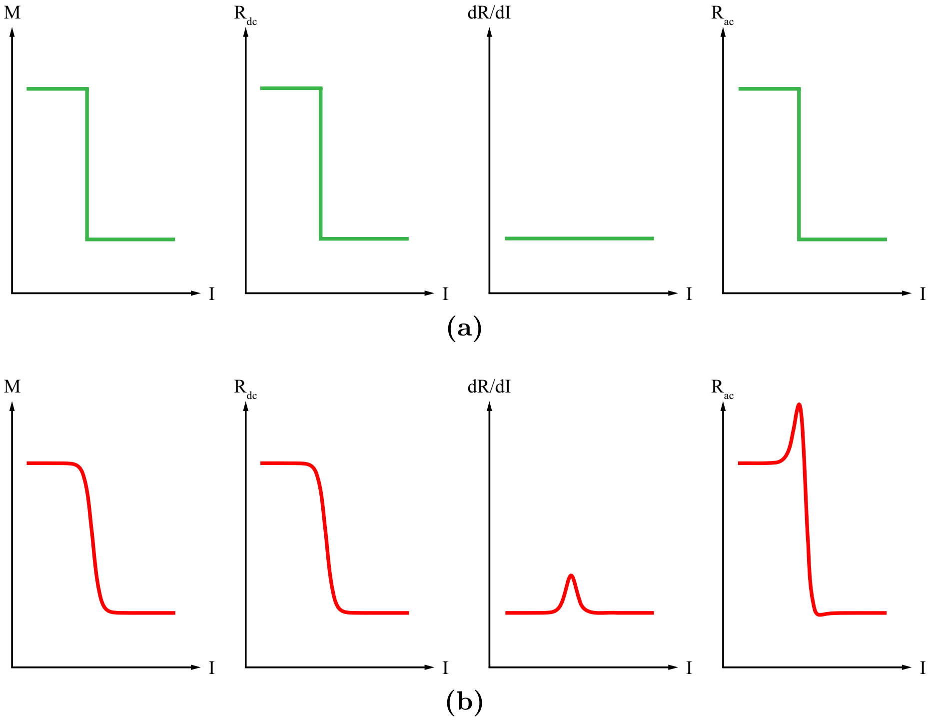

(a)

(b)

Figure 6.3 – Scheme of the resistance measurement in the dc and of the ac cases (a) for a pure irreversible reversal and (b) for a progressive reversal.

valve and varies with the intensity of the injected current. As a result, the lock-in accesses to the slope of the resistance as a function of the injected current curve of the nanopillar. Indeed,

$$R_{\text{ac}} = \frac{dV}{dI} = \frac{d\,(RI)}{dI} = R_{\text{dc}} + I\frac{dR}{dI}$$

where R_{ac} is the resistance obtained from the lock-in technic.

Consequently, the dc and the ac resistance measurements give the same results only if the slope of the resistance versus the injected current is always zero (see figure 6.3a). This is the case for a pure irreversible reversal only. On the contrary, if this slope is non zero these two measurements give different results. This is the case when the magnetization changes its orientation progressively to reverse. It generally results in the presence of pics in the R_{ac} measurements (see figure 6.3b and 3.6a) often interpreted as a sign of magnetization precessions[5–8] but not always[81,85].

Part III

Current and field phase diagrams
Diagramme de phase courant-champ

French summary
Résumé en français

Cette partie présente une étude globale des propriétés magnétiques et électriques des vannes de spin aux aimantations perpendiculaires basée sur l'examen d'une figure particulière appelée diagramme de phase. Après s'être intéressé dans le premier chapitre à la définition et à l'obtention d'un diagramme de phase, le second chapitre traite de la modélisation analytique de ces diagramme de phase afin de mieux comprendre leur allure. Pour finir, une interprétation entièrement énergétique de l'évolution de nos systèmes est décrite dans le dernier chapitre afin d'analyser en profondeur l'origine physique du comportement de ces systèmes parfois contre-intuitif.

Un diagramme de phase est une figure qui permet de représenter de manière synthétique les différents états magnétiques accessibles à une vanne de spin en fonction du champ magnétique appliqué et du courant électrique injecté.

Nos vannes de spin aux aimantations perpendiculaires possèdent deux principaux états magnétiques si l'aimantation de la couche de référence reste fixe : un état d'aimantations parallèles et un état d'aimantations antiparallèles. Du fait de leurs propriétés magnétiques et électriques, elles évoluent entre ces deux états de manière hystérétique à la fois avec le champ magnétique appliqué et avec le courant électrique injecté. Pour obtenir le diagramme de phase d'une de ces vannes de spin, il faut donc mesurer une grande quantité de cycles d'hystérésis en champ à différents courants et/ou de cycles d'hystérésis en courant à différents champs. En effet, un cycle d'hystérésis divise l'axe des champs magnétiques ou des courants en trois régions : à une extrémité, une où la vanne de spin est dans l'état parallèle, à l'autre extrémité, une où la vanne de spin est dans l'état antiparallèle et entre les deux, une région bistable où la vanne de spin peut être soit dans l'état parallèle, soit dans l'état antiparallèle. Les deux frontières entre la région bistable et la région antiparallèle d'une part et entre la région bistable et la région parallèle d'autre part sont signalées par les champs ou les courants de renversement (voir figure 7.4a page 86). Ainsi, le tracé de l'évolution des courants de renversement en fonction du champ magnétique appliqué permet de dessiner le diagramme de phase d'une vanne de spin.

Expérimentalement, on observe, par exemple, que les cycles d'hystérésis en champ se déportent vers les champs magnétiques négatifs au fur et à mesure que le courant injecté passe des valeurs négatives aux valeurs positives. Ceci est bien en accord avec les conventions de champ et de courant utilisées dans ce manuscrit : un champ appliqué dans la même direction que l'aimantation de la couche de référence et un courant injecté de manière à ce que les électrons circulent du polariseur vers la couche libre sont comptés positivement et favorisent l'état parallèle. En plus de ce déplacement, on remarque également que la partie bistable des cycles d'hystérésis en champ diminue au fur et à mesure que le courant injecté passe des valeurs négatives aux valeurs positives. Au final, il arrive qu'à courant positif et champ négatif le cycle d'hystérésis disparaisse pour laisser place à de larges pics mesurés uniquement sur la résistance différentielle (voir figure 7.6 page 89). Ils sont le signe de mouvements réversibles de l'aimantation généralement interprétés comme un mouvement de précession d'après certaines études théoriques.

Afin de comprendre l'allure de ces diagrammes de phase, nous avons essayé de les modéliser analytiquement.

Le modèle le plus simple permettant de représenter nos vannes de spin aux aimantations perpendiculaires est le suivant. La température considérée est nulle. Toutes les aimantations sont modélisées par des macrospins. L'aimantation de la couche de référence est fixe pointant dans la direction perpendiculaire aux couches. L'aimantation de la couche libre est également maintenue dans la direction perpendiculaire grâce à une anisotropie uniaxiale dont l'axe de facile aimantation est dans la direction perpendiculaire. Le champ magnétique est appliqué et le courant injecté circule également dans la direction perpendiculaire. Au final, toutes les contributions magnétiques et électriques se concentrent dans la direction perpendiculaire aux couches. Il s'agit d'une modélisation uniaxiale (voir figure 8.1 page 92). Dans le cadre de ce modèle, il est possible de calculer analytiquement l'évolution des courants de renversement avec le champ magnétique appliqué. Il s'agit d'une évolution purement linéaire qui ne correspond pas complètement aux observations expérimentales (voir figure 8.3 page 97). En effet, bien qu'une évolution linéaire soit présente dans les diagrammes de phase expérimentaux, elle est interrompue autour du champ de renversement à courant nulle. Autour de cette valeur de champ, il semble que le courant n'a qu'un très faible effet sur le renversement. Il doit atteindre des valeurs critiques pour que l'évolution linéaire prédite dans le cadre de ce modèle simple soit finalement observée.

Pour trouver le paramètre du système à l'origine de ce comportement singulier, nous avons comparé des diagrammes de phase mesurés dans des conditions différentes. Ceci nous a permis de tester l'influence des trois hypothèses principales de notre modèle simple : l'absence d'activation thermique (voir figure 8.4 page 99), l'uniformité de l'aimantation de la couche libre (voir figure 8.5 page 100) et l'uniaxialité (voir figure 8.6 page 101). La conclusion de ces comparaisons est que l'absence d'uniaxialité dans nos systèmes doit certainement être à l'origine de l'apparition des courants critiques. Des composantes magnétiques non-perpendiculaires peuvent y apparaître à la fois par des contributions intrinsèques telles qu'un axe d'anisotropie légèrement penché ou par des contributions extrinsèques telles qu'un champ magnétique appliqué légèrement désaxé.

Pour confirmer l'influence d'une contribution magnétique non-perpendiculaire sur le diagramme de phase d'une vanne de spin aux aimantations perpendiculaires, nous avons affiné notre précédent modèle en y introduisant un champ magnétique appliqué avec un certain angle par rapport à la direction perpendiculaire (voir figure 8.7 page 102). Il est alors possible de calculer analytiquement la nouvelle évolution des courants de renversement avec le champ magnétique appliqué. Les courants critiques apparaissent et le diagramme de phase obtenu est beaucoup plus proche des diagramme expérimentaux (voir figure 8.9a page 107).

Bien qu'il semble qu'une contribution non-perpenculaire soit à l'origine des courants critiques, il reste très contre-intruitif que le transfert de spin ne puisse affecter le renversement de la couche libre pour une certaine gamme de courant. Afin de clarifier ce phénomène, nous avons développé une interprétation purement énergétique de l'évolution de nos systèmes.

Cette interprétation allie l'étude de l'énergie magnétique de l'aimantation de la couche libre avec le calcul de la puissance totale qu'elle reçoit grâce aux couples de dissipation et de transfert de spin. En effet, contrairement à une étude énergétique classique d'un système physique, le transfert de spin place le système dans un état hors équilibre où il peut soit dissiper de l'énergie soit en recevoir. Les positions d'équilibres statiques stables ne correspondent donc plus simplement aux minimums d'énergie mais aussi aux maximums. Seul le signe de la puissance totale reçue par le système permet de déterminer si un extremum correspond à une position d'équilibre stable ou non (voir figure 9.1 page 110).

Afin de montrer que le courants critiques apparaissent quelque soit l'origine de la contribution non-perpendiculaire, nous montrons ici l'étude réalisée dans le cas d'un axe d'anisotropie penché de quelques degrés par rapport à la direction perpendiculaire (voir figure 9.2 page 111). Dans un premier temps, nous démontrons que cette approche permet de reproduire et de comprendre le diagramme de phase obtenu dans le cadre du modèle simple uniaxiale (voir figure 9.4 page 115). Dans un second temps, nous examinons le cas non-uniaxiale. La différence entre ces deux cas provient du fait qu'au renversement à courant nul l'aimantation dissipe de l'énergie dans le cas non-uniaxiale alors qu'elle n'a aucun échange énergétique avec le milieu extérieur dans le cas uniaxiale. Par conséquent, le couple de transfert de spin doit apporter une puissance critique afin de vaincre cette dissipation intrinsèque existante dans le cas non-uniaxial et non dans le cas uniaxial. D'où l'apparition des courants critiques dans les diagrammes de phase lorsqu'une contribution magnétique non-uniaxiale apparaît (voir figure 9.6 page 117). De plus, cette interprétation énergétique permet également de comprendre l'existence non-prévue de certains pics dans les mesures de résistances différentielles situés dans le prolongements du champ de renversement à courant nul.

Chapter 7

Experimental phase diagrams

An injected current and applied magnetic field phase diagram is a map of the magnetic states available for a nanopillar spin-valve in the (H, I) parameter space. It gives in one glance a readable picture on the impact of the applied magnetic field and of the spin polarized current on the spin-valve magnetization. This chapter explains how to measure, draw and read such a phase diagram.

7.1 Field and current hysteresis loops

7.1.1 Field hysteresis loops

The experimental setup described in the previous chapter (see chapter 6 page 69) allows to measure the resistance variations of a nanopillar spin-valve as a function of the applied magnetic field. Thanks to the giant magnetoresistance effect (see chapter 2 page 29), this resistance is related to its magnetic state.

Figures 7.1a and 7.1b present the evolution of the differential resistance as a function of the applied magnetic field of a nanopillar spin-valve with an elliptical shape of 50 nm by 300 nm and perpendicular magnetizations. The hard layer is made of Pt (3 nm) / [Co (0.25 nm)/Pt (0.52 nm)]×4 / Co (0.25 nm) / [Ni (0.6 nm)/Co (0.1 nm)]×2. The free layer is made of [Co (0.1 nm)/Ni (0.6 nm)]×2 / Co (0.2 nm) / Pt (3 nm).

Figure 7.1a is a major hysteresis loop corresponding to the scheme 2.4 page 34 where both the hard and free layers of the spin-valve reverse. At $|H| = 140$ mT is the reversal of the free layer and at $|H| = 460$ mT the reversal of the hard layer. These values are in good agreement with the kerr measurements presented in figures 5.3a and 5.3b page 64 taking into account that here the free layer perpendicular anisotropy is enhanced by the addition of a platinum layer and

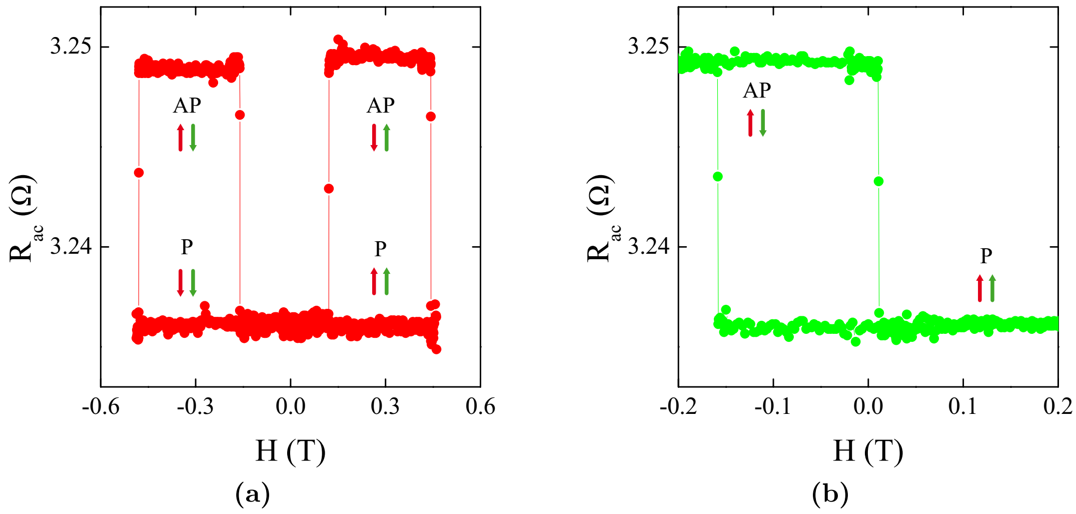

Figure 7.1 – Differential resistance as a function of the applied magnetic field at I = 0 mA of an elliptical nanopillar spin-valve of 50 nm by 300 nm with a hard layer made of [Co/Pt]/[Co/Ni] and a free layer made of [Co/Ni] with a platinum layer on top. (a) Major and (b) minor hysteresis loops.

that its reversal is shifted by the dipolar field emitted by the hard layer (see section 1.2.3 page 20).

Figure 7.1b is a minor hysteresis loop corresponding to the reversal of the free layer only. A large enough positive magnetic field is applied at the beginning to saturate the sample in the parallel state. The field is then decreased. The free layer reverses around $H = -140$ mT and the spin-valve goes into the antiparallel state. Before the hard layer can reverse, the magnetic field is increased back. The free layer reverses again around $H = 10$ mT and the spin-valve returns to the parallel configuration. This hysteresis loop is not symmetric around the zero field because of the dipolar field emitted by the hard layer which favors the parallel configuration (see figure 1.4 page 20). Therefore, the hysteresis loop is shifted towards the negative magnetic fields. This shift gives the value of the dipolar field and corresponds to the magnetic field required to center the hysteresis loop. Here we have $H_{\mathrm{dip}} = 75$ mT. To remove this contribution, we will use sometimes the net magnetic field applied to the free layer, $H_{\mathrm{net}} = H + H_{\mathrm{dip}}$.

From now on, since the hard and free layers reversals are well separated in these samples, we will focus on the free layer reversal only considering that the applied magnetic fields are too weak to affect the magnetic state of the hard layer. Moreover, we will keep the following convention: the magnetic field is counted positive when it is applied in the same direction as the magnetization of the hard layer. In this case, it favors a parallel alignment of the magnetizations.

7.1.2 Current hysteresis loops

The experimental setup described in the previous chapter (see chapter 6 page 69) also permits to measure the resistance variations of a nanopillar spin-valve as a function of the injected current. In this manuscript we will keep the following convention for the current: it is counted positive when the electrons flow from the polarizer to the free layer. In this case, it favors a parallel alignment of the magnetizations.

Figure 7.2 presents the differential resistance variation of a nanopillar spin-valve similar to the previous one as a function of the injected current with a zero net applied magnetic field. The parallel and the antiparallel resistance states are clearly identifiable on this curve as two parabolic branches. The switching of the spin-valve between these states is hysteretic.

The parabolic shape of the two resistance branches are due to the Joule heating of the current flow which increases the temperature of this metallic system as well as its resistance. This resistance increase is proportional to the power dissipated by the Joule heating proportional itself to the square of the current intensity. Hence the parabolic evolution of the resistance with the injected current.

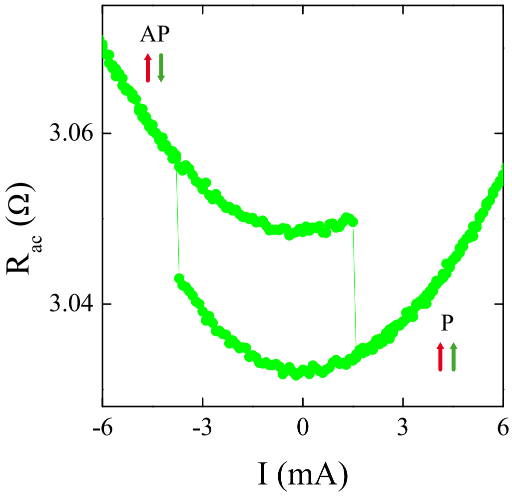

Figure 7.2 – Differential resistance as a function of the injected current at $H_{\text{net}} = 0$ T of an elliptical nanopillar spin-valve of 50 nm by 300 nm with a hard layer made of [Co/Pt]/[Co/Ni] and a free layer made of [Co/Ni] with a platinum layer on top.

The reversal is hysteretic since the sign of the spin-transfer torque depends on the sign of the current. However, the switching currents are not symmetric around zero. The spin-valve reverses from a parallel to an antiparallel state at $I = -3.8$ mA and reverses back to the parallel state at $I = 1.6$ mA. This is not an effect of the dipolar field emitted by the hard layer since the net applied magnetic field is zero. Actually, spin-transfer is more efficient to switch the magnetization from an antiparallel to a parallel state than the contrary because of the difference in the mechanisms of current spin polarization between these two cases. Indeed, to switch from an antiparallel to a parallel magnetic configuration at $H_{\mathrm{net}} = 0$, the injected current has to be positive. The electrons flow from the polarizer to the free layer and they are directly polarized during their transmission through the polarizer. This mechanism is efficient because the electrons responsible for the spin-transfer torque flow in the same direction as the one imposed by the current flow. On the other hand, to switch from a parallel to an antiparallel magnetic configuration at $H_{\mathrm{net}} = 0$, the injected current has to be negative. The electrons flow from the free layer to the polarizer. The electrons responsible for the spin-transfer torque are in this case the ones reflected by the polarizer that have to flow in the opposite direction as the one imposed by the current. This mechanism is consequently less efficient than the previous one and the required current has to increase to allow the switching.

This difference of efficiency of the spin-transfer effect in asymmetric nanopillar spin-valves appears in some theoretical works presented before (see subsection 3.2.5 page 45). Indeed, in the phenomenological approach we detailed the $\mathcal{G}(\theta)$ function is symmetric but in all the diffusive approaches it becomes asymmetric. The efficiency of the spin-transfer torque is expected to be higher in the antiparallel state than in the parallel one as observed experimentally.

7.1.3 Current influence on the field hysteresis loops

Because of the spin-transfer effect, the injected current has an impact on the field hysteresis loops of our nanopillar spin-valves. The height of the jump between the two resistance states remains constant because the giant magnetoresistance ratio is not affected by the injected current but it modifies the switching fields.

Figure 7.3 shows the evolution of the hysteretic behavior of a nanopillar spin-valve with perpendicular magnetizations similar to the previous ones for three different injected currents. It is clear from these curves that going from negative to positive currents the field hysteresis loop moves to the left, toward the negative fields values. Since a positive current favors the parallel state, the parallel to

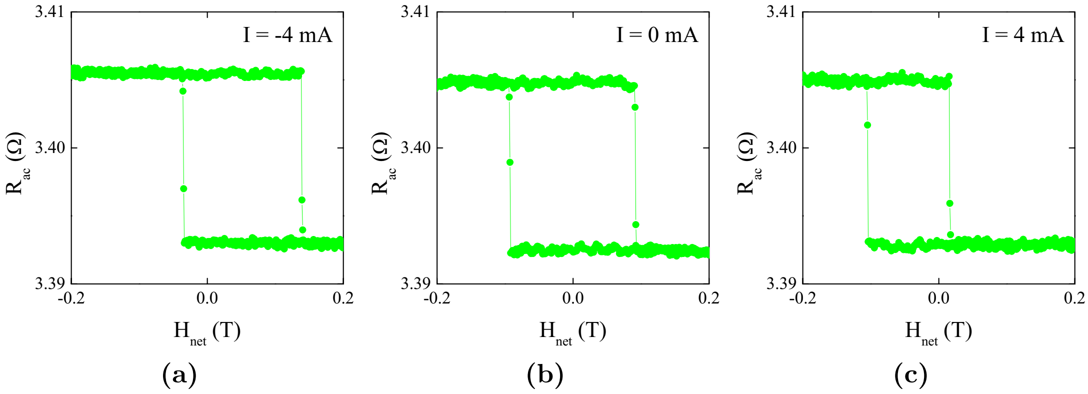

(a) (b) (c)

Figure 7.3 – Differential resistance evolution as a function of the net applied magnetic field of an elliptical nanopillar spin-valve of 50 nm by 300 nm with a hard layer made of [Co/Pt]/[Co/Ni] and a free layer made of [Co/Ni] with a platinum layer on top. The injected current is (a) $I = -4$ mA, (b) $I = 0$ mA and (c) $I = 4$ mA.

antiparallel switching requires an higher negative field whereas the antiparallel to parallel switching occurs for a lower positive fields. Besides, the action of the spin-transfer torque on the two switching fields is not symmetric (see subsection 7.1.2 page 83). Therefore, going from negative to positive currents the width of the hysteresis loop shrinks.

Similarly, an applied magnetic field impacts the switching currents of the current hysteresis loops.

7.2 Phase diagram of a nanopillar spin-valve

7.2.1 From hysteresis loops to phase diagram

The evolution of the field hysteresis loops for different injected currents allows to draw a phase diagram. Indeed, for one value of the injected current a field hysteresis loop divides the magnetic field axis into three regions of different magnetic configurations. In the middle, the spin-valve can be either in the parallel or antiparallel states. This is the bistable region. Going to the positive field, only the parallel configuration becomes available whereas going to the negative field, only the antiparallel configuration becomes available. The two borders between these three regions are marked by the switching fields (see figure 7.4a). Therefore, a plot of the evolution of these switching fields as a function of the injected current gives a phase diagram.

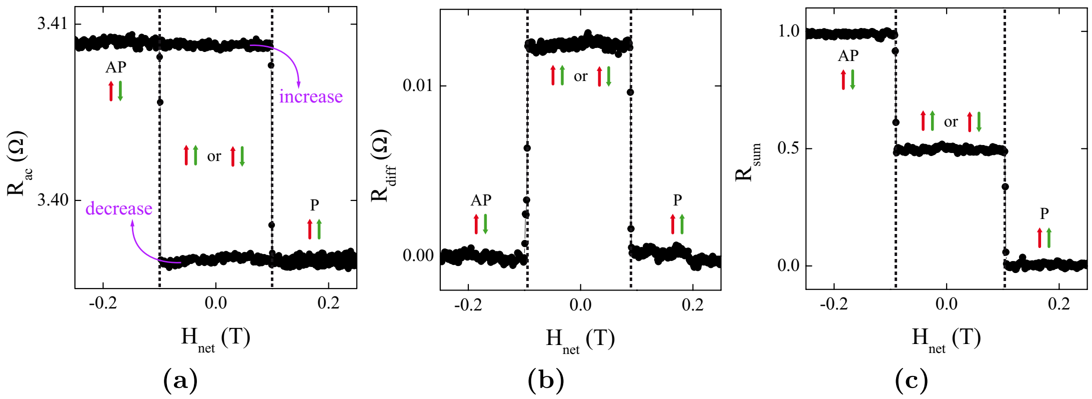

Figure 7.4 – (a) Differential resistance evolution as a function of the net applied magnetic field at $I = 0$ mA of an elliptical nanopillar spin-valve of 50 nm by 300 nm with a hard layer made of [Co/Pt]/[Co/Ni] and a free layer made of [Co/Ni] with a platinum layer on top. (b) Corresponding difference of resistances between the increasing and the decreasing parts of the hysteresis loop. (c) Corresponding half sum of the normalized resistances between the increasing and the decreasing parts of the hysteresis loop. These curves highlight three regions of different available magnetic configurations: the parallel (P) or the antiparallel (AP) states only or the bistable region.

Another way to represent a phase diagram from field hysteresis loops at different injected currents is to use a computer assisted treatment of the data. For instance, the difference of resistances between the increasing and the decreasing parts of an hysteresis loop that is to say $R_{\text{diff}}(H) = R_{\text{inc}}(H) - R_{\text{dec}}(H)$ highlights the bistable region of the phase diagram (see figure 7.4b). Indeed, the parallel and the antiparallel magnetic configuration regions correspond to a zero resistance level ($R_{\text{inc}}(H) = R_{\text{dec}}(H)$) whereas the positive resistance level corresponds to the bistable region. Another treatment is to compute the half sum of resistances between the increasing and the decreasing parts of the hysteresis loop that is to say $R_{\text{sum}}(H) = \frac{1}{2}[R_{\text{inc}}(H) + R_{\text{dec}}(H)]$. This method transforms the hysteresis loop into a step curve where each step corresponds to a specific region of the phase diagram (see figure 7.4c). With these two methods, the phase diagram is then obtained by building a two dimensional colored map in the (H, I) parameter space where each point corresponds to a specific couple of current and field. Its color is given by the value of R_{diff} or R_{sum} at these coordinates (see figure 7.5). Each of its lines corresponds to a unique value of the injected current and is determined from the field hysteresis loop measured at this current.

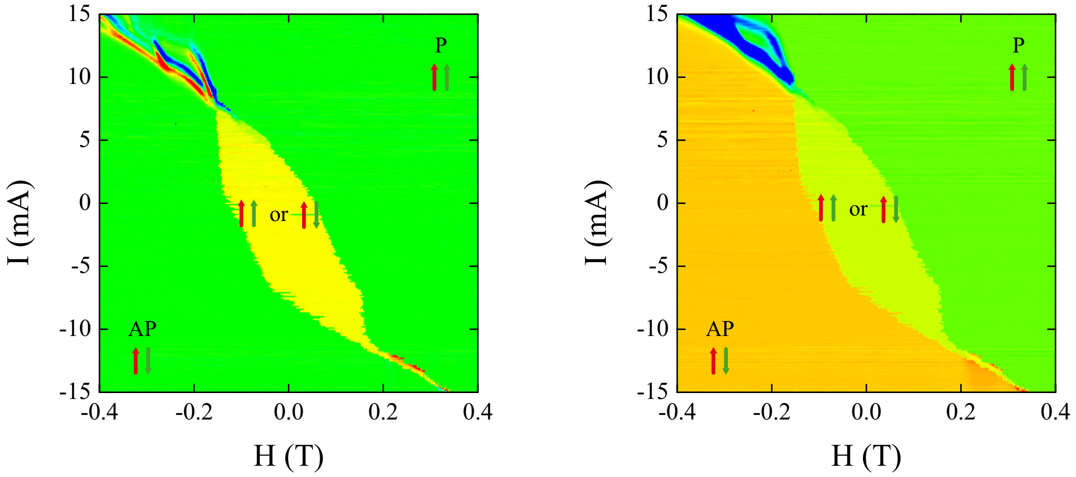

(a) (b)

Figure 7.5 – Phase diagram of an elliptical nanopillar spin-valve of 50 nm by 300 nm with a hard layer made of [Co/Pt]/[Co/Ni] and a free layer made of [Co/Ni] with a platinum layer on top obtained (a) from the difference of differential resistances treatment and (b) from the half sum of differential resistances treatment. The applied magnetic field step is of 1 mT and the injected current step is of 0.1 mA.

In order to compare the lines obtained for different injected currents, the parabolic evolution of the nanopillar resistance due to the Joule heating has to be taken into account (see subsection 7.1.2 page 83). Using the treatment with the difference of resistances this problem disappears because the giant magnetoresistance ratio is not affected by the Joule heating. On the contrary, using the treatment with the half sum of resistances, this effect induces a vertical contrast that can complicate the reading of the phase diagram. To remove this contribution, we normalize the resistance values of the concerned hysteresis curves using the following formula $R_{\text{norm}} = \frac{R - R_{\text{P}}}{R_{\text{AP}} - R_{\text{P}}}$. As a result, the normalized resistances of the parallel and of the antiparallel states are respectively 0 and 1 (see figure 7.4c).

Figure 7.5 presents the phase diagram of a nanopillar spin-valve with perpendicular magnetizations similar to the previous ones. Figure 7.5a is obtained from the difference of resistances and figure 7.5b from the half sum of resistances. These two phase diagrams exhibit a similar behavior. However, the one obtained from the difference highlights the bistable region whereas the one obtained from the half sum highlights the behavior of the nanopillar in the high field and current regions. These two treatments are therefore complementary.

7.2.2 Reading of a phase diagram

A phase diagram is a convenient figure as soon as one can read through it the magnetic behavior of the nanopillar it represents. In other word, it means to be able to determine the main features of the field or current hysteresis loops of a spin-valve looking only at its phase diagram.

Figure 7.6 represents the same phase diagram as figure 7.5b along with three characteristic hysteresis loops for three different injected currents. These field hysteresis loops are horizontal cross-sections of the phase diagram at the ordinate given by the value of the injected current. Similarly, a current hysteresis loop is a vertical cross-section of the phase diagram at the abscissa given by the value of the applied magnetic field. As a result, the phase diagram gathers the information given by many field and current hysteresis loops.

As mentioned previously, a phase diagram is mainly divided into three regions: one where the spin-valve is in the parallel state, one where it is in the antiparallel state and one where it can be in these two states, the bistable region. Because of our experimental conventions, the parallel state region is for the positive field and current (the green region in figure 7.6) whereas the antiparallel state region is for the negative field and current region (the orange region in figure 7.6). Between these two regions we find the bistable region (the yellow region in figure 7.6). A field hysteresis loop crossing these three regions gives a curve such as the one represented for $I = 0$ mA. The switching fields are given by the left and right limits of the bistable region whereas the switching currents are given by the up and down limits of the bistable region.

Furthermore, two additional regions appear if the current and the field are high enough. As mentioned previously, going to the positive currents the width of the hysteresis loop shrinks because of the difference of efficiency of the spin-transfer effect between the parallel and the antiparallel states (see subsection 7.1.3 page 84). Consequently, in the upper left corner corresponding to a high positive current and a high negative field, the hysteresis loop ends up disappearing. Instead of an hysteretic behavior, the spin-valve goes back and forth between the parallel and the antiparallel state passing through similar magnetic states. This region is generally characterized by pics in the differential resistance like in the differential resistance as a function of the magnetic field curve at $I = 11$ mA. The width of these pics appears in blue in the phase diagram and they may be the sign of magnetization precessions. These pics should not appear in the phase diagram obtained from the difference of resistances method because the increasing and the decreasing part of the hysteresis curve are in principal identical. Actually,

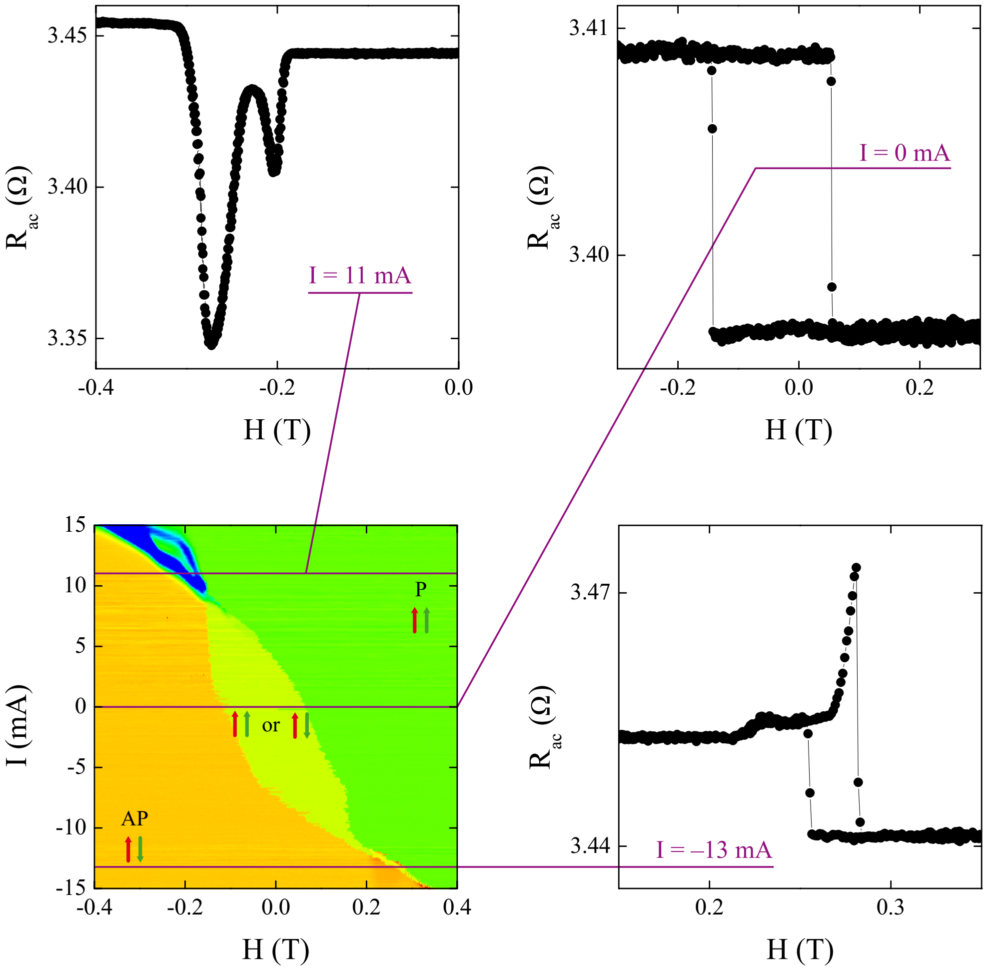

Figure 7.6 – Phase diagram of an elliptical nanopillar spin-valve of 50 nm by 300 nm with a hard layer made of [Co/Pt]/[Co/Ni] and a free layer made of [Co/Ni] with a platinum layer on top obtained from the half sum method along with three characteristic hysteresis loops at $I = -13$ mA, $I = 0$ mA and $I = 11$ mA.

their position between the increasing and the decreasing parts of the hysteresis are slightly shifted because of the field sweep, so the difference of resistance gives a positive value at one side of the pic and a negative one at the other side. Consequently, the pics appear as a couple of a blue and red lines more complicate to interpret than in the representation with the half sum treatment (see figure 7.5a). In the opposite corner corresponding to a high negative current and a high positive field the hysteresis loop also shrinks and even disappears sometimes. Here, the differential resistance curves are often characterized by a mix of an hysteresis of small width, pics and shoulders like in the curve measured at $I = -13$ mA. The shoulder before the hysteresis part results in a gradual increase of the color intensity from orange to red in the phase diagram. The hysteretic part still corresponds to the small yellow band and the pic appears as a red coloration inside the bistable region.

Now that we described the general shape of the experimental phase diagrams of a nanopillar spin-valve with perpendicular magnetizations, we will try to understand its physical origin in the next two chapters.

Chapter 8

Analytical modeling of the phase diagrams

This chapter focuses on the analytical modeling of nanopillar spin-valves with perpendicular magnetizations. Its aim is to determine the theoretical phase diagram of our samples and to compare it with the experimental results presented in the previous chapter. This comparison will help us to refine the modeling.

8.1 Stable equilibria with spin-transfer

In subsection 1.3.2 page 24, the theoretical field hysteresis loop with no injected current of a uniformly magnetized nanomagnet is determined thanks to a method based on the minimization of the energy of the system. The results highlight a characteristic magnetic field, the coercive field $H_\mathrm{c} = \frac{2K}{\mu_0 M_\mathrm{s}}$. The bistable region corresponds to $-H_\mathrm{c} \leqslant H \leqslant H_\mathrm{c}$, the parallel one to $H \geqslant H_\mathrm{c}$ and the antiparallel one to $H \leqslant -H_\mathrm{c}$.

As soon as a current is injected through the spin-valve this method cannot be used anymore because the spin-transfer effect can bring energy to the system so that the magnetization does not have to always reach a minimum of energy at the equilibrium. The LLGS equation (see section 3.3 page 47) allows then to determine the stable equilibrium positions of the system. This equation can be written using an apparent effective field $\boldsymbol{H}^*_{\mathbf{eff}}$

$$\frac{d\boldsymbol{m}}{dt} = -\gamma_0 \boldsymbol{m} \times \boldsymbol{H}^*_{\mathbf{eff}} + \alpha \boldsymbol{m} \times \frac{d\boldsymbol{m}}{dt} \tag{8.1}$$

where $\boldsymbol{H}^*_{\mathbf{eff}} = \boldsymbol{H}_{\mathbf{eff}} + \frac{\beta I \mathcal{G}(\theta)}{\gamma_0} \boldsymbol{m} \times \boldsymbol{p}$ and includes the effective magnetic field and the injected current contributions to the magnetization dynamics.

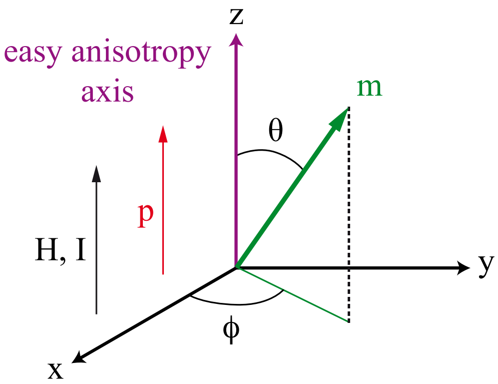

Figure 8.1 – Uniaxial modeling of nanopillar spin-valves with perpendicular magnetizations

At the equilibrium when $\frac{d\boldsymbol{m}}{dt} = \mathbf{0}$ the magnetization of the free layer is aligned with the apparent effective field. Therefore, the system of equations giving in spherical coordinates (see figure 8.1) the equilibrium positions of the magnetization is

$$\begin{cases} \boldsymbol{H}^*_{\textbf{eff}} \cdot \mathbf{e}_{\boldsymbol{\theta}} = 0 \\ \boldsymbol{H}^*_{\textbf{eff}} \cdot \mathbf{e}_{\boldsymbol{\phi}} = 0 \end{cases} \tag{8.2}$$

To simplify the analytical study of their stability, we will make the assumption in this chapter that the movement of the magnetization along the $\mathbf{e}_{\boldsymbol{\phi}}$ direction is negligible from the reversal point of view. It implies that the magnetization remains close from the perpendicular direction at the equilibrium. Thanks to this approximation, the stability of the equilibrium positions is only determined by the action of the torques exerted on the magnetization along the $\mathbf{e}_{\boldsymbol{\theta}}$ direction. They have to maintain the magnetization in an equilibrium to make it stable. Consequently, the stability criterion we will use is

$$\left[\frac{d}{d\theta}\left(\frac{d\boldsymbol{m}}{dt} \cdot \mathbf{e}_{\boldsymbol{\theta}}\right)\right]_{(\theta=\theta_{eq},\phi=\phi_{eq})} \leqslant 0 \tag{8.3}$$

We will also use an equivalent form of the damping torque: $\boldsymbol{\Gamma}_{\textbf{dam}} = -\alpha\gamma_0 \boldsymbol{m} \times (\boldsymbol{m} \times \boldsymbol{H}_{\textbf{eff}})$. Moreover, we will not take into account the θ dependance of the $\mathcal{G}(\theta)$ function during the derivation but each equilibrium position will be characterized by a different $\mathcal{G}(\theta)$ value. For instance, $\mathcal{G}(0)$ and $\mathcal{G}(\pi)$ will represent the value of the $\mathcal{G}(\theta)$ function respectively in the parallel and antiparallel states whatever is the real angular position of these magnetic configurations.

8.2 Uniaxial theoretical phase diagram

8.2.1 Framework of the model

To model and understand the behavior of nanopillar spin-valves with perpendicular magnetizations we want to determine analytically their theoretical phase diagram. In this way, we need to calculate the evolution of the switching currents as a function of the applied magnetic field starting from a parallel or an antiparallel magnetic state. The switching occurs when these stable equilibrium positions become unstable based on the stability criterion given by equation 8.3.

A first and simple approach to describe current-induced magnetization reversal in nanopillar spin-valves is to consider the hard layer magnetization as fixed and the free layer magnetization as uniform (see figure 8.1). They can be modeled as macrospins (see subsection 1.3.1 page 23). Besides, the magnetic layers possess an uniaxial magnetocrystalline anisotropy with an easy axis along the z direction perpendicularly to their planes (see subsection 1.2.4 page 21). The magnetic field is applied and the current flows also along the z direction. Therefore, all the contributions of the effective magnetic field (see section 1.4.1 page 26) and of the polarization of the current are along the same axis. This is an uniaxial approach. Finally, the temperature is zero.

8.2.2 Evolution of the switching currents

To determine the theoretical evolution of the switching currents as a function of the applied magnetic field thanks to equations 8.2 and 8.3, the expression of the effective magnetic field is required.

The effective field derives from the expression of the magnetic energy of the system (see section 1.4.1 page 26). In the framework of this uniaxial modeling, it is given by

$$E\left(\theta, H\right) = KV\sin^2\theta - \mu_0 M_\mathrm{s} V H \cos\theta \tag{8.4}$$

with V the volume of the free layer. The effective field is related to the magnetic energy by $\boldsymbol{H}_\mathbf{eff} = -\frac{1}{\mu_0 M_\mathrm{s} V}\frac{\partial E}{\partial \boldsymbol{m}}$. As a result, in the basis $(\mathbf{e}_\mathrm{x}, \mathbf{e}_\mathrm{y}, \mathbf{e}_\mathrm{z})$ it is given by (see appendix C.1 page 177 for a detailed explanation of this calculation)

$$\boldsymbol{H}_\mathbf{eff} = \left(H + H_\mathrm{c}\cos\theta\right)\mathbf{e}_\mathrm{z} \tag{8.5}$$

where $H_\mathrm{c} = \frac{2K}{\mu_0 M_s}$ is the coercive field. Both the dipolar coupling between the two magnetic layers and the demagnetizing field of the free layer are not taken into account in this description. However, they can be included respectively by shifting the magnetic field origin and by modifying the anisotropy constant K. Besides, in the basis $(\mathbf{e}_\mathrm{x}, \mathbf{e}_\mathrm{y}, \mathbf{e}_\mathrm{z})$ we have $\boldsymbol{m} \times \boldsymbol{p} = (\sin\theta \sin\phi)\, \mathbf{e}_\mathrm{x} - (\sin\theta\cos\phi)\, \mathbf{e}_\mathrm{y}$. In this modeling the apparent effective field is so given by

$$\boldsymbol{H}^*_{\mathbf{eff}} = \frac{\beta I \mathcal{G}(\theta)}{\gamma_0} \left[(\sin\theta\sin\phi)\, \mathbf{e}_\mathrm{x} - (\sin\theta\cos\phi)\, \mathbf{e}_\mathrm{y}\right] + (H + H_\mathrm{c}\cos\theta)\, \mathbf{e}_\mathrm{z} \tag{8.6}$$

Therefore, from equations 8.2 the equilibrium positions are the solutions of the following system

$$\begin{cases} (H + H_\mathrm{c}\cos\theta)\sin\theta = 0 \\ I\sin\theta = 0 \end{cases} \tag{8.7}$$

The valid solutions at any injected current corresponds to the exact parallel or antiparallel magnetic configurations, that is to say $\theta = 0$ or π. Their stability is determined by the criterion given by equation 8.3. Here, we have

$$\frac{d\boldsymbol{m}}{dt} \cdot \mathbf{e}_{\boldsymbol{\theta}} = -\left[\alpha\gamma_0 \left(H + H_\mathrm{c}\cos\theta\right) + \beta I \mathcal{G}(\theta)\right]\sin\theta$$

With the simplifying hypothesis presented at the end of section 8.1 page 91, the stability criterion becomes in the uniaxial modelling

$$\left[(h + \mathcal{G}(\theta) i)\cos\theta + \cos(2\theta)\right]_{\theta = 0 \text{ or } \pi} \geqslant 0 \tag{8.8}$$

where we used reduced coordinates for the applied magnetic field $h = \frac{H}{H_\mathrm{c}}$ and for the injected current $i = \frac{\beta I}{\alpha\gamma_0 H_\mathrm{c}}$. In this modeling, the stability of the equilibrium positions strictly depends on their movements along the $\mathbf{e}_{\boldsymbol{\theta}}$ direction since they correspond to the poles of the spherical coordinates. So, the hypothesis that the movement along $\mathbf{e}_{\boldsymbol{\phi}}$ is negligible is not required here. From the inequation above we can deduce that the parallel and the antiparallel states are respectively stable only if $i \geqslant i^\mathrm{P}_\mathrm{s}(h)$ and $i \leqslant i^\mathrm{AP}_\mathrm{s}(h)$ with

$$i^\mathrm{P}_\mathrm{s}(h) = -\frac{h+1}{\mathcal{G}(0)} \Leftrightarrow I^\mathrm{P}_\mathrm{s}(H) = -\left(\frac{2e\mu_0}{\hbar}\right)\frac{\alpha M_\mathrm{s} V}{\mathcal{G}(0)}(H + H_\mathrm{c}) \tag{8.9}$$

$$i^\mathrm{AP}_\mathrm{s}(h) = -\frac{h-1}{\mathcal{G}(\pi)} \Leftrightarrow I^\mathrm{AP}_\mathrm{s}(H) = -\left(\frac{2e\mu_0}{\hbar}\right)\frac{\alpha M_\mathrm{s} V}{\mathcal{G}(\pi)}(H - H_\mathrm{c}) \tag{8.10}$$

At high positive current the spin-valve is saturated in the parallel state. Decreasing the current, at $I = I^\mathrm{P}_\mathrm{s}$ the parallel state becomes unstable and the spin-valve generally switches to the antiparallel state and remains in this configuration as long as the current decreases. On the contrary, if the current increases the antiparallel state becomes unstable at $I = I_{\mathrm{s}}^{\mathrm{AP}}$ and the spin-valve generally reaches back the parallel state and remains in this configuration as long as the current increases. Therefore, equations 8.9 and 8.10 are the theoretical expressions of the switching currents of the spin-valve. They give among other things the extremities of the current hysteresis loops presented in subsection 7.1.2 page 83 for any applied magnetic field.

Two remarks has to be made about the expressions of the switching currents. First, the $\mathcal{G}(\theta)$ function is equal to zero when $\theta = 0$ or π (see subsection 3.2.4 page 44). Indeed, there is no spin-transfer when the magnetizations are perfectly aligned. As a result, we need to consider that the spin-valve is infinitely close to the parallel or antiparallel state but not exactly in one of these configurations. Besides, they can be inverted in order to express the switching fields as a function of the injected current.

$$h_{\mathrm{s}}^{\mathrm{P}}(i) = -\mathcal{G}(0)i - 1 \Leftrightarrow H_{\mathrm{s}}^{\mathrm{P}}(I) = -\left(\frac{\hbar}{2e\mu_0}\right)\frac{\mathcal{G}(0)}{\alpha M_{\mathrm{s}} V} I - H_{\mathrm{c}} \tag{8.11}$$

$$h_{\mathrm{s}}^{\mathrm{AP}}(i) = -\mathcal{G}(\pi)i + 1 \Leftrightarrow H_{\mathrm{s}}^{\mathrm{AP}}(I) = -\left(\frac{\hbar}{2e\mu_0}\right)\frac{\mathcal{G}(\pi)}{\alpha M_{\mathrm{s}} V} I + H_{\mathrm{c}} \tag{8.12}$$

These expressions describe the field hysteresis loops at any injected current. They are in agreement with the theoretical hysteresis loop presented in subsection 1.3.2 page 24 when no current is injected through the spin-valve.

8.2.3 Theoretical phase diagram

Experimentally, the measurement of the field or of the current hysteresis loops permits to built a phase diagram. Likewise, the theoretical determination of the switching currents given by equations 8.9 and 8.10 allows to built the theoretical phase diagram of a nanopillar spin-valve with perpendicular magnetizations in this uniaxial approach.

Figures 8.2a and 8.2b gives the information obtained thanks to the theoretical expressions of the switching currents respectively in the parallel and in the antiparallel states. They divide the (H, I) plane into two regions, one where the equilibrium position is stable and one where it is unstable based on the stability criterion given by equation 8.3. The border between these two regions is given by the equation of the switching current evolution as a function of the applied magnetic field. In these two cases, this relation is linear so it is represented by a straight line.

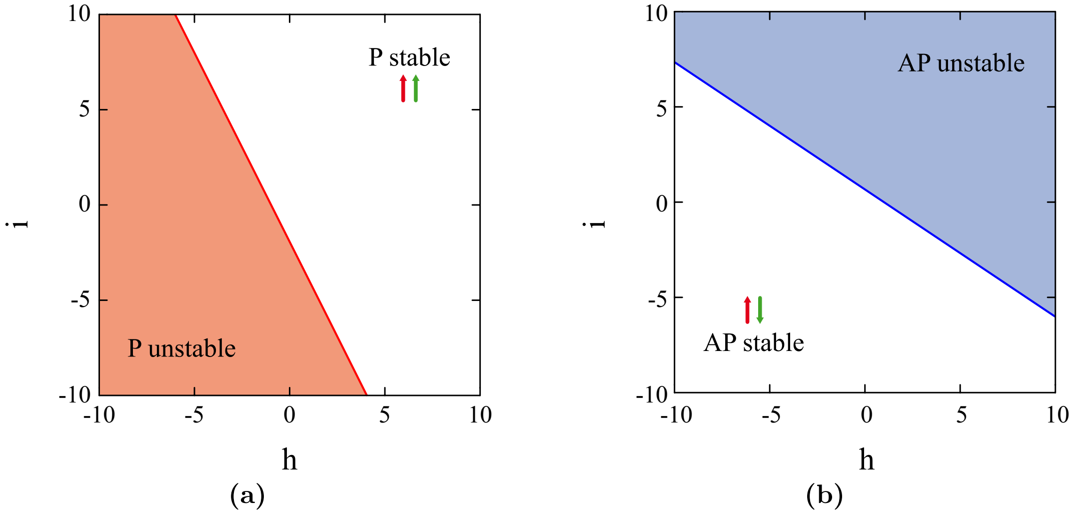

(a) (b)

Figure 8.2 – Stability diagrams in the applied magnetic field and injected current plane in reduced coordinates. The colored areas correspond to the unstable regions and the line to the theoretical evolution of the switching currents with the applied magnetic field. (a) Case of the parallel state. (b) Case of the antiparallel state.

The phase diagram of figure 8.3a is a combination of the information given by the figures 8.2a and 8.2b. Since the spin-transfer torque is more efficient in the antiparallel configuration than in the parallel one (see subsection 7.1.2 page 83) the slopes of the two borders which depend on the $\mathcal{G}(\theta)$ function are different. So, they cross and divide the (H, I) plane into four regions. In three of them the magnetization has access to at least one stable magnetic configuration: parallel, antiparallel or both of them. In the fourth one, there is no stable and static magnetic states anymore. Therefore, the magnetization has to be in a dynamic state where $\frac{d\boldsymbol{m}}{dt} \neq \mathbf{0}$. The coordinates of the crossing point are

$$h_{\mathrm{d}} = \frac{\mathcal{G}(\pi) + \mathcal{G}(0)}{\mathcal{G}(\pi) - \mathcal{G}(0)} \text{ and } i_{\mathrm{d}} = \frac{2}{\mathcal{G}(\pi) - \mathcal{G}(0)} \tag{8.13}$$

Therefore, no field hysteresis loop is expected if $i \geqslant i_{\mathrm{d}}$ nor current hysteresis loop if $h \leqslant h_{\mathrm{d}}$.

Such theoretical phase diagrams has been described in the literature by different methods[14,94,95]. A careful analytical study of the fourth region shows that steady magnetization precessions around the perpendicular axis are expected[95].

8.2.4 Comparison with the experimental results

There are lots of similarities between the theoretical phase diagram calculated in this uniaxial approach and the experimental phase diagrams (see figure 8.3).

Both of them are composed of two borders dividing the (H, I) plane into the same four regions. At high positive field and current, the spin-valve is in the parallel state whereas at high negative field and current it is in the antiparallel state. At high positive field and negative current, it can be either parallel or antiparallel, this is the bistable region characterized by hysteresis loops. At high negative field and positive current it is neither parallel nor antiparallel. From the theoretical results, the field hysteresis loops has to shift toward the negative field when the current increases while its width shrinks. It corresponds to most of the experimental observations (see figure 7.3 page 7.3). When the two borders cross, the hysteresis loops give way to series of pics in the differential resistance in the experimental phase diagrams (see figure 7.6 page 89). These pics are compatible

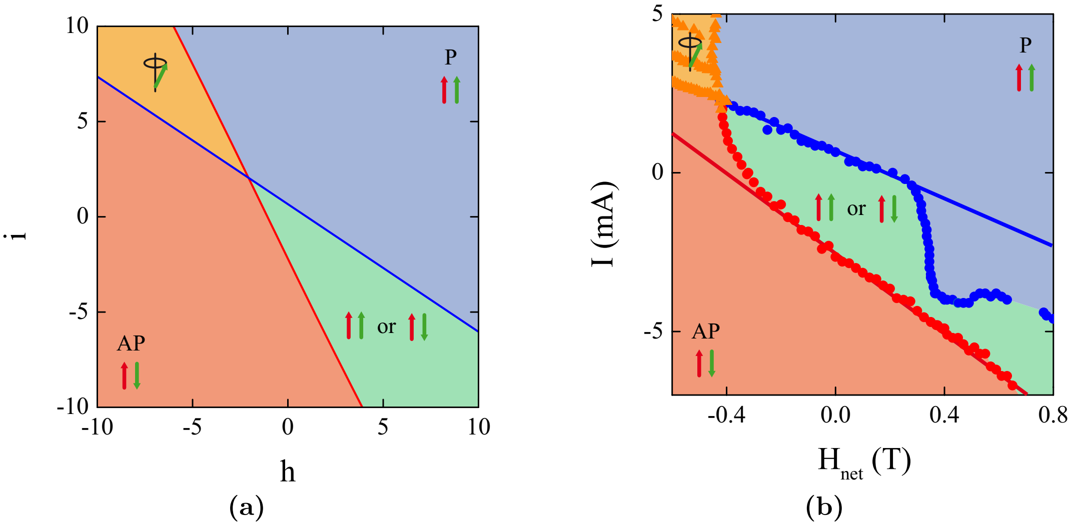

(a)

(b)

Figure 8.3 – (a) Theoretical phase diagram of a nanopillar spin-valve with perpendicular magnetizations in the the case of a uniaxial, macrospin and 0 K approach. (b) Experimental phase diagram of an hexagonal nanopillar spin-valve of 100 nm by 200 nm with a hard layer made of [Co/Pt]/[Co/Ni] and a free layer made of [Co/Ni]. The blue and red circles are for the measured switching fields and the orange triangle indicate the presence of a pic in the differential resistance measurements. The blue and red lines presents what could corresponds to the expected evolution of the switching current as a function of the applied magnetic field of our simple modeling.

with the magnetization precessions predicted by the theory. Such precessions are commonly recorded in spin-valves with at least one magnetization in-plane because they generate an alternative voltage thanks to the angular dependance of the giant magnetoresistance. However, in these all perpendicular spin-valves, a uniform precession of the magnetization of the free layer around the out-of-plane axis does not affect the angle between the magnetizations of the free layer and of the polarizer. As a consequence, no alternative voltage can be generated in first approximation. These precessions have to be detected indirectly thanks to differential measurements and a lock-in technic. Unfortunately, these methods cannot guarantee that every measured pics are the consequence of magnetization precessions.

Another similarity is that the borders determined by the switching fields or currents evolve mainly linearly (see figure 8.3b). However, a large deviation from this linear evolution occurs around the zero current switching fields. Experimentally it seems that the magnetization reversal becomes virtually independent of the injected current around these two fields and the current has to reach a critical value before the linear evolution appears. This observation seems paradoxical contrary to the theoretical predictions because the spin-transfer effect is expected to always modify the damping by increasing or decreasing the impact of the damping torque (see section 3.3 page 3.3). Moreover, this modification is proportional to the intensity of the injected current. As a result, the switching fields should always vary. If the current favors the reversal the switching field should decrease and vice versa, if the current does not favor it the switching field should increase. This is what both theory and intuition suggest. Nevertheless, the experimental results show that something is missing in our simple modeling and in our intuitive interpretation of the spin-transfer effect. The experimental phase diagrams in this perpendicular geometry are actually much closer to the phase diagrams in the planar geometry[8,57,95–97] than expected. The next section looks for the key parameter at the origin of this behavior.

8.3 Origin of the critical currents

The previous modeling is based on three main hypothesis: there is no thermal activation, the hard and free layers can be modeled by a macrospin and the system is uniaxial. The aim of this section is to use experimental measurements of phase diagrams to determine the impact of these three hypothesis on their shapes.

8.3.1 Impact of the thermal activation

Let's look first at the impact of the thermal activation on the phase diagram. Figure 8.4 compares two experimental phase diagrams measured on an hexagonal nanopillar spin-valve of 100 nm by 200 nm with a hard layer made of [Co/Pt]/[Co/Ni] and a free layer made of [Co/Ni] at room temperature (see figure 8.4a) and at $T = 20$ K (see figure 8.4b). Both of them exhibit regions around the zero current switching fields where the current influence on the reversal is weak. However, the absolute values of the critical currents seem to increase when the temperature decreases. Besides, between the critical currents the current influence is even weaker at low temperature since the borders look like vertical lines. Consequently, the origin of the critical currents is not the thermal activation.

This conclusion is confirmed by numerical calculations of the phase diagram of a nanopillar spin-valve with perpendicular magnetization by Zhu and Visscher[98]. In their modeling, they consider the same hypothesis as our simple modeling excepted the temperature which is finite. In this case, they found a theoretical phase diagram similar to the one presented in figure 8.3a with a linear evolution of the switching currents.

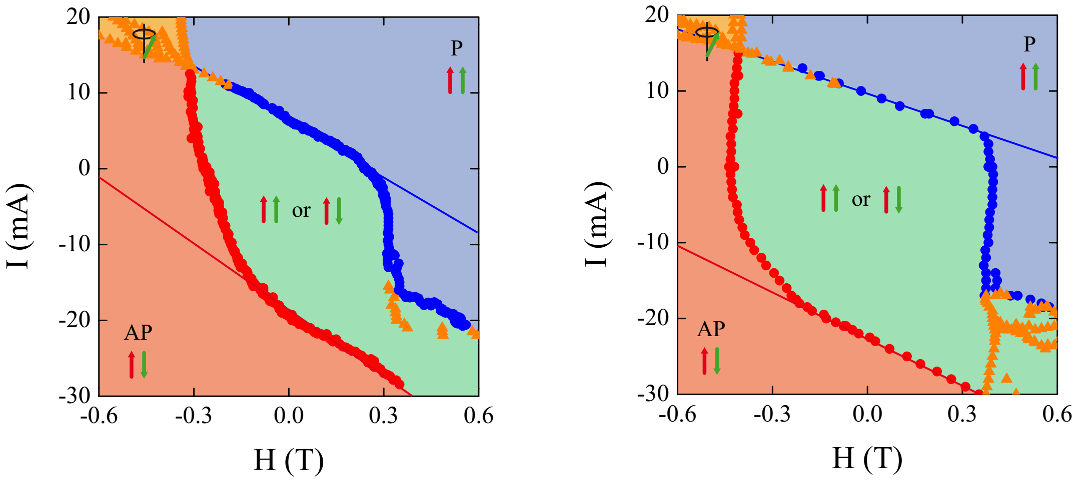

(a)

(b)

Figure 8.4 – Experimental phase diagrams of an hexagonal nanopillar spin-valve of 100 nm by 200 nm with a hard layer made of [Co/Pt]/[Co/Ni] and a free layer made of [Co/Ni] measured at (a) $T = 290$ K and at (b) $T = 20$ K. The blue and red lines presents what could corresponds to the expected evolution of the switching current as a function of the applied magnetic field of our simple modeling.

8.3.2 Impact of the macrospin approach

To test the impact of the macrospin approach on the experimental phase diagram, figure 8.5 compares the phase diagrams obtained for two hexagonal nanopillar spin-valves with a hard layer made of [Co/Pt]/[Co/Ni] and a free layer made of [Co/Ni] of different sizes. Note that to compare two phase diagrams measured on samples with different sizes, the phase diagram are plotted with the current density ($J = \frac{I}{S}$ with S the area of the nanopillar) instead of the current intensity. The first nanopillar is an hexagon of 100 nm by 200 nm (see figure 8.5a) and the second one an hexagon fourth times smaller of 50 nm by 100 nm (see figure 8.5b).

Smaller samples are closer from the macrospin approach because it is easier for the exchange interaction to dominate over the demagnetizing field (see subsection 1.3.1 page 23). However, there is no clear evidence for a difference of behavior between figures 8.5b and 8.5a. Indeed, when the size of the nanopillar decreases the current range where the injected current has a weak impact on the switching fields seems to decrease for the parallel to antiparallel reversal whereas it seems to slightly increase for the opposite one. Actually, these differences could be explained by inhomogeneities in the composition of the spin-valves since they come from different part of a wafer.

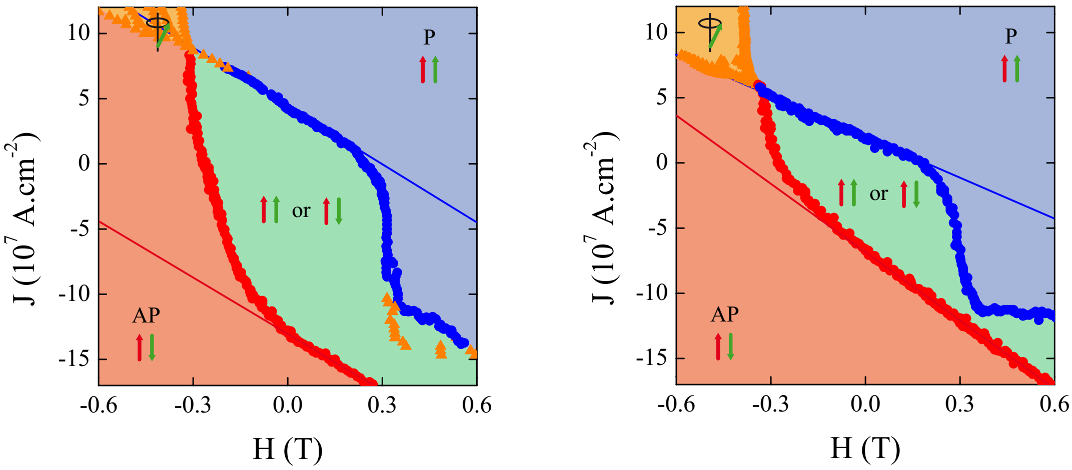

(a) (b)

Figure 8.5 – Experimental phase diagrams of an hexagonal nanopillar spin-valve with a hard layer made of [Co/Pt]/[Co/Ni] and a free layer made of [Co/Ni] of (a) 100 nm by 200 nm and of (b) 50 nm by 100 nm. The blue and red lines presents what could corresponds to the expected evolution of the switching current as a function of the applied magnetic field of our simple modeling.

As a result, it is not obvious that introducing a micromagnetic approach into the modeling of the spin-valve will reproduce much better the experimental observations. This conclusion is confirmed by the micromagnetic simulation presented by Mangin *et al.* where they found a theoretical phase diagram close from the analytical phase diagram presented here[14] (see figure 9.7 page 119).

8.3.3 Impact of the uniaxial approximation

The last important hypothesis of our modeling is that all the contributions of the system are along the same axis. This is the uniaxial approximation. There are a lot of reasons for the system not to respect this hypothesis. For instance, the magnetic layers are composed of small grains which anisotropy axis can be tilted of few degrees from one another. The magnetic field may be applied experimentally in a direction slightly different from the perpendicular direction.

To test the impact of the uniaxial symmetry on the experimental phase diagrams, figure 8.6 compares two experimental phase diagrams measured on the same elliptical nanopillar spin-valve of 50 nm by 300 nm with a hard layer made of

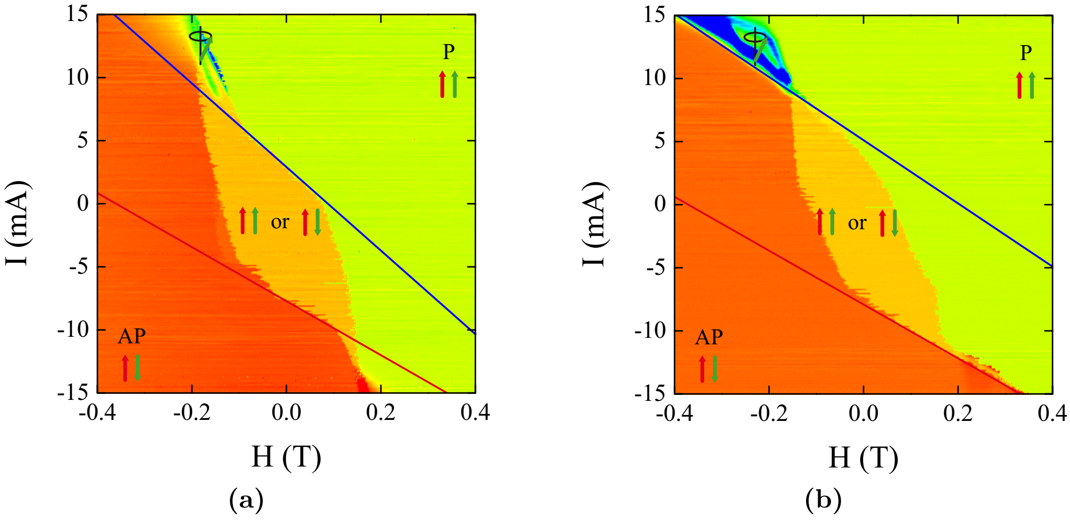

Figure 8.6 – Experimental phase diagrams of an elliptical nanopillar spin-valve of 50 nm by 300 nm with a hard layer made of [Co/Pt]/[Co/Ni] and a free layer made of [Co/Ni]. The magnetic field is applied at an angle Ψ toward the perpendicular axis. (a) $\Psi = 40°$ and (b) $\Psi = 0°$. The blue and red lines presents what could corresponds to the expected evolution of the switching current as a function of the applied magnetic field of our simple modeling.

[Co/Pt]/[Co/Ni] and a free layer made of [Co/Ni]. The magnetic field is applied in two different directions. In figure 8.6a, it is applied at 40° from the perpendicular direction whereas in figure 8.6b it is applied close to the perpendicular axis. When the magnetic field is applied away from the perpendicular direction, the effective field has a non-perpendicular component which breaks the uniaxial symmetry. In this case it seems that the current range where the injected current has a weak impact on the switching fields increases not only for the parallel to antiparallel reversal but also for the opposite one. Therefore, the experimental phase diagrams deviate more from our modeling if the uniaxial symmetry is broken.

This conclusion is confirmed by a study of the distortion of the Stoner Wohlfarth astroid by a spin polarized current of these nanopillar spin-valves[99]. Indeed, it shows that above a critical angle of application of the magnetic field, the injected current has no impact on the magnetization reversal. In the next section we will try to refine our modeling by considering a non-uniaxial effective field exerted on the free layer due to the application of a magnetic field away from the perpendicular direction.

8.4 Non-uniaxial theoretical phase diagram

8.4.1 Framework of the model

In this non-uniaxial approach, we will use the same modeling as the previous one except the orientation of the applied magnetic field. Here, it can be applied in the yz plane at an angle Ψ with the perpendicular direction with $\Psi \in [0; \frac{\pi}{2}[$ (see

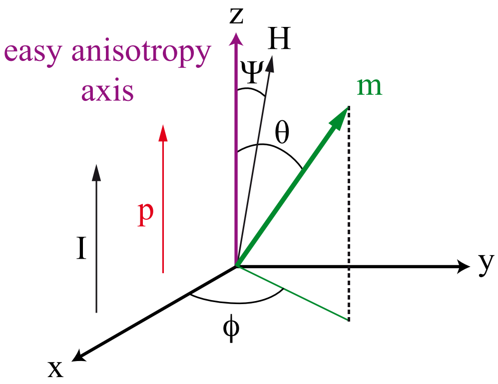

Figure 8.7 – Non-uniaxial modeling of nanopillar spin-valves with perpendicular magnetizations and a tilted applied magnetic field.

figure 8.7). We will then use the equations 8.2 to obtain the equilibrium positions and the equation 8.3 to study their stability.

In order to perform the calculation analytically, we will assume that the magnetization is close to the parallel or to the antiparallel configurations at the equilibrium. Even if these conditions are very restrictive, the following analysis shows that they nicely reproduce the behavior of our nanopillar. A more rigorous method of calculation developed by Bazaliy *et al.* can be found in the literature[95]. The general aspects of the theoretical phase diagram obtained by these two methods are similar.

8.4.2 Evolution of the switching currents

To calculate the evolution of the switching currents as a function of the applied magnetic field we need first to calculate the expression of the effective field in the framework of this non-uniaxial modeling.

According to the description of the system, its magnetic energy is given by

$$E(\theta, H) = KV \sin^2\theta - \mu_0 M_\mathrm{s} V \boldsymbol{m} \cdot \boldsymbol{H} \tag{8.14}$$

where V is the volume of the free layer. The effective field related to this magnetic energy is given in the basis $(\mathbf{e}_\mathrm{x}, \mathbf{e}_\mathrm{y}, \mathbf{e}_\mathrm{z})$ by (see appendix C.2 page 178 for a detailed explanation of this calculation)

$$\boldsymbol{H}_\mathbf{eff} = (H \sin\Psi)\,\mathbf{e}_\mathrm{y} + (H\cos\Psi + H_\mathrm{c}\cos\theta)\,\mathbf{e}_\mathrm{z} \tag{8.15}$$

where $H_\mathrm{c} = \frac{2K}{\mu_0 M_s}$ is the coercive field. The dipolar coupling and the demagnetizing field can be included in this modeling as explained previously (see subsection 8.2.2 page 93). In the basis $(\mathbf{e}_\mathrm{x}, \mathbf{e}_\mathrm{y}, \mathbf{e}_\mathrm{z})$ we still have $\boldsymbol{m} \times \boldsymbol{p} = (\sin\theta\sin\phi)\,\mathbf{e}_\mathrm{x} - (\sin\theta\cos\phi)\,\mathbf{e}_\mathrm{y}$. As a result, the apparent effective field is

$$\begin{aligned}\boldsymbol{H}^*_\mathbf{eff} = \frac{\beta I \mathcal{G}(\theta)}{\gamma_0} & \left[(\sin\theta\sin\phi)\,\mathbf{e}_\mathrm{x} - (\sin\theta\cos\phi)\,\mathbf{e}_\mathrm{y}\right] \\ & + (H\sin\Psi)\,\mathbf{e}_\mathrm{y} + (H\cos\Psi + H_\mathrm{c}\cos\theta)\,\mathbf{e}_\mathrm{z}\end{aligned} \tag{8.16}$$

Therefore, from equations 8.2 the equilibrium positions are the solutions of the following system

$$\begin{cases} (H\cos\Psi + H_\mathrm{c}\cos\theta)\sin\theta = H\sin\Psi\cos\theta\sin\phi \\ \beta I \mathcal{G}(\theta)\sin\theta = \gamma_0 H \sin\Psi\cos\phi \end{cases} \tag{8.17}$$

The stability of the these equilibrium positions is determined by the criterion given by equation 8.3. Here, we have

$$\frac{d\boldsymbol{m}}{dt}\cdot\mathbf{e}_{\boldsymbol{\theta}} = -\left[\alpha\gamma_0\left(H\cos\Psi + H_{\mathrm{c}}\cos\theta\right) + \beta I\mathcal{G}(\theta)\right]\sin\theta \\ + \alpha\gamma_0 H\sin\Psi\cos\theta\sin\phi + \gamma_0 H\sin\Psi\cos\phi$$

So, with the simplifying hypothesis presented at the end of section 8.1 page 91 the stability criterion in this non-uniaxial modeling becomes

$$\left[\left(h\cos\Psi + \mathcal{G}(\theta)i\right)\cos\theta + h\sin\Psi\sin\phi\sin\theta + \cos(2\theta)\right]_{(\theta=\theta_{eq},\phi=\phi_{eq})} \geqslant 0 \qquad (8.18)$$

where we used reduced coordinates for the applied magnetic field $h = \frac{H}{Hc}$ and for the injected current $i = \frac{\beta I}{\alpha\gamma_0 H_{\mathrm{c}}}$.

To solve analytically these equations we will consider by analogy with the previous modeling that the magnetization can be into two opposite magnetization configurations: one close to the parallel state where $\theta \sim 0$ and $\phi \sim {}^{\pi}\!/_{2}$ and one close to the antiparallel state where $\theta \sim \pi$ and $\phi \sim -{}^{\pi}\!/_{2}$. As a result, the movement of the magnetization along the $\mathbf{e}_{\boldsymbol{\phi}}$ direction is indeed negligible from the reversal point of view.

Case of the parallel to antiparallel switching

In the case where the magnetization is close to a pure antiparallel configuration we have $\theta \sim 0$ and $\phi \sim {}^{\pi}\!/_{2}$. So, in first order approximation the system of equation 8.17 gives the following coordinates for the equilibrium position

$$\theta = -\frac{H\sin\Psi}{H\cos\Psi + H_{\mathrm{c}}} = -\frac{h\sin\Psi}{h\cos\Psi + 1} \qquad (8.19)$$

$$\phi = \frac{\pi}{2} - \frac{\beta I\mathcal{G}(\theta)}{\gamma_0\left(H\cos\Psi + H_{\mathrm{c}}\right)} = \frac{\pi}{2} - \frac{\alpha\mathcal{G}(\theta)i}{h\cos\Psi + 1} \qquad (8.20)$$

Here, contrary to the first modeling the position of the magnetization of the free layer at the equilibrium evolves as a function of the applied magnetic field. Moreover, it is not contained in the yz plane because of the action of the spin-transfer torque.

In first order approximation and injecting the θ value of the equilibrium position of equation 8.19 the stability criterion given by the inequation 8.18 becomes for the parallel magnetic configuration

$$h^2 + \left[\left(\mathcal{G}(0)i + 2\right)\cos\Psi\right]h + \mathcal{G}(0)i + 1 \geqslant 0 \qquad (8.21)$$

Therefore, in this non-uniaxial modeling the region of the (H, I) plane where the parallel magnetic configuration is stable is given by the following inequation of the switching current as a function of the applied magnetic field

$$i \geqslant -\frac{h^2 + 2h\cos\Psi + 1}{\mathcal{G}(0)\,(h\cos\Psi + 1)} \tag{8.22}$$

If $\Psi = 0$, equation 8.22 returns the previous result of the uniaxial modeling. In the non-uniaxial case ($\Psi \neq 0$), the evolution of the switching current is represented on figure 8.8a. A vertical asymptote at $h = -\frac{1}{\cos\Psi}$ divides the curve into two branches. If $h < -\frac{1}{\cos\Psi}$ the switching current decreases with the applied magnetic field until it reaches a minimum value at $h = -\frac{1+\sin\Psi}{\cos\Psi}$. If $h > -\frac{1}{\cos\Psi}$ the switching current increases with the applied magnetic field until it reaches a maximum value at $h = -\frac{1-\sin\Psi}{\cos\Psi}$. The expressions of this local minimum and of this local maximum of the switching current are respectively given by

$$i_h^P = \frac{2}{\mathcal{G}(0)}\left(\frac{\sin^2\Psi + \sin\Psi}{\cos^2\Psi}\right) \tag{8.23}$$

$$i_l^P = \frac{2}{\mathcal{G}(0)}\left(\frac{\sin^2\Psi - \sin\Psi}{\cos^2\Psi}\right) \tag{8.24}$$

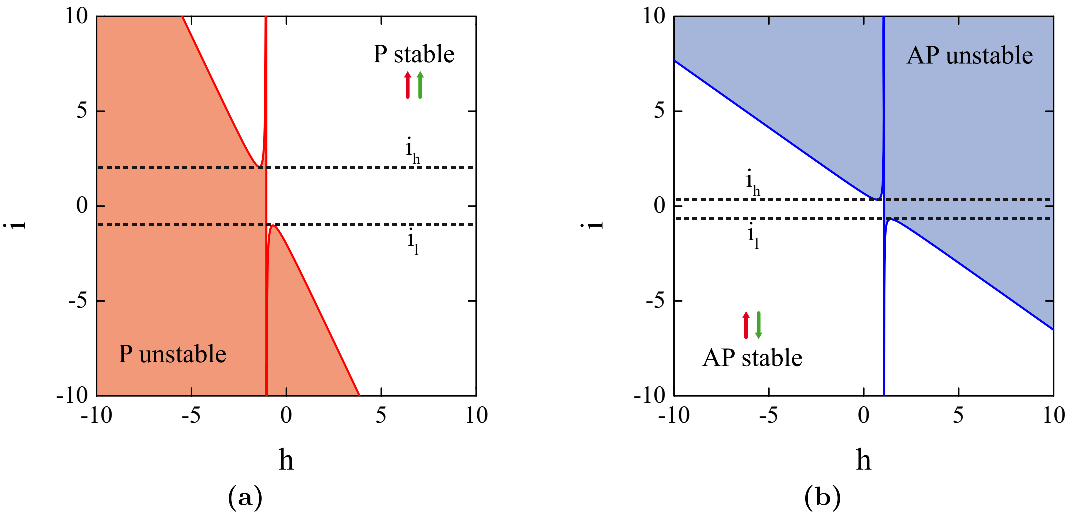

Figure 8.8 – Stability diagrams in the applied magnetic field and injected current plane in reduced coordinates. The colored areas correspond to the unstable regions and the lines to the theoretical evolution of the switching currents with the applied magnetic field. (a) Case of the parallel state. (b) Case of the antiparallel state.

When the injected current is comprised between these two values, the stability diagram of the parallel magnetic configuration shows that the parallel state becomes unstable for a constant applied magnetic field $h = -\frac{1}{\cos\Psi}$ (see figure 8.8a). Therefore, in this region the spin-transfer torque does not affect the stability of the parallel state. It has to reach the i_h^P or i_l^P value depending on its sign to have an impact on the parallel to antiparallel reversal. These values correspond to the critical currents highlighted in the experimental phase diagrams. Outside these critical currents, the evolution of the switching currents tends to be linear and close the evolution predicted by the uniaxial model.

Case of the antiparallel to parallel switching

Here, we consider the magnetization to be close to a pure antiparallel configuration that is to say $\theta \sim \pi$ and $\phi \sim -\pi/2$. So, in first order approximation the system of equation 8.17 gives the following coordinates for the equilibrium position

$$\theta = \pi - \frac{H\sin\Psi}{H\cos\Psi - H_c} = \pi - \frac{h\sin\Psi}{h\cos\Psi - 1} \tag{8.25}$$

$$\phi = \frac{\beta I \mathcal{G}(\theta)}{\gamma_0\left(H\cos\Psi - H_c\right)} - \frac{\pi}{2} = \frac{\alpha\mathcal{G}(\theta)i}{h\cos\Psi - 1} - \frac{\pi}{2} \tag{8.26}$$

The magnetization of the free layer at the equilibrium still evolves with the applied magnetic field and is also not contained in the yz plane because of the action of the spin-transfer torque.

In first order approximation and injecting the θ value of the equilibrium position of the equation 8.19 the stability criterion given by the inequation 8.18 becomes for the antiparallel magnetic configuration

$$i \leqslant -\frac{h^2 - 2h\cos\Psi + 1}{\mathcal{G}(\pi)\left(h\cos\Psi - 1\right)} \tag{8.27}$$

If $\Psi = 0$, equation 8.27 returns the previous result of the uniaxial modeling. In the non-uniaxial case ($\Psi \neq 0$), the evolution of the switching current is represented on figure 8.8b and is very similar to the parallel to antiparallel switching. We can still defined two critical currents given by

$$i_h^{AP} = -\frac{2}{\mathcal{G}(\pi)}\left(\frac{\sin^2\Psi - \sin\Psi}{\cos^2\Psi}\right) \tag{8.28}$$

$$i_l^{AP} = -\frac{2}{\mathcal{G}(\pi)}\left(\frac{\sin^2\Psi + \sin\Psi}{\cos^2\Psi}\right) \tag{8.29}$$

When the injected current is comprised between these two values the spin-transfer torque does not affect the stability of the antiparallel state. It has to reach the i_h^{AP} or i_l^{AP} value depending on its sign to have an impact on the antiparallel to parallel reversal. Outside these critical currents, the evolution of the switching currents also tends to be linear and close to the evolution predicted by the uniaxial model

8.4.3 Contributions of the non-uniaxial phase diagram

The theoretical determination of the switching currents given by equations 8.22 and 8.27 allows to draw a theoretical phase diagram of a nanopillar spin-valve with perpendicular magnetizations in this non-uniaxial approach.

Figure 8.9a presents the theoretical phase diagram obtained in this non-uniaxial approach. Contrary to the uniaxial modeling where the evolution of the switching current is always linear (see figure 8.3a page 97), in this modeling the quasi-linear evolution of the switching current is broken between critical current values (see figure 8.9b). Between these critical currents, the reversal of the magnetization does not depend anymore on the injected current. Indeed, the switching field remains constant at its value when there is no injected current.

This non-uniaxial modeling gives a closer description of the experimental observations (see figure 8.3b page 8.3b). Therefore, it seems that the breaking of the

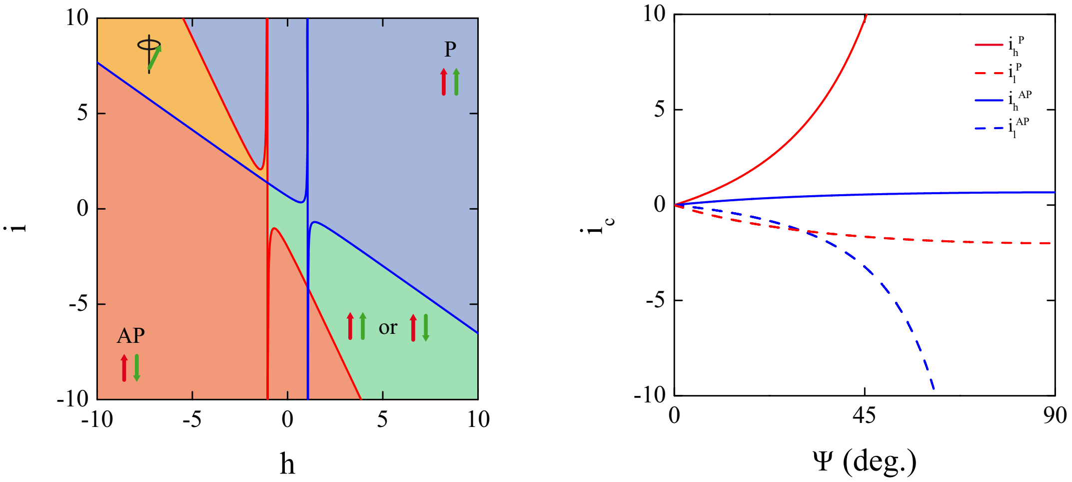

(a)

(b)

Figure 8.9 – (a) Theoretical phase diagram of a nanopillar spin-valve with perpendicular magnetizations in the the case of a non-uniaxial ($\Psi = 20^o$), macrospin and 0 K approach. (b) Theoretical evolution of the critical currents as a function of the angle of application of the magnetic field.

uniaxial symmetry of the spin-valve with perpendicular magnetizations is the key parameter to understand the shape of the phase diagrams in these system. The origin of the non-uniaxiality can either be extrinsic as a misaligned magnetic field or intrinsic as a deviation of the easy axis of the magnetocrystalline anisotropy of the free layer or of the polarizer from the perpendicular direction. However, in the experimental results, the deviation from the linear evolution of the switching currents does not results strictly in vertical lines contrary to our modeling. This is maybe an effect of the thermal activation on the switching or/and of the non-uniform magnetization of the magnetic layers of the spin-valve.

This section highlights the main parameter impacting the shape of the phase diagrams of our nanopillar spin-valves with perpendicular magnetizations. Indeed, we demonstrate that the apparition of the critical currents observed experimentally is due to the breaking of their uniaxial symmetry. Nevertheless, it remains counterintuitive that the spin-transfer torque may have no effect on the magnetization reversal. The next section gives a physical explanation of this phenomenon thanks to a purely energetic analysis of these system.

Chapter 9

Numerical energetic analysis and phase diagram

The previous chapter highlights the impact of the uniaxial symmetry breaking on the applied magnetic field and injected current phase diagram for a spin-valve with perpendicular magnetizations. It consists mainly in the apparition of critical currents defining a region where the spin polarized current has virtually no impact on the switching fields. This chapter traces the origin of this phenomenon thanks to an energetic analysis of magnetization reversal in these systems.

9.1 Principle of the energetic analysis

9.1.1 Interest of the total received power

The energetic analysis of a physical system is usually performed by studying the shape of its energy landscape. Indeed, because of non-conservative dissipative interactions it ends up in a minimum of energy which corresponds to a stable equilibrium position. On the contrary, the maxima of energy correspond to unstable equilibrium positions.

The particularity of our system is that the magnetization switching is driven by the competition between two non-conservative interactions, the spin-transfer and the damping torques. The damping torque is a dissipative interaction. As a result, when no current is injected through the spin-valve an energetic analysis based only on the search for the minima of energy works perfectly (we used it to determine the theoretical hysteresis loop of a magnet in section 1.3.2 page 24). On the contrary, the spin-transfer torque can either take away or give energy to the system. Depending on the intensity of the injected current, the spin-transfer can

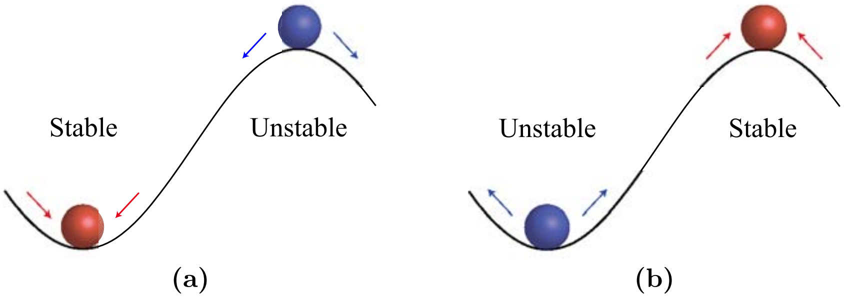

Figure 9.1 – Stability of a static equilibrium position with a total received power (a) negative and (b) positive.

even give more energy to the system than the damping dissipates so there is no reason anymore for the system to always reach a minimum of energy. Therefore, we have to distinguish two kinds of equilibrium positions: first, the extrema of energy where the system is in a static configuration and any other constant energy trajectory where the system is in a dynamic configuration. These dynamic configurations occur when the magnetization is not in an energy extremum and when the energy received from the spin-transfer torque compensates exactly the energy dissipated by the damping torque. They may correspond to magnetization precessions.

An energetic analysis of such a physical system requires more than the study of the evolution of the energy landscape. Here, we will calculate the total algebraic power received by the system from the spin-transfer and the damping torques. A positive power means that the magnetization globally receives energy whereas a negative power means that it dissipates energy. Then, the stability of a static equilibrium position is given by the shape of the energy landscape and by the sign of the total power in the vincinity of the given position (see figure 9.1). For instance, an energy minimum will be a stable position if when the magnetization is slightly tilted, the system gives away energy to fall back into this energy minimum but unstable if the magnetization receives energy during the same process. On the contrary, an energy maximum will be a stable position if when the magnetization is slightly tilted, the system receives energy to rise back into this energy maximum but unstable if the magnetization dissipates energy. Actually, this stability criterion derives from the previous stability criterion extracted from the LLGS equation (see section 8.1 page 91). However, it clarifies the energetic mechanisms and likewise the understanding of magnetization reversal in spin-valves assisted or induced by spin-transfer effect.

9.1.2 Expression of the total power

Let's consider a spin-valve structure similar to the one described in the uniaxial analytical modeling (see section 8.2 page 93) except that the easy anisotropy axis is in the yz plane making an angle λ with the perpendicular direction (see figure 9.2). If $\lambda \neq 0$ the uniaxial symmetry of the system is broken. The origin of this breaking is different from the one used in the non-uniaxial analytical modeling to insist on the fact that the critical currents appear whatever is the cause of the uniaxial symmetry breaking (the energetic analysis in the case of a tilted applied magnetic field is presented in the appendix D page 179).

In this framework, the energy of the free layer magnetization is given by

$$E\left(\theta, H\right) = KV\left[1 - \left(\boldsymbol{m} \cdot \boldsymbol{u}\right)^2\right] - \mu_0 M_\mathrm{s} V H \cos\theta \tag{9.1}$$

with V the volume of the free layer and $\boldsymbol{u}$ an unit vector in the direction of the easy anisotropy axis (see figure 9.2). The dipolar coupling and the demagnetizing field can be included in this modeling as explained previously (see subsection 8.2.2 page 93). In the basis $(\mathbf{e}_\mathrm{x}, \mathbf{e}_\mathrm{y}, \mathbf{e}_\mathrm{z})$, the effective field related to this magnetic energy is given by (see appendix C.3 page 178 for a detailed explanation of this calculation)

$$\begin{aligned}\boldsymbol{H}_\mathbf{eff} = {} & \left[H_\mathrm{c} \sin\lambda \left(\sin\lambda \sin\theta \cos\phi + \cos\lambda \cos\theta\right)\right] \mathbf{e}_\mathrm{y} \\ & + \left[H + H_\mathrm{c} \cos\lambda \left(\sin\lambda \sin\theta \cos\phi + \cos\lambda \cos\theta\right)\right] \mathbf{e}_\mathrm{z}\end{aligned} \tag{9.2}$$

where $H_\mathrm{c} = \frac{2K}{\mu_0 M_\mathrm{s}}$ is the coercive field.

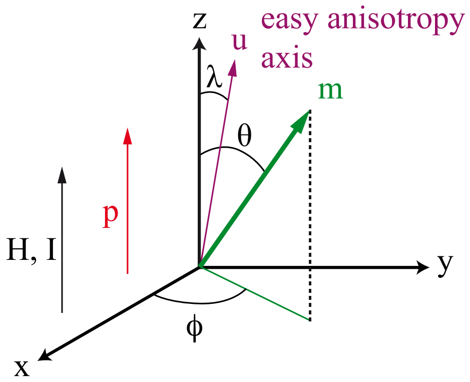

Figure 9.2 – Non-uniaxial modeling of nanopillar spin-valves with perpendicular magnetizations and a tilted easy anisotropy axis

The magnetization reversal is controlled by the LLGS equation composed of three torques: the effective field torque Γ_{eff}, the damping torque Γ_{dam} and the spin-transfer torque Γ_{str} (see section 3.3 page 47). The power received by a physical system due to the action of a torque Γ is defined by $P = \boldsymbol{\Omega} \cdot \boldsymbol{\Gamma}$ where $\boldsymbol{\Omega}$ is the rotation vector of the system. In our case, the rotation vector of the magnetization of the free layer can be extracted from equation 1.12 page 26, $\boldsymbol{\Omega} = \gamma_0 \boldsymbol{H}_{\text{eff}}$. Therefore, the power generated by the effective field torque is zero: it is conservative. On the contrary, the damping and the spin-transfer torques are non-conservative torques. The powers that they generate is given by

$$P_{\text{dam}} = \boldsymbol{\Omega} \cdot \boldsymbol{\Gamma}_{\text{dam}} = -\alpha \gamma_0 \mu_0 M_{\text{s}} V \left[(\boldsymbol{H}_{\text{eff}} \cdot \mathbf{e}_{\text{y}}) \cos\theta - (\boldsymbol{H}_{\text{eff}} \cdot \mathbf{e}_{\text{z}}) \sin\theta \right]^2 \tag{9.3}$$

$$P_{\text{str}} = \boldsymbol{\Omega} \cdot \boldsymbol{\Gamma}_{\text{str}} = \mu_0 M_{\text{s}} V \beta \mathcal{G}(\theta) \left[(\boldsymbol{H}_{\text{eff}} \cdot \mathbf{e}_{\text{y}}) \cos\theta \sin\theta - (\boldsymbol{H}_{\text{eff}} \cdot \mathbf{e}_{\text{z}}) \sin^2\theta \right] I \tag{9.4}$$

These expressions clearly show that the power due to the spin-transfer torque can either be positive or negative depending on the sign of the current and on the effective field orientation whereas the power due to the damping torque is always negative.

In the following, the *power* will refer to the total power received by the system calculated from the mean value of the total power received by its magnetization tilted by an angle of 0.05° from its equilibrium position in the +y and −y directions. In this way, the value of the *power* takes into account that the magnetization can receive or dissipate energy in different parts of its trajectory. To sum up, the stable equilibrium positions are determined by these two factors: 1) the energy landscape providing the static equilibrium positions and 2) the *power* which sign determines the stability of these positions. Indeed, a positive *power* pulls up the system to a maximum of energy whereas a negative *power* pushes it to a minimum of energy (see figure 9.1 page 110).

9.2 Energetic analysis of a uniaxial system

For clarity purpose, we will first study the uniaxial case ($\lambda = 0$) and show that this approach reproduces the expected results presented in section 8.2 page 93.

In this case, the energy of the system is simply given by

$$E(\theta, H) = KV \sin^2\theta - \mu_0 M_{\text{s}} V H \cos\theta$$

From this formula, different shapes of energy landscapes are available depending on the magnetic field value as shown on the upper part of figure 9.3 but the

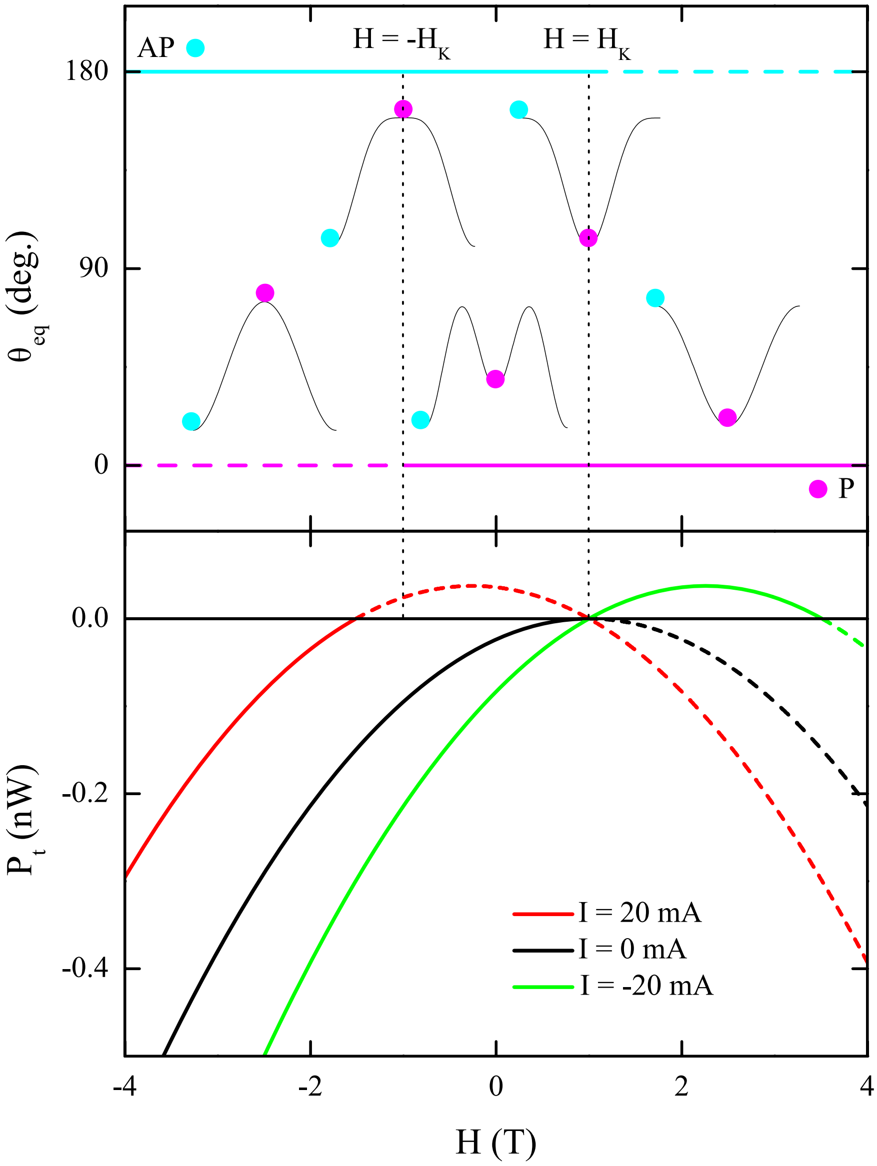

Figure 9.3 – Energetic analysis in the uniaxial case. (Top) θ equilibrium positions as a function of the applied magnetic field with schematic views of the characteristic energy landscapes for different field ranges. The plain lines correspond the energy minima and the dash lines to the maxima. The circles mark on the energy landscapes the equilibrium position involved in the reversal. (Bottom) *Power* in the antiparallel state as a function of the applied magnetic field for different injected currents. The plain lines are for the *power* before the reversal to the parallel state occurs and the dash lines for after this reversal occurs.

equilibrium positions are always at $\theta = 0$ for the parallel state and $\theta = \pi$ for the antiparallel state. For $H < -H_\mathrm{c}$ the antiparallel state is an energy minimum whereas the parallel state is a maximum. For $-H_\mathrm{c} < H < H_\mathrm{c}$ both parallel and antiparallel states are minima. For $H > H_\mathrm{c}$ the parallel state is a minimum and the antiparallel state a maximum. A saddle point for which the antiparallel (resp. the parallel) state switches from a minimum to a maximum appears at $H = H_\mathrm{c}$ (resp. $H = -H_\mathrm{c}$). Finally, the total *power* is simply given by

$$\begin{aligned} P_\mathrm{tot} &= P_\mathrm{dam} + P_\mathrm{str} \\ &= \mu_0 M_\mathrm{s} V \sin^2\theta H_\mathrm{eff} \left(\alpha\gamma_0 H_\mathrm{eff} + \beta\mathcal{G}(\theta) I\right) \end{aligned} \tag{9.5}$$

where $H_\mathrm{eff} = H + H_\mathrm{c}\cos\theta$ with $H_\mathrm{c} = \frac{2K}{\mu_0 M_\mathrm{s}}$ the coercive field.

Let's now focus on the antiparallel to parallel magnetic configuration switching which corresponds to one line of the phase diagram. The same study can be performed on a similar way for the other switching from parallel to antiparallel to obtain a complete phase diagram. The system is initially set in the antiparallel state with a high negative applied magnetic field maintaining it in this position. We are going to determine the magnetic field where the system leaves the antiparallel state to go to the parallel state for different injected currents.

The bottom part of figure 9.3 presents the evolution of the *power* received by the free layer as a function of the applied magnetic field when the magnetization is tilted by an angle of 0.05° from the antiparallel state for various values of the injected current. Each curve is a concave parabola. At zero current, the *power* is always negative. Since the magnetization can only lose energy, the switching occurs when the antiparallel state becomes a maximum that is to say when $H = H_\mathrm{c}$. A key point to notice is that the *power* tends to zero at the reversal. As a result, as soon as a current is injected through the spin-valve the *power* becomes positive over a certain field range so that any injected current will affect the switching. Indeed, if a positive current is injected through the spin-valve the *power* becomes positive for $H < H_\mathrm{c}$. At this point, the magnetization starts to receive energy and becomes able to leave the minimum of the antiparallel state to reach the parallel state. The switching occurs for a lower field than with no current which is in agreement with the fact that a positive current favors the parallel state. On the contrary, if a negative current is injected to the system, the *power* starts to be positive for $H = H_\mathrm{c}$. As soon as the antiparallel state becomes an energy maximum the magnetization receives energy to remain in this

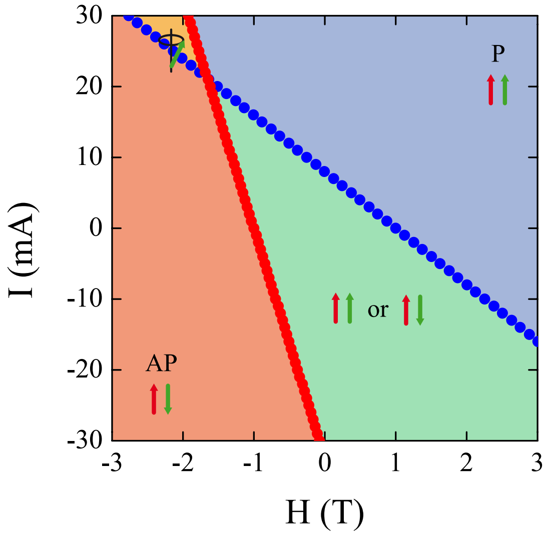

Figure 9.4 – Theoretical phase diagram numerically calculated for a uniaxial system with the energetic approach.

maximum. As a result, the switching occurs for higher magnetic fields when the *power* starts to decrease and becomes negative again.

Figure 9.4 presents the phase diagram numerically calculated using this method. It is clear that the switching currents evolve linearly with the applied magnetic field as expected for a uniaxial system. Solving the equation $P_{\mathrm{tot}} = 0$ even gives the right analytical expression for the switching current

$$I_{\mathrm{s}}^{AP}(H) = -\frac{\alpha\gamma_0}{\beta\mathcal{G}(\pi)}(H - H_{\mathrm{c}}) \Leftrightarrow i_{\mathrm{s}}^{AP}(h) = -\frac{h-1}{\mathcal{G}(\pi)} \tag{9.6}$$

9.3 Energetic analysis of a non-uniaxial system

9.3.1 Physical origin of the critical currents

Let's now focus on the non-unixial case ($\lambda \neq 0$). The calculations in this section are performed with $\lambda = 5°$, a reasonable order of magnitude for our samples.

The upper part of figure 9.5 presents the typical shapes of the energy landscapes for different field ranges in a non-uniaxial case for $\phi = \frac{\pi}{2}$ that is to say a magnetization in the yz plane. This approximation is valid if the intensity of the injected current is moderate. For the following discussion, we will define H_{r} as $H = H_{\mathrm{r}}$ (resp. $H = -H_{\mathrm{r}}$) is the saddle point for which the antiparallel (resp. parallel) state switches from an energy minimum to a maximum. The main dif-

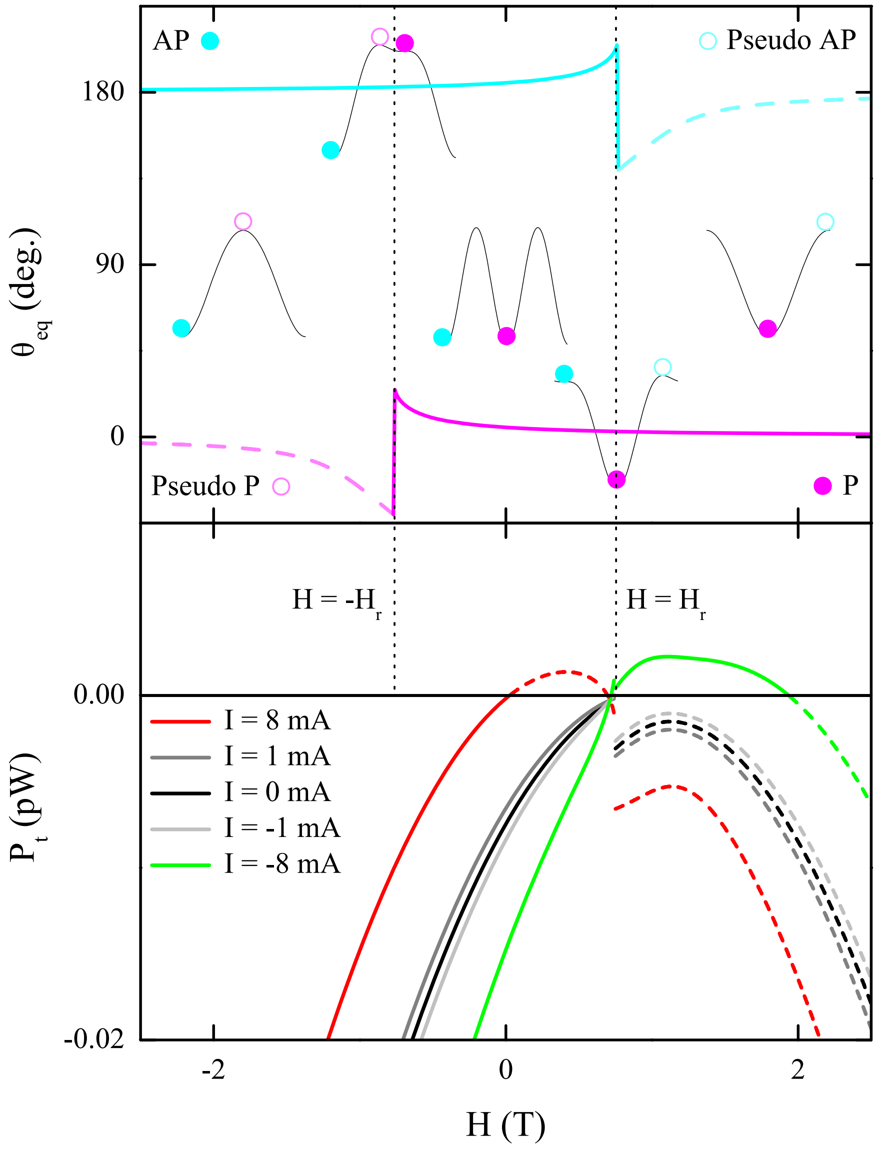

Figure 9.5 – Energetic analysis a non-uniaxial case ($\lambda = 5°$). (Top) θ equilibrium positions as a function of the applied magnetic field with schematic views of the characteristic energy landscapes for different field ranges. The plain lines correspond the energy minima and the dash lines to the maxima. The circles mark on the energy landscapes the equilibrium position involved in the reversal. (Bottom) *Power* in the antiparallel state as a function of the applied magnetic field for different injected currents. The plain lines are for the *power* before the reversal to the parallel state occurs and the dash lines for after this reversal occurs.

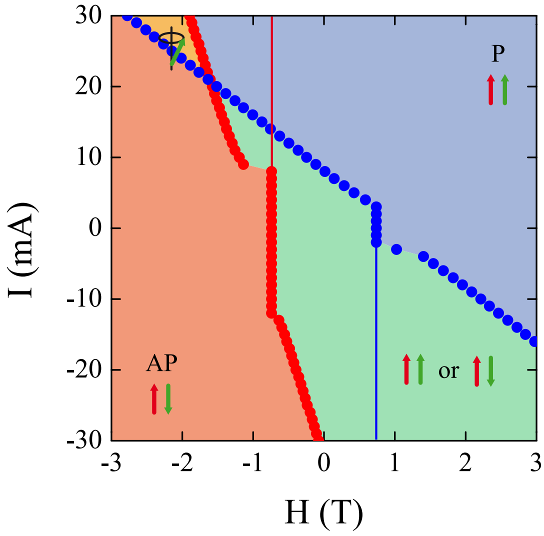

Figure 9.6 – Theoretical phase diagram numerically calculated for a non-uniaxial system ($\lambda = 5°$) with the energetic approach. The vertical lines mark the transitions to a pseudo magnetic state.

ference with the uniaxial case is that the extremum positions that is to say the magnetization equilibrium positions vary with the magnitude of the applied magnetic field. Moreover, when an extremum goes trough a saddle point it vanishes. For example, if $H < H_\mathrm{r}$ the antiparallel state corresponds to a minimum of energy but, after it becomes a saddle point at $H = H_\mathrm{r}$, this equilibrium position disappears. It does not mean that there is no antiparallel state anymore but rather that the antiparallel state position jumps suddenly to a new equilibrium position corresponding to a maximum. We will call this maximum a pseudo antiparallel state (see the upper part of figure 9.5).

Again, let's carefully analyze the antiparallel to parallel transition. The bottom part of figure 9.5 presents the evolution of the *power* as a function of the applied magnetic field in the antiparallel state for various injected currents. At zero current, the *power* evolution is similar to the uniaxial case. It has a shape close to a parabola and the small jump at $H = H_\mathrm{r}$ is simply due to the jump from the antiparallel to the pseudo antiparallel state mentioned previously. The *power* is always negative so the switching occurs when the antiparallel state becomes a maximum, like in the uniaxial case, at $H = H_\mathrm{r}$. Indeed, in the absence of current the system has no energy to reach the pseudo antiparallel state. Contrary to the uniaxial case, the *power* is strictly negative. It never tends to zero which means that if the injected current is too moderate, the *power* remains negative and the switching process is the same as if they were no current. The reversal still occurs at $H = H_\mathrm{r}$. This is the key difference with the uniaxial case. Therefore, the injected current has to exceed a critical value for each polarity to affect the magnetization switching. The physical origin of this phenomenon is this existence of an intrinsic dissipation appearing in the non-uniaxial system during the reversal at zero current. Above these thresholds, a positive current will reduce the switching field and a negative current will increase it as in the uniaxial case.

Figure 9.6 presents the theoretical phase diagram numerically calculated with this approach for $\lambda = 5°$ and indeed, around the zero current reversal fields $-H_\mathrm{r}$ and H_r, the magnetization switching is not affected by the the injected current unless it reaches critical values. Above these values the switching currents quickly start to evolve linearly with the magnetic field.

9.3.2 Beyond the description of the critical currents

Another interest of this energetic analysis is a better understanding of the presence of some pics in the differential resistance measurements in specific regions of the experimental phase diagrams where they are not expected.

All the experimental phase diagrams of nanopillar spin-valves with perpendicular magnetizations exhibit strong pics in the differential resistance (see figure 7.6 page 89) for a high positive injected current and a high negative applied magnetic field (see figures 7.5, 8.3b, 8.4, 8.5 and 8.6 pages 87, 97, 99, 100 and 101). In this specific corner of a phase diagram they are expected by different theories as the sign of magnetization precessions. However, the experimental phase diagrams sometimes exhibit features in the differential resistance measurements which are not expected by any theory. For instance, in the continuity of the vertical lines centered on the switching magnetic fields at zero current, pics in the differential resistance are often recorded either at high positive current and high negative field or at high negative current and high positive field (see figures 8.4, 8.5a and 8.6 pages 99, 100 and 101). These lines appear in the non-uniaxial theoretical phase diagram obtained analytically because of the vertical asymptotes (see figure 8.9a page 107). The energetic analysis performed here shows that they correspond to a transition toward a pseudo parallel or antiparallel states. Indeed, starting from an antiparallel state and injecting a negative current above the corresponding critical currents, the antiparallel state disappears at $H = H_\mathrm{r}$ but the magnetization gets energy from the spin-transfer torque to jump to what we called a pseudo antiparallel state where the magnetization is canted compared to the original antiparallel state. Therefore, a new line appears in the antiparallel state region in negative current at $H = H_\mathrm{r}$ showing the transition from the antipar-

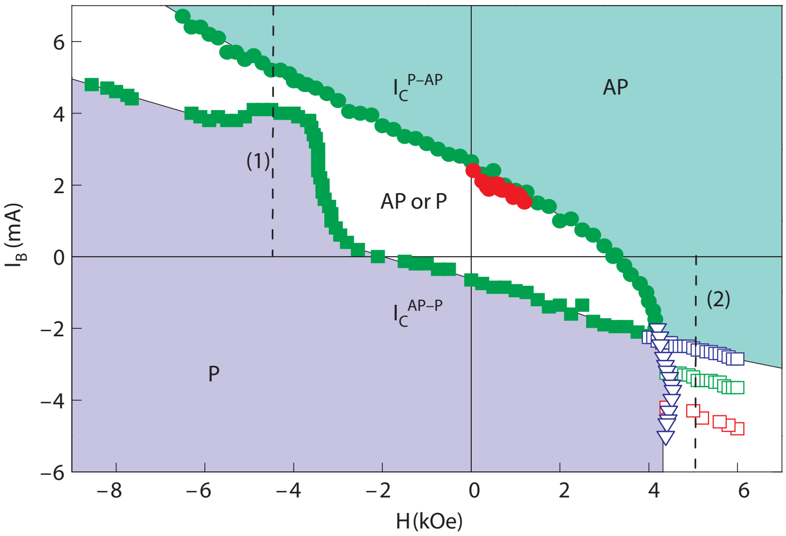

(a)

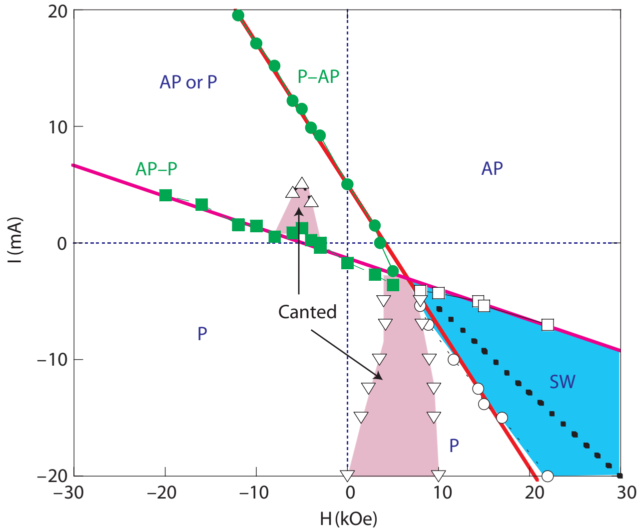

(b)

Figure 9.7 – (a) Experimental phase diagram of an hexagonal nanopillar spin-valve of 50 nm by 100 nm with a hard layer made of [Co/Pt]/[Co/Ni] and a free layer made of [Co/Ni]. The opened symbols mark the presence of pics in the differential resistance. (b) Micromagnetic simulation of the phase diagram of an hexagonal nanopillar spin-valve of 50 nm by 100 nm with perpendicular magnetizations. The canted states predicted here could correspond to the opened triangles of the experimental phase diagram. Note that the convention of sign for the applied magnetic field and the injected current is inverted here. Figure extracted from Mangin *et al.*[14].

allel to the pseudo antiparallel state. The symmetric result is obtained in the parallel state region at $H = -H_{\mathrm{r}}$ when the current is positive (see the lines in figure 9.6). Surely, these transitions have been already observed experimentally and presented as transitions to canted states thanks to micromagnetic simulations[14] (see figure 9.7).

Nevertheless, the breaking of the uniaxial symmetry is not enough to explain totally the shape of the field and current phase diagrams. Indeed, the non-uniaxial theory expects vertical lines for the switching fields around the zero current switching field and for the evolution of the pics in the differential resistance showing a transition to a pseudo state. Experimentally however, we generally observe a decrease of the impact of the injected current on the switching fields but not a total disappearing of it. Indeed, these lines tends to curve. This is for instance clearly visible on the differential resistance pics at the bottom right corner of figure 8.4a page 99. Besides, some more intricated features may appear in this region. The bistability region may even disappear at high positive field and high negative current like in the opposite corner. From the experimental measurements, it is clear that thermal activation and non-uniformities of the magnetization can influence the shape of these vertical lines where the impact of the current on the system is weak. For instance, these lines are more vertical if the temperature decreases (see figure 8.4 page 99). Therefore, thermal activation and non-uniformities in the magnetization of the free layer may play a non-negligible role on these discrepancies.

Part IV

Nucleation and domain wall propagation
Nucléation et propagation de paroi

French summary
Résumé en français

Cette partie s'intéresse au processus de retournement de l'aimantation dans nos vannes de spin aux aimantations perpendiculaires. Le premier chapitre démontre qu'il implique deux mécanismes : la nucléation d'un domaine magnétique suivi d'une propagation de paroi de domaine magnétique. Le second chapitre examine l'influence du champ magnétique et du transfert de spin sur ces deux mécanismes.

Le processus de renversement de l'aimantation dans des nanopiliers aimantés dans le plan des couches est proche de celui d'un macrospin avec un renversement cohérent de tous les moments magnétiques atomiques. Ils restent pratiquement en permanence parallèles les uns par rapport aux autres. Une des raisons à cela est l'importante largeur des parois de domaine dans ces matériaux qui limite leur apparition dans ces structures de quelques dizaines de nanomètres. Au contraire, cette largeur est fortement réduite, jusqu'à une vingtaine de nanomètres, dans les couches magnétiques à anisotropie perpendiculaire utilisées au cours de cette thèse. La probabilité d'y trouver ces parois devient donc non-négligeable. Ainsi, les simulations micromagnétiques montrent que le renversement de ces couches commence par la nucléation d'un domaine d'aimantation opposée et se poursuit par la propagation d'une paroi de domaine à travers le reste de la couche.

L'existence de ces parois de domaine se remarque également dans les cycles d'hystérésis mesurés grâce au phénomène de magnétorésistance géante. En effet, il arrive que des niveaux de résistance situés entre la résistance de l'état parallèle et celle de l'état antiparallèle apparaissent. Plusieurs caractéristiques de ces états de résistance intermédiaire démontrent qu'il s'agit en réalité d'états d'aimantation non-uniforme où la couche libre s'est brisée en deux domaines d'aimantations opposées séparés par une paroi de domaine. Par exemple, ces états s'observent lorsque le champ de renversement est proche d'un champ ressenti par le couche libre nul. Dans ce cas, l'aimantation n'a plus d'orientation privilégiée le long de l'axe perpendiculaire et peut donc se briser en deux domaines afin de minimiser l'énergie du champ démagnétisant. Egalement, le nombre de ces états augmente lorsque la température diminue ce qui est compatible avec le caractère thermiquement activé des processus de piégeage et de dépiégeage de paroi. Enfin, l'évolution angulaire du champ pour lequel le système quitte ces états de résistance intermédiaire est celle attendue pour un processus de dépiégeage de paroi. Il s'agit donc bien d'état de paroi.

Les phénomènes liés à l'activation thermique sont très importants dans la gamme de champ et de courant où ces états de paroi sont observés. En réalité, nous avons observé des signaux de type bruit télégraphique en s'intéressant à l'évolution temporelle de la résistance des états magnétiques générés dans ces conditions particulières. Le bruit télégraphique est caractéristique d'un système stochastique dont l'état magnétique n'est pas constant au cours du temps mais qui est capable sous l'effet de l'activation thermique de faire des allers-retours entre différentes configurations. L'étude statistique de ces signaux permet de remonter au temps de vie des différents états magnétiques impliqués dans le bruit télégraphique. Ces temps de vie sont liés à l'effet du champ magnétique et du transfert de spin sur le système. Par conséquent, l'étude de l'évolution de ces temps de vie en fonction des paramètres champ et courant permet de remonter à l'influence du transfert de spin sur les processus de nucléation de domaine et de propagation de paroi.

Les échantillons mesurés pour cette étude sont de forme hexagonale. A partir des mesures magnétorésistives des cycles d'hystérésis, il semble que cette géométrie influence la formation des états de paroi. De plus, nous sommes en mesure d'étudier deux types d'états de paroi différents : un premier où la paroi est piégée près du centre de la couche libre et un second où elle est piégée au niveau du rétrécissement triangulaire de la couche.

En ce qui concerne le processus de nucléation, nous avons étudiés deux signaux de bruit télégraphique impliquant soit l'état parallèle soit l'état antiparallèle. La transition d'un de ces états d'aimantation uniforme vers un autre état magnétique est bien liée à la nucléation d'un domaine. L'évolution des temps de vie de ces états est clairement linéaire aussi bien en fonction du champ magnétique appliqué que du courant injecté. Des déviations par rapport à ces comportements linéaires sont observables mais nous pouvons néanmoins les expliquer par la disparition d'un des deux états magnétiques mis en jeu dans les signaux de bruit télégraphique étudiés. Ces évolutions sont parfaitement en accord avec les prédictions théoriques basées sur un modèle de Néel-Brown modifié.

Pour le processus de dépiégeage de paroi de domaine, les résultats obtenus sont plus surprenant. Les mesures de bruit télégraphique montrent que l'effet du champ magnétique sur une paroi piégée au centre de la couche libre ou sur une extrémité correspond au comportement théorique attendu. En revanche, le transfert de spin n'a pas toujours un effet visible sur le dépiégeage des parois. En effet, les mesures de bruit télégraphique ne montrent aucune évolution des temps de vie des états de paroi constitués d'une paroi piégée au centre de la couche avec le courant injecté. Ce phénomène est confirmé par la mesure des diagrammes de phase de ces états paroi ainsi que par la simulation micromagnétique de ces diagrammes de phase. En effet, les champs de dépiégeage ne sont pas modifiés par l'injection d'un courant polarisé en spin. Pour ce qui est des parois piégée près d'une extrémité de l'hexagone, le transfert de spin influence le dépiégeage uniquement si la paroi se déplace ensuite vers le rétrécissement triangulaire près duquel elle était piégée. Si elle se déplace dans le sens opposé, alors l'étude du diagramme de phase de ce type d'état de paroi ne montre aucun effet du transfert de spin. Ces observations pourrait s'expliquer par la structure des parois de domaine présentes dans nos échantillons. En effet, d'après les simulations micromagnétiques réalisées, lorsque la paroi est de type Néel le transfert de spin n'a aucun effet sur son dépiégeage. Lorsqu'elle est piégée au centre de la couche, l'effet du courant est de commencer par modifier sa structure par une rotation des moments magnétiques avant de la dépiéger. Il la transforme alors en paroi à mi-chemin entre une paroi de Bloch et une paroi de Néel. De plus, toujours d'après ces simulations, il semble que la structure de la paroi, généralement de type Néel dans les partie à largeur constante de la couche, se modifie vers une structure de type Bloch lorsqu'elle pénètre dans un des rétrécissements triangulaires situés aux extrémités de la couche libre. Ce phénomène pourrait expliquer la dissymétrie observée dans le comportement du transfert de spin dans le cas d'une paroi piégée près d'un de ces rétrécissements suivant sa direction de propagation.

Chapter 10

Static and dynamic observations of domain walls

The previous part deals with the field and current phase diagrams of a uniformly magnetized free layer modeled by a macrospin. Its magnetization may not actually be uniform especially during its reversal. This chapter combines results from 3D LLG micromagnetic calculations using the Scheinfein code and from experimental measurements giving evidences of the presence of magnetic domain walls inside the free layer of our devices. Besides, it explains how thermally activated domain wall dynamic can be observed and used to investigate the influence of both the applied magnetic field and the spin polarized current on single domain wall dynamics.

10.1 Magnetization reversal process

10.1.1 Coherent reversal of the magnetization

The magnetization reversal of an ideal magnet is described by the Stoner Wohlfart model (see subsection 1.3.2 page 24) where the magnet is considered perfectly homogeneous and modeled by a macrospin. This reversal process implies a simultaneous reversal of all the atomic magnetic moments of the ferromagnet. This is a coherent reversal.

A pure macrospin system is hard to obtain experimentally. It requires to grow very small magnets of few nanometers perfectly homogeneous[75]. Nevertheless, many reversal processes are well described by a macrospin model especially with nanomagnets. In this case, the atomic magnetic moments do not remain exactly parallel but rather close from one another and no well-defined domain wall

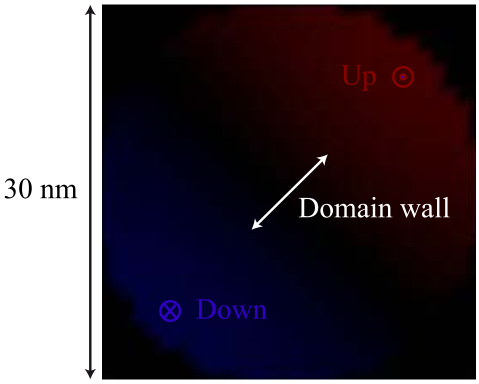

Figure 10.1 – Magnetic state of the free layer of a circular nanopillar spin-valve with perpendicular magnetizations of 30 nm of diameter at half its current-induced reversal obtained from micromagnetic simulations.

is created. For instance, both experimental measurements and micromagnetic simulations suggest the formation of complex domain structures under low current densities in nanopillar spin-valves with in-plane magnetizations[5,8,61,100–103]. No well-defined domain walls are expected however because their typical size is on the same scale as the device. The mean domain wall width in permalloy is above 100 nm for exemple. On the contrary, the typical size of a domain wall in [Co/Ni] multilayers is around 20 nm due to the strong perpendicular anisotropy. Consequently, domain walls are more easily found in nanopillar spin-valves with perpendicular magnetizations[104–106]. Figure 10.1 shows the magnetic state of the free layer of a circular nanopillar spin-valve with perpendicular magnetizations of 30 nm of diameter at half its current-induced reversal obtained from a micromagnetic simulation. The blue domain nucleates and a domain wall propagates so that the red domain vanishes. From the micromagnetic simulations, this reversal is controled by a nucleation and a domain wall propagation until the diameter of the nanopillar decreases below 15 nm (see appendix E page 183 for a detailed presentation of the parameters used for the simulations presented in this part).

10.1.2 Nucleation and propagation of a domain wall

In perpendicularly magnetized nanopillar spin-valves, the micromagnetic simulations show that the magnetization reversal generally occurs in a two steps process. First, a domain of opposite magnetization is nucleated with a domain wall delimiting its position. Second, this domain wall propagates leading to the reversal of the entire layer.

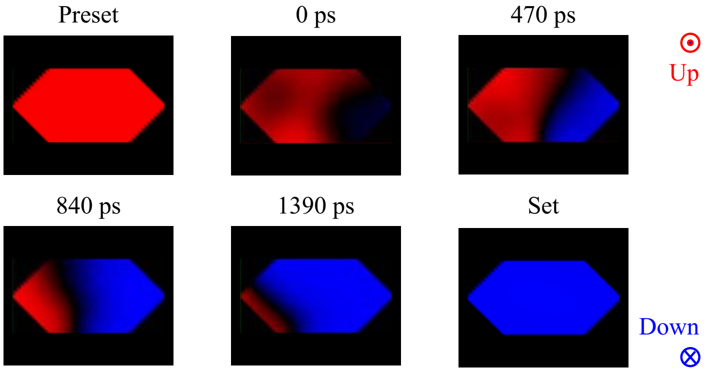

Figure 10.2 – Current-induced reversal of the free layer of an hexagonal nanopillar spin-valve with perpendicular magnetizations of 100 nm by 200 nm obtained from micromagnetic simulations.

The nucleation occurs in a specific location of the magnetic layer. This location depends on the shape of the nanopillar, on its size or on the nature of the polarizer. Indeed, there is a competition between the action of the dipolar field emitted by the polarizer and the demagnetizing field induced by the free layer magnetization. The dipolar field tends to tilt the atomic magnetic moments on the edges of the free layer which favors a nucleation on these edges whereas the demagnetizing field is stronger in the center of the free layer and favors a nucleation there. The position of the nucleation site may also depends on the presence of defects inside the free layer. For instance, a grain with a reduced perpendicular anisotropy reverses at a lower applied magnetic field. As a consequence, the reversal starts with this grain.

Figure 10.2 presents the reversal process of an hexagonal nanopillar spin-valve with perpendicular magnetizations of 100 nm by 200 nm similar to the ones we measure experimentally. The blue domain nucleates in one of the triangular extremities of the hexagon. Then, it grows until it fills the entire triangular extremity and the domain wall propagates to the opposite edge. This simulation is in agreement with our experimental observations.

10.2 Stabilization of a domain wall

10.2.1 Domain wall and intermediate resistance states

The existence of magnetic domain walls in spin-valves with perpendicular magnetizations can also be observed in the magnetoresistance measurements[104–106].

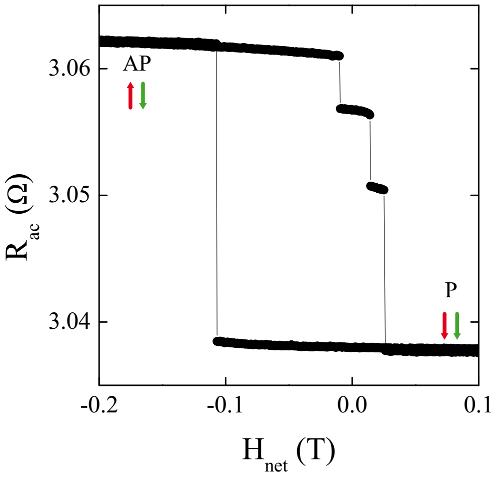

Figure 10.3 – Resistance evolution as a function of the net applied magnetic field at $I = 2.2$ mA of an hexagonal nanopillar spin-valve of 100 nm by 200 nm with a hard layer made of [Co/Pt]/[Co/Ni] and a free layer made of [Co/Ni].

Until now, the hysteresis loops presented exhibited only two resistance levels corresponding to the parallel and antiparallel magnetic states. Additional levels may actually appear corresponding to non-uniform magnetic states (see figure 10.3). Since these are static measurements, the presence of these resistance levels indicates that they are related to stable magnetic configurations. Many experimental observations lead to the conclusion that these intermediate resistance states are created by a two-domains structure with a domain wall pinned on an intrinsic or extrinsic defect of the free layer. We will call these magnetic states domain wall states.

Firstly, these intermediates resistance states appear in a specific region of the field and current phase diagrams, centered around a zero net applied magnetic field (for a definition of the net applied magnetic field see subsection 7.1.1 page 81). Figure 10.4a shows the phase diagram of an hexagonal nanopillar spin-valve with perpendicular magnetizations of 100 nm by 200 nm with a hard layer made of [Co/Pt]/[Co/Ni] and a free layer made of [Co/Ni]. Inside the red bistable region, some parts appear in different colors (in orange or yellow) because the difference of resistance between the decreasing and the increasing parts of the hysteresis loops used to build it do not correspond to the difference of resistance between the parallel and the antiparallel magnetic states (for an explanation of the construction of this figure see subsection 7.2.1 page 85). For instance, the hysteresis loop presented in figure 10.3 were used to build this phase diagram.

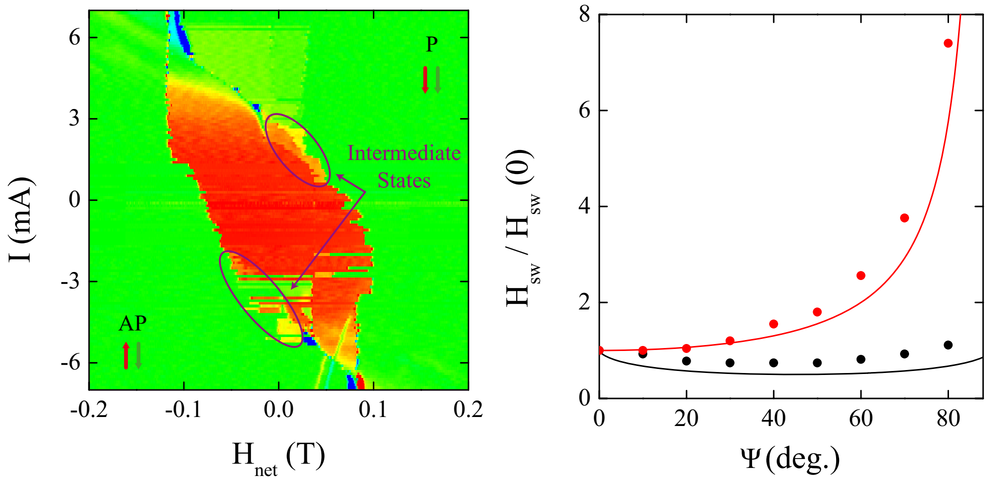

(a) (b)

Figure 10.4 – Intermediate resistance states of an hexagonal nanopillar spin-valve of 100 nm by 200 nm with a hard layer made of [Co/Pt]/[Co/Ni] and a free layer made of [Co/Ni]. (a) Experimental phase diagram. (b) Evolution of the switching field as a function of the angle of application of the magnetic field for a transition between two uniformly magnetized states (in black) and between an intermediate resistance state and a uniformly state (in red). The angle is defined toward the perpendicular direction. The lines represents two different theoretical expectations: one for the Stoner-Wohlfarth model and one for a domain wall depinning model.

Looking at the positive injected currents, the orange region corresponds to the highest intermediate resistance state of this hysteresis loop and the yellow region to the other one. The presence of these domain wall states around the zero net applied magnetic field is consistent with the fact that a domain wall may be favorably stabilized when there is no preferential orientation of the magnetization induced by the applied magnetic field or the dipolar field. The magnetic layer can then break into domains to minimize the demagnetizing energy (see subsection 1.2.3 page 20).

Secondly, the number of intermediate resistance states increases experimentally at low temperature. This is consistent with the thermally activated character of domain wall depinning process[104,105,108].

Finally, the angular variation of the switching fields in these intermediate resistance states is very specific to a domain wall depinning process. Once created an intermediate resistance state can be stabilized at zero injected current. Figure 10.4b compares the angular variation of the switching field at $I = 0$ for a direct transition between two uniformly magnetized states (antiparallel to parallel reversal) and for a transition from an intermediate resistance state to a uniformly magnetized state (intermediate resistance to parallel state reversal). The first evolution is consistent with the reversal of an uniaxial macrospin from Stoner Wohlfarth model. It shows that this reversal may be described by a macrospin model as we did it in the previous part dealing with field and current phase diagrams. The second evolution involving the intermediate resistance state follows the $\frac{1}{\cos\theta}$ dependence expected for a domain wall depinning process[104].

These three points lead to the same conclusion. The intermediate resistance states centered around the zero net applied magnetic field come from the presence of a domain wall state.

10.2.2 Nucleation, domain wall propagation and pinning

The magnetization reversal process of a nanopillar spin-valve with perpendicular magnetizations implies the nucleation of a domain and the propagation of a domain wall. This domain wall can be pinned during its propagation by defects of the free layer. Each defect is characterized by a pinning field which needs to be overcome to resume the propagation and leads to the creation of a domain wall state. The resistance level of this state depends on the spatial location of

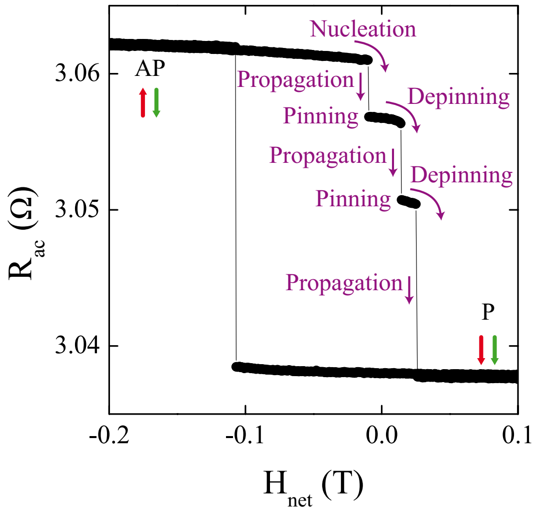

Figure 10.5 – Resistance evolution as a function of the net applied magnetic field at $I = 2.2$ mA of an hexagonal nanopillar spin-valve of 100 nm by 200 nm with a hard layer made of [Co/Pt]/[Co/Ni] and a free layer made of [Co/Ni]. The different steps of the antiparallel to parallel state reversal are indicated on the curve.

the domain wall that is determined by randomly distributed extrinsic or intrinsic pinning sites. As a result, the domain wall may be pinned several times during its propagation (see figure 10.5).

To observe a domain wall state, the nucleation field has to be lower than the pinning field of the defects otherwise the domain wall is never stopped during its propagation. Yet, at zero current the nucleation field is typically higher than the pinning field and no domain wall states are observed. Therefore, spin-transfer effect is essential to reduce the nucleation field below the pinning field to generate domain wall states. This is why domain wall states are usually observed when both current and field are applied to the system.

10.3 Thermally activated domain wall motion

10.3.1 Thermal activation and hysteresis loops

The magnetization reversal of the free layer of a nanopillar spin-valve with perpendicular anisotropies depends on its nucleation field and on the pinning fields of its defects. At $T = 0$ K, the applied magnetic field has to reach the nucleation field value to start the switching and a unique hysteresis loop is achievable. At room temperature however, thermal activation will modify the magnetization reversal because the nucleation process becomes stochastic (see subsection 4.1.2 page 52). Moreover, the same phenomenon occurs for the pinning and the depinning processes of the domain wall. Consequently, many different hysteresis loops are achievable because of the dispersion of the nucleation and pinning fields.

Figure 10.6 illustrates the impact of thermal activation on the measurement of hysteresis loops. It presents the superposition of ten normalized resistance evolution curves as a function of the applied magnetic field measured at room temperature, at an injected current of $I = -2$ mA with the applied magnetic field swept from 90 to -70 mT at a constant sweeping rate of 1 mT/s (see subsection 7.2.1 page 85 for a definition of the normalized resistance). Starting from a parallel state, the system switches into several intermediate states as the field decreases from positive to negative values before reaching the antiparallel state. Up to seven intermediate resistance states could be identified in this sample. They correspond to seven different pinning sites for a single domain wall propagating through the layer. On the contrary, as the applied magnetic field increases from negative to positive values the system drops directly from the antiparallel to the

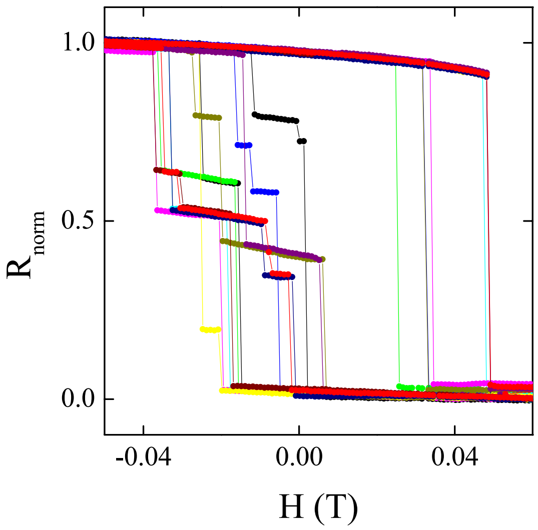

Figure 10.6 – Superposition of ten normalized resistance evolution curves as a function of the applied magnetic field measured in the same conditions at $I = -2$ mA and at room temperature for an hexagonal nanopillar spin-valve of 100 nm by 200 nm with a hard layer made of [Co/Pt]/[Co/Ni] and a free layer made of [Co/Ni].

parallel state because the nucleation field in this configuration at this current is higher than the pinning fields of the defects.

The stochasticity induced by the thermal activation of the reversal is clearly evidenced by the dispersion of the nucleation fields and of the depinning fields. Besides, the fact that each domain wall state may or may not be visited during any particular field sweep highlights the stochastic dynamic of domain wall motion in these nanopillars with perpendicular magnetizations. This kind of features leads us to study the stability of the magnetic states generated in these regions of fields and currents where the domain wall states appear.

10.3.2 Thermal activation and telegraph noise

The stochasticity of domain wall motion in nanopillars with perpendicular magnetizations is highlighted by the temporal evolution of the magnetic states generated in the region of the field and current phase diagram where domain wall states are detected.

Figure 10.7a, 10.7b and 10.7c present the time evolution at room temperature of the normalized resistance of the same nanopillar spin-valve measured in figure 10.6. The injected current is constant at $I = -2$ mA and different magnetic field are applied, $H_{\text{net}} = 4.5$, -15.5 and -23.5 mT respectively. These measure-

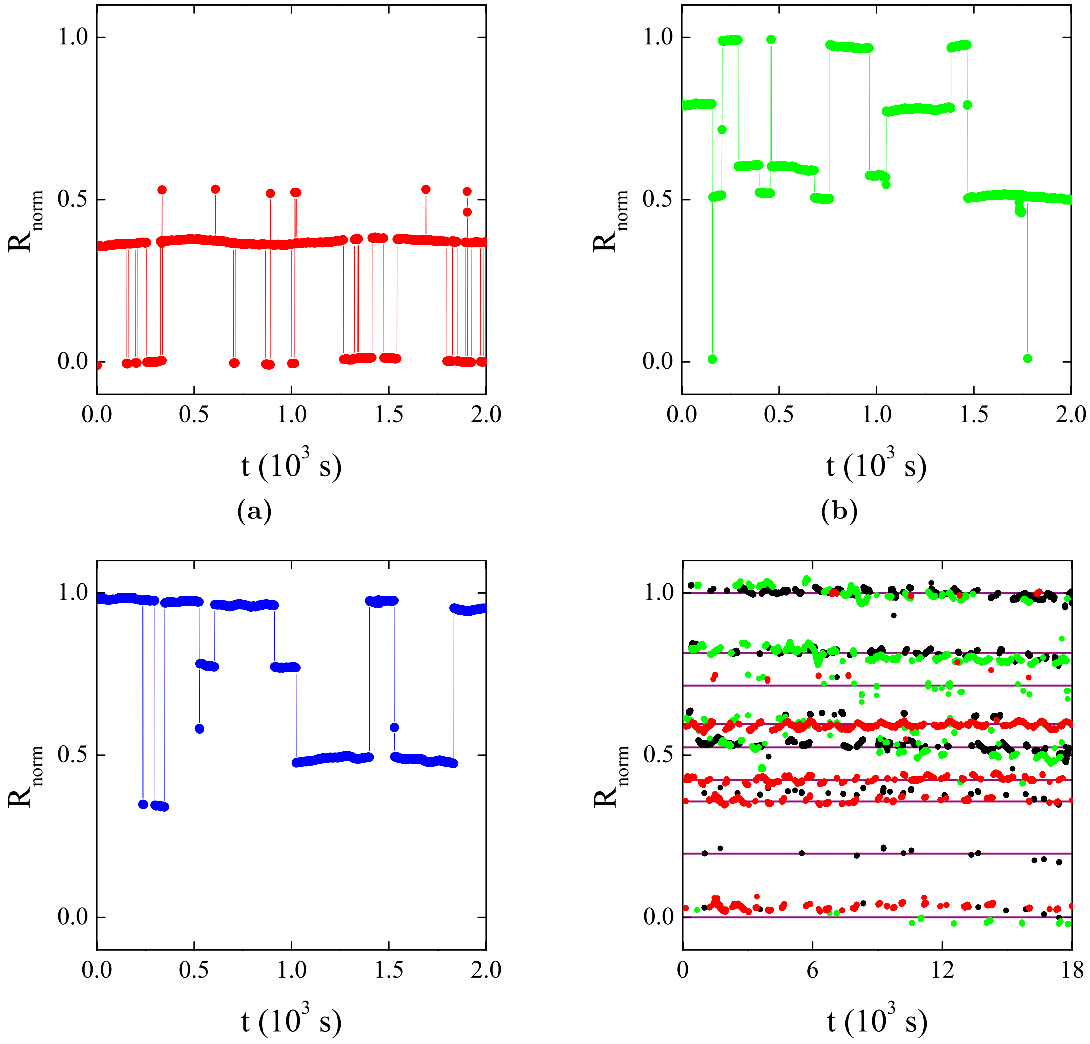

(a) (b) (c) (d)

Figure 10.7 – Normalized resistance evolution as a function of time at room temperature, at $I = -2$ mA and (a) at $H_{\text{net}} = 4.5$ mT, (b) at $H_{\text{net}} = -15.5$ mT and (c) at $H_{\text{net}} = -23.5$ mT. (d) Superposition of normalized resistance evolution curves as a function of time at room temperature, at $I = -2$ mA and for several net applied magnetic fields between -23.5 and 4.5 mT. The purple lines highlight the nine resistance states appearing in this figure. These results come from an hexagonal nanopillar spin-valve of 100 nm by 200 nm with a hard layer made of [Co/Pt]/[Co/Ni] and a free layer made of [Co/Ni].

ments were performed during five hours but these curves show only half an hour of the recorded data to make the evolution clearer. The resistance jumps back and forth between well-defined levels with a time scale from about a few seconds to a few hundreds of seconds. This kind of temporal signal is called telegraph noise. It has already been observed for nanopillars with in-plane anisotropies but between fully magnetized states only with no domain wall involved and the time scales are reduced to few microseconds to few seconds[77,80–86]. Here, both the magnetic states involved and the typical dwell times are tuned by the magnetic field. Indeed, the system switches mainly between the parallel state and a domain wall state for $H_{\text{net}} = 4.5$ mT whereas it switches between the antiparallel state and several domain wall states for $H_{\text{net}} = -23.5$ mT. As we will show it later, the spin polarized current also has an impact on the telegraph noise via spin-transfer effect.

Besides, the magnetic states involved in these telegraph noise signals correspond to the domain wall states identified in the hysteresis loops of figure 10.6. Indeed, figure 10.7d presents a superposition of several telegraph noise signals recorded at $I = -2$ mA for different net applied magnetic fields between 4.5 and -23.5 mT on the same device as for figure 10.6. Apart from the parallel and the antiparallel states levels, seven intermediate resistance states are clearly distinguishable. Their positions are exactly the same as the position of the domain wall states of the hysteresis loops. Moreover, only the states observed during the field sweeps are detected in the telegraph noise measurements. Therefore, these telegraph noise signals are explained by the stochastic domain nucleation and a single domain wall motion between different pinning sites activated by thermal fluctuations.

10.3.3 Processing of telegraph noise signals

To simplify the following analysis of the telegraph noise signals, we focused on samples exhibiting two states fluctuations only between a fully magnetized state and a domain wall state (see figure 10.8a).

From a theoretical point of view, this case can be described by two potential wells separated by an energy barrier, each one corresponding to one of the two available magnetic states (see figure 10.9). The height of the energy barrier is generally different looking from these two wells but the telegraph noise signals indicates that the free layer is able to switch back and forth between these two configurations that is to say able to cross the energy barrier from both sides thanks to thermal activation.

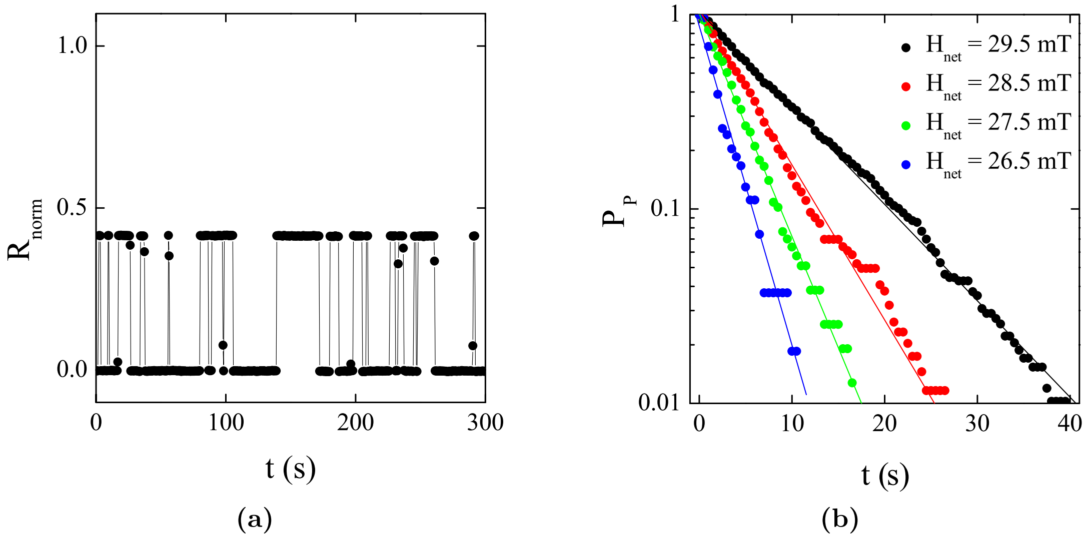

Figure 10.8 – Processing of telegraph noise signals recorded at $I = -4.6$ mA for an hexagonal nanopillar spin-valve of 100 nm by 200 nm with a hard layer made of [Co/Pt]/[Co/Ni] and a free layer made of [Co/Ni]. (a) Telegraph noise signal between the parallel state and a nearly centeted domain wall state. (b) Evolution in logarithmic scale of the probability to remain in the parallel state as a function of time for four different applied magnetic fields extracted from telegraph noise signals such as the one on the left. The lines are a linear fit of these data.

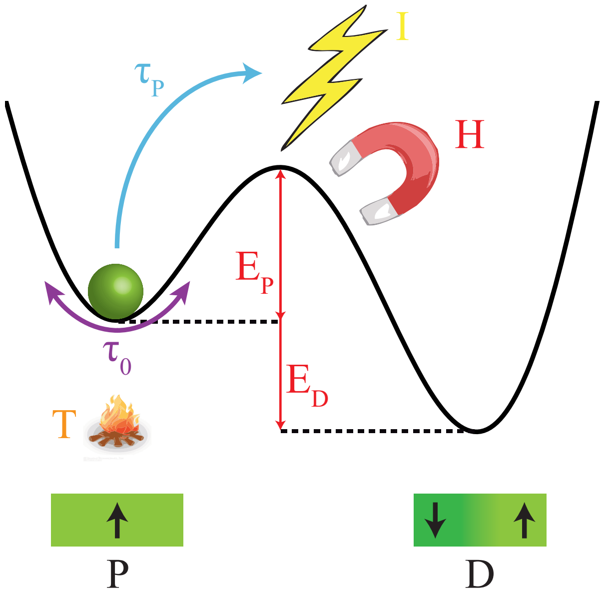

Figure 10.9 – Scheme of the telegraph noise description between the parallel state (P) and a domain wall state (D).

According to the theoretical expectations presented in subsection 4.2.2 page 54, the probability to remain in one of these two magnetic states should decrease exponentially. We developed a *Matlab* program able to extract the list of the times of residence in a specific magnetic configuration from the telegraph noise signals. From this list, it builds the evolution in time of the probability to remain in this magnetic state. The results for our devices are in perfect agreement with the theory since the measured decrease is indeed exponential (see figure 10.8b). It is characterized by a life time τ specific to the considered magnetic state (see subsection 4.1.2 page 52). Based on theory, this life time is expected to depends on three parameters acting on the system: the applied magnetic field, the injected current and the temperature

$$\tau = \tau_0 \exp\left[\frac{E_\mathrm{b}\left(H\right)}{k_\mathrm{B}T}\left(1-\frac{I}{I_\mathrm{sw}}\right)\right] \tag{10.1}$$

where τ_0 corresponds to the characteristic time of fluctuation of the system at the bottom of a well. As a result, starting from the telegraph noise signals we can extract the life times of a magnetic state and analyze their evolution as a function of the applied magnetic field and of the injected current.

Two state fluctuations between a fully magnetized state and a domain wall state involved two different magnetic processes. Indeed, going from a fully magnetized state to a domain wall state implies a domain nucleation whereas going from a domain wall state to a fully magnetized state implies a domain wall depinning process. Therefore, we are able to analyze the impact of the applied magnetic field and of the spin-transfer effect on the two magnetic processes implied in the reversal of our nanopillar spin-valves with perpendicular magnetizations: the nucleation of a domain and the pinning of a domain wall.

Chapter 11

Field and current interaction with a domain wall

This chapter investigates the action of the applied magnetic field and of the injected current on the domain nucleation and on the domain wall depinning processes in the free layer of a nanopillar spin-valve with perpendicular magnetizations. Thanks to the telegraph noise signals, we study the evolution as a function of the applied magnetic field and of the injected current of the life times of fully magnetized and domain wall states. We also compare our results with the theoretical predictions presented in the first part of this manuscript (see section 4.2.2 page 54). Finally, we study the field and current phase diagram of domain wall states and combine our results with micromagnetic simulations to corroborate and understand the exploitation of the telegraph noise signals.

11.1 Specificities of the measured devices

11.1.1 Presentation of the devices

The experimental results presented in this chapter mainly come from the same device but its behavior is characteristic from the others studied during this thesis. Moreover, the comparison with theoretical expectations and other experiments mentioned at the end of this chapter ensures that the conclusions deduced from it can be generalized to most of our spin-valves with perpendicular magnetizations. This section gives a general presentation of this device.

The devices measured for this study consist in hexagonal nanopillar spin-valves of 100 nm by 200 nm. Their hard layer is made of Pt (3 nm) / [Co (0.25 nm)/Pt (0.52 nm)]×5 / Co (0.2 nm) / [Ni (0.6 nm)/Co (0.1 nm)]×2 / Co (0.1 nm)

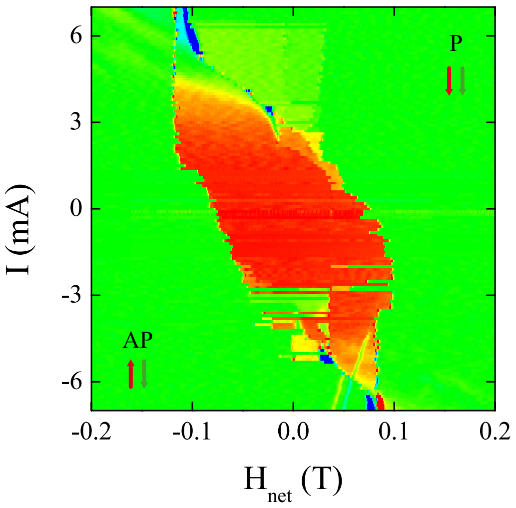

Figure 11.1 – Field and current phase diagram of the principal device measured for this study, an hexagonal nanopillar spin-valve of 100 nm by 200 nm with a hard layer made of [Co/Pt]/[Co/Ni] and a free layer made of [Co/Ni].

and their free layer of Co (0.1 nm) / [Co (0.1 nm)/Ni (0.6 nm)]×4. Compared to the samples used in the previous part, the free layer is not terminated by a platinum layer. Removing this layer lowers its perpendicular anisotropy. As a result, the nucleation field is reduced and the probability to observe domain wall states increases. For instance, these devices exhibit up to seven domain wall states such as the one presented in the previous chapter (see figure 10.6 page 134).

Figure 11.1 presents the field and current phase diagram of the principle device used for the exploitation of the telegraph noise signals. Its shape is similar to the one discussed in the previous part concerning phase diagrams. The switching fields evolves more or less linearly with the injected current excepted for specific current ranges where they remain virtually constant. Nevertheless, the bistability region is closed at both extremities and then pics in the differential resistance start to appear both in the upper left and in the bottom right corners. One of the principal discrepancies between this phase diagram and the ones presented in the previous part is the presence of domain wall states. They appear as orange and yellow regions centered around the zero net applied magnetic field. They are more easily visible for positive current values than for the negative ones but this is only an artifact due to the experimental setup we used to perform this measurement. Indeed, the power supply generating the applied magnetic field was at this time unipolar and we had to use a mechanical switch to reverse the poles of the electromagnet. This setup induces unfortunately some perturbation to the sample during the inversion of the field high enough sometimes to reverse the magnetization of the free layer. We finally solved this problem by using a bipolar power supply.

11.1.2 Evidence of two pinning sites

Since two domain wall states appear in this phase diagram, it means that two different pinning sites exist in this sample. They are efficient to pin a domain wall both for a positive and a negative current (see figure 11.2a and 11.2c). For negative current we recorded telegraph noise signals between the parallel state and a domain wall state corresponding to a domain wall pinned in the middle of the device (see figures 11.2a and 11.2b) whereas at positive current we recorded telegraph noise signals between the antiparallel state and a domain wall state corresponding to a domain wall pinned close to the corner of the device (see figures 11.2c and 11.2d).

An interesting feature with the domain wall states in these hexagonal devices is that they are always observed for a normalized resistance between around 0.17 and around 0.83. This is indeed the case for the five samples of this kind measured during this thesis. It means that for the domain wall states of these devices at least 17 % of the volume of the free layer is reversed and at most 17 % of it remains unreversed. Their hexagonal shape may explain this phenomenon. It is composed of a 100 nm square in the middle with two triangles on two opposite sides corresponding to its extremities to form at the end a 100 nm by 200 nm hexagon. A basic calculation shows that the volume of one of these extremities represents about 17 % of the total volume of the free layer. Therefore, it seems that a domain wall states appears only if its domain wall is pinned in the central square part of the hexagon. One may imagine that a domain wall is so strained inside a triangular extremity that it has to propagate through the square part where it can finally be pinned. The domain wall states which normalized resistance is equal to 0.17 or 0.83 may so be induced by a domain wall pinned at the borders between the central square part of the hexagon and its triangular extremities (see the schematic top view of the free layer magnetization on figure 11.2d). Their pinning may either be induced by the geometry of the free layer itself or by an intrinsic defect located close to these extremities. Concerning the domain wall state close to the middle of the free layer (see the schematic top view of the free layer magnetization on figure 11.2b), it seems that it is totally induced by an intrinsic defect since the edge roughness of our devices is very low. Anyway, the geometry of the sample influences the pinning of the domain walls.

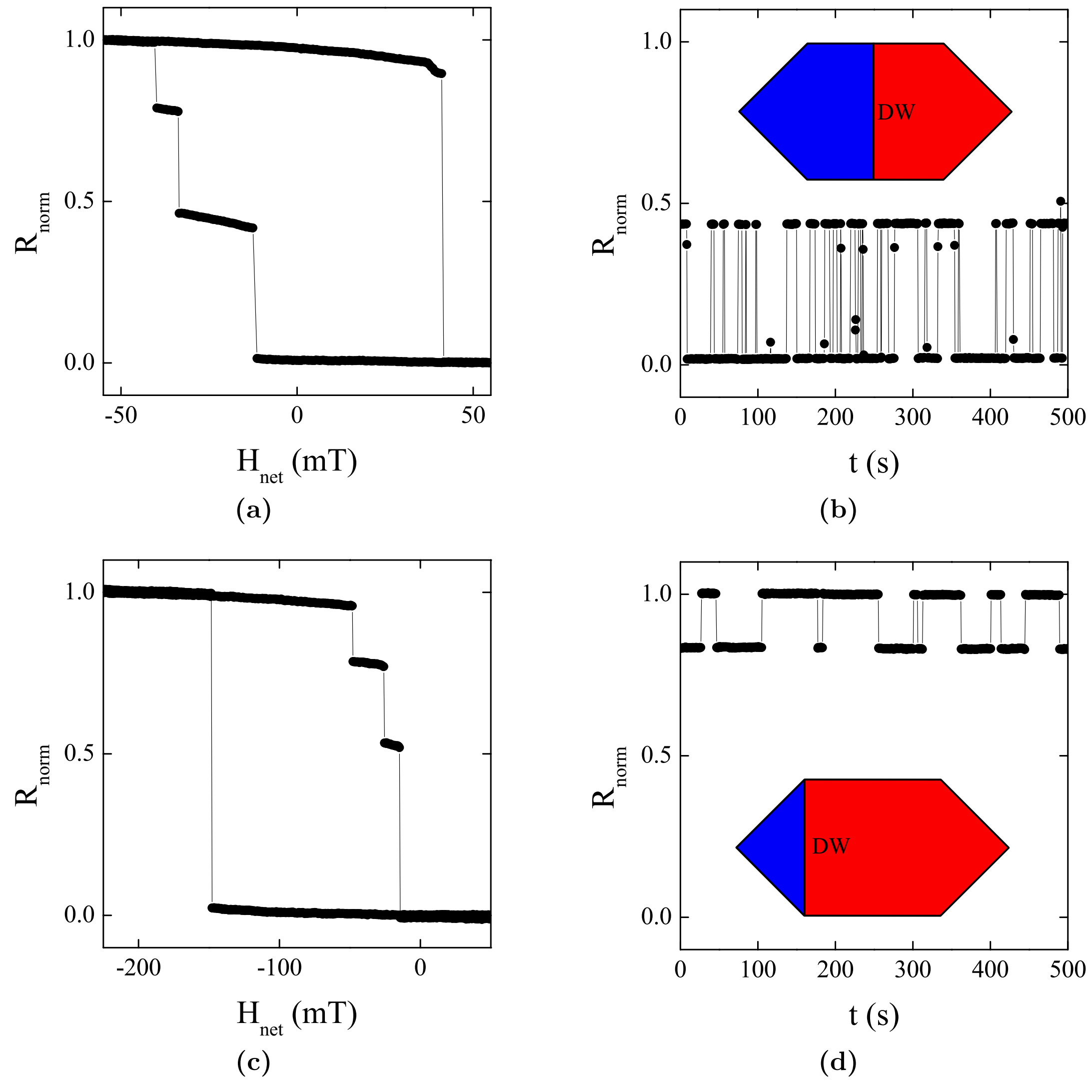

(a) (b)

(c) (d)

Figure 11.2 – (a) Normalized resistance evolution as a function of the applied magnetic field at room temperature and at $I = -4.6$ mA. (b) Telegraph noise recorded at room temperature, at $I = -4.6$ mA and at $H_{\mathrm{net}} = 29$ mT with a schematic top view of a compatible magnetization state for the domain wall state. (c) Normalized resistance evolution as a function of the applied magnetic field at room temperature and at $I = 2.2$ mA. (d) Telegraph noise recorded at room temperature, at $I = 2.2$ mA and at $H_{\mathrm{net}} = -16$ mT with a schematic top view of a compatible magnetization state for the domain wall state. The device is an hexagonal nanopillar spin-valve of 100 nm by 200 nm with a hard layer made of [Co/Pt]/[Co/Ni] and a free layer made of [Co/Ni].

Concerning the depinning of a domain wall from these two types of pinning sites, we can expect a different behavior. For instance, the presence of a domain wall in the middle of the free layer creates a flux closure. This stabilizing effect decreases as soon as the domain wall moves toward the extremities. Moreover, the depinning process of a domain wall pinned in the middle of the free layer is symmetric and should not depend on its direction of propagation after the depinning. On the contrary, a domain wall pinned close to one extremity of the hexagon has two choices. Either to propagate towards this extremity or towards the opposite direction. In the first case, it has to curve to penetrate inside the triangular extremity whereas in the other case the depinning process looks similar to the one of a domain wall pinned in the middle of the free layer. Consequently, the device we measured here gives access to several depinning processes.

11.2 Investigation of the nucleation process

The nucleation process represents the transition from a fully magnetized state to a domain wall state or another fully magnetized state. Indeed a domain has to be nucleated to create a domain wall state. For the device presented before, we will study the parallel to a domain wall state transition for negative currents (see figure 11.2b) and the antiparallel to a domain wall state transition for positive currents (see figure 11.2d).

11.2.1 Magnetic field and nucleation process

Let's look at the impact of the applied magnetic field on the evolution of the life times of the fully magnetized state deduced from the telegraph noise signals (for an explanation of how we extract the life times from the telegraph noise signals see subsection 10.3.3 page 136).

Figure 11.3a and 11.3b represent the evolution of the mean life times extracted from telegraph noise signals measured at room temperature as a function of the applied magnetic field at different injected currents for the parallel state and the antiparallel state of the device described above. The mean life time of the parallel state increases with the applied magnetic field and when the injected current becomes less and less negative. This evolution is perfectly explained by the action of a positive magnetic field and current which stabilizes the parallel state. As a result, its potential well becomes deeper and deeper, the energy barrier to leave it increases as its mean life time. The same phenomenon occurs for the antiparallel state which is stabilized by an applied magnetic field more and more negative and an injected current less and less positive.

With the logarithmic scale, it seems that the evolution of the mean life time is mainly linear with the applied magnetic field (see the guides for the eyes on figures 11.3a and 11.3b). A modification of the injected current results only in a translation of the curve. The evolution remains linear and the slope unchanged. Huge discrepancies appears for the mean life times of the antiparallel state when the applied magnetic field becomes too negative. These discrepancies also increase with the injected current. As we will show it later, the domain wall state involved in the telegraph noise signal with the antiparallel state is about to disappear from the field and current phase diagram for these values of applied magnetic field and of injected current. Since we are looking at transitions between this domain wall state and the antiparallel state, one can imagine that the disappearing of the domain wall state induces a modification of the linear evolution of the mean life time of the antiparallel state.

11.2.2 Spin-transfer and nucleation process

The previous section briefly mentioned the impact of the spin-transfer torque on the nucleation process in the parallel or in the antiparallel states. Now, let's look at it more carefully.

Figure 11.4a and 11.4b represent the evolution of the mean life times extracted from telegraph noise signals measured at room temperature as a function of the injected current at different applied magnetic fields for the parallel state and the antiparallel state of the same device as in the previous section. Their evolutions are still coherent with the fact that a positive magnetic field and current favor the parallel state whereas a negative magnetic field and current favor a antiparallel magnetic state. One can note that the impact of the spin-transfer torque is huge on the mean life time of the parallel state because it is modified by three order of magnitude when the current evolves of only 0.4 mA.

These curves measured independently of the previous ones are also coherent between each other (compare figure 11.3a with figure 11.4a and figure 11.3b with figure 11.4b). Indeed, for the parallel state the mean life time evolution curve with the applied magnetic field is translated downward when the current becomes more and more negative. It seems that the step of this translation is proportional to the injected current. Therefore, one can expect a linear evolution of the mean life of the parallel state with the injected current and a upward translation of this curve when the applied magnetic field increases. This is exactly what we measured.

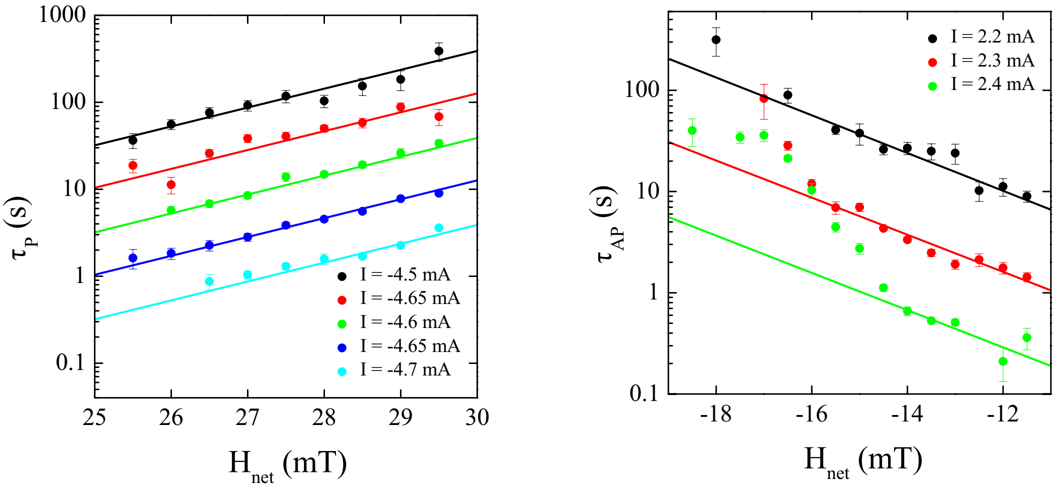

(a) **(b)**

Figure 11.3 – Evolution of the mean life times extracted from telegraph noise signals measured at room temperature as a function of the net applied magnetic field at different injected currents (a) for the parallel state and (b) for the antiparallel state. The lines are guides for the eyes. The device is an hexagonal nanopillar spin-valve of 100 nm by 200 nm with a hard layer made of [Co/Pt]/[Co/Ni] and a free layer made of [Co/Ni].

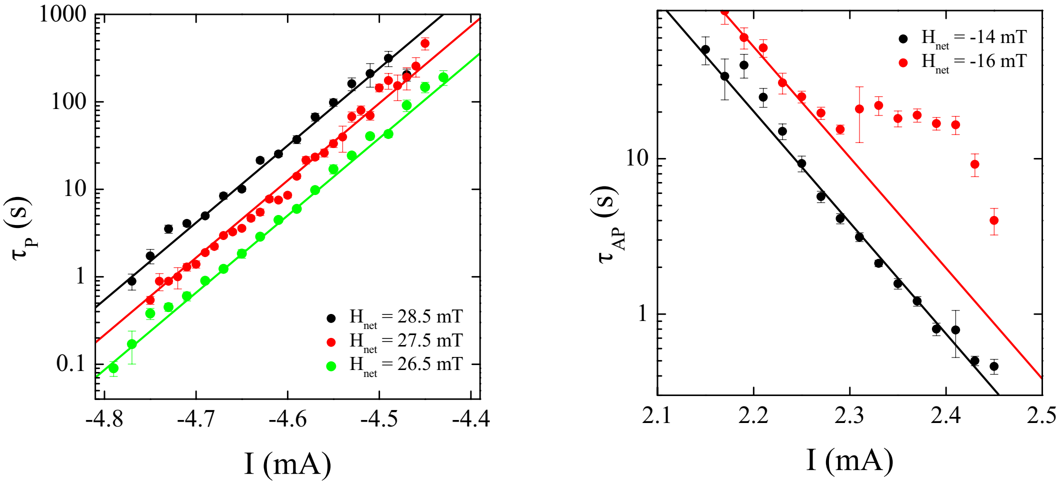

(a) **(b)**

Figure 11.4 – Evolution of the mean life times extracted from telegraph noise signals measured at room temperature as a function of the injected current at different net applied magnetic fields (a) for the parallel state and (b) for the antiparallel state. The lines are guides for the eyes. The device is an hexagonal nanopillar spin-valve of 100 nm by 200 nm with a hard layer made of [Co/Pt]/[Co/Ni] and a free layer made of [Co/Ni].

For the antiparallel state, as long as the disappearing of the domain wall state does not affect the measurements, the injected current translates regularly the mean life time evolution curve with the applied magnetic field. As a result, we can also expect a linear evolution of the mean life time of the antiparallel state with the injected current and a downward translation of this curve when the applied magnetic field decreases. However, the disappearing of the domain wall state modifies this behavior. At $H_{\mathrm{net}} = -14$ mT no impact of this disappearing is expected at least until $I = 2.4$ mA from figure 11.3b. On the contrary, at $H_{\mathrm{net}} = -16$ mT, the evolution of the mean life time as a function of the applied magnetic field shows that no evolution with the current is expected between $I = 2.3$ and 2.4 mA. This is exactly what we observed in figure 11.4b.

11.2.3 Modelization of the experimental results

Ignoring the region where one of the two states of the telegraph noise signal disappears, the measurements of the evolution of mean life times of the fully magnetized states as a function of the applied magnetic field and of the injected current show that they are proportional to these two parameters in logarithmic scale. These results give the following evolution law for the mean life time of a fully magnetized state

$$\tau = \tau_0 \exp\left[\frac{\mathrm{a}I + \mathrm{b}H_{\mathrm{net}} + \mathrm{c}}{k_{\mathrm{B}}T}\right] \tag{11.1}$$

where $\frac{1}{\tau_0}$ is an attempt frequency (see subsection 4.1.2 page 52) and a, b and c three constants. Both theoretical and experimental works demonstrated that when there is no spin-transfer inside a magnetic layer, the energy barrier to cross for the nucleation to occur evolves linearly with the applied magnetic field[110]. This evolution is ruled by the following law $E\left(H_{\mathrm{net}}\right) = 2M_{\mathrm{s}}V_{\mathrm{n}}\left(H_{\mathrm{net}} + H_{\mathrm{n}}\right)$ where V_{n} is the nucleation volume of the magnetic layer and H_{n} its nucleation field. This linear evolution is in agreement with our experimental results. Therefore, the evolution law of the mean life time of a fully magnetized state in our system can be expressed by

$$\tau = \tau_0 \exp\left[\frac{2M_{\mathrm{s}}V_{\mathrm{n}}\left(H_{\mathrm{net}} + H_{\mathrm{n}} + \epsilon I\right)}{k_{\mathrm{B}}T}\right] \tag{11.2}$$

where ϵ can be called the spin-transfer efficiency factor since it gives a conversion factor between the injected current and the applied magnetic field[111].

V_n	1.5×10^{-24} m^3
H_n	20 mT
ϵ	40 T/A

To exploit our experimental curves for the parallel state, we chose a reasonable order of magnitude for the attempt frequency in our system, $\tau_0 = 10^{-10}$ s. This parameter could have been measured from the evolution of the telegraph noise signals with temperature but we never succeeded in performing these experiments. It is moreover not necessary constant and may depend on various experimental factors[74]. However, modifying its value of one order of magnitude does not actually impact the order of magnitude obtained for the parameters deduced from our experimental curves. From magnetic measurements, we also put the value of the saturation magnetization at $M_\mathrm{s} = 6.5 \times 10^5$ A/m. Thanks to these two assumptions, we were able to deduce the other parameters of the evolution law of the life time of a fully magnetized state. They are presented in the table above. The value obtained for the nucleation volume is very satisfying since it represents about 4 % of the volume of the free layer. Supposing that the the nucleation energy $2M_\mathrm{s}V_\mathrm{n}H_\mathrm{n}$ is equal to KV_n the anisotropy energy to overcome to nucleate, we found that the uniaxial anisotropy constant is equal to 2.7×10^5 J.m^{-3}. This value is in agreement with the anisotropy constant expected from magnetic measurements. Finally, the spin torque efficiency factor gives the same order of magnitude as the slope deduced from the linear evolution of the switching current as a function of the applied magnetic field for the parallel to antiparallel transition. All these results confirm that equation 1.12 is indeed the evolution law describing the influence of thermal activation on the nucleation process in our spin-valves with perpendicular magnetizations.

The theoretical expectations presented in subsection 4.2.2 page 54 show that the logarithm of the mean life time should evolve proportionally to the product of the energy barrier evolution as a function of the applied magnetic field with a linear function of the injected current.

$$\tau = \tau_0 \exp\left[\frac{E_\mathrm{b}(H)}{k_\mathrm{B}T}\left(1 - \frac{I}{I_\mathrm{sw}}\right)\right] \tag{11.3}$$

At first sight, this evolution seems quite different from our experimental conclusions. Indeed, from this formula the injected current should not only modified the y-intercepts in logarithmic scale of the mean life time evolution curves as a function of the applied magnetic field but also their slopes. Identifying $\frac{H_\mathrm{n}}{I_\mathrm{sw}}$ with ϵ

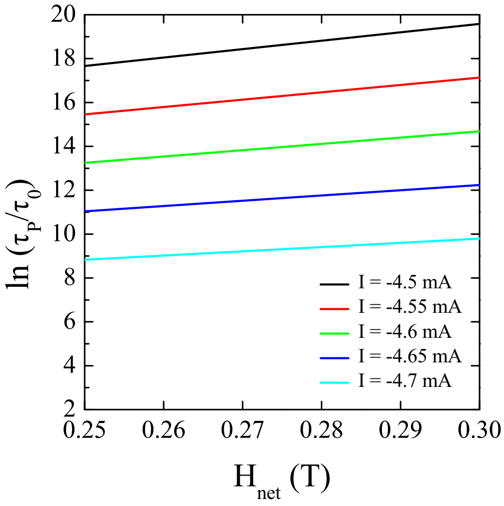

Figure 11.5 – Evolution of the logarithm of the parallel state life time multiplied by the attempt frequency as a function of the net applied magnetic field. This evolution is deduced from equation 11.3 with the parameters calculated thanks to a fitting of the experimental curves.

we find $I_{\mathrm{sw}} = -4.9$ mA. A plot of $\ln \tau$ as a function of the applied magnetic field using equation 11.3, considering $E_{\mathrm{b}}(H) = 2M_{\mathrm{s}}V_{\mathrm{n}}(H_{\mathrm{net}} + H_{\mathrm{n}})$, injecting the values of the parameters deduced from the previous fitting and injecting the values of the injected current of figure 11.3a shows that the modification of the slopes is hardly detectable because of the range of current exploited here contrary to the modification of the y-intercepts (see figure 11.5). Therefore, we have all reasons to believe that our experimental results concerning the nucleation process in nanopillar spin-valves with perpendicular magnetizations is in agreement with the theoretical expectations of the modified Néel-Brown model.

11.3 Investigation of the depinning process

The depinning process represents the transition from a domain wall state to another domain wall state or to a fully magnetized state. Indeed, a domain wall has to be depinned to leave a domain wall state. For the device presented at the beginning of this chapter, we will study the domain wall to parallel state transition at negative current (see figure 11.2b) and the domain wall to antiparallel state transition at positive current (see figure 11.2d).

11.3.1 Case of a domain wall pinned in the middle

Let's focus first on the case of a domain wall state composed of a domain wall pinned in the middle of the free layer probably on an intrinsic defect. Its normalized resistance is around 0.5. The direction of depinning should not affect the process in this case.

Study of the telegraph noise signals

Figure 11.6a presents the evolution of the mean life time of this domain wall state as a function of the applied magnetic field at different injected currents deduced from telegraph noise signals. These different curves mainly show that the applied magnetic field has a linear influence on the mean life time in logarithmic scale. This observation is in agreement with theory[112]. Indeed, when no current is injected through the device the energy barrier to cross to depin the domain wall evolves as $E\left(H_{\mathrm{net}}\right) = 2M_{\mathrm{s}}V_{\mathrm{p}}\left(H_{\mathrm{net}} + H_{\mathrm{p}}\right)$ where V_{p} is a characteristic activation volume of the depinning process and H_{p} the pinning field. Fitting these evolutions, we could estimate the pinning field to be around 40 mT. This value is very close from the ones estimated by other experiments such as for 200 nm wide nanowires made of the similar material[113]. At $I = -4.7$ mA starting from $H_{\mathrm{net}} = 27$ mT, it seems that the evolution of the mean life time deviates from the linear behavior we have just described. This phenomenon may be explained in a similar way as the deviations observed for the mean life time of the antiparallel state in the nucleation process (see subsection 11.2.1 page 143). Indeed, in this case these values of the applied magnetic field and of the injected current correspond to the disappearing of the parallel state from the current and field phase diagram of the sample. This disappearing may induce a deviation from the normal behavior such as a quicker increase of the mean life time of the remaining state that is to say the domain wall state.

The comparison between the mean life time evolution of this domain wall state as a function of the applied magnetic field at different injected current seems to indicate that the spin-transfer torque as virtually no impact on the depinning process of the domain wall. Figure 11.6b presents the evolution of its mean life time as a function of the injected current at different applied magnetic fields deduced from telegraph noise signals. From these curves, it seems indeed that the injected current does not modify the value of the mean life time of the domain wall state at least as long as the injected current does not become too negative. Below $I = -4.65$ mA the mean life time quickly increases surely because we reached the region of the field and current phase diagram where the parallel state

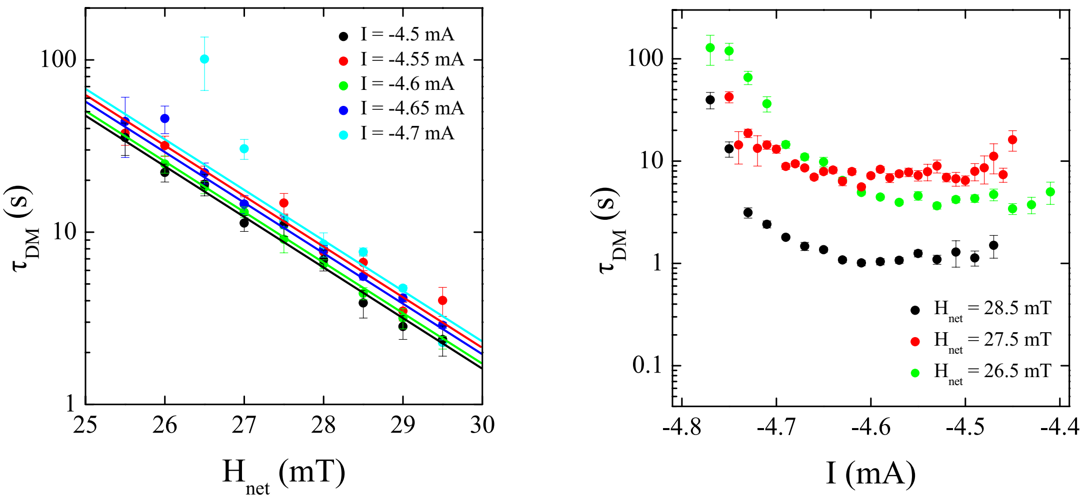

(a) (b)

Figure 11.6 – Evolution of the mean life times extracted from telegraph noise signals measured at room temperature for a domain wall state composed of a domain wall pinned in the middle of the free layer (a) as a function of the applied magnetic field at different injected currents and (b) as a function of the injected current at different applied magnetic fields. The lines are guides for the eyes. The device is an hexagonal nanopillar spin-valve of 100 nm by 200 nm with a hard layer made of [Co/Pt]/[Co/Ni] and a free layer made of [Co/Ni].

disappears. One can notice that these curves are in good agreement with the previous ones of figure 11.6a where the first impact of the disappearing of the parallel state occurs for the curve at $I = -4.7$ mA.

Since this observation of the ineffectiveness of the spin-transfer torque to depinn a domain wall comes from the measurement of telegraph noise signals of a single device, we need others measurements to confirm it. Moreover, because of the nature of the telegraph noise phenomenon the range of applied magnetic fields and of injected currents where it is observed is very limited. To corroborate the analysis coming from the telegraph noise measurements we decided to work on the field and current phase diagram of this kind of domain wall states.

Study of the domain wall state phase diagram

Figure 11.7a presents the field and current domain wall state phase diagram measured on a different device from the one mentioned above for the analysis of the telegraph noise signals but of the same composition and shape. The domain

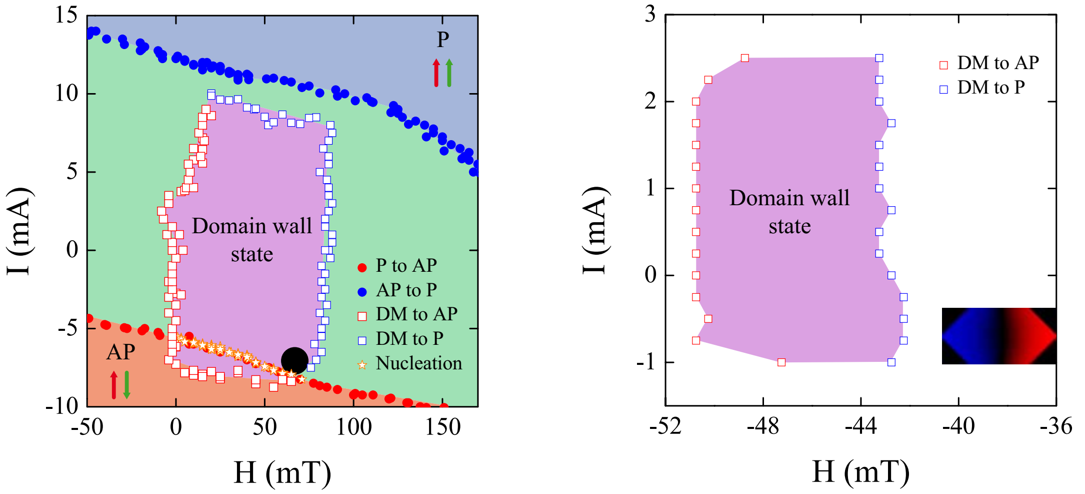

(a) (b)

Figure 11.7 – Field and current phase diagram of a domain wall state composed of a domain wall pinned in the middle obtained (a) from experimental measurements (the device is an hexagonal nanopillar spin-valve of 100 nm by 200 nm with a hard layer made of [Co/Pt]/[Co/Ni] and a free layer made of [Co/Ni]) and (b) from 3D LLG micromagnetic simulations using the Scheinfein code (the domain wall is pinned by a 16 nm side square located in the middle of the free layer and where the anisotropy constant is divided by two).

wall state studied here has a normalized resistance close to 0.5 that is to say that it is composed of a domain wall pinned in the middle of the free layer like the domain wall state studied before. To measure such a phase diagram the first step is to create the domain wall state. Then, by moving the applied magnetic field and the injected current one can detect its disappearing.

On figure 11.7a, the region corresponding to the existence of the domain wall state is colored in purple. Its borders are marked by red opened square when the domain wall state switches to the antiparallel state and by blue opened square when it switches to the parallel state. The orange opened stars are for the nucleation points of the domain wall state. Superposed with the domain wall state phase diagram is the conventional phase diagram of the device with here the regions of existence of the parallel and the antiparallel states and the bistability zone. The black circle put on the domain wall state region represents the approximate location where the telegraph noise signals are recorded if this phase diagram was the one of the device mentioned for the exploitation of the telegraph noise signals. It confirms that in this particular location going to negative fields and to negative currents the parallel state tends to disappear which could explained some deviation of the experimental curves from the conventional behavior.

From this phase diagram, we can observe that the depinning fields of the domain wall weakly depend on the injected current since they correspond to borders nearly vertical. Therefore, it confirms that spin-transfer does not affect the depinning process of a domain wall pinned in the middle of the free layer. To ensure that this experimental domain wall state phase diagram is characteristic of the phase diagram of any domain wall state composed of a domain wall pinned in the middle of the free layer, we used 3D LLG micromagnetic simulations with the Scheinfein code to determine the theoretical phase diagram expected in this case (see appendix E page 183 for a detailed presentation of the parameters used for the simulations presented in this part). Figure 11.7b presents the result of this simulation. It was obtained starting from a magnetic configuration where a domain wall is pinned in the middle of the free layer of an hexagonal nanopillar spin-valve with perpendicular magnetizations by the presence of a 16 nm side square where the anisotropy constant of the layer is divided by a factor two (see the picture in figure 11.7b). Then, like the experimental measurements, the disappearing of the domain wall is analyzed by moving the applied magnetic field and the injected current. The results of this simulation allow two conclusions. First, the experimental phase diagram of the domain wall state composed of a domain wall pinned in the middle of the free layer is characteristic of the phase diagram of such a domain wall state. Second, spin-transfer has indeed no effect on the depinning process of such a domain wall.

11.3.2 Case of a domain wall pinned at the corner

Now, let's focus on the case of a domain wall state composed of a domain wall pinned at the corner of the free layer. Its normalized resistance is around 0.17 or 0.83 depending on which sides the domain wall is pinned. The direction of the depinning is important here since the domain wall can either curve to enter into the corner of the hexagon or propagate in an environment of constant width.

Study of the telegraph noise signals

Figure 11.8a presents the evolution of the mean life time of this domain wall state as a function of the applied magnetic field at different injected currents deduced from telegraph noise signals. These signals consist in two state transitions between the antiparallel state of the devices and a domain wall state of normalized

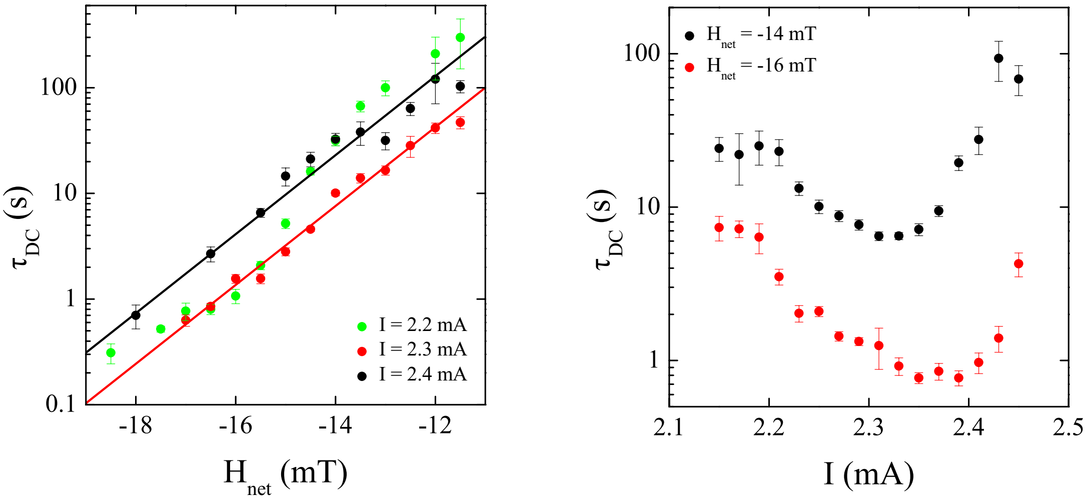

(a) **(b)**

Figure 11.8 – Evolution of the mean life times extracted from telegraph noise signals measured at room temperature for a domain wall state composed of a domain wall pinned at a corner of the free layer (a) as a function of the applied magnetic field at different injected currents and (b) as a function of the injected current at different applied magnetic fields. The lines are guides for the eyes. The device is an hexagonal nanopillar spin-valve of 100 nm by 200 nm with a hard layer made of [Co/Pt]/[Co/Ni] and a free layer made of [Co/Ni].

resistance around 0.17 (see figure 11.2d page 142). Therefore, the domain wall propagates toward the closest extremity of the hexagon after its depinning where its width is non-uniform. The exploitation of the mean life time evolution is less easy than for the previous domain wall state. At $I = 2.2$ mA and $I = 2.3$ mA, it seems that the applied magnetic field has a linear effect on the mean life time in logarithmic scale just as for the domain wall pinned in the middle of the hexagon. However, at $I = 2.4$ mA the evolution is not linear anymore. From the comparison of these curves at different injected currents it seems that the spin-transfer torque has a non negligible impact on the depinning process for this domain wall state.

Figure 11.8b presents the evolution of the mean life time as a function of the injected current at different applied magnetic fields also deduced from telegraph noise signals. These curves confirm that the injected current has a visible and non-linear impact on the depinning process of a domain wall pinned at the corner. We observe a similar evolution for the two curves presented here: first a decrease of the mean life time of the domain wall state and then an increase. It means that the domain wall state is first destabilized and than stabilized by the injected current.

As for the previous domain wall state, the applied magnetic field and injected current ranges of this study are very limited. Moreover, such a strange behavior could come from the particular device we chose for these telegraph noise experiments. As a result, we decided to corroborate these observations by the analysis of this kind of domain wall states phase diagram.

Study of the domain wall state phase diagram

Figure 11.7a presents the field and current domain wall state phase diagram measured on a different device from the one mentioned above for the exploitation of the telegraph noise signals but of the same composition and shape. The domain wall state studied here has a normalized resistance close to 0.83 that is to say that it is composed of a domain wall pinned at the corner of the free layer like the domain wall state studied above. This phase diagram has been measured in a similar way as the previous domain wall state phase diagram presented in this manuscript. It is presented with the same conventions.

This experimental domain wall phase diagram is clearly different from the previous one. The domain wall is nucleated from the antiparallel state. Its propagation is stopped and the domain wall state generated corresponds to a normalized resistance of 0.83 that is to say at 0.17 from the antiparallel state normalized resistance level. As a consequence, to go back to the antiparallel state the domain wall has to penetrate again inside the corner extremity of the free layer whereas to go to the parallel state it has to propagate first through its central square part of constant width similarly to the case where the domain wall is pinned in the middle of the free layer. This observation is very interesting because the right border of the domain wall state region on this phase diagram corresponding to the transition from the domain wall state to the parallel state seems to be weakly dependent of the injected current. This behavior is very close from the domain wall pinned in the middle of the free layer. Indeed, the depinning fields on the right side of the domain wall state phase diagram form a nearly vertical line. On the contrary, the left border of this phase diagram corresponding to the transition from the domain wall state to the antiparallel state exhibits a clear dependence of the depinning fields with the injected current.

This first global analysis of this domain wall state phase diagram corroborates the conclusions deduced from the exploitation of the telegraph noise signals. Indeed, in the case of a depinning process including an initial propagation in a part

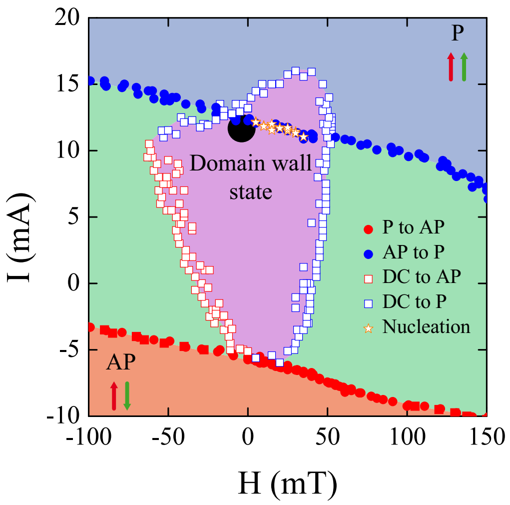

Figure 11.9 – Field and current phase diagram a domain wall state composed of a domain wall pinned at a corner of the free layer obtained from experimental measurements. The device is an hexagonal nanopillar spin-valve of 100 nm by 200 nm with a hard layer made of [Co/Pt]/[Co/Ni] and a free layer made of [Co/Ni].

of the free layer of constant width spin-transfer is ineffective. However, in the case of a depinning process including an initial propagation in a part of the free layer of non-constant width such as a triangular extremity spin-transfer has a visible impact on the stability of the domain wall state.

The black circle on the domain wall state region of the phase diagram represents the approximate location where the telegraph noise signals would be recorded if this phase diagram were the one of the device mentioned for the exploitation of the telegraph noise signals. In this region, the border marked by the blue filled circles represents the disappearing of the potential well of the antiparallel state whereas the border marked by the blue opened squares represents the disappearing of the potential well of the domain wall state. Both of these borders depends on the injected current. So does the telegraph noise signals either looking at the antiparallel state or at the domain wall state. In our case, it seems from the phase diagram of the sample used for the telegraph noise measurements that the region where the telegraph noise signals are recorded is slightly closer from the border marking the disappearing of the antiparallel state potential well than from the border marking the disappearing of the domain wall state. Therefore, the evolution of the mean life time observed on figure 11.8b may be understood as followed. When the current increases, the device gets closer from the two borders mentioned above. So the domain wall state becomes less and less stable. That is why the mean life times start to decrease. However, as the system comes closer to the border marking the disappearing of the antiparallel state one can imagine that it will disturb the normal evolution of the mean life time of the domain wall state just like the huge increase of the mean life times observable on figure 11.6b. This could explained the increase of the mean life times also observed here.

Unfortunately, I did not succeed to simulate with the Scheinfein code such a phase diagram for a domain wall pinned close to an extremity of the free layer to ensure that this experimental phase diagram is characteristic of this kind of domain wall state phase diagram. Nevertheless, we are able to corroborate the telegraph noise experiments performed on one sample with the domain wall state phase diagram measured on another sample of the same kind. So we can be confident that the main conclusion of this section is exact. Spin-transfer has an effect on the depinning process of a domain wall pinned close to an extremity of the free layer if its direction of propagation drives it back to this extremity.

Competition between two processes to leave the domain wall state

A strange phenomenon occurs in the evolution of the probability to remain in the domain wall state as a function of time deduced from the telegraph noise signals when the system is close from the border marking the disappearing of the potential well of the antiparallel state. Indeed, these curves cannot be fitted by single exponentials anymore as if a new process appears on top of the depinning of the domain wall to eliminate the domain wall state. This phenomenon may be also understood from the analysis of the domain wall state phase diagram. Indeed, the classical depinning of the domain wall means to cross the border marked by blue opened square. However, the other border marking the disappearing of the antiparallel state is also close from the region where the nucleation occurs in the free layer. Therefore, one can imagine that the new process appearing when getting close to this region is a second nucleation starting in a similar way as the first one. As a result, a second domain wall propagates toward the first one. They annihilate each other and the domain wall state goes back to the antiparallel state.

This observation is also a confirmation that the experimental domain wall state phase diagram presented above and measured on a first device can be related to the telegraph noise signals measured on another device. The experimental phase diagram presented here really seems to be characteristic of a domain wall state composed of a domain wall pinned at an extremity of the free layer of our hexagonal nanopillar spin-valves with perpendicular magnetizations.

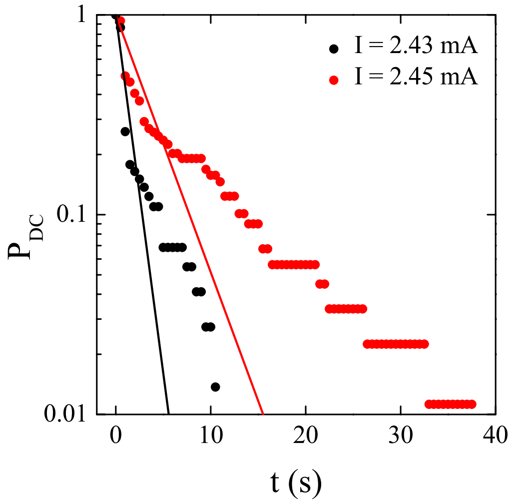

Figure 11.10 – Evolution in logarithmic scale of the probability to remain in the domain wall state composed of a domain wall pinned at a corner of the free layer as a function of time at $H_{\text{net}} = -16$ mT and at two different injected currents $I = 2.43$ mA and $I = 2.45$ mA. These data are extracted from telegraph noise signals. The lines correspond to a fit of these data with the following law $\mathrm{P}_{\mathrm{DC}} = \exp\left(-{}^{t}\!/\!_{\tau}\right)$. The device is an hexagonal nanopillar spin-valve of 100 nm by 200 nm with a hard layer made of [Co/Pt]/[Co/Ni] and a free layer made of [Co/Ni].

11.3.3 Spin-transfer and domain wall structure

The ineffectiveness of the spin-transfer torque to depinn a domain wall seems very striking judging from the important bibliography about current-induced domain wall motion. Nevertheless, one has to remember that in our geometry the current is not injected in the direction of propagation of the domain wall but perpendicularly to it. This is a key difference with the majority of current-induced domain wall motion experiments. Recently, few experimental and theoretical results performed in nanowires with in-plane anisotropy dealt with the problematic of injecting a current perpendicularly to the direction of propagation of a domain wall[114,115]. Each time, the presence of a current flowing perpendicularly to the domain wall increases considerably its velocity sometimes up to 800 m/s at current densities below 10^7 A/cm^2. On the contrary, spin-transfer has mainly no effect on a domain wall in our system where all the current flows perpendicularly to the direction of propagation of the domain wall.

To understand this behavior, we studied the equilibrium magnetization states of a domain wall state obtained from micromagnetic calculations in three different locations of the domain wall state phase diagram corresponding to a domain wall

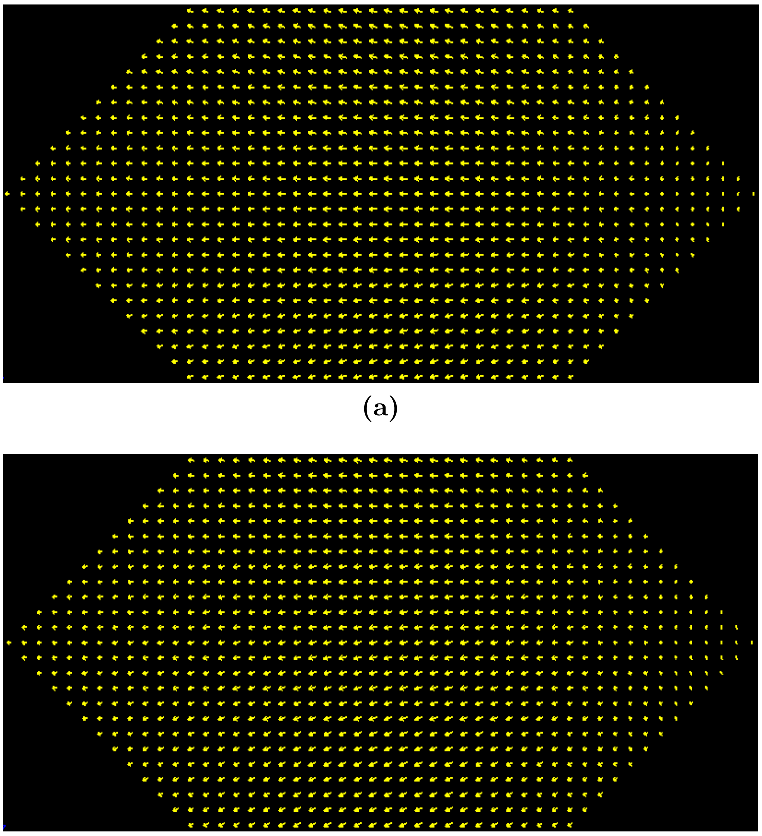

(a)

(b)

Figure 11.11 – Magnetization state of a domain wall state in the free layer of a nanopillar spin-valve with perpendicular magnetizations obtained from micromagnetic simulations (a) for an applied magnetic field $H = -47$ mT and an injected current $I = 0$ mA and (b) for an applied magnetic field $H = -47$ mT and an injected current $I = 1$ mA. The domain wall is pinned by a 16 nm side square located in the middle of the free layer and where the anisotropy constant is divided by two.

pinned in the middle of the free layer (see figure 11.7b). Figure 11.11a presents the magnetization state of this domain wall state in the middle of its phase diagram at $H = -47$ mT when no current is injected trough the spin-valve. This is a Néel wall. This structure may be consistent with the value of the anisotropy constant and of the saturation magnetization chosen for this simulation. Indeed, the quality factor $Q = \frac{2K}{\mu_0 M_s^2}$ is slightly inferior to one ($Q = 0.98$) which means that a Néel wall could be cheaper in energy than a Bloch wall. The value of this quality factor also shows that the domain wall may be close from a transition from a Néel to a Bloch wall.

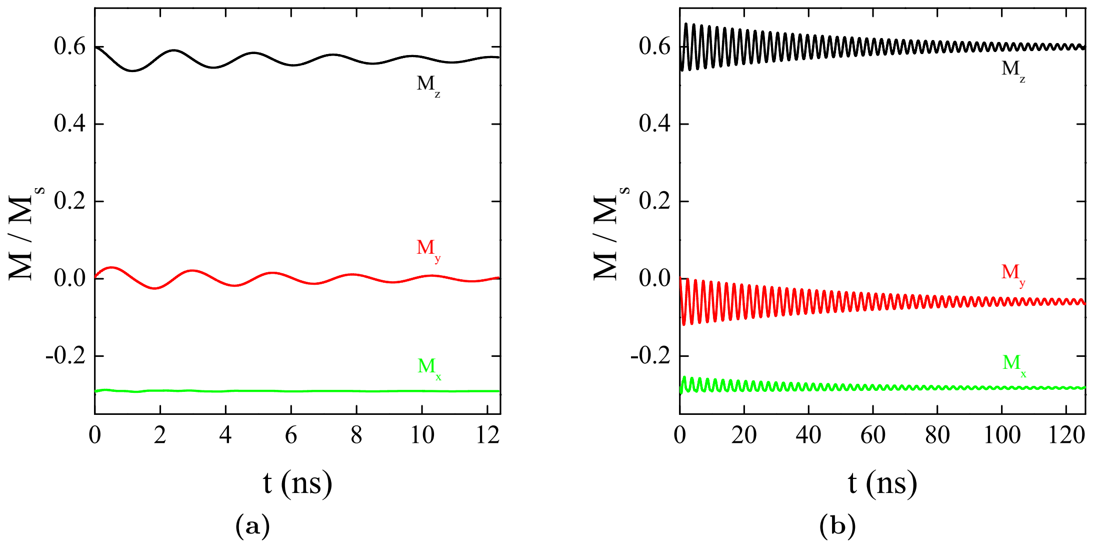

Figure 11.12 – Evolution toward the equilibrium of a domain wall state in the free layer of a nanopillar spin-valve with perpendicular magnetizations as a function of time obtained from micromagnetic simulations starting from the equilibrium state at $H = -47$ mT and at $I = 0$ mA (a) for an applied magnetic field $H = -49$ mT and an injected current $I = 0$ mA and (b) for an applied magnetic field $H = -47$ mT and an injected current $I = -1$ mA. The domain wall is pinned by a 16 nm side square located in the middle of the free layer and where the anisotropy constant is divided by two.

Figure 11.12 presents the evolution toward the equilibrium of a domain wall state in the free layer of a nanopillar spin-valve with perpendicular magnetizations. The domain wall is pinned in the middle of the free layer by a 16 nm side square where the anisotropy constant is divided by two. The initial magnetization state corresponds to the equilibrium state of this domain wall state at $H = -47$ mT when no current is injected trough the spin-valve (see figure 11.11a). In this magnetization state we have $m_{\mathrm{x}} = -0.3$, $m_{\mathrm{y}} = 0$ and $m_{\mathrm{z}} = 0.6$. In a first case, there is still no current flowing through the spin-valve but the applied magnetic field is set to $H = -49$ mT (see figure 11.12a). The magnetization starts to oscillate around its new equilibrium position. The magnetization state in this new equilibrium state is similar to the initial one since m_{x} and m_{y} oscillate around their initial values. The domain wall still is a Néel wall. However, m_{z} oscillates around a lower value than its initial one. It means that the domain wall moved so that the spin-valves get closer from the antiparallel state. In a second case, the applied magnetic field remains at its initial value $H = -47$ mT but a current is injected with $I = -1$ mA (see figure 11.12b). Again, the magnetization starts to oscillate around its new equilibrium position. Contrary to the previous case, the domain wall did not move since m_z oscillates around its initial value. However, both m_x and mostly m_y oscillates around different values than their initial ones. It means that spin-transfer did not move the domain wall but rather changed its structure. Figure 11.11b presents a view of this new equilibrium state where it is visible that the magnetic moments inside the wall rotated compared to the equilibrium state at zero current (see figure 11.11a).

Therefore, these simulations seems to indicate that, in our geometry where the current is injected perpendicularly to the domain wall direction of propagation with a perpendicular polarization, the spin-transfer torque is not able to move a Néel wall. It may have first to modify its magnetic structure before being able to affect its depinning. This could explain the behavior of the spin-transfer torque on the domain wall state composed of a domain wall pinned in the middle of the free layer. Besides, these micromagnetic simulations show that when a Néel wall propagates toward a triangular extremity of the hexagon, its structure changes as soon as it penetrates inside this extremity. It is not a Néel wall anymore. This could explain why the spin polarized current affects the depinning of the domain wall pinned close to one extremity of the free layer only if this one propagates after its depinning toward this extremity. Of course, further investigations are required to ensure this explanation. One has to understand for instance why the spin-transfer torque modifies the domain wall structure or why this modification does not affect the depinning fields.

Conclusion

This thesis focuses on the study of spin-transfer effects in nanopillar spin-valves with perpendicular magnetizations.

The first approach of this thesis is a global approach based on the understanding of the field and current phase diagrams of our devices.

These phase diagrams are convenient to sum up in one figure the overall behavior of a spin-valve depending on the applied magnetic field and on the injected current. We measured experimentally phase diagrams for various samples and common features appeared. They can be divided into four different regions, three marking the presence of static magnetic states (the parallel state alone, the antiparallel state alone and in between a bistability region where either the parallel or the antiparallel states can be observable) and a last one marking the presence of dynamic states. The borders between the bistability region and the ones corresponding to the parallel and to the antiparallel states alone are also characteristic. Close to the zero injected current switching field, there is a current range marked by critical currents where the spin-transfer torque does not modify the switching field value. Outside this range, the switching field evolves linearly with the injected current.

Using a macrospin and uniaxial model of our system we determined the theoretical phase diagram expected for a nanopillar spin-valve with perpendicular magnetizations. It predicts only a linear evolution of the switching fields with the injected current. Based on experimental observations, we determined that the key parameter to explain the apparition of a region where the spin-transfer torque is ineffective is non-uniaxial contributions in the magnetic energy of the system. They can arise from extrinsic phenomena such as a non-uniaxial applied magnetic field or from intrinsic phenomena such as a tilted anisotropy axis due to the structure of the magnetic layers. Thanks to some approximations, we were able to determined analytically the theoretical phase diagram of our devices in the first case considered above, a tilted applied magnetic field. The linear evolution predicted by the uniaxial model is broken by a region where the switching fields remain constant at its value when no current is injected through the structure. This simple but efficient approach confirms that the apparition of the critical currents in the experimental phase diagram originates from at least one non-uniaxial contribution in the magnetic energy of our devices.

Nevertheless, even knowing that the critical currents arise from a breaking of the uniaxial symmetry of the system, it does not explain totally this counter-intuitive behavior. Indeed, considering at first sight the theory of spin-transfer torque, it should always affect the switching fields. To get a clear vision of the action of the spin-transfer torque in our devices, we developed an energetic interpretation of the action of all the torques acting on the magnetization of the free layer of our spin-valves. These torques are actually the ones present in the equation describing the magnetization dynamics. This description uses the analysis of the evolution of the magnetic energy of the system combined with the calculation of the evolution the total power it received from all these torques. It allows to determine for each field and current value the stable and static magnetic configuration of the spin-valve. This approach not only reproduces nicely the experimental results but also points out the physical origin of the critical currents: when no current is injected through the system, as soon as a non-uniaxial contribution appears in the magnetic energy, it will always dissipates energy whatever is the applied magnetic field because the effective field does not vanish. On the contrary, in a uniaxial system there is no energy dissipation at the switching field when no current is injected through it. Therefore, in the non-uniaxial case the power brought by the spin-transfer torque has to overcome the energy dissipation naturally present in the system at the switching field and at zero current before affecting its reversal.

The second approach of this thesis takes advantage of the presence of unique pinned domain walls inside the free layer of our spin-valve to study the impact of the applied magnetic field and of the spin-transfer torque on these magnetic configurations. We interested particularly to their nucleation and their domain wall depinning processes.

Various experimental works showed that the reversal of the free layer magnetization of a spin-valve with perpendicular anisotropies occurs by the nucleation and the propagation of a domain wall. In our devices, this domain wall can sometimes be pinned on some intrinsic or extrinsic defects of the free layer resulting in the observation of domain wall states in the hysteresis loops measured experimentally. Thanks to thermal activation, we observed two state fluctuations in our devices, a phenomenon called telegraph noise and observed in lots of systems in physics. It arises from the thermally activated back and forth crossing of the energy barrier separating two different magnetic configurations of the free layer. We explained how we can exploit these temporal signals to study the evolution of the mean life time of different magnetic states of the device.

Using telegraph noise signals implying both fully magnetized states and domain wall states combined with experimental measurements of domain wall states phase diagrams and micromagnetic simulations we studied the impact of the applied magnetic field and of the spin-transfer torque on the nucleation and on the domain wall depinning processes in our nanopillar spin-valve with perpendicular magnetizations. Thanks to the telegraph noise signals, we demonstrated that their nucleation process is perfectly described by the theoretical modified Néel-Brown model. We even estimated reasonable order of magnitudes for the values of the nucleation fields, of the pinning fields and of the nucleation volume of our samples. On the contrary, the domain wall depinning process is more complicate to understand. We explained that our hexagonal devices exhibit two different domain wall states that we were able to study. The first one consisted in a domain wall pinned close from the middle of the free layer. The analysis of the telegraph noise signals shows that the applied magnetic field has an impact expected by the theory on the depinning process of this domain wall whereas spin-transfer is inefficient to affect it. We corroborated these conclusions thanks to the measurement of this domain wall state phase diagram and micromagnetic simulations. The second domain wall state consisted in a domain wall pinned close from an extremity of the free layer. The telegraph noise signals showed that spin-transfer has an effect on the depinning process of this domain wall when it is depinned in the direction of this extremity. We corroborated this behavior thanks to the measurement of this domain wall state phase diagram. It also showed that spin-transfer is inefficient to depin this domain wall in the opposite direction. These conclusions about the impact of spin-transfer on the domain wall depinning process inside our spin-valves with perpendicular magnetizations could be explained by the structure of the domain wall. Indeed, it seems from the micromagnetic simulations that spin-transfer cannot move a Néel wall in our specific geometry where the current is injected perpendicularly to the direction of propagation of the domain wall with a perpendicular polarization.

French conclusion

Conclusion

Cette thèse se concentre sur l'étude des effets de transfert de spin dans des nanopiliers aux aimantations perpendiculaires.

La première approche de cette thèse consiste à comprendre le comportement général de nos dispositifs grâce à l'étude de leur diagramme de phase courant-champ.

Un diagramme de phase est une figure très utile résumant le comportement en champ et un courant d'une vanne de spin. En mesurant les diagrammes de phase de plusieurs échantillons nous avons remarqué des points communs. Tout d'abord, ces figures divisent le plan champ courant en quatre régions distinctes : trois marquant la présence de configurations magnétiques statiques (état d'aimantations parallèles, état d'aimantations antiparallèles et état bistable ou les deux configurations précédentes sont disponibles) et une dernière région d'états dynamiques. Ensuite, l'allure des frontières entre ces régions sont également caractéristiques. Près du champ de renversement à zéro courant, le transfert de spin ne modifie pas la valeur des champs de renversements pour une certaine gamme de courant marquée par des courants critiques. En dehors de ces courants critiques, les champs de renversement évoluent linéairement avec le courant injecté.

A partir d'un modèle macrospin et uniaxiale de nos systèmes, nous avons déterminé le diagramme de phase théorique attendu pour un nanopilier aux aimantations perpendiculaires. Ce modèle prédit uniquement une évolution linéaire des champs de renversement avec le courant injecté. Grâce à des mesures expérimentales, nous avons déterminé le paramètre clé à l'origine de la différence de comportement entre les diagrammes de phase expérimentaux et ce diagramme théorique. Il s'agit de l'uniaxialité du système. Toutes contributions non-uniaxiales semblent, en effet, augmenter la gamme de courant sur laquelle le transfert de spin n'affecte pas le renversement de la couche libre. En considérant un champ magnétique appliqué en dehors de la direction perpendiculaire, nous avons pu déterminer analytiquement le nouveau diagramme de phase théorique dans le cadre d'un modèle non-uniaxiale. Dans ce cas, l'évolution linéaire des champs de renversement avec le courant injecté est brisée sur une gamme de courant où le transfert de spin n'agit plus sur le retournement de l'aimantation. Cette simple approche nous a permis de confirmer que l'origine des courants critiques est liée à la non-uniaxialité de nos vannes de spin.

Néanmoins, notre précédent modèle ne permet pas de remonter à l'origine physique de ce comportement contre intuitif. En effet, la théorie du transfert de spin amène à penser que le courant injecté devrait toujours affecter la valeur des champs de renversement. Afin de clarifier l'action du couple de transfert de spin sur nos systèmes, nous avons développé une interprétation purement énergétique du retournement de l'aimantation. Cette description combine l'analyse de l'énergie magnétique du système avec le calcul de la puissance totale qu'il reçoit de la part des différents couples présents dans son équation d'évolution. Cette méthode reproduit non seulement nos résultats expérimentaux mais pointe aussi l'origine physique des courants critiques : quand aucun courant est injecté dans la vanne de spin, dès qu'une contribution non-uniaxiale apparaît dans l'énergie magnétique alors le système dissipera toujours de l'énergie quelque soit la valeur du champ magnétique appliqué. Cela s'explique par le fait que dans un système non-uniaxiale, le champ effectif ne s'annule jamais. Au contraire, au champ de renversement à zéro courant, une vanne de spin ne dissipe aucune énergie dans un cas uniaxiale. Par conséquent, dans le cas non-uniaxiale, le transfert de spin doit surpasser la dissipation naturellement présente dans la vanne de spin au champ de renversement à courant nul afin d'affecter le retournement de l'aimantation.

La seconde approche de cette thèse se sert de la présence de parois de domaine unique à l'intérieur de la couche libre de nos vannes de spin afin d'étudier l'impact du champ magnétique et du transfert de spin sur ces configurations magnétiques. Nous nous sommes particulièrement intéressé aux processus de nucléation et de propagation de paroi.

Plusieurs travaux expérimentaux précédant cette thèse ont montré que le renversement de l'aimantation de la couche libre d'une vanne de spin aux aimantations perpendiculaires commence par la nucléation d'un domaine d'aimantation opposée et se poursuit par la propagation d'une paroi de domaine. Dans nos systèmes, cette paroi de domaine peut parfois se piéger sur des défauts d'origine intrinsèque ou extrinsèque répartis aléatoirement dans toute la couche libre. Ce phénomène s'observe dans la mesure magnétorésistive des cycles d'hystérésis par la présence d'états de résistance intermédiaire appelés états de paroi. Du fait de l'activation thermique, nous avons observé des signaux de bruit télégraphique correspondant à des allers-retours stochastiques de la vanne de spin entre différentes configurations magnétiques. Nous nous sommes servis de ces signaux pour déterminer les temps de vie moyens des états magnétiques impliqués dans le bruit télégraphique et étudier leur évolution avec le champ magnétique appliqué et le courant injecté.

A partir de signaux de bruit télégraphique entre des états d'aimantation uniforme et des états de paroi, de mesures expérimentales des diagrammes de phase de ces états de paroi et de simulations micromagnétiques, nous avons étudié l'impact du champ magnétique et du courant injecté sur les processus de nucléation et de dépiégeage de paroi dans nos nanopiliers aux aimantations perpendiculaires. Grâce au bruit télégraphique, nous avons démontré que le processus de nucléation est parfaitement décrit par le modèle théorique de Néel-Brown modifié pour prendre en compte le transfert de spin. Nous avons également estimé à partir de ce modèle des ordres de grandeur raisonnables pour certains paramètres physiques liés à la nucléation. En revanche, le processus de dépiégeage est plus complexe à décrire. Grâce à nos dispositifs de forme hexagonale, nous avons étudié deux états de paroi distincts. Le premier se compose d'une paroi de domaine piégée au milieu de la couche libre. L'analyse des signaux de bruit télégraphique montre que le champ magnétique affecte le dépiégeage de la manière attendue par les théories déjà connues alors que le transfert de spin reste complètement inefficace. Ces conclusions sont corroborées par la mesure du diagramme de phase de ces états de paroi et par la simulation micromagnétique de ce même diagramme de phase. Le second état de paroi que nous avons étudié consiste en une paroi piégée à proximité d'un rétrécissement triangulaire de l'hexagone composant la couche libre. Le bruit télégraphique indique que le transfert de spin affecte le dépiégeage de la paroi si celle-ci se propage ensuite dans la direction de ce même rétrécissement triangulaire. Ce phénomène est également confirmé par la mesure du diagramme de phase de cet état de paroi. Elle montre aussi que le transfert de spin n'a aucun effet sur le dépiégeage de cette paroi si elle se déplace dans la direction opposée c'est à dire dans la partie à largeur constante de la couche libre. Ces observations peuvent peut-être s'expliquer par la structure des parois de domaine impliquées dans ces états de parois. En effet, il s'agit en général d'une paroi de Néel d'après les simulations micromagnétiques. Il semble, toujours d'après ces simulations, que le transfert de spin ne peut pas déplacer ce type de paroi dans notre géométrie où le courant est injecté perpendiculairement à la direction de propagation de la paroi avec une polarization perpendiculaire.

Appendices

Appendix A

Calculation of spin-transfer torque

A.1 Calculation of the wave functions

The incident part of the electron wave function propagates in the non magnetic material in the positive z direction so that its propagation term is $\exp(\mathrm{i}kz)$. The wave function is consequently represented by the wave function

$$\boldsymbol{\varphi}_{\mathbf{in}} = \frac{\exp\left(\mathrm{i}kz\right)}{\sqrt{\Omega}} \left(a_{\mathrm{in}} \left|\uparrow\right\rangle + b_{\mathrm{in}} \left|\downarrow\right\rangle\right)$$

with Ω a normalization volume and $(k, a_{\mathrm{in}}, b_{\mathrm{in}}) \in \mathbb{R}^3$ because $E > V_\downarrow > V_\uparrow$ (see figure 3.2 page 41). Moreover, the projections of the wave function on the spin up and spin down states are determined by the orientation of the electron spin polarization respectively to the quantization axis z. Indeed, the mean value of the spin polarization along the z (resp. x) axis is $\cos\theta$ (resp. $\sin\theta$). Therefore $\Omega \left\langle \boldsymbol{\varphi}_{\mathbf{in}} \middle| \boldsymbol{\sigma}_{\mathbf{z}} \middle| \boldsymbol{\varphi}_{\mathbf{in}} \right\rangle = \cos\theta$ and $\Omega \left\langle \boldsymbol{\varphi}_{\mathbf{in}} \middle| \boldsymbol{\sigma}_{\mathbf{x}} \middle| \boldsymbol{\varphi}_{\mathbf{in}} \right\rangle = \sin\theta$ with

$$\Omega \left\langle \boldsymbol{\varphi}_{\mathbf{in}} \middle| \boldsymbol{\sigma}_{\mathbf{z}} \middle| \boldsymbol{\varphi}_{\mathbf{in}} \right\rangle = \Omega \frac{\exp\left(-\mathrm{i}kz\right)}{\sqrt{\Omega}} \begin{pmatrix} a_{\mathrm{in}} & b_{\mathrm{in}} \end{pmatrix} \begin{pmatrix} 1 & 0 \\ 0 & -1 \end{pmatrix} \frac{\exp\left(\mathrm{i}kz\right)}{\sqrt{\Omega}} \begin{pmatrix} a_{\mathrm{in}} \\ b_{\mathrm{in}} \end{pmatrix} = a_{\mathrm{in}}^2 - b_{\mathrm{in}}^2$$

$$\Omega \left\langle \boldsymbol{\varphi}_{\mathbf{in}} \middle| \boldsymbol{\sigma}_{\mathbf{x}} \middle| \boldsymbol{\varphi}_{\mathbf{in}} \right\rangle = \Omega \frac{\exp\left(-\mathrm{i}kz\right)}{\sqrt{\Omega}} \begin{pmatrix} a_{\mathrm{in}} & b_{\mathrm{in}} \end{pmatrix} \begin{pmatrix} 0 & 1 \\ 1 & 0 \end{pmatrix} \frac{\exp\left(\mathrm{i}kz\right)}{\sqrt{\Omega}} \begin{pmatrix} a_{\mathrm{in}} \\ b_{\mathrm{in}} \end{pmatrix} = 2a_{\mathrm{in}}b_{\mathrm{in}}$$

The satisfaction of these spin polarization conditions gives the system

$$\begin{cases} a_{\text{in}}^2 - b_{\text{in}}^2 = \cos\theta \\ 2a_{\text{in}}b_{\text{in}} = \sin\theta \end{cases}$$

which solutions are $a_{\text{in}} = \cos\frac{\theta}{2}$ and $b_{\text{in}} = \sin\frac{\theta}{2}$. The incident part of the wave function consequently is

$$\boldsymbol{\varphi}_{\mathbf{in}} = \frac{\exp(\mathrm{i}kz)}{\sqrt{\Omega}}\left(\cos\frac{\theta}{2}\left|\uparrow\right\rangle + \sin\frac{\theta}{2}\left|\downarrow\right\rangle\right) \tag{A.1}$$

The reflected wave function propagates in the non magnetic material in the negative z direction so that its propagation term is $\exp(-\mathrm{i}kz)$. On the contrary, the transmitted wave function propagates in the ferromagnet in the positive direction so it is composed of two propagation terms $\exp(\mathrm{i}k_\uparrow z)$ and $\exp(\mathrm{i}k_\downarrow z)$, one for each spin state. The reflected and the transmitted wave functions are consequently represented respectively by

$$\begin{aligned} \boldsymbol{\varphi}_{\mathbf{re}} &= \frac{\exp(-\mathrm{i}kz)}{\sqrt{\Omega}}\left(a_{\text{re}}\left|\uparrow\right\rangle + b_{\text{re}}\left|\downarrow\right\rangle\right) \\ \boldsymbol{\varphi}_{\mathbf{tr}} &= \frac{\exp(\mathrm{i}k_\uparrow z)}{\sqrt{\Omega}}a_{\text{tr}}\left|\uparrow\right\rangle + \frac{\exp(\mathrm{i}k_\downarrow z)}{\sqrt{\Omega}}b_{\text{tr}}\left|\downarrow\right\rangle \end{aligned}$$

The continuity of the wave function and of its derivative at the interface with the ferromagnet at $z = 0$, that is to say $\boldsymbol{\varphi}_{\mathbf{in}}(0) + \boldsymbol{\varphi}_{\mathbf{re}}(0) = \boldsymbol{\varphi}_{\mathbf{tr}}(0)$ and $\frac{d\boldsymbol{\varphi}_{\mathbf{in}}}{dz}(0) + \frac{d\boldsymbol{\varphi}_{\mathbf{re}}}{dz}(0) = \frac{d\boldsymbol{\varphi}_{\mathbf{tr}}}{dz}(0)$, leads to two systems, one for each spin state, of two equations

$$\begin{cases} \cos\frac{\theta}{2} + a_{\text{re}} = a_{\text{tr}} \\ k\left(\cos\frac{\theta}{2} - a_{\text{re}}\right) = k_\uparrow a_{\text{tr}} \end{cases} \qquad \begin{cases} \sin\frac{\theta}{2} + b_{\text{re}} = b_{\text{tr}} \\ k\left(\sin\frac{\theta}{2} - b_{\text{re}}\right) = k_\downarrow b_{\text{tr}} \end{cases}$$

Solving these two systems gives the solutions $a_{\text{re}} = \frac{k-k_\uparrow}{k+k_\uparrow}\cos\frac{\theta}{2}$, $b_{\text{re}} = \frac{k-k_\downarrow}{k+k_\downarrow}\sin\frac{\theta}{2}$, $a_{\text{tr}} = \frac{2k}{k+k_\uparrow}\cos\frac{\theta}{2}$ and $b_{\text{tr}} = \frac{2k}{k+k_\downarrow}\sin\frac{\theta}{2}$. With the hypothesis $k_\uparrow = k$, the solutions corresponding to the spin up state can be simplified into $a_{\text{re}} = 0$ and $a_{\text{tr}} = \cos\frac{\theta}{2}$. Finally, the reflected and the transmitted part of the wave function are

$$\boldsymbol{\varphi}_{\mathbf{re}} = \frac{\exp(-\mathrm{i}kz)}{\sqrt{\Omega}}\frac{k-k_\downarrow}{k+k_\downarrow}\sin\frac{\theta}{2}\left|\downarrow\right\rangle \tag{A.2}$$

$$\boldsymbol{\varphi}_{\mathbf{tr}} = \frac{\exp(\mathrm{i}k_\uparrow z)}{\sqrt{\Omega}}\cos\frac{\theta}{2}\left|\uparrow\right\rangle + \frac{\exp(\mathrm{i}k_\downarrow z)}{\sqrt{\Omega}}\frac{2k}{k+k_\downarrow}\sin\frac{\theta}{2}\left|\downarrow\right\rangle \tag{A.3}$$

A.2 Calculation of the spin current densities

In the model presented here, the current flow is unidirectional. As a result, the second order tensor of the spin current density reduces to a vector noted $\boldsymbol{j}_\mathbf{s} = (j_\mathrm{s}^\mathrm{zx}, j_\mathrm{s}^\mathrm{zy}, j_\mathrm{s}^\mathrm{zz})$ where j_s^zi with $\mathrm{i} \in \{\mathrm{x}, \mathrm{y}, \mathrm{z}\}$ is the spin current density of spins along the i axis flowing along the z direction. It corresponds to the column with the z component of the velocity of the matrix of spin current density.

Let's consider the spin current density generated by a single electronic wave function given by

$$\boldsymbol{\varphi} = \frac{1}{\sqrt{\Omega}} \left[\exp\left(\mathrm{i}\kappa z\right) a \left|\uparrow\right\rangle + \exp\left(\mathrm{i}\kappa' z\right) b \left|\downarrow\right\rangle\right] \tag{A.4}$$

where $(\kappa, \kappa', a, b) \in \mathbb{R}^4$ for the same reasons as before. Thanks to equation 3.2, the component j_s^zi with $\mathrm{i} \in \{\mathrm{x}, \mathrm{y}, \mathrm{z}\}$ of the spin current density vector is defined as $\frac{\hbar^2}{2m}\Im[\langle\boldsymbol{\varphi}|\boldsymbol{\sigma}_\mathbf{i}|{}^{d\boldsymbol{\varphi}}/_{dz}\rangle]$. So,

$$\begin{aligned}
j_\mathrm{s}^\mathrm{zx} &= \frac{\hbar^2}{2m}\Im\left[\left\langle \boldsymbol{\varphi} \middle| \boldsymbol{\sigma}_\mathbf{x} \middle| \frac{d\boldsymbol{\varphi}}{dz} \right\rangle\right] \\
&= \frac{\hbar^2}{2m}\Im\left[\frac{1}{\sqrt{\Omega}}\begin{pmatrix} a\exp\left(-\mathrm{i}\kappa z\right) & b\exp\left(-\mathrm{i}\kappa' z\right)\end{pmatrix}\begin{pmatrix} 0 & 1 \\ 1 & 0 \end{pmatrix}\frac{1}{\sqrt{\Omega}}\begin{pmatrix} \mathrm{i}a\kappa\exp\left(\mathrm{i}\kappa z\right) \\ \mathrm{i}b\kappa'\exp\left(\mathrm{i}\kappa' z\right)\end{pmatrix}\right] \\
&= \frac{\hbar^2 ab}{2m\Omega}\left(\kappa + \kappa'\right)\cos\left[\left(\kappa - \kappa'\right) z\right]
\end{aligned}$$

$$\begin{aligned}
j_\mathrm{s}^\mathrm{zy} &= \frac{\hbar^2}{2m}\Im\left[\left\langle \boldsymbol{\varphi} \middle| \boldsymbol{\sigma}_\mathbf{y} \middle| \frac{d\boldsymbol{\varphi}}{dz} \right\rangle\right] \\
&= \frac{\hbar^2}{2m}\Im\left[\frac{1}{\sqrt{\Omega}}\begin{pmatrix} a\exp\left(-\mathrm{i}\kappa z\right) & b\exp\left(-\mathrm{i}\kappa' z\right)\end{pmatrix}\begin{pmatrix} 0 & \mathrm{i} \\ -\mathrm{i} & 0 \end{pmatrix}\frac{1}{\sqrt{\Omega}}\begin{pmatrix} \mathrm{i}a\kappa\exp\left(\mathrm{i}\kappa z\right) \\ \mathrm{i}b\kappa'\exp\left(\mathrm{i}\kappa' z\right)\end{pmatrix}\right] \\
&= \frac{\hbar^2 ab}{2m\Omega}\left(\kappa + \kappa'\right)\sin\left[\left(\kappa - \kappa'\right) z\right]
\end{aligned}$$

$$\begin{aligned}
j_\mathrm{s}^\mathrm{zz} &= \frac{\hbar^2}{2m}\Im\left[\left\langle \boldsymbol{\varphi} \middle| \boldsymbol{\sigma}_\mathbf{z} \middle| \frac{d\boldsymbol{\varphi}}{dz} \right\rangle\right] \\
&= \frac{\hbar^2}{2m}\Im\left[\frac{1}{\sqrt{\Omega}}\begin{pmatrix} a\exp\left(-\mathrm{i}\kappa z\right) & b\exp\left(-\mathrm{i}\kappa' z\right)\end{pmatrix}\begin{pmatrix} 1 & 0 \\ 0 & -1 \end{pmatrix}\frac{1}{\sqrt{\Omega}}\begin{pmatrix} \mathrm{i}a\kappa\exp\left(\mathrm{i}\kappa z\right) \\ \mathrm{i}b\kappa'\exp\left(\mathrm{i}\kappa' z\right)\end{pmatrix}\right] \\
&= \frac{\hbar^2}{2m\Omega}\left(\kappa a^2 - \kappa' b^2\right)
\end{aligned}$$

To sum up these results, the spin current density generated by a wave function of the form given by equation A.4 is

$$\boldsymbol{j}_{\mathbf{s}} = \frac{\hbar^2}{2m\Omega} \begin{pmatrix} ab\left(\kappa+\kappa'\right)\cos\left[\left(\kappa-\kappa'\right)z\right] \\ ab\left(\kappa+\kappa'\right)\sin\left[\left(\kappa-\kappa'\right)z\right] \\ \kappa a^2 - \kappa' b^2 \end{pmatrix} \tag{A.5}$$

In the case of the incident and of the reflected wave functions we have respectively $\kappa = \kappa' = k$ and $\kappa = \kappa' = -k$. The components a and b are given by the equation A.1 and A.2. The transmitted wave function has two different wave vectors so that $\kappa = k_\uparrow$ and $\kappa' = k_\downarrow$. Its components are given equation A.3. As a result, applying these expressions to the equation A.5 with the simplifying hypothesis $k_\uparrow = k$ (see chapter 3 subsection 3.2.1 page 40), we get

$$\boldsymbol{j}_{\mathbf{s}}^{\mathbf{in}} = \frac{\hbar^2 k}{2m\Omega}\left(\sin\theta\mathbf{e_x} + \cos\theta\mathbf{e_z}\right) \tag{A.6}$$

$$\boldsymbol{j}_{\mathbf{s}}^{\mathbf{re}} = \frac{\hbar^2 k}{2m\Omega}\left(\frac{k-k_\downarrow}{k+k_\downarrow}\sin\frac{\theta}{2}\right)^2 \mathbf{e_z} \tag{A.7}$$

$$\begin{aligned}\boldsymbol{j}_{\mathbf{s}}^{\mathbf{tr}} = \frac{\hbar^2 k}{2m\Omega}\Bigg[&\sin\theta\cos\left[\left(k_\uparrow - k_\downarrow\right)z\right]\mathbf{e_x} - \sin\theta\sin\left[\left(k_\uparrow - k_\downarrow\right)z\right]\mathbf{e_y} \\ &+ \left(\cos^2\frac{\theta}{2} - \frac{4kk_\downarrow}{(k+k_\downarrow)^2}\sin^2\frac{\theta}{2}\right)\mathbf{e_z}\Bigg]\end{aligned} \tag{A.8}$$

Appendix B

Experimental setup

This appendix presents in more details the experimental setup used for the electrical measurements of the nanopillars.

The nanopillars were grown on 5 inches wafers (see figure B.1a) devided in different sectors. One sector is cutted in eight pieces each one containing around fifty nanopillars. These small pieces are mounted on a chip and connected to it using wire bonding (see figure B.1b). These chips are plugged on a sample holder (see figure B.1c) connected to the experimental setup via wire cables.

The magnetic part of the experimental setup is composed of an electromagnet with mobile poles. Between them, we built a rotating mounting for the sample holder (see figure B.1d). As a power supply, we used first a monopolar ALBS 40 V - 15 A one with a mechanical switch all remotely controlled by a computer via a data acquisition card. We changed it for a bipolar power supply Kepco BOP 72 V - 14 A more powerful controlled via the GPIB protocol to remove the mechanical switch that generated pertubations during the switching phase. With this power supply and moving the magnetic poles as close as possible from the sample, the highest magnetic field reached is around 0.7 T. This magnetic field is measured by an hall probe connected to an Agilent 34401A multimeter.

For the electric measurements, we used different configurations of equipment. To access to the dc resistance, a Keithley 2400 can play the part of both the dc current source and of the voltmeter. A gain of about one order of magnitude in the signal to noise ratio can be obtained using the combination of a Keithley 6221 or 6220 as a dc current source and a Keithley 2182A as a nanovoltmer. For the ac measurements, we used either a lock-in from Standford Research System, the SR 830, or a LakeShore 370 AC resistance bridge (see figure B.1e). The AC resistance bridge has the advantage of giving very precise measurements. However, it works at a fixed and very low frequency of 13.7 Hz so that its signal is very hard to remove from the dc measurement branche. As a results, it is very hard to measure simultaneously the ac and the dc behavior of the sample using the AC resistance bridge. On the contrary, the lock-in technic allows to choose the work frequency between 1 mHZ to 1 MHz. Since the dc equipments are not significantly affected by an ac signal of frequency starting around 1 kHz, it is a lot easier to perform dc and ac measurements at the same time. All the measurements are controlled by a computer using Labview home made programs (see figure B.1f).

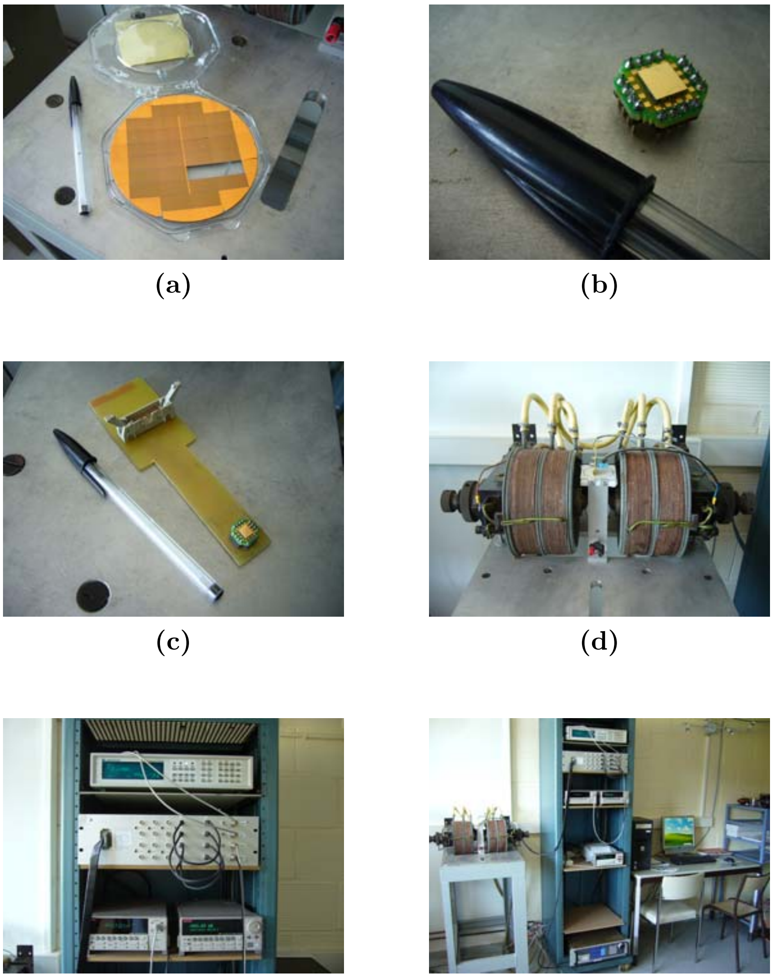

(a) **(b)** **(c)** **(d)** **(e)** **(f)**

Figure B.1 – Pictures of the experimental setup. (a) Wafer of silicon with the lithographed nanopillars. (b) Chip with a small piece of wafer paste on it with two nanopillars connected with wire bonding. (c) Sample holder to connect the nanopillar to the experimental setup. (d) Electromagnet with the rotating mounting and the sample holder. (e) Electric equipments for the resistance measurements (f) General overview of the experimental setup.

Appendix C

Calculation of the effective fields

The effective field appearing in the LLG and LLGS equations is related to the energy of the magnetic system by the following relation in the basis $(\mathbf{e}_\mathrm{x}, \mathbf{e}_\mathrm{y}, \mathbf{e}_\mathrm{z})$

$$\boldsymbol{H}_{\mathbf{eff}} = -\frac{1}{\mu_0 M_\mathrm{s} V}\frac{\partial E}{\partial \boldsymbol{m}} = -\frac{1}{\mu_0 M_\mathrm{s} V}\begin{pmatrix} \frac{\partial E}{\partial m_\mathrm{x}} \\ \frac{\partial E}{\partial m_\mathrm{y}} \\ \frac{\partial E}{\partial m_\mathrm{z}} \end{pmatrix} \tag{C.1}$$

Therefore, we need to express the magnetic energy of the system as a function of the magnetization components.

C.1 In the uniaxial modeling

In the uniaxial modeling of the spin-valves with perpendicular magnetizations, the magnetic energy is given by (see section 8.2 page 93)

$$E(\theta, H) = KV\sin^2\theta - \mu_0 M_s V H\cos\theta \tag{C.2}$$

$$= KV\left(1-\cos^2\theta\right) - \mu_0 M_\mathrm{s} V H\cos\theta \tag{C.3}$$

with V the volume of the free layer. This expression can be rewritten as a function of m_z.

$$E(\boldsymbol{m}, H) = KV\left(1-m_\mathrm{z}^2\right) - \mu_0 M_\mathrm{s} V H m_\mathrm{z} \tag{C.4}$$

As a result, the effective field corresponding to this magnetic energy is given in the basis $(\mathbf{e}_\mathrm{x}, \mathbf{e}_\mathrm{y}, \mathbf{e}_\mathrm{z})$ by

$$\boldsymbol{H}_{\mathbf{eff}} = \left(H + \frac{2K}{\mu_0 M_\mathrm{s}} m_\mathrm{z}\right)\mathbf{e}_\mathrm{z} = \left(H + H_\mathrm{c}\cos\theta\right)\mathbf{e}_\mathrm{z} \tag{C.5}$$

C.2 With a tilted magnetic field

In the non-uniaxial modeling with a tilted applied magnetic field, the magnetic energy is given by (see section 8.4 page 102)

$$\begin{aligned} E(\theta, H) &= KV\sin^2\theta - \mu_0 M_\mathrm{s} V \boldsymbol{m}\cdot\boldsymbol{H} && \text{(C.6)}\\ &= KV\left(1-\cos^2\theta\right) - \mu_0 M_\mathrm{s} V H\left(\sin\theta\sin\phi\sin\Psi + \cos\theta\cos\Psi\right) && \text{(C.7)} \end{aligned}$$

with V the volume of the free layer. This expression can be rewritten as a function of m_y and m_z.

$$E(\boldsymbol{m}, H) = KV\left(1-m_\mathrm{z}^2\right) - \mu_0 M_\mathrm{s} V H\left(m_\mathrm{y}\sin\Psi + m_\mathrm{z}\cos\Psi\right) \tag{C.8}$$

As a result, the effective field corresponding to this magnetic energy is given in the basis $(\mathbf{e}_\mathrm{x}, \mathbf{e}_\mathrm{y}, \mathbf{e}_\mathrm{z})$ by

$$\boldsymbol{H}_\mathbf{eff} = (H\sin\Psi)\,\mathbf{e}_\mathrm{y} + (H\cos\Psi + H_\mathrm{c}\cos\theta)\,\mathbf{e}_\mathrm{z} \tag{C.9}$$

C.3 With a tilted easy anisotropy axis

In the non-uniaxial modeling with a tilted anisotropy axis, the magnetic energy is given by (see section 9.1.2 page 111)

$$E(\theta, H) = KV\left[1-(\boldsymbol{m}\cdot\boldsymbol{u})^2\right] - \mu_0 M_\mathrm{s} V H\cos\theta \tag{C.10}$$

with V the volume of the free layer and $\boldsymbol{u}$ an unit vector in the direction of the easy anisotropy axis (see figure 9.2). We have $(\boldsymbol{m}\cdot\boldsymbol{u})^2 = \sin^2\lambda\sin^2\theta\sin^2\phi + \cos^2\lambda\cos^2\theta + \sin(2\lambda)\sin\theta\sin\phi\cos\theta$. Then, the expression of the magnetic energy of the system can be rewritten as a function of m_y and m_z.

$$\begin{aligned} E(\boldsymbol{m}, H) = KV\left(1 - m_\mathrm{y}^2\sin^2\lambda - m_\mathrm{z}\cos^2\lambda - \sin(2\lambda)\,m_\mathrm{y}m_\mathrm{z}\right)&\\ - \mu_0 M_\mathrm{s} V H m_\mathrm{z}& \qquad \text{(C.11)} \end{aligned}$$

Consequently, in the basis $(\mathbf{e}_\mathrm{x}, \mathbf{e}_\mathrm{y}, \mathbf{e}_\mathrm{z})$ the effective field corresponding to this magnetic energy is given by

$$\begin{aligned} \boldsymbol{H}_\mathbf{eff} = \left[H_\mathrm{c}\sin\lambda\left(\sin\lambda\sin\theta\cos\phi + \cos\lambda\cos\theta\right)\right]\mathbf{e}_\mathrm{y}&\\ + \left[H + H_\mathrm{c}\cos\lambda\left(\sin\lambda\sin\theta\cos\phi + \cos\lambda\cos\theta\right)\right]\mathbf{e}_\mathrm{z}& \qquad \text{(C.12)} \end{aligned}$$

Appendix D

Energetic analysis with a tilted magnetic field

This appendix presents the results of the energetic analysis in a non-unixial case where the breaking of the uniaxial symmetry is due to an applied magnetic field in the yz plane at an angle Ψ toward the perpendicular direction (see figure 8.7 page 102). The calculations in figure D.1 we performed with $\Psi = 45°$ to get an exact value for the switching field when no current is injected ($\frac{H_\mathrm{c}}{2}$) and to make the evolution more visible.

The upper part of figure D.1 presents some typical aspects of the energy landscapes for different field range in a non-uniaxial case for $\phi = \frac{\pi}{2}$ that is to say a magnetization in the yz plane. This approximation is valid if the intensity of the injected current is not too high. For the following discussion, we will define $H_\mathrm{r} = \frac{H_\mathrm{c}}{2}$. Like in the tilted anisotropy axis, the extremum positions that is to say the magnetization equilibrium positions vary with the magnitude of the applied magnetic field. Similarly, when an extremum goes trough a saddle point it vanishes. For instance, if $H < H_\mathrm{r}$ the antiparallel state corresponds to a minimum of energy but, after it becomes a saddle point at $H = H_\mathrm{r}$, this equilibrium position disappears. It does not mean that there is no antiparallel state anymore but rather that the antiparallel state position jumps suddenly to a new equilibrium position which corresponds to a maximum. We will call this maximum a pseudo antiparallel state (see the upper part of figure D.1).

Let's carefully analyze the antiparallel to parallel transition. The bottom part of figure D.1 presents the evolution of the total *power* in function of the applied magnetic field in the antiparallel state for various injected current. At zero current, the total *power* evolution is similar to the uniaxial case. It has a shape close to a parabola and the small jump at $H = H_\mathrm{r}$ is simply due to the jump

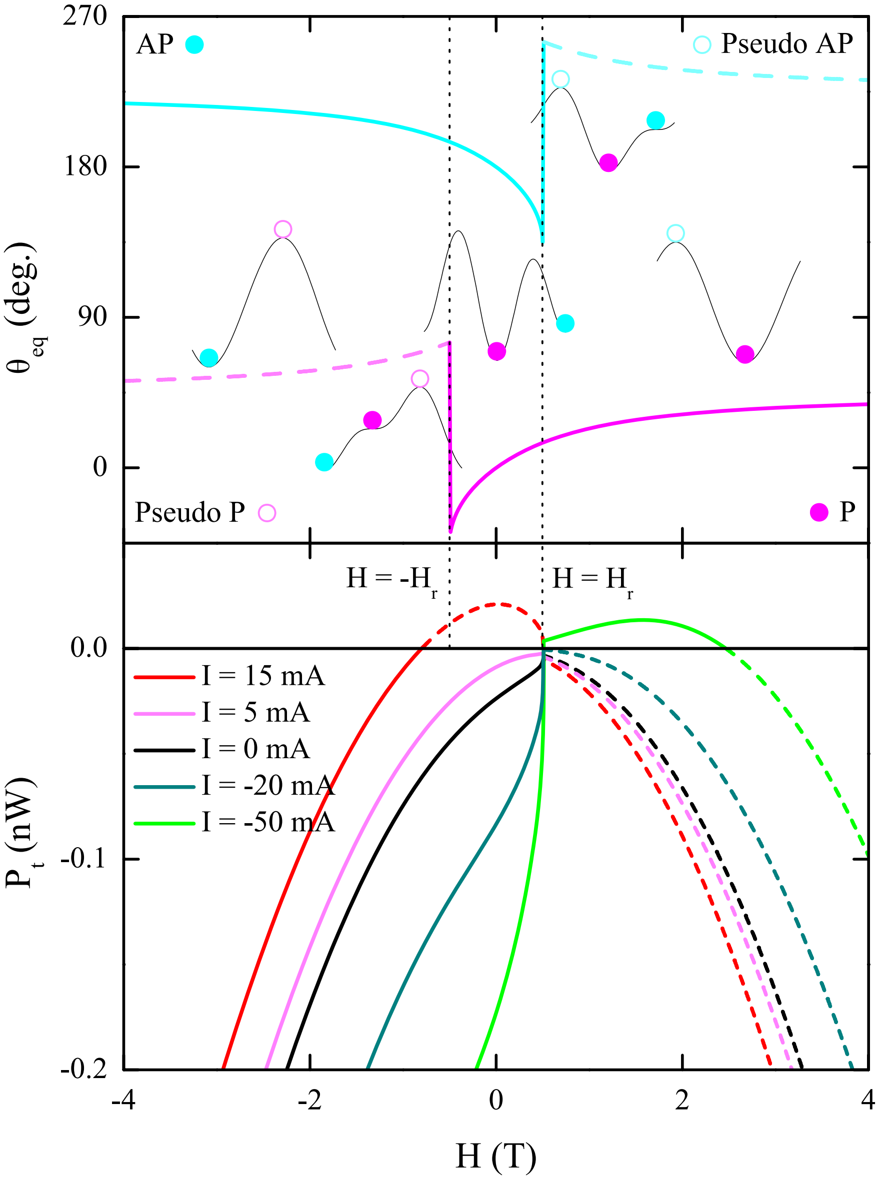

Figure D.1 – Energetic analysis a non-uniaxial case ($\Psi = 45°$). (Top) θ equilibrium positions as a function of the applied magnetic field with schematic views of the characteristic energy landscapes for different field ranges. The plain lines correspond the energy minima and the dash lines to the maxima. The circles mark on the energy landscapes the equilibrium position involved in the reversal. (Bottom) *Power* in the antiparallel state as a function of the applied magnetic field for different injected currents. The plain lines are for the *power* before the reversal to the parallel state occurs and the dash lines for after this reversal occurs.

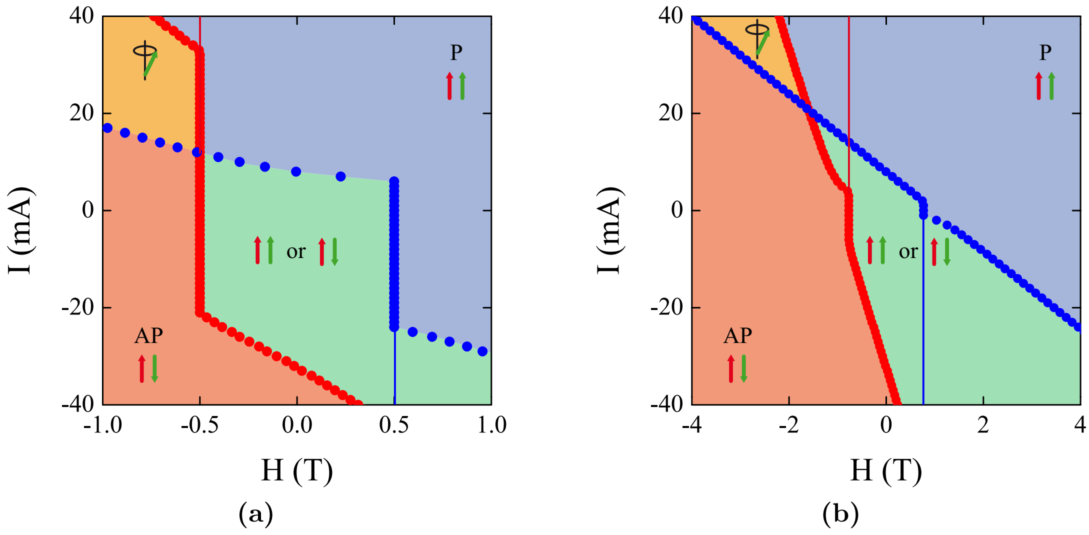

(a)

(b)

Figure D.2 – Theoretical phase diagram numerically calculated in the framework of the energetic approach for a non-uniaxial system due to a tilted applied magnetic field. (a) $\Psi = 45°$ anb (b) $\Psi = 5°$. The vertical lines mark the transitions to a pseudo magnetic state.

of the antiparallel to pseudo antiparallel state mentioned previously. The total *power* is always negative so, like in the uniaxial case, the switching occurs when the antiparallel state becomes a maximum at $H = H_\mathrm{r}$. Indeed, in the absence of current the system has no energy to reach the pseudo antiparallel state. Like in the tilted anisotropy case, the total *power* is strictly negative. It never tends to zero which means that if the injected current is not high enough, the total *power* will remain negative and the switching process will be the same as if they were no current. The reversal will still occur at $H = H_\mathrm{r}$. This is the key difference with the uniaxial case common to every system where the uniaxial symmetry is broken. Therefore, the injected current has to exceed a critical value for each polarity to affect the magnetization switching. The physical origin of this phenomenon is that the total *power* received by the magnetization when no current is injected through the structure, that is to say the *power* dissipated by the damping torque is never equal to zero. Above these thresholds, a positive current will reduce the switching field and a negative current will increase it like in the uniaxial case.

Figure D.2 presents the theoretical phase diagram numerically calculated with this method for $\Psi = 45°$ and for $\Psi = 5°$. Around the zero current reversal fields $-H_\mathrm{r}$ and H_r, the magnetization switching is not affected by the the injected current unless it reaches critical values. Above these values the switching current quickly starts to evolve linearly. Besides, the presence of the pseudo magnetic states also explains the presence of some pics in the differential resistance measurements that seems to align in the continuity of the vertical lines (see the lines in figure D.2a and figure D.2b).

Appendix E

Micromagnetic simulations

We performed our micromagnetic simulations on a commercial software named *LLG Micromagnetic Simulator* based on the Scheinfein code. This software uses the

The volume used for the simulations is a 100 nm by 200 nm rectangle with a thickness of 12 nm divided in cells of 4 nm by 4nm with a thickness of 3 nm. We cut an hexagonal shape in this rectangle to form a 100 nm by 200 nm hexagon with a thickness of 12 nm (see figure E.1). The hard layer is 6 nm thick and the free layer is 3 nm thick. They are separated by a 3nm thick non-magnetic space.

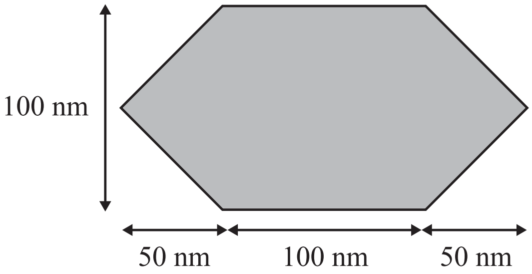

Figure E.1 – Scheme the mask used to define the hexagonal nanopillar

The magnetic properties of the hard and free layer are sumed up in the table below. For both layers the intra-layer exchange between cells was $A_{\mathrm{exc}} = 2 \times 10^{-6}$ erg.cm^{-1}, the polarization $P = 0.35$ and the damping constant $\alpha = 0.1$. The calculations were carried out assuming zero temperature and sweeping either the current or the magnetic field.

Properties	Hard layer	Free layer
M_{s}	500 emu.cm^{-3}	650 emu.cm^{-3}
K	3.3×10^{6} erg.cm^{-3}	2.5×10^{6} erg.cm^{-3}

Bibliography

[1] M. N. Baibich, J.M. Broto, A. Fert, F. Nguyen Van Dau, F. Petroff, P. Etienne, G. Creuzet, A. Friederich, and J. Chazelas, *Phys. Rev. Lett.* **61**, 2472 (1988).

[2] G. Binasch, P. Grünberg, F. Saurenbach, and W. Zinn, *Phys. Rev. B* **39**, 4828 (1989).

[3] L. Berger, *Phys. Rev. B* **54**, 9353 (1996).

[4] J. C. Slonczewski, *J. Magn. Magn. Mater.* **159**, L1 (1996).

[5] J. A. Katine, F. J. Albert, R. A. Buhrman, E. B. Myers, and D. C. Ralph, *Phys. Rev. Lett.* **84**, 3149 (2000).

[6] M. Tsoi, A. G. M. Jansen, J. Bass, W.-C. Chiang, M. Seck, V. Tsoi, and P. Wyder, *Phys. Rev. Lett.* **80**, 4281 (1998).

[7] M. Tsoi, AGM Jansen, J. Bass, W.C. Chiang, V. Tsoi, and P. Wyder, *Nature* **406**, 46 (2000).

[8] S. I. Kiselev, J. C. Sankey, I. N. Krivorotov, N. C. Emley, R. J. Schoelkopf, R. A. Buhrman, and D. C. Ralph, *Nature* **425**, 380 (2003).

[9] V. S. Pribiag, I. N. Krivorotov, G. D. Fuchs, P. M Braganca, O. Ozatay, J. C. Sankey, Ralph D. C., and R. A. Buhrman, *Nat. Phys.* **3**, 498 (2007).

[10] L. Gan, S. H. Chung, K. Aschenbach, M. Dreyer, and R. D. Gomez, *IEEE Trans. Magn.* **36**, 3047 (2000).

[11] J. Grollier, P. Boulenc, V. Cros, A. Hamzić, A. Vaurès, A. Fert, and G. Faini, *Appl. Phys. Lett.* **83**, 509 (2003).

[12] S.S.P. Parkin, M. Hayashi, and L. Thomas, *Science* **320**, 190 (2008).

[13] S. Mangin, Y. Henry, D. Ravelosona, J. A. Katine, and Eric E. Fullerton, *Appl. Phys. Lett.* **94**, 012502 (2009).

[14] S. Mangin, D. Ravelosona, J. A. Katine, M. J. Carey, B. D. Terris, and E. E. Fullerton, *Nat. Mater.* **5**, 210 (2006).

[15] T. Seki, S. Mitani, K. Yakushiji, and K. Takanashi, *Appl. Phys. Lett.* **88**, 172504 (2006).

[16] H. Meng and J.-P. Wang, *Appl. Phys. Lett.* **88**, 172506 (2006).

[17] E. C. Stoner, *Proc. R. Soc. Lond. A* **165**, 372 (1938).

[18] P. Fischer, T. Elmüller, G. Schütz, P. Guttmann, G. Schmahl, K. Pruegl, and G. Bayreuther, *J. Phys. D: Appl. Phys.* **31**, 649 (1998).

[19] E. C. Stoner and E. P. Wohlfarth, *Proc. R. Soc. Lond. A* **240**, 599 (1948).

[20] L. Landau and E. Lifshitz, *Phys. Z. Sowjetunion* **8**, 153 (1935).

[21] T. L. Gilbert, *Phys. Rev.* **130**, 1677 (1963).

[22] A. Barthélémy, A. Fert, M. N. Baibich, S. Hadjoudj, F. Petroff, P. Etienne, R. Cabanel, S. Lequien, F. Nguyen Van Dau, and G. Creuzet, *J. Appl. Phys.* **58**, 2271 (1990).

[23] A. Fert and I. A. Campbell, *Phys. Rev. Lett.* **21**, 1190 (1968).

[24] A. Barthélémy, A. Fert, J.-P. Contour, M. Bowen, V. Cros, J. M. De Teresa, A. Hamsic, J. C. Faini, J. M. George, J. Grollier, F. Montaigne, F. Pailloux, F. Petroff, and C. Vouille, *J. Magn. Magn. Mater.* **242**, 68 (2002).

[25] M. Jullière, *Phys. Lett. A* **54**, 225 (1975).

[26] S. S. P. Parkin, K. P. Roche, M. G. Samant, P. M. Rice, R. B. Beyers, R. E. Scheuerlein, E. J. O'Sullivan, S. L. Brown, J. Bucchigano, D. W. Abraham, Yu Lu, M. Rooks, P. L. Trouilloud, R. A. Wanner, and W. J. Gallagher, *J. Appl. Phys.* **85**, 5828 (1999).

[27] P. C. van Son, H. van Kempen, and P. Wyder, *Phys. Rev. Lett.* **58**, 2271 (1987).

[28] T. Valet and A. Fert, *J. Magn. Magn. Mater.* **121**, 378 (1993).

[29] T. Valet and A. Fert, *Phys. Rev. B* **48**, 7099 (1993).

[30] Luc Berger, *J. Appl. Phys.* **49**, 2156 (1978).

[31] Luc Berger, *J. Appl. Phys.* **50**, 2137 (1979).

[32] P. P. Freitas and Luc Berger, *J. Appl. Phys.* **57**, 1266 (1985).

[33] C.-Y. Hung and Luc Berger, *J. Appl. Phys.* **63**, 4276 (1988).

[34] L. Berger, *J. Appl. Phys.* **81**, 4880 (1997).

[35] X. Waintal, E. B. Myers, P. W. Brouwer, and Ralph D. C., *Phys. Rev. B* **62**, 12317 (2000).

[36] X. Waintal and P. W. Brouwer, *Phys. Rev. B* **63**, R220407 (2001).

[37] S. Zhang, P. M. Levy, and A. Fert, *Phys. Rev. Lett.* **88**, 236601 (2002).

[38] M. D. Stiles and A. Zangwill, *Phys. Rev. B* **66**, 014407 (2002).

[39] M. D. Stiles and A. Zangwill, *J. Appl. Phys.* **91**, 6812 (2002).

[40] D. C. Ralph and M. D. Stiles, *J. Magn. Magn. Mater.* **320**, 1190 (2009).

[41] A. A. Kovalev, A. Brataas, and G. E. W. Bauer, *Phys. Rev. B* **66**, 224424 (2002).

[42] J. C. Slonczewski, *J. Magn. Magn. Mater.* **247**, 324 (2002).

[43] A. Fert, V. Cros, J.-M. George, J. Grollier, Jaffrès H., A. Hamzic, A. Vaurès, G. Faini, J. Ben Youssef, and H. Le Gall, *J. Magn. Magn. Mater.* **272**, 1706 (2004).

[44] Jiang Xiao, M. D. Stiles, and A. Zangwill, *Phys. Rev. B* **70**, 172405 (2004).

[45] J. Barnas, A. Fert, M. Gmitra, Weymann I., and V. K. Dugaev, *Phys. Rev. B* **72**, 024426 (2005).

[46] D. M. Edwards, F. Federici, J. Mathon, and A. Umerski, *Phys. Rev. B* **71**, 054407 (2005).

[47] J. Slonczewski, *Phys. Rev. B* **39**, 6995 (1989).

[48] T. Yan, T. Kimure, and Y. Otani, *Nat. Phys.* **4**, 851 (2008).

[49] S. Urazhdin, N. O. Birge, W. P. Pratt, and J. Bass, *Appl. Phys. Lett.* **84**, 1516 (2004).

[50] M. AlHajDarwish, H. Kurt, S. Urazhdin, A. Fert, R. Loloee, W. P. Pratt, and J. Bass, *Phys. Rev. Lett.* **93**, 157203 (2004).

[51] O. Boulle, V. Cros, J. Grollier, L. G. Pereira, C. Deranlot, F. Petroff, G. Faini, J. Barnas, and A. Fert, *Nat. Phys.* **3**, 492 (2007).

[52] S. Urazhdin and S. Button, *Phys. Rev. B* **78**, 172403 (2008).

[53] M. Gmitra and J. Barnas, *Phys. Rev. B* **72**, 012403 (2009).

[54] K. W. Cheng, C. Yu, L. K. Lin, Y. D. Yao, Y. Liou, J. H. Huang, and S. F. Lee, *Appl. Phys. Lett.* **96**, 093110 (2010).

[55] F. J. Albert, J. A. Katine, R. A. Buhrman, and D. C. Ralph, *Appl. Phys. Lett.* **77**, 3809 (2000).

[56] J. Z. Sun, D. J. Monsma, D. W. Abraham, M. J. Rooks, and R. H. Koch, *Appl. Phys. Lett.* **81**, 2202 (2002).

[57] J. Grollier, V. Cros, A. Hamzić, J. M. Georges, G. Faini, J. Ben Youssef, H. Le Gall, and A. Fert, *Phys. Rev. B* **67**, 174402 (2003).

[58] S. Urazhdin, N. O. Birge, W. P. Pratt, and J. Bass, *Phys. Rev. Lett.* **91**, 146803 (2003).

[59] J.-E. Wegrove, D. Kelly, Y. Jaccard, Ph. Guittienne, and J.-Ph. Ansermet, *Europhys. Lett.* **45**, 626 (1999).

[60] E. B. Myers, D. C. Ralph, J. A. Katine, R. N. Louie, and R. A. Buhrman, *Science* **285**, 867 (1999).

[61] W. H. Rippart, M. R. Pufall, S. Kaka, S. E. Russek, and T. J. Silva, *Phys. Rev. Lett.* **92**, 027201 (2004).

[62] D. Houssameddine, U. Ebels, B. DelaÎt, B. Rodmacq, I. Firastrau, F. Fonthenier, M. Brunet, C. Thirion, Michel J.-P., L. Prejbeanu-Buda, M.-C. Cyrille, O. Redon, and B. Dieny, *Nat. Mater.* **6**, 447 (2007).

[63] W. H. Rippart, A. M. Deac, M. R Pufall, J. M. Shaw, M. W. Keller, S. E. Russek, G. E. W. Bauer, and C. Serpico, *Phys. Rev. B* **81**, 014426 (2010).

[64] R. Law, E.-L. Tan, R. Sbiaa, T. Liew, and T. C. Chong, *Appl. Phys. Lett.* **94**, 062516 (2009).

[65] A. Kent, B. Ozyilmaz, and E. del Barco, *Appl. Phys. Lett.* **84**, 3897 (2004).

[66] K. J. Lee, O. Redon, and B. Dieny, *Appl. Phys. Lett.* **86**, 022505 (2005).

[67] J. A. Katine and Eric E. Fullerton, *J. Magn. Magn. Mater.* **320**, 1217 (2008).

[68] W. F. Jr. Brown, *Phys. Rev.* **100**, 1243 (1955).

[69] G. Grinstein and R. H. Koch, *Phys. Rev. Lett.* **90**, 207201 (2003).

[70] L. Néel, *Ann. Geophys.* **5**, 99 (1949).

[71] H.-J. Suh, C. Heo, C.-Y. You, and W. Kim, *Phys. Rev. B* **78**, 064430 (2008).

[72] W. T. Coffey, D. S. F. Crothers, J. L. Dormann, L. J. Geoghegan, and E. C. Kennedy, *Phys. Rev. B* **58**, 3249 (1998).

[73] Y. P. Kalmykov, W. T. Coffey, B. Ouari, and S. V. Titov, *J. Magn. Magn. Mater.* **292**, 372 (2005).

[74] S. Krause, G. Herzog, T. Stapelfeldt, L. Berbil-Bautista, M. Bode, E. Y. Vedmedenko, and R. Wiesendanger, *Phys. Rev. Lett.* **103**, 127202 (2009).

[75] W. Wernsdorfer, E. Bonet Orozco, K. Hasselbach, A. Benoit, B. Barbara, N. Demoncy, A. Loiseau, H. Pascard, and D. Mailly, *Phys. Rev. Lett.* **78**, 1791 (1997).

[76] J. Sun, *IBM J. Res. & Dev.* **50**, 81 (2006).

[77] Z. Li and S. Zhang, *Phys. Rev. B* **69**, 134416 (2004).

[78] D. M. Apalkov and P. B. Visscher, *Phys. Rev. B* **72**, 180405(R) (2005).

[79] D. M. Apalkov and P. B. Visscher, *J. Magn. Magn. Mater.* **286**, 370 (2005).

[80] E. B. Myers, F. J. Albert, J. C. Sankey, E. Bonet, R. A. Buhrman, and D. C. Ralph, *Phys. Rev. Lett.* **89**, 196801 (2002).

[81] S. Urazhdin, N. O. Birge, W. P. Jr. Pratt, and J. Bass, *Phys. Rev. Lett.* **91**, 146803 (2003).

[82] S. Urazhdin, H. Kurt, W. P. Jr. Pratt, and J. Bass, *Appl. Phys. Lett.* **83**, 114 (2003).

[83] A. Fábián, C. Terrier, S. Serrano Guisan, X. Hoffer, M. Dubey, L. Gravier, J.-P. Ansermet, and J.-E. Wegrowe, *Phys. Rev. Lett.* **91**, 257209 (2003).

[84] I. N. Krivorotov, N. C Emley, A. G. F. Garcia, J. C. Sankey, S. I. Kiselev, D. C. Ralph, and R. A. Buhrman, *Phys. Rev. Lett.* **93**, 166603 (2004).

[85] W. L. Lim, N. Anthony, A. Higgings, and S. Urazhdin, *Appl. Phys. Lett.* **92**, 172501 (2008).

[86] M. Eltschka, M. Wötzel, J. Rhensius, S. Krzyk, U. Nowak, M. Kläui, T. Kasama, R. E. Dunin-Borkowski, L. J. Heyderman, H. J. van Driel, and R. A. Duine, *Phys. Rev. Lett.* **105**, 056601 (2010).

[87] D. Bedau, H. Liu, J. Z. Sun, E. E. Fullerton, S. Mangin, and A. D. Kent, *to be published.*

[88] C. Chappert and P. Bruno, *J. Appl. Phys.* **64**, 5736 (1988).

[89] L. Néel, *J. Phys. Rad.* **15**, 376 (1954).

[90] U. Gradmann, *J. Magn. Magn. Mater.* **54**, 733 (1986).

[91] P. F. Carcia, A. D. Meinholdt, and A. Suna, *Appl. Phys. Lett.* **47**, 178 (1985).

[92] P. F. Carcia, *J. Appl. Phys.* **63**, 5066 (1988).

[93] G. H. O. Daalderop, P. J. Kelly, and F. J. A. den Broeder, *Phys. Rev. Lett.* **68**, 682 (1992).

[94] Y. B. Bazaliy, B. A. Jones, and S. C. Zhang, *J. Appl. Phys.* **89**, 6793 (2001).

[95] Y. B. Bazaliy, B. A. Jones, and S. C. Zhang, *Phys. Rev. B* **69**, 094421 (2004).

[96] H. Morise and S. Nakamura, *Phys. Rev. B* **71**, 014439 (2005).

[97] J. Xiao, A. Zangwill, and M. D. Stiles, *Phys. Rev. B* **72**, 014446 (2005).

[98] Ru Zhu and P. B. Visscher, *J. Appl. Phys.* **103**, 07A722 (2008).

[99] Y. Henry, S. Mangin, J. Cucchiara, J. A. Katine, and Eric E. Fullerton, *Phys. Rev. B* **79**, 214422 (2009).

[100] Grollier J., V. Cros, A. Hamzic, J. M. George, H. JaffrËs, A. Fert, G. Faini, B. Ben Youssef, and H. Legall, *Appl. Phys. Lett.* **78**, 3663 (2001).

[101] D. Chiba, Y. Sato, T. Kita, F. Matsukura, and H. Ohno, *Phys. Rev. Lett.* **93**, 216602 (2004).

[102] J. Miltat, G. Albuquerque, A. Thiaville, and C. Vouille, *J. Appl. Phys.* **89**, 6982 (2001).

[103] D. V. Berkov and N. L. Gorn, *Phys. Rev. B* **72**, 094401 (2005).

[104] D. Ravelosona, S. Mangin, Y. Lemaho, J. A. Katine, B. D. Terris, and Eric E. Fullerton, *Phys. Rev. Lett.* **96**, 186604 (2006).

[105] D Ravelosona, S. Mangin, Y. Henry, Y. Lemaho, J. A. Katine, B. D. Terris, and Eric E. Fullerton, *J. Phys. D: Appl. Phys.* **40**, 1253 (2007).

[106] T. Seki, S. Mitani, and K. Takanashi, *Phys. Rev. B* **77**, 214414 (2008).

[107] D. P. Bernstein, B. Brauer, R. Kukreja, J. Stohr, T. Hauet, J. Cucchiara, S. Mangin, J. A. Katine, T. Tyliszczak, K. W. Chou, and Y. Acremann, *to be published.*

[108] D. Ravelosona, D. Lacour, J. A. Katine, B. D. Terris, and C. Chappert, *Phys. Rev. Lett.* **95**, 117203 (2005).

[109] P. Gaunt, *J. Appl. Phys.* **59**, 4129 (1986).

[110] J.-P. Jamet, S. Lemerle, S. Meyer, Ferré J., Bartenlian B., N. Bardou, C. Chappert, P. Veillet, F. Rousseaux, D. Decanini, and H. Launois, *Phys. Rev. B* **57**, 14320 (1998).

[111] Boulle O., J. Kimling, P. Warnicke, M. Kläui, U. Rüdiger, G. Malinowski, H. J. M. Swagten, B. Koopmans, Ulysse C., and G. Faini, *Phys. Rev. Lett.* **101**, 216601 (2008).

[112] J. Ferré, "Spin dynamics in confined magnetic structures I," (Springer, New York, 2002) p. 127.

[113] D Ravelosona, S. Mangin, J. A. Katine, Eric E. Fullerton, and B. D. Terris, *Appl. Phys. Lett.* **90**, 072508 (2007).

[114] A. V. Khvalkovskiy, K. A. Zvezdin, Ya. V. Gorbunov, V. Cros, J. Grollier, A. Fert, and A. K. Zvezdin, *Phys. Rev. Lett.* **96**, 067206 (2009).

[115] C. T. Boone, J. A. Katine, M. Carey, J. R. Childress, X. Cheng, and I. N. Krivorotov, *Phys. Rev. Lett.* **102**, 097203 (2010).

Spin-transfer effects in nanopillars with perpendicular magnetizations

The discover of spin-transfer opens a new way to control the magnetization of a nanomagnet using a spin polarized current instead of a magnetic field. Many studies showed that it is particularly efficient in nanopillar spin-valves with perpendicular magnetizations. Therefore, we decided to analyse into more details the impact of a spin polarized current on these devices during this thesis

First, we were interested in a global approach of the behavior of these systems based on the understanding of their field and current phase diagrams. Comparing our experimental results with various theoretical predictions, we demonstrated that their main features are explained by a breaking of the uniaxial symmetry of the spin-valves due, for instance, to a non-perpendicular anisotropy axis or applied magnetic field. Moreover, we developed a purely energetic description of these devices allowing to understand simply the physical origin of their behavior.

Then, we focused on the magnetization reversal process of these nanopillars dominated by a domain nucleation followed by a domain wall propagation. We combined for this study the analysis of a thermally activated phenomenon called telegraph noise, of phase diagrams and of micromagnetic simulations. They all lead to the conclusion that the nucleation process is well described by a Stoner-Wohlfarth behavior whereas the propagation process seems very dependent on the structure of the domain wall especially for the action of the spin-transfer.

Keywords: Spintronics, Spin-transfer, Magnetic domain wall, Perpendicular magnetocrystalline anisotropy, Telegraph noise

Effets de transfert de spin dans des nanopiliers aux aimantations perpendiculaires

Le transfert de spin ouvre la voie à un nouveau contrôle de l’aimantation d’un nanoaimant utilisant un courant polarisé en spin plutôt qu’un champ magnétique. Plusieurs travaux ont montré l’efficacité de ce phénomène dans des nanopiliers aux aimantations perpendiculaires. Par conséquent, nous avons décidé pour cette thèse d’analyser en détail l’effet du transfert de spin sur ces dispositifs.

Dans un premier temps, nous nous sommes intéressés à une approche globale du comportement de ces systèmes basée sur l’étude de leurs diagrammes de phase courant-champ. Grâce à la comparaison de nos données expérimentales avec différentes prédictions théoriques nous avons démontré que la plupart de nos observations sont expliquées par la brisure de la symmétrie uniaxiale de nos systèmes engendrée sans doute par un axe d’anisotropie et/ou un champ magnétique non-perpendiculaires. De plus, nous avons développé une description purement énergétique de ces dispositifs permettant de comprendre simplement l’origine physique de leur comportement.

Dans un deuxième temps, nous nous sommes intéresés au processus de retournement de l’aimantation de ces nanopiliers commençant par la nucléation d’un domaine et se poursuivant par la propagation d’une paroi de domaine. Notre étude combine les analyses de phénomènes thermiquement activés, de diagrammes de phase et de simulations micromagnétiques. Elles tendent toutes à montrer que le processus de nucléation est proche d’un comportement de type Stoner-Wohlfarth alors que le processus de propagation semble très dépendant de la structure de la paroi de domaine en particulier pour l’action du transfert de spin.

Mots-clés : Electronique de spin, Transfert de spin, Domaines magnétiques, Anisotropie magnéto-cristalline perpendiculaire, Bruit télégraphique